



# A. Yücel Odabaşı Colloquium Series

## ***4<sup>th</sup> International Meeting Proceedings Ship Design & Optimization and Energy Efficient Devices for Fuel Economy***

15 - 16 DECEMBER 2022

Faculty of Naval Architecture and Ocean Engineering

ISTANBUL TECHNICAL UNIVERSITY

[www.ayocol.itu.edu.tr](http://www.ayocol.itu.edu.tr)

Edited by

Ömer GÖREN  
Devrim Bülent DANIŞMAN  
Çağatay Sabri KÖKSAL

**İTÜ**



**250<sup>TH</sup>**  
YEAR  
1773 - 2023



İTÜ



250<sup>TH</sup> YEAR  
1773-2023

# A.Yücel ODABAŞI Colloquium Series



## 4<sup>th</sup> International Meeting

### Ship Design & Optimization and Energy Efficient Devices for Fuel Economy

**15-16**  
DECEMBER  
2022



Faculty of Naval Architecture  
and Ocean Engineering  
ITU Ayazaga Campus, Maslak,  
Istanbul, TURKEY



[www.ayocol.itu.edu.tr](http://www.ayocol.itu.edu.tr)

SCAN FOR  
PROCEEDINGS





## TABLE OF CONTENTS

SPONSORS	.....	i
PREFACE	.....	iii
COLLOQUIUM COMMITTEES	.....	v
PROF. A. YÜCEL ODABAŞI	.....	vii

### Keynote Addresses

Keynote Address 1: Holistic Approach to Ship Design <i>Apostolos D. Papanikolaou</i>	.....	1
Keynote Address 2: Ship Propelled by Waves: A Mathematical Model of a Ship with Wings Powered by Waves <i>Kirill V. Rozhdestvensky</i>	.....	13
Keynote Address 3: Design-Space Dimensionality Reduction in Shape Optimization: Recent Developments and Way Forward <i>Matteo Diez</i>	.....	15

### Papers

The Performance Prediction and Energy Saving Evaluation for the Retrofit of a Gate Rudder System on a General Cargo Vessel using CFD Procedures <i>Kurt Mizzi, Mariana Zammit Munro, Ahmet Gurkan, Batuhan Aktas, Mehmet Atlar, Noriyuki Sasaki</i>	.....	27
Computational Optimization of the Ship Hull Shape by Constrained Transformation of the Longitudinal Volume Distribution <i>Marek Kraskowski</i>	.....	37
A Systematic Optimisation on the Energy Saving Devices for Ship, in Particular, Combination of Pre-Swirl Stator (PSS) and Duct <i>Selahattin Özsayan, Çağrı Aydın, Çağatay Sabri Köksal, Emin Korkut</i>	.....	49
Assessing the Performance of Kriging and Artificial Neural Network in Simulation-based Design Optimization <i>Hayriye Pehlivan Solak, Devrim Bülent Danışman, Ömer Gören</i>	.....	57
Power Efficient Thrust Allocation Algorithms in Design of Dynamically Positioned Ships <i>Agnieszka Piekło, Anna Witkowska, Tomasz Zubowicz</i>	.....	67
Experimental Powering Performance Analysis of M/V ERGE in Calm Water and Waves <i>Çağatay Sabri Köksal, Batuhan Aktas, Ahmet Yusuf Gürkan, Emin Korkut, Noriyuki Sasaki, Mehmet Atlar</i>	.....	75

Greener shipping: An Investigation of an ORC-based Waste Heat Recovery System for a Methanol-fueled Marine Engine <i>Mehmet Akman, Selma Ergin</i>	.....	81
Low Cavitation Twisted Rudder Design for DTMB 5415 Surface Combatant <i>Mustafa Kültür, Serhan Gökçay, Ahmet Ziya Saydam, Mustafa İnsel</i>	.....	87
Data-Driven Fuel Consumption Rate Estimation by Using Deep Learning <i>Serhan Gökçay, Ahmet Ziya Saydam, Mustafa İnsel</i>	.....	97
On the Full-Scale Powering Extrapolation of Ships with Gate Rudder System (GRS) <i>Cihad Çelik, Selahattin Özsayan, Çağatay Sabri Köksal, Devrim Bülent Danışman, Emin Korkut, Ömer Gören</i>	.....	103
Predicting the Effect of Hull Roughness on Ship Resistance using a Fully Turbulent Flow Channel and CFD <i>Roberto Ravennal, Ryan Ingham, Soonseok Song, Clifton Johnston, Claire De Marco Muscat-Fenech, Tahsin Tezdogan, Mehmet Atlar, Yigit Kemal Demirel</i>	.....	109
The Effect of the Addition of Tubercles on the Performance of Moth-Tfoil <i>Margot G. C. Cocard, Sandy Day, Tahsin Tezdogan, Moritz Troll, Tonio Sant</i>	.....	119
Investigation of Gate Rudder Blade Design for Ship Powering Using the Design of Experiment (DoE) Method <i>Ahmet Yusuf Gurkan, Batuhan Aktas, Uğur Oral Unal, Mehmet Atlar</i>	.....	127

## SPONSORS



# GISBIR

## TURKISH SHIPBUILDERS' ASSOCIATION





## **PREFACE**

As a tribute to the late Professor A. Yücel Odabaşı's (1945 – 2009) life-long endeavours in promoting the science of Naval Architecture and in particular Naval Hydrodynamics, a biennial international colloquium aiming to focus on a different theme on each occasion, gathering specialists from around the world, was first organized in 2014 at Istanbul Technical University and the second and the third meetings were held in 2016 and 2018, respectively. After the interruption due to pandemia, fourth colloquium is now scheduled to take place on December 15-16, 2022. The theme of the fourth colloquium is selected as ‘Ship Design & Optimization and Energy Efficient Devices for Fuel Economy’. The goal of this colloquium would be to gather specialists and to create a platform where the recent developments in ship design and optimization, as well as in energy efficient devices are discussed and new opportunities for collaborative research are sought.

We are thankful to the key-note lecturers, to the authors and to our sponsors whose efforts and contributions made this Colloquium possible. We believe and hope that their contribution and participation to the colloquium create efficient scientific environment and fruitful discussions for those who seek to pursue research in “Ship Design & Optimization and in Energy Efficient Devices”.

Devrim Bülent Danışman

Chair

Local Organizing Committee



## **COLLOQUIUM COMMITTEES**

### **Standing Committee**

Prof. Mehmet Atlar (University of Strathclyde, UK)

Prof. Sander Çalışal (UBC, Canada and Piri Reis University)

Prof. Atilla İncecik (University of Strathclyde, UK)

Assoc.Prof. Barbaros Okan (ITU)

### **Technical Committee**

Prof. Apostolos D. Papanikolaou (NTUA, Greece)

Prof. Kirill V. Rozhdestvensky (State Marine Tech. University, Russia)

Dr. Matteo Diez (CNR-INM, Italy)

Prof. Ömer Goren (ITU)

### **Local Organizing Committee**

Assoc.Prof. D. Bülent Danışman (Chair)

Assoc.Prof. Erdem Üçer (Secretary)

Assoc.Prof. U. Oral Ünal

Assist.Prof. M. Cansın Özden

Dr. Çağatay S. Köksal

M.Sc. Deniz Öztürk



## **PROF. A. YÜCEL ODABAŞI**



(1945-2009)

Professor Odabaşı, a graduate of ITU (1967), earned his Ph.D. degree from the same university in 1971. Following his Ph.D., he joined Strathclyde University where his work on the application of Lyapunov's theory to ship stability gained him a well deserved international reputation which was acknowledged by STAB Award in 2012 post mortem. In 1974 he joined BSRA where he worked on every field of ship hydrodynamics and made significant contributions, in particular in the field of wake scaling. In 1988 he moved to USA to set up BMT International as its first director and CEO. He returned to ITU-Turkey in 1991 where he inspired a generation of young academics while at the same time succeeding to lead Turkish Lloyd to worldwide recognition. He was awarded the gold medal of NECIES-UK and numerous awards from NAVSEA, SNAME, BSRA.



## **Holistic Approach to Ship Design**

**Apostolos D. Papanikolaou<sup>1\*</sup>**

<sup>1</sup>*Ship Design Laboratory, National Technical University of Athens, Athens 15773, Greece*

**Abstract:** The recently completed Horizon 2020 European Research project—HOLISHIP—Holistic Optimization of Ship Design and Operation for Life Cycle (2016–2020) has developed suitable tools and software platforms which are necessary for the creation of innovative design solutions meeting the set low-emission strategic objectives. The present paper introduces an innovative, holistic approach to ship design and the development of integrated design software platforms and tools, which are used in practical applications. In the era of the 4th industrial revolution, this project sets out to substantially advance ship design via the introduction of a fully computerized, multi-disciplinary optimization approach to ship design and life-cycle operation. The approach enables the exploration of a huge design space in a relatively short time, as well as the distributed/multi-site working and the virtual reality testing; thus, it is a strong asset for the development of innovative maritime concepts in response to the needs of the 21<sup>st</sup> century.

**Keywords:** holistic ship design; multi-criteria optimization; innovative designs; life-cycle assessment; design software platform

## 1 INTRODUCTION

The concept of a holistic approach to ship design was introduced more than 10 years ago by the author (Papanikolaou, 2010). It is based on the philosophical notion of *holism* introduced by Aristoteles in his treatise *Metaphysics* (384 B.C.–322 B.C.). *Holism* originates from the Greek notion *ὅλος*, *holos*, meaning “all included, whole, entire” and it simply postulates that the whole is more than the sum of parts; thus, systems of different type (physical, biological, chemical, social, economic, mental, etc.) and their properties should be viewed as wholes, not just as a collection of parts. This is trivial in mathematical nonlinear systems and obvious in systems theory.

The wide implementation of a holistic approach to ship design was achieved in the EU funded project HOLISHIP (2016–2020), which is a HORIZON 2020 Large Scale RTD project. HOLISHIP stands for the “Holistic Optimization of Ship Design and Operation for Life Cycle”, and represents the joint effort of 40 European maritime RTD stakeholders: HSVA (coordinator)—Germany; ALS Marine—Greece; AVEVA—United Kingdom; BALance—Germany; Bureau Veritas—France; Cetena—Italy; Center of Mari-time Technologies—Germany; CNR—Italy; Damen—Netherlands; Danaos—Cyprus; DCNS-Naval Group—France; DLR—Germany; DNV-GL—Norway/Greece; Elomatic—Finland; Epsilon—Malta; Fraunhofer-AGP—Germany; Fincantieri—Italy; Friendship Systems—Germany; Hochschule Bremen—Germany; IRT SystemX—Germany; Institute of Shipping and Logistics—Germany; Kongsberg Mari-time—Norway; Lloyd’s Register—United Kingdom; MARIN—Netherlands; SINTEF—Norway; Meyer Werft—Germany, Navantia—Spain; National Technical University of Athens—Greece; Sirehna—France; SMILE FEM—Germany; Starbulk—Greece; TNO—Netherlands; TRITEC—United Kingdom; Uljanik—Croatia; Univ. Genoa—Italy; Univ. Liege—Belgium; Univ. Strathclyde—United Kingdom; van der Velden—Netherlands.

In the era of the 4<sup>th</sup> industrial revolution (Sullivan et al., 2020), this project sets out to substantially advance ship design by the introduction of a fully computerized, multi-disciplinary optimization approach to ship design and life-cycle operation. The approach enables the exploration of a huge design space in relatively short time, as well as investigations into the distributed/multi-site working and the virtual reality testing. Thus, it is a strong asset for the development of innovative maritime concepts in response to the needs of the 21<sup>st</sup> century. Moreover, the HOLISHIP, multi-objective optimization approach to green shipping, has been recently presented with a subset of its functionality, namely the design of two green design RoPAX case studies (Papanikolaou et al., 2022a).

## 2 HOLISHIP DESIGN APPROACH

We interpret the holistic approach to ship design, as implemented in the HOLISHIP project, as the parametric, multi-objective and multi-disciplinary optimization of maritime products for life cycle. The HOLISHIP approach

includes. virtual reality (VR) product modelling and VR prototyping. The HOLISHIP project has also enabled and demonstrated multi-disciplinary collaboration through multi-site cloud working of the integrated HOLISHIP design platforms CAESSES<sup>®</sup> and RCE<sup>®</sup>, in which a large number of design and performance simulation tools have been integrated (Papanikolaou et al., 2022b).

Ship design was in the past more an art discipline than a science, highly dependent on experienced naval architects, with good background in various fundamental and specialized scientific and engineering subjects. Inherently coupled with the design process is design optimization, namely the selection of the best solution out of many feasible ones. In traditional naval architecture, optimization means taking the best out of 2–3 feasible solutions, and it is up to the designer to make decisions about the assessment procedure and applicable decision criterion (or criteria) on the basis of his experience. Of course, the space of feasible design solutions is huge, the relevant assessment criteria are plenty and complex, as are the many feasible design constraints; after all, the assessment procedure must be rational and not intuitive, thus according with the contemporary state of the art. All this calls for a step change in the design process in naval architecture, something which has been the main objective of the HOLISHIP project.

Modern, systemic approaches to ship design consider a ship’s overall system in a modular way, namely as the assembly of a series of modules. These may be replaced by others over a ship’s life cycle either when serving a different transport/operational scenario, or when undergoing retrofitting for improved and/or safer transport services. The decomposition of the system into parts is a top-down approach and may be trivial in ship design. However, when talking of a software system supporting the entire ship design and all its components, the top-down approach becomes very complex, and the use of such software systems requires special training. Such systems are known in the CAD market and are used as advanced design tools by designers for solving problems in the maritime industry (e.g., NAPA<sup>®</sup>, FORAN<sup>®</sup>, AVEVA<sup>®</sup>, etc.).

The evolution of the HOLISHIP approach to ship design has been rather 1 a bottom-up systemic approach, operating by piecing together of sub-systems to give rise to a more complex software platform. The approach was initiated by various researchers in the 80s and its use continues to this day. It first referred to ship design optimization with respect to specific prime objectives, e.g., minimizing a ship’s structural weight, maximizing ship’s hydrodynamic performance (hydrodynamic hull form design), maximizing ship’s safety (Design for Safety and Risk-based Design), optimizing ship’s operation (Design for Operation), optimizing performance/efficiency (Design for Efficiency) and environmental protection (Design for Zero Emissions or Zero Pollution). This type of study later came to include more complex and multiple objectives, e.g., the

life-cycle economic and environmental performance (Design for Life-Cycle) (Figure 1)

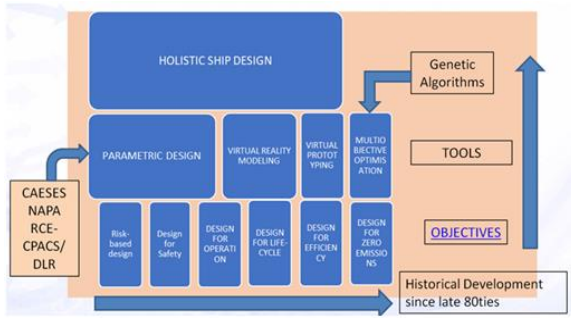


**Figure 1.** Evolution of Holistic Approach to Ship Design: Bottom-Up Systemic Approach

Several applications of the multi-objective ship design optimization approach were accomplished by the Ship Design Laboratory of NTUA under the direction of the author of this paper. They integrated well-established naval architectural and optimization software packages (e.g., NAPA®, modeFRONTIER®, CAESES®) with various application methods and software tools (Shipflow®, STAR-CCM+®, in house s/w tools), such as are necessary for the evaluation of stability, resistance, seakeeping, structural integrity, etc., as listed below. Below national and EU funded projects cover the period 1988–2022.

- Hull form optimization of high-speed mono- and twin hulls for least resistance, wave wash and best seakeeping (AEGEAN QUEEN SWATH, EU VRSHIP-ROPAX2000, EU FLOWMART, EU TrAM).
- Optimization of the compartmentation of RoPax and cruise vessels for increased damage stability and survivability, minimum potential loss of lives (PLL) (EU SAFER-EURORO, EU ROROPROB, EU NEREUS, EU GOALDS, EMSA).
- Optimization of arrangements of containerships for the maximum number of deck-containers, least overstowage and minimum ballast (GL-CONTIOPT).
- Optimization of naval ships for increased survivability in case of damage in seaways and least structural weight (NAVAL OPT).
- Optimization of an LNG floating terminal (FSRU) for reduced motions and wave attenuation on terminal's lee side (EU GIFT).
- Logistics-based optimization of ship design (EU LOGBASED).
- Risk-based design optimization of tankers for increased cargo capacity, least environmental impact, minimum ballast (EU SAFEDOR, GL-BEST).

This evolution was enabled by the parallel development of IT technology and soft-ware tools, encompassing the parametric modelling and design, virtual reality modelling and prototyping, along with multi-objective optimization tools on the basis of genetic algorithms. Several of these types of software tools are nowadays integrated into

advanced design software platforms, e.g., in the frame of HOLISHIP:

- the CAESES® platform of Friendship Systems (<https://www.friendship-sys-tems.com/products/caeses/>, accessed on 9th November 2022),
- the NAPA® platform of NAPA Oy (<https://www.napa.fi>, accessed on 9th November 2022)
- the RCE®/CPACS® platform of DLR (Deutsche Luft- und Raumfahrt, [https://www.dlr.de/sc/desktopdefault.aspx/tabid-5625/9170\\_read-17513/](https://www.dlr.de/sc/desktopdefault.aspx/tabid-5625/9170_read-17513/), accessed on 9th November 2022)
- the CADMATIC® platform of Elomatic (<https://www.cadmatic.com/en/>, accessed on 9th November 2022)
- the SAR® platform of Naval Group (Le Néna et al., 2019)

The above design platforms are all integrated into the HOLISHIP design framework, enabling their communication, the interchange in data and the use of tools/design procedures, as necessary for the address of a specific design tasks related to a ship or a maritime product in general. As an example, the interchange in data with the powerful naval architectural software package NAPA® is herein particularly highlighted. This is enabled by the development of dedicated macros (coded design procedures) for specific design tasks. These macros enable researchers to conduct of complex naval architectural calculation and design procedures, like the evaluation of the intact/damage ship stability and the preliminary structural design by NAPA®. Consequently, results are transferred to CAESES® for design synthesis, processing/optimization and final assessment (Figure 2).

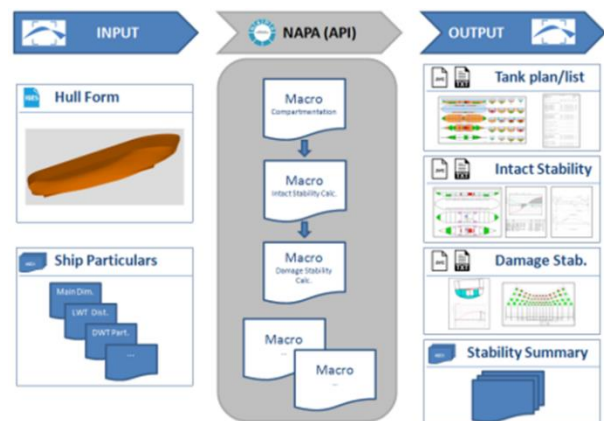


**Figure 2.** HOLISHIP Collaborating platforms CAESES and NAPA. Intact and damage stability determined by NAPA; pre- and postprocessing conducted by CAESES, NTUA & Hochschule Bremen (HSB) (Zaraphonitis et al., 2019).

For the simulation of ship's energy management, the software tool Bureau Veritas SEECAT® may be used. In Figure 3, the simulation of the energy management of a hybrid diesel-engine/battery driven double-ended ferry is schematically shown. It enables the comparison of

alternative propulsion plants (conventional diesel engines, hybrid diesel/battery system and full electrical/battery system) with respect to the overall energy management efficiency, CAPEX/OPEX and environmental impact (greenhouse gas emissions) (Jokinen et al., 2021).

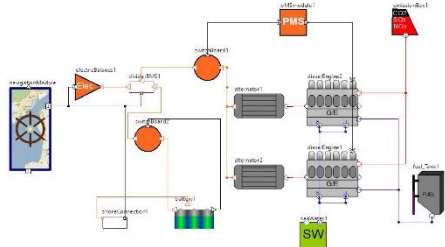


**Figure 3.** SEECAT<sup>®</sup>—Simulation of Energy Management of Hybrid DE Ferry (BV-Elomatic).

The COSMOS<sup>®</sup> tool of Det Norske Veritas (DNV) (<https://www.dnv.com/news/dnv-gl-introduces-next-generation-energy-efficiency-methodology-6607>, accessed on 9th November, 2022) has been also integrated into the CAESSES<sup>®</sup> platform and has been used in other application cases.

A synthesis of tools for the simulation of ship maneuvering and virtual prototyping of two alternative rudders has been realized with the Bridge Simulator of MARIN (Figure 4). Thereby, the following tools have been integrated into the RCE (Remote Component Environment of DLR) platform:

- CPACS<sup>®</sup>: Common Parametric Aircraft Configuration Schema of DLR
- HOLISPEC<sup>®</sup>: Marine Version of CPACS developed in HOLISHIP
- GES<sup>®</sup>: the initial design software tool of TNO
- CFD ReFresco and other maneuvering simulation tools of MARIN
- Rudder design tools of Damen MC

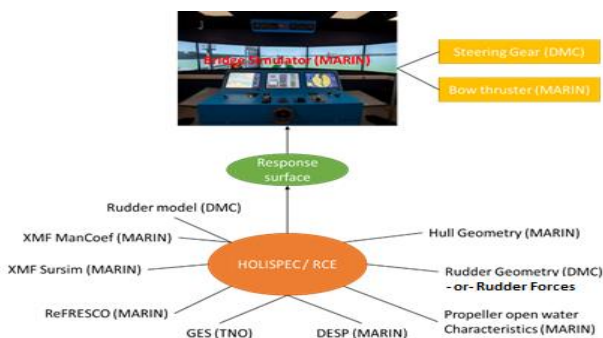


**Figure 4.** Simulation of Ship Maneuvering and Virtual Prototyping of Rudders (MARIN) (Hooijmans et al., 2021).

The Life-Cycle Cost and Environmental Impact Assessment of HOLISHIP is being conducted by the developed LCPA tool, a joint development of BALANCE, EPSILON and CETENA (Figure 5).

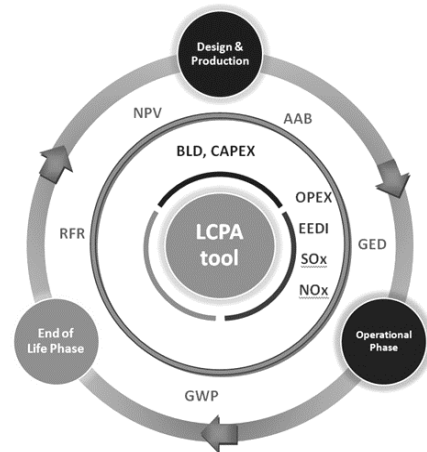


**Figure 5.** Stages of a vessel life cycle and HOLISHIP LCPA tool (Maggioncalda et al., 2019).

### 3 SHIP DESIGN OPTIMIZATION

Optimization is an inherent attribute of ship design, even though in practice we often may encounter feasible, but not optimal (or only partly optimal), design solutions. When considering ship design over a ship’s life cycle, we split the design procedure into various stages that are traditionally composed of the concept/preliminary design, the contractual and detailed design, the ship construction/fabrication process, and the ship’s operation with possible retrofitting and finally scrapping/recycling (“from cradle to grave or back to cradle”). It is evident that the optimal ship, with respect to her whole life cycle is the outcome of a holistic optimization of the entire, above-defined ship system over its life cycle. It is noted that mathematically, every constituent of the above defined life-cycle ship system evidently itself forms a complex nonlinear optimization problem for the ensuing design variables, with a variety of constraints and criteria/objective functions to be jointly optimized.

The traditional approach to ship design may be represented by the design spiral of J. H. Evans (1959), even if outdated by today’s state of the art (Nowacki, 2019). It is an iterative, serial and gradually effort-increasing process that moves from the concept design, to the preliminary, contract and detailed designs (Figure 6a, (Taggart,1980 & Papanikolaou, 2014)). Characteristically, when moving to the next stage, the effort in manpower increases by a factor between 12 to 17. Even if the cited manpower/days data refer to the manual design of ship in the late 50s and they are nowadays reduced by a factor in the range 15–20 in view of modern CAD systems, the relationships with respect to the comparable effort in the different design stages remain unchanged.

In contrast to the serial processing of the design spiral, the HOLISHIP approach adopts the parallel processing and synthesis of design tools, as elaborated in Figure 6b [Nowacki, 2010) , Harries & Abt, 2019].

Characteristically, the processing of the various design steps is conducted in parallel with fully automated or semi-automated procedures calling a core ship database embedded in the used design platform. The depth of the assessment of a specific ship design attribute, e.g., ship's hydrodynamic performance, can be adjusted to high accuracy at early design stage.

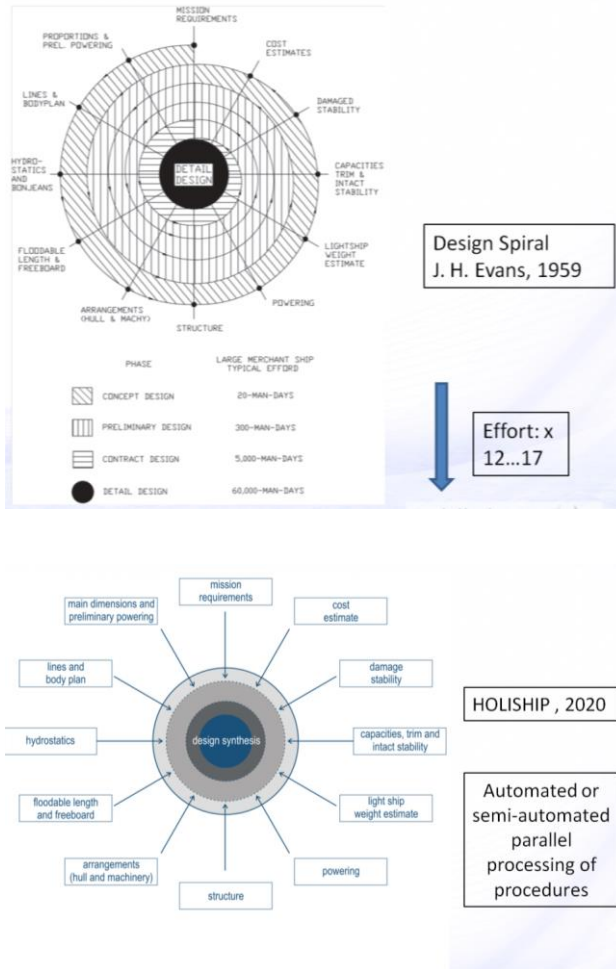


**Figure 6.** (a) Design Spiral/Serial Processing (Taggart, 1980). (b) Design Synthesis/Parallel Processing (Harries & Abt, 2019).

The progress of ship design optimization in the last 5 decades has been revolutionary and in line with developments in the IT hardware and software knowledge, moving from single-objective optimization for the required freight rate (RFR) of a tanker (Nowacki & Brusis, 1970) to multi-objective ship design optimization of various types of ships for a variety of criteria (Figure 7a,b).

An important feature of the multi-objective optimization procedure presented in Figure 7b is the Parametric Ship Modelling, namely the variation of design parameters for the generation of digital “siblings” (Figure 8). This refers to the variation in the ship’s geometry, in space and main outfitting arrangements, in main structural elements, etc. by the use of selected design parameters that are optimized

in the frame of a defined optimization procedure. Digital “siblings” are higher-level digital “twins”, with enough modelling accuracy to allow for the exploration of the huge design space in the frame of a global optimization procedure.

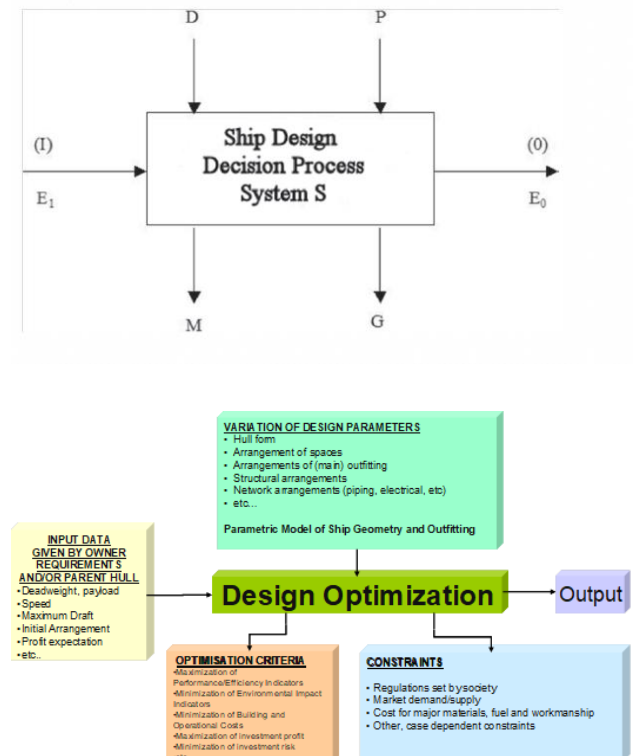


**Figure 7.** (a) Ship Design from Single- to Multi-Objective Optimization (Harries & Abt, 2019). (b) Ship Design from Single- to Multi-Objective Optimization (Papanikolaou, 2010).

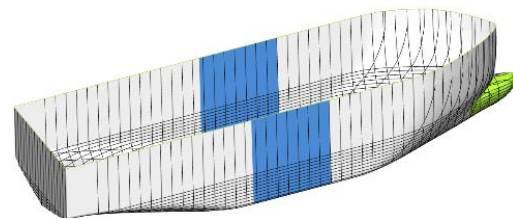


**Figure 8.** Digital Siblings: Two hull forms with lengthened and shortened parallel mid-body (shown in blue), but with identical displacement and longitudinal centers of buoyancy (Harries & Abt, 2021).

For the synthesis of software tools, the PIDO environment (Process Integration and Design Optimization) of CAESES® (www.caeses.com, accessed on 9th November, 2022) was used in HOLISHIP and in the studies presented herein (Figure 9).

CAESES® is a versatile CAD system for the parametric modeling of geometry, particularly hull forms, propulsion systems and appendages. Complementary, it is a flexible integration platform, allowing the execution of tools across operating systems and re-placing expensive simulations with fast surrogates (i.e., metamodels). The key components needed for running and combining many different design tools and simulation codes are:

- Parametric modeling and robust variation of geometry in order to run design studies (variable geometry);
- Conversion and preparation of data for simulations to provide geometry and information to and between various tools and codes (preprocessing);
- Flexible and easy coupling of any external tools and codes, using task-specific input and output files as templates (software connection);
- Data extraction and aggregation from tools and codes (postprocessing);
- Variant generation by means of design-of-experiments (DoE) (exploration) and optimization strategies (exploitation) along with variant management and design assessment.

The integration of tools is rather straightforward and allows for the extending of synthesis models as needed and as design processes advance. Within HOLISHIP, about two dozen different simulation codes were coupled (Nowacki & Brusis, 1970), ranging from simple spreadsheet calculations, notably using Excel (Microsoft), via potential flow-codes like NEWDRIFT+ (NTUA) and high-fidelity RANSE codes like FreSCO+ (HSVA), to computer-aided engineering platforms like NAPA (NAPA Oy) and CADMATIC (Elomatic), as well as ship energy efficiency modeling tools like SEECAT (BV) and COSMOS (DnV).

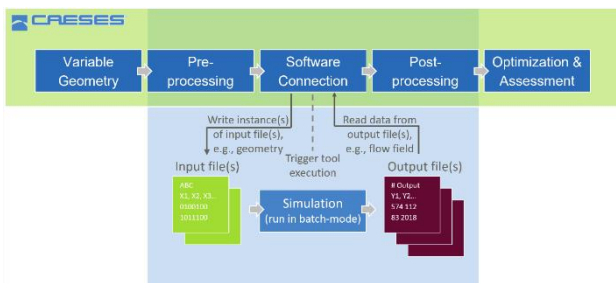


**Figure 9.** Overview of CAESES® main functionalities with a selection of integrated software systems & providers from the HOLISHIP consortium.

Several simulation codes (CFD, FEA) typically need quite a lot of execution time, dedicated licenses, special hardware (e.g., an HPC) and, very importantly, expert knowledge of how to establish and run them properly. In

general, for a design team facing a multi-disciplinary and multi-objective design task, it is far from trivial to dispose of all the software, hardware and expertise. Furthermore, a RANS simulation may take several hours per variant, while a single probabilistic damage stability analysis might still require some ten to fifteen minutes on a standard PC. Thus, if interactive study-design options are required, quickly and efficiently, the direct calculation procedure becomes prohibitive. Besides, for a formal optimization process that is executed automatically, the logistics of many tools having to run concurrently are burdensome and prone to failure. Consequently, within HOLISHIP a new approach was investigated and successfully applied, namely the encapsulation of simulation results by means of surrogates. To this end, large sets of design variants were generated and independently assessed to determine key performance indicators, such as the attained index of damage stability, the resistance in calm water, the added resistance in waves, the structural weight, life-cycle costs, etc. Designs of experiments, such as a SOBOL or a Latin hypercube sampling technique, were utilized to generate variants for pre-selected free variables, the superset of all free variables representing the design space for the design task when subsequently combining surrogates. For the surrogates modeling, different techniques were made available via CAESES®, such as kriging, artificial neural networks analysis and polynomial regression.

A typical surrogate model for the resistance of a double-ended ferry studied in project HOLISHIP is shown in Figure 10. There, the change in calm water resistance has been calculated upfront via the use of a computing power- and time-intensive RANSE code with respect to a variation in length and beam (other parameters may be added) of design variants; point results are expressed by a surrogate model function, enabling fast postprocessing when searching for the design variants with lowest resistance.

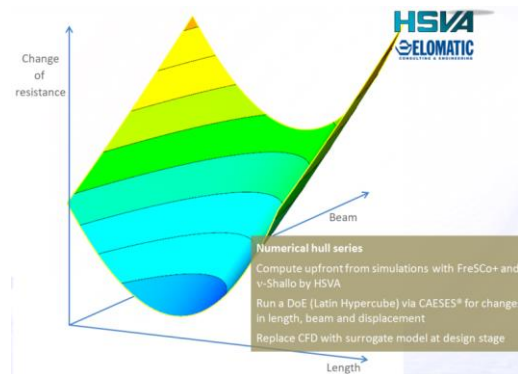


**Figure 10.** Surrogate model for DE-ferry (Jokinen et al., 2021).

A synthesis of tools for the parametric design optimization of a RoPax by the CAESES® platform is shown in Figure 11. Hull forms of digital siblings, parametrically generated by use of the CAESES model (step 1), are hydrodynamically evaluated for their calm water resistance by use of the potential theory panel code v-Shallo (step 2)

and RANSE code FreSco+ of HSVA (step 3), as well with respect to seakeeping and added resistance in waves by use of the code NEWDRIFT+ of NTUA (step 4). An assessment of the intact and damage stability of the variants by use of NAPA follows in step 5, assuming a conceptual ship arrangement and internal subdivision. The preliminary structural design of the variants by the use of Mars/BV, or alternatively NAPA steel, follows in step 6. The life-cycle economic and environmental impact assessment of the parametrically generated designs is conducted by a CAESES feature, or the more advanced LCPA tool of HOLISHIP, in step 7. Final space and outfitting arrangements are developed in step 8, but only for the identified optimal design(s), via a proper CAD drawing tool (NAPA or AUTOCAD). It is noted that the above-outlined step procedures 1–7 may be conducted in parallel, as they are independent from each other, except for the basic information about the hull form and conceptual space arrangements that are defined in step 1. Obtained results for the various properties of the generated design variants/siblings (resistance, propulsion power, stability metrics, structural weight, displacement, etc.) are postprocessed by the use of surrogate models that enable the fast identification of the best design variants by the application of multi-objective genetic algorithms (MOGA), available on the CAESES platform (Dakota toolkit, <https://dakota.sandia.gov/>, accessed on 9th November 2022).

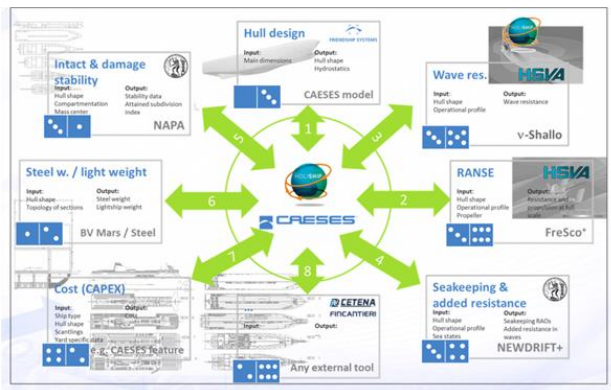


**Figure 11.** CAESES®/Friendship Systems Synthesis of Tools for RoPax Parametric Design Optimization.

In the frame of a RoPax optimization study, in Figure 12 (upper part) we see the results of the exploration of the design space of some hundreds of automatically generated RoPax ships in terms of the margin of the attained subdivision index (positive means: attained subdivision index is larger than the required one) in the indicated range of beam and length. Note that points in orange color indicate non-feasible designs due to the violation of some set design criterion (here: mostly damage stability). In Figure 12 (lower part) we see the net present value (NPV) of the generated RoPax design vs. the attained subdivision index margin and a clear Pareto Frontier of the feasible designs. Details of these studies and an elaboration of the RoPax design can be found in (Tuzcu et al., 2021).

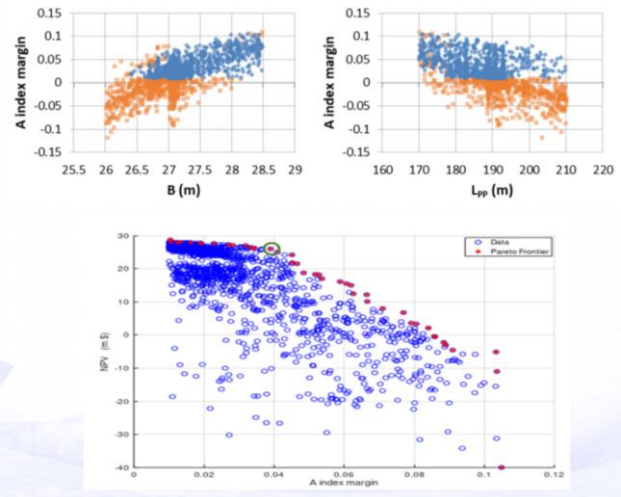


**Figure 12.** HOLISHIP Optimization RoPax (Tuzcu et al., 2021).

Beyond the global optimization of main ship dimensions/parameters, a local optimization generally follows for the most promising design variants. In Figure 13, the transom stern of a fast catamaran has been parametrically modelled by the use of 10 design parameters, and detailed flow CFD calculation was conducted for the optimal transom stern geometry, while considering the interaction with the fitted propeller, the propeller shaft, brackets and rudder (project TrAM, (Boulougouris et al., 2021)). This local optimization process led to a remarkable overall propulsive efficiency of about 80%, proving the feasibility of the battery driven high-speed design concept (Xing-Kaeding & Papanikolaou, 2021 and Papanikolaou et al., 2020).



**Figure 13.** Numerical mesh around the stern tunnel area for the local optimization by FreSCO+ of the Stavanger Demonstrator (5.7M)—H2020 TrAM Project Battery driven fast Catamaran Local Optimization of Transom Stern (Xing-Kaeding & Papanikolaou, 2021).

**4 CONVENTIONAL VS. HOLISHIP DESIGN APPROACH: WHAT IS THE DIFFERENCE?!**

The holistic approach to ship design implemented in the HOLISHIP project is not simply a new verbal notion, without substance. We claim that it is a step change in ship design, as elaborated in the following tabular comparison with the conventional approach on the basis of defined assessment criteria (Table 1).

**Table 1.** Conventional vs. HOLISHIP Approach to Ship Design.

Criterion	Conventional	HOLISHIP
Concept design	Empirical approach; supported by available computer-added calculation and graphics processing procedures, manual generation of 1...3 variants of baseline design and intuitive selection of the most promising variant	Automated parametric generation of hundreds of variants ( <i>digital siblings</i> ; “cloning”, Figure 8) and comparison to baseline design, including their documentation ; <i>global optimization</i> of main ship dimensions and main characteristics; rational (mathematical) identification of most promising variants on the basis of set criteria.
Preliminary/Contract design	Sequential processing of design steps (design spiral, Figure 6a); individual optimization of design properties (hydrodynamic s, structures, machinery, economics) of just a few design variants	Parallel processing of design steps and design synthesis (Figure 6b); multi-objective and multi-disciplinary optimization of several/hundreds of design variants (Figure 12); local hull form optimization (Figure 13).

Accuracy of calculation methods	Low at concept design level (mostly empirical modeling); high at contract design level	High at any design level, depending on the capability of the employed s/w tools; use of surrogate models for intensive calculation tasks (Figure 10).
Design lead time and person months effort	<p><i>Assuming the availability of a baseline design:</i></p> <p><u>Concept design</u>: some person days, depending on the experience of the design team (Figure 6a)</p> <p><u>Contract design</u>: several person months, depending on the experience of the design team</p> <p><i>If no baseline is available:</i></p> <p><u>Concept design</u>: many person days of collecting information, identifying and analyzing similar ships already built from public data</p>	<p><i>Assuming the availability of suitable parametric models, e.g., from a previous design campaign:</i></p> <p><u>Concept and contract design</u>: lead times are significantly reduced by a factor &gt; 5 (est.); smaller design team with less need for experience of all team members</p> <p><i>If no parametric models are at hand:</i></p> <p>Several days to weeks for building up robust and meaningful parametric models, depends on modeler’s experience</p>
Costs	The effect of design variants on cost is done at early design stage intuitively by designer’s experience or at best by checking the	Early assessment of the effect of hundreds of design variants on cost leads to significant cost reductions in the production cost (CAPEX)

	costs of only a few design variants	and operational cost (OPEX) or maximization of the Net Present Value (NPV) (Figure 12, lower part)
Quality of design (concept and contract)	Highly depend on the designer's and yards' experience	Superior quality thanks to systematic optimization and selection of the best out of hundreds of variants; consolidated standard design documentation ; Quality assurance via consistency in the assessment of variants
Safety of ship & the marine environment	Rule-based design with undefined safety level	Risk-based design with quantifiable risk consequences and safety level

- The design for maintainability of the engine system of a research vessel, coordinated by Fincantieri Shipyard;
- The concept and contract design of a multi-purpose ocean vessel, coordinated by the Naval Group;
- The virtual vessel mockup for the simulation of the maneuvering of a cargo ship, coordinated by MARIN;
- The hydrodynamic optimization of a containership and a bulk carrier, as well as the presentation of a weather routing system, coordinated by NTUA on behalf of DANAOS;
- The concept design of a gravity base foundation for an offshore platform operating in icy shallow waters, coordinated by Elomatic;
- The optimization of a conventional and an advanced engine/propulsion technology RoPax, coordinated by Tritec Marine;
- The design of a double ended ferry, coordinated by Elomatic.

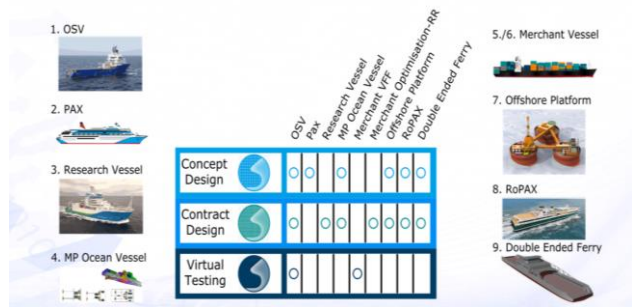


**Figure 14.** HOLISHIP Demonstrators.

## 5 OVERVIEW OF APPLICATION CASES OF HOLISHIP

In the HOLISHIP project, nine (9) basic and three (3) variant demonstrators were developed by the participating European industrial partners of HOLISHIP, supported by research institutes, societies and university laboratories. The development of these demonstrators, which are all innovative with respect to the adopted design procedures and the demonstrated performance, presumes the familiarization of the design teams with the HOLISHIP concept and its software platforms and tools, prior to application in practice. Elaborated application cases refer to concept and contract design stage, while in two cases, virtual testing by digital mock-ups was demonstrated. The following basic application cases were elaborated the by use of the developed HOLISHIP software infra-structure (Figure 14):

- The optimization of the design and operation of an Offshore Support Vessel (OSV), coordinated by Kongsberg Maritime;
- Light weight design issues of cruise vessels, coordinated by Meyer Werft;

All above application case studies were conducted by use of methods and tools de-scribed in volume I of the book “A Holistic Approach to Ship Design” (Papanikolaou, 2019), whereas de-tails of the application case studies are elaborated in volume II (Papanikolaou, 2021). In addition, two more application studies referring to green shipping were recently presented (Papanikolaou et al., 2022a), namely

- The design of an LNG fueled RoPax vessel for operation between Italy and Greece
- The design of a battery driven double ended ferry for operation in Finish coastal waters.

## 6. SUMMARY AND CONCLUDING REMARKS

A holistic approach to ship design, which was introduced earlier as a novel ship design concept, was widely applied in the HOLISHIP project, proving its viability. The concept was implemented in versatile, integrated design platforms, offering the user a vast variety of options for the efficient development of alternative ship designs by the use of tools for their analysis and multi-objective optimization with respect to all relevant (ship) design disciplines, as well as virtual prototyping. An open architecture allows for continuous adaptation to current and emerging design and

simulation needs, flexibly setting up dedicated synthesis models for different application cases. The exploration of the huge design space is enabled by the use of automated parametric models of significant depth, which are processed with reduced lead time.

The achievements and introduced innovations of the HOLISHIP project are summarized below:

- Design synthesis and integration of software tools realized via a combined bottom-up and top-down approach;
- Parametric, multi-objective design optimization enabled via CAESES® platform;
- Flexible combination of tools as needed for specific design tasks;
- Continuous growth of syntheses models with more application cases;
- Replacement of resource-intensive simulations with surrogate models;
- VR modeling via RCE platform known from German aviation industry (DLR);
- Distributed Working enabled via RCE cloud computing;
- Holistic approach to ship design proven in a series of application studies;
  - Effective exploration of huge design space in short time;
  - Seamless consideration of important design aspects at early stage;
  - Rationally optimized designs by state-of-the-art tools;
  - Consideration of human factors in ship design by virtual modeling and VR testing.

In the future, further dedicated tools and applications addressing requirements arising from contemporary emission reduction policies will be integrated into the HOLISHIP Platforms and thus provide the path towards the zero-emission maritime transport goal set out by the EU and the waterborne community.

**Funding:** HORIZON 2020 project HOLISHIP, contract number 689074

**Acknowledgments:** The HOLISHIP project is the joint effort of 40 representatives of the European Maritime Industry and Research Community. The work was partly funded by EU in the frame of the HORIZON 2020 project HOLISHIP, contract number 689074, [www.holiship.eu](http://www.holiship.eu) (accessed on 9th November 2022)

**Note:** This paper has been also presented as Key-Note paper at MARTECH22, the 6th International Conference on Maritime Technology and Engineering, Lisbon, Portugal, 24–26 May 2022, republished open access: Papanikolaou, A., *Holistic Approach to Ship Design*, *J. Mar. Sci. Eng.* 2022, 10(11), 1717; <https://doi.org/10.3390/jmse10111717> (registering DOI) - 10 Nov 2022

## REFERENCES

- Boulougouris, E.; Papanikolaou, A.; Dahle, M.; Tolo, E.; Xing-Kaeding, Y.; Jürgenhake, C.; Seidenberg, T.; Sachs, C.; Brown, G.; Jensen, F. (2021) Implementation of Zero Emission Fast Shortsea Shipping. In Proceedings of the Proc. SNAME Maritime Convention, SMC2021, Houston, TX, USA, 25–29 October.
- Evans, J.H. (1959) “Basic Design Concepts”, American Society of Naval Engineers: Alexandria, VA, USA.
- Harries, S.; Abt, C. (2021) Integration of Tools for Application Case Studies, Chapter 2 in Book A Holistic Approach to Ship Design, Volume 2: Application Cases; Papanikolaou, A., Ed.; Springer: Berlin/Heidelberg, Germany; ISBN 978-3030710903.
- Harries, S.; Abt, C. (2019) CAESES—The HOLISHIP Platform for Process Integration and Design Optimization, Chapter 8 in Book “A Holistic Approach to Ship Design”, Volume 1: Optimisation of Ship Design and Operation for Life Cycle; Papanikolaou, A., Ed.; Springer: Berlin/Heidelberg, Germany, 2019; ISBN 978-3-030-02809-1.
- HOLISHIP (2016–2020), Holistic Optimisation of Ship Design and Operation for Life Cycle. Project Funded by the European Commission, H2020-DG Research, Grant Agreement 689074. Available online: <http://www.holiship.eu> (accessed on 9th November 2022).
- Hooijmans, P.; van Hees, M.T.; Verkerk, F. Virtual Vessel Framework for Merchant Ship Maneuvering Operation, (2021) Chapter 7 in Book “A Holistic Approach to Ship Design”, Volume 2: Application Cases; Papanikolaou, A., Ed.; Springer: Berlin/Heidelberg, Germany; ISBN 978-3030710903.
- Jokinen, M.; Broglia, R.; Gatchell, S.; Aubert, A.; Gunawan, R.; Schellenberger, G.; Harries, S.; von Zadow, H. Design of a Double Ended Ferry, (2021) Chapter 12 in Book A Holistic Approach to Ship Design, Volume 2: Application Cases; Papanikolaou, A., Ed.; Springer: Berlin/Heidelberg, Germany, ISBN 978-3030710903.
- Le Néna, R.; Alan Guégan, A.; Rafine, B. (2019) Systemic Approach to Ship Design, Chapter 5 in Book A Holistic Approach to Ship Design, Volume 1: Optimisation of Ship Design and Operation for Life Cycle; Papanikolaou, A., Ed.; Springer: Berlin/Heidelberg, Germany, ISBN 978-3-030-02809-1.
- Maggioncalda, M.; Gualeni, P.; Notaro, C.; Cau, C.; Bonazountas, M. Stamatis, S. Life Cycle Performance Assessment (LCPA) Tools, (2019) Chapter 11 in Book A Holistic Approach to Ship Design, Volume 1: Optimisation of Ship Design and Operation for Life Cycle; Papanikolaou, A., Ed.; Springer: Berlin/Heidelberg, Germany, 2019; ISBN 978-3-030-02809-1.

- Nowacki, H. (2010) Five decades of Computer-Aided Ship Design. *J. Computer-Aided Des.*, 42, pp.956–969, <https://doi.org/10.1016/j.cad.2009.07.006>.
- Nowacki, H. (2016) “A Farewell to the Design Spiral”, Invited Note Presented at the Mini-Symposium on Ship Design, Ship Hydrodynamics & Maritime Safety, Athens, September 30, 2016. Available online: [https://www.academia.edu/42261670/A\\_Farewell\\_to\\_the\\_Design\\_Spiral\\_A\\_Farewell\\_to\\_the\\_Design\\_Spiral](https://www.academia.edu/42261670/A_Farewell_to_the_Design_Spiral_A_Farewell_to_the_Design_Spiral) (accessed on 9th November 2022).
- Nowacki, H.; Brusis, F. (1970) “Swift, P.M. Tanker Preliminary Design—An Optimization Problem with Constraints”. *Trans. SNAME*, 78, pp. 357–390.
- Papanikolaou, A. (2010) “Holistic Ship Design Optimization”. *J. Computer-Aided Design*, 42, pp.1028–1044.
- Papanikolaou, A. (2014) *Ship Design—Methodologies of Preliminary Design*; 628p, 575 illus.; Springer: Berlin/Heidelberg, Germany, ISBN 978-94-017-8751-2; 978-94-017-8750-5.
- Papanikolaou, A. (Ed.) (2019) *A Holistic Approach to Ship Design, Volume 1: Optimisation of Ship Design and Operation for Life Cycle*; Springer: Berlin/Heidelberg, Germany, ISBN 978-3-030-02809-1.
- Papanikolaou, A. (Ed.) (2021) *A Holistic Approach to Ship Design, Volume 2: Application Cases*; Springer: Berlin/Heidelberg, Germany, ISBN 978-3030710903.
- Papanikolaou, A.; Harries, S.; Hooijmans, P.; Marzi, J.; Le Nena, R.; Torben, S.; Yrjänäinen, A.; Boden, B. (2022b) *A Holistic Approach to Ship Design: Tools and Applications*. *J. Ship Res.*, 66, pp. 25-53, <https://doi.org/10.5957/JOSR.12190070>.
- Papanikolaou, A.; Xing-Kaeding, Y.; Strobel, H.; Kanellopoulou, A.; Zaraphonitis, G.; Tolo, E. (2020) “Numerical and Experimental Optimization Study on a Fast, Zero Emission Catamaran”. *J. Mar. Sci. Eng.*, 8, 657. <https://doi:10.3390/jmse8090657>. Available online: <https://www.mdpi.com/2077-1312/8/9/657> (accessed on 9th November 2022).
- Papanikolaou, A.; Zaraphonitis, G.; Jokinen, M.; Aubert, A.; Harries, S.; Marzi, J.; Mermiris, G.; Gunawan, R. (2022a) *Holistic Ship Design for Green Shipping*. *Proceedings of the SNAME Maritime Convention 2022, Houston, TX, USA, 26–29 September*.
- Sullivan, B.; Shantanoo, D.; Sole, J.; Rossi, M.; Ramundo, L.; Terzi, S. (2020) “Maritime 4.0—Opportunities in Digitalization and Advanced Manufacturing for Vessel Development”. *Procedia Manuf.*, 42, pp. 246–253.
- Taggart, R. (Ed) (1980) *Ship Design and Construction*; SNAME Publications: New York, NY, USA.
- Tuzcu, C.; Dinsdale, C.; Hawkins, J.; Zaraphonitis, G.; Papadopoulos, F. (2021) “RoPax Design Revisited—Evolution or Revolution?” Chapter 11 in Book *A Holistic Approach to Ship Design, Volume 2: Application Cases*; Papanikolaou, A., Ed.; Springer: Berlin/Heidelberg, Germany, 2021; ISBN 978-3030710903.
- Xing-Kaeding, Y.; Papanikolaou, A. (2021) *Optimisation of the propulsive efficiency of a fast catamaran*, *J. Mar. Sci. Eng.*, 9, 492. <https://doi.org/10.3390/jmse9050492>
- Zaraphonitis, G.; Plessas, T.; Kraus, A.; Gudenschwager, H.; Schellenberger, G. (2019) *Parametric Optimisation in Concept and Pre-contract Ship Design Stage*, Chapter 7 in the Book “*A Holistic Approach to Ship Design*”, Volume 1: *Optimisation of Ship Design and Operation for Life Cycle*; Papanikolaou, A., Ed.; Springer: Berlin/Heidelberg, Germany, 2019; ISBN 978-3-030-02809-1.



## **A Mathematical Model of a Ship with Wings Propelled by Waves**

**Kirill V. Rozhdestvensky<sup>1</sup>, Zin Min Htet<sup>1</sup>**

<sup>1</sup>Saint-Petersburg State Marine Technical University

**Abstract:** This paper discusses mathematical modeling of a ship equipped with energy-saving wing devices. Therewith, the ship is mathematically represented by an elongated hull with high-aspect-ratio wings mounted near its bow and stern. Equations, describing ship motions in regular oncoming waves, are written in the spirit of strip theory with account of inertial and damping influence of energy-saving wing elements with the use of linear expansion of wing-related forces with respect to heave and pitch perturbations. This approach readily yields fast numerical solutions for the propulsion of a ship with wings in waves. The latter solutions are then used as an input for calculation of thrust on wing elements on the basis of classical unsteady foil theories corrected for finite aspect ratio. To evaluate speed of the ship in the modes which allow cruising exclusively by wave power, it is hypothetically assumed that in this case, the wave-generated thrust on the wings equals total drag of the ship-plus-wings system, the latter being defined as a sum of its viscous, wave-making, induced (for wing elements) and added-wave components. Excepting the added-wave term and wings' contributions, the total drag is calculated herein by Holtrop method whereas added-wave resistance is evaluated with Beukelman-Gerritsma formula involving kinematic parameters of heaving and pitching motions of the ship calculated both without and with account of the wings. Also discussed in the paper is a decrease of added wave resistance for a ship with wings as compared to that of ship without wings. Finally, the energy efficiency design index (EEDI) introduced by the International Maritime Organization (IMO) is discussed for representative sea conditions as a measure of ship environmental friendliness.

**Keywords:** Ship motions; Energy-Saving Wing Devices; Wave Propulsion; Added Resistance; IMO; EEDI.



# Design-Space Dimensionality Reduction in Shape Optimization: Recent Developments and Way Forward

Matteo Diez\*, Andrea Serani

CNR-INM, National Research Council-Institute of Marine Engineering, Rome, Italy

**Abstract:** In shape optimization of complex industrial products (such as hull forms, rudder and appendages, propellers), there exists an inherent similarity between global optimization (GO) and uncertainty quantification (UQ): they rely on an extensive exploration of the design and operational spaces, respectively; often, they need local refinements to ensure accurate identification of optimal solutions or probability density regions (such as distribution tails), respectively; they both are dramatically affected by the curse of dimensionality as GO and UQ algorithms' complexity and especially computational cost rapidly increase with the problem dimension. Therefore, there exists a natural ground for transferring dimensionality reduction methods for UQ to GO. These enable the efficient exploration of large design spaces in shape optimization, which, in turn, enable global optimization (possibly in a multidisciplinary and stochastic setting). The paper reviews and discusses recent techniques for design-space dimensionality reduction in shape optimization, based on the Karhunen-Loève expansion (equivalent to proper orthogonal decomposition and, at the discrete level, principal component analysis), spanning from geometry-based approaches to physics-informed formulations. A recent methodological advancement, namely the parametric model embedding, is also briefly recalled, which is very attractive for use with CAD/CAE software. An example is shown and discussed for the hydrodynamic optimization of a ship hull.

**Keywords:** Shape optimization, Design-space dimensionality reduction, Karhunen-Loève expansion, Proper orthogonal decomposition, Principal component analysis.

## 1 INTRODUCTION

The simulation-based or simulation-driven design (SBD, SDD) paradigms have demonstrated the capability of driving the design process, providing large sets of design options possibly assessing the design performance for a large number of operating and environmental conditions. The recent development of high performance computing (HPC) systems has driven the SBD towards integration with global optimization (GO) algorithms and uncertainty quantification (UQ) methods, moving the SBD paradigm to automatic deterministic and stochastic SBD optimization (SBDO, e.g. Campana et al. 2006), possibly aiming at global solutions to the design problem. In shape design, SBDO consists of three main elements: (i) a deterministic and/or stochastic simulation tool (integrating physics-based multi-disciplinary solvers with UQ), (ii) an optimization algorithm, and (iii) a shape parameterization/modification tool. Automatic SBDO is also referred to as simulation-driven design (SDD, e.g. Harries & Abt 2019), as the automatic process of finding the optimal design is driven by simulation outputs (and the optimization algorithm).

Despite the recent increase of computational power and robustness of numerical algorithms, high-fidelity SBDO for shape optimization still remains a challenging process, from theoretical, algorithmic, and technological viewpoints. Among others, one of the most complex challenge is how to deal with high-dimensional, large design spaces, especially

when computationally-expensive multi-disciplinary black-box tools are used for the performance analysis and a global optimum is sought after. Potential design improvements significantly depend on dimension and extension of the design space. Obviously, high dimension and variability spaces are more difficult and expensive to explore but, at the same time, potentially allow for bigger improvements. Even if efficient GO algorithms have been proposed and applied with success to SBDO, finding a potentially global optimal solution within reasonable computational time/cost remains a critical issue and a technological challenge. Additionally, UQ of complex applications is computationally very demanding, especially if high-order statistical moments and/or quantiles are required as in robust and reliability-based design optimization. Both GO and UQ are affected by the *curse of dimensionality* as the algorithms' complexity and computational cost rapidly increase with the problem dimension. This is generally true also if metamodels are used. Therefore, there exists a natural ground for transferring dimensionality reduction methods for UQ (Le Maître & Knio, 2010) to GO. These enable the efficient exploration of large design spaces in shape optimization, which, in turn, enable global multidisciplinary optimization under uncertainty

Shape optimization research has traditionally focused on shape and topology parameterizations, as critical factors to achieve the desired level of design variability. Obviously, the

---

\* Corresponding author email: [matteo.diez@cnr.it](mailto:matteo.diez@cnr.it)

choice of the shape parameterization technique has a large impact on the practical implementation and the success of the optimization process. Shape modification methods have been an area of continuous and extensive research and a wide variety of techniques have been proposed during recent years, e.g., Haftka & Grandhi (1986); Samareh (2001); Sieger et al. (2015). In order for the SBDO to overcome the curse of dimensionality, the parameterization method must efficiently describe the design variability with as few variables as possible.

On-line and linear design-space dimensionality reduction techniques have been developed, requiring the evaluation of the objective function or its gradient. Principal component analysis (PCA) or proper orthogonal decomposition (POD) methods have been applied for local reduced-dimensionality representations of feasible design regions (Raghavan et al., 2013). The associated POD/PCA-based expansions are not truncated and the dimensionality reduction is achieved by a local representation of an  $\alpha$ -manifold of feasible designs, embedding the design constraints (whose evaluation is required) in the design parameterization and preserving the original design variability. A POD/PCA-type of approach is used in the active subspace method (Lukaczyk et al., 2014) to discover and exploit low-dimensional monotonic trends in the objective function, based on the evaluation of its gradient. This type of methods improve the optimization efficiency by basis rotation and/or dimensionality reduction. Nevertheless, they do not directly provide with an assessment of the design space and associated shape parameterization before optimization is performed or objective function and/or its gradient are evaluated. Moreover, if gradients are not directly provided (as in the case of black-box tools) their evaluation by finite differences may be inaccurate due to numerical noise and/or residuals affecting the solution. Finally, these methods are local in nature and their extension to GO is not straightforward. Off-line or up-front linear methods have been developed with focus on design-space variability and dimensionality reduction for efficient optimization procedures. One of the first examples can be found in Robinson & Keane (2001), where an orthogonal representation of supercritical airfoil sections was achieved by an iterative least-square fitting of known sections and subsequent Gram-Schmitt orthogonalization. In Toal et al. (2010) the POD is used to reduce the design-space dimensionality in a transonic airfoil optimization. POD is used in Poole et al. (2015) to derive an efficient reduced-dimensionality set of airfoil design parameters. Geometric data reduction by POD is used in Cinquegrana & Iuliano (2018) for an airfoil design, where new reduced-dimensionality design spaces are iteratively identified as the optimization progresses. Although the dimensionality reduction is embedded in an iterative procedure, geometric filtration by POD is performed in an outer loop before evolutionary optimization is performed and is based on geometry only. In Borzì et al. (2010) and Schillings et al. (2011) the Karhunen-Loève expansion (KLE) is used for rep-

resenting distributed geometrical uncertainties and building a reduced-order spatial model for uncertainty quantification. A method based on the KLE has been formulated in Diez et al. (2015) for the assessment of the shape modification variability and the definition of a reduced-dimensionality global model of the shape modification vector. The method was recently extended to embed the original parameters via the so-called parameter model embedding (PME, Serani & Diez 2022), which makes the methodology very attractive for industrial applications heavily relying on CAD/CAE models. KLE/PCA methods have been successfully applied for deterministic (Serani et al., 2016a) and stochastic (Diez et al., 2018) hull form optimization of mono-hulls and catamarans in calm water and waves, respectively. In D'Agostino et al. (2020) KLE/PCA is used to assess, compare, and reduce in dimensionality three design spaces obtained by different shape modification methods. A discussion on the industrial application of KLE/PCA methods to design-space dimensionality reduction is given in Harries & Abt (2019). It may be noted that KLE is formulated in the continuous domain and reduces to the eigenproblem of an integral operator. The discretization of the shape domain (and associated integral equation) yields the eigenproblem of the autocovariance matrix of the discretized shape modification vector. This corresponds to solving the PCA of the discretized shape modification vector.

Generally, off-line POD/KLE/PCA approaches are formally equivalent, may be applied to arbitrary shape modification methods, and require no objective function/gradient evaluation, as the dimensionality reduction is based on the concept of geometric/shape variability. Interestingly, this is referred to as geometric variance and energy of the mode shapes in KLE (Diez et al., 2015) and POD (Poole et al., 2015) approaches, respectively. These methods improve the shape optimization efficiency by reparameterization and dimensionality reduction, providing the assessment of the design space and the shape parameterization before optimization and/or performance analysis are carried out. The assessment is based on the geometric variability associated to the design space, making the method fully off-line and computationally very efficient and attractive, as no simulations are required. Nevertheless, the lack of physical information may become a critical issue in all those applications where small shape variations have a significant effect on the physics, such as in flow separations, sonic shocks, etc. For this reason, extension to physics-informed formulations have been proposed (Serani et al., 2017; Serani & Diez, 2018; Serani et al., 2019). Furthermore, if strongly nonlinear relationships exist between design variables, shape modification, and physical parameters, extensions may be of interest to nonlinear dimensionality reduction methods (D'Agostino et al., 2018; Serani et al., 2020).

The paper reviews and discusses recent methods for design-space dimensionality reduction based on the KLE. A discussion is provided on the use of geometry-based and physics-

informed formulations. The extension to PME is also briefly recalled, which is very attractive for use with CAD/CAE software. An example is shown and discussed for the hydrodynamic optimization of a naval destroyer.

## 2 DESIGN-SPACE DIMENSIONALITY REDUCTION IN SHAPE OPTIMIZATION

### 2.1 Geometry-Based Formulation

Consider a geometric domain  $\mathcal{G}$  (which identifies the initial shape) and a set of coordinates  $\boldsymbol{\xi} \in \mathcal{G}$ . Assume that  $\mathbf{u} \in \mathcal{U}$  is the design variable vector, which defines a shape modification vector  $\boldsymbol{\delta}$  (see Figure 1). Consider the vector space of all possible square-integrable modifications of the initial shape,  $\boldsymbol{\delta}(\boldsymbol{\xi}, \mathbf{u}) \in L^2_\rho(\mathcal{G})$ , where  $L^2_\rho(\mathcal{G})$  is the Hilbert space defined by a generalized inner product

$$(\mathbf{a}, \mathbf{b})_\rho = \int_{\mathcal{G}} \rho(\boldsymbol{\xi}) \mathbf{a}(\boldsymbol{\xi}) \cdot \mathbf{b}(\boldsymbol{\xi}) d\boldsymbol{\xi} \quad (1)$$

with associated norm  $\|\mathbf{a}\|_\rho = (\mathbf{a}, \mathbf{a})_\rho^{1/2}$ , where  $\rho(\boldsymbol{\xi}) \in \mathbb{R}$  is an arbitrary weight function. Generally,  $\boldsymbol{\xi} \in \mathbb{R}^n$  with  $n = 1, 2, 3$ ,  $\mathbf{u} \in \mathbb{R}^M$  with  $M$  number of design variables, and  $\boldsymbol{\delta} \in \mathbb{R}^m$  with  $m = 1, 2, 3$  (with  $m$  not necessarily equal to  $n$ ).

Assume that, before running the shape optimization procedure, the design problem is affected by *epistemic uncertainty*, being the optimal design not known a priori. Therefore,  $\mathbf{u}$  may be given a probability density function  $f(\mathbf{u})$ , which represents the degree of belief that the optimal design will be found in certain regions of the design space. The associated mean shape modification is then

$$\langle \boldsymbol{\delta} \rangle = \int_{\mathcal{U}} \boldsymbol{\delta}(\boldsymbol{\xi}, \mathbf{u}) f(\mathbf{u}) d\mathbf{u} \quad (2)$$

where  $\langle \boldsymbol{\delta} \rangle$  is a function of  $\boldsymbol{\xi}$ , being  $\langle \cdot \rangle$  the ensemble average over  $\mathbf{u}$ . The variance associated to the shape modification vector (geometric variance) is defined as

$$\sigma^2 = \langle \|\hat{\boldsymbol{\delta}}\|^2 \rangle = \int_{\mathcal{U}} \int_{\mathcal{G}} \rho(\boldsymbol{\xi}) \hat{\boldsymbol{\delta}}(\boldsymbol{\xi}, \mathbf{u}) \cdot \hat{\boldsymbol{\delta}}(\boldsymbol{\xi}, \mathbf{u}) f(\mathbf{u}) d\boldsymbol{\xi} d\mathbf{u} \quad (3)$$

where  $\hat{\boldsymbol{\delta}}(\boldsymbol{\xi}, \mathbf{u}) = \boldsymbol{\delta}(\boldsymbol{\xi}, \mathbf{u}) - \langle \boldsymbol{\delta} \rangle$ .

The aim of the KLE is to find an optimal basis of orthonormal functions for  $\hat{\boldsymbol{\delta}}$ :

$$\hat{\boldsymbol{\delta}}(\boldsymbol{\xi}, \mathbf{u}) \approx \sum_{k=1}^N x_k(\mathbf{u}) \boldsymbol{\varphi}_k(\boldsymbol{\xi}) \quad (4)$$

where

$$x_k(\mathbf{u}) = (\hat{\boldsymbol{\delta}}, \boldsymbol{\varphi}_k)_\rho = \int_{\mathcal{G}} \rho(\boldsymbol{\xi}) \hat{\boldsymbol{\delta}}(\boldsymbol{\xi}, \mathbf{u}) \cdot \boldsymbol{\varphi}_k(\boldsymbol{\xi}) d\boldsymbol{\xi} \quad (5)$$

are the basis-function components or coefficients, used hereafter as new design variables.

The optimality condition associated to the KLE refers to the geometric variance resolved by the basis functions through Eq. (4). Combining Eqs. (3)–(5) yields

$$\sigma^2 = \sum_{k=1}^{\infty} \sum_{j=1}^{\infty} \langle x_k x_j \rangle (\boldsymbol{\varphi}_k, \boldsymbol{\varphi}_j)_\rho = \sum_{j=1}^{\infty} \langle x_j^2 \rangle = \sum_{j=1}^{\infty} \langle (\hat{\boldsymbol{\delta}}, \boldsymbol{\varphi}_j)_\rho^2 \rangle \quad (6)$$

The basis resolving the maximum variance is formed by the solutions  $\boldsymbol{\varphi}$  of the variational problem

$$\begin{aligned} & \text{maximize}_{\boldsymbol{\varphi} \in L^2_\rho(\mathcal{G})} \mathcal{J}(\boldsymbol{\varphi}_k) = \langle (\hat{\boldsymbol{\delta}}, \boldsymbol{\varphi}_k)_\rho^2 \rangle \\ & \text{subject to} \quad (\boldsymbol{\varphi}_k, \boldsymbol{\varphi}_k)_\rho^2 = 1 \end{aligned} \quad (7)$$

which yields (e.g., Diez et al. 2015)

$$\mathcal{L}\boldsymbol{\varphi}_k(\boldsymbol{\xi}) = \int_{\mathcal{G}} \rho(\boldsymbol{\xi}') \langle \hat{\boldsymbol{\delta}}(\boldsymbol{\xi}, \mathbf{u}) \otimes \hat{\boldsymbol{\delta}}(\boldsymbol{\xi}', \mathbf{u}) \rangle \boldsymbol{\varphi}_k(\boldsymbol{\xi}') d\boldsymbol{\xi}' = \lambda_k \boldsymbol{\varphi}_k(\boldsymbol{\xi}) \quad (8)$$

where  $\otimes$  indicates the outer product and  $\mathcal{L}$  is a selfadjoint integral operator whose eigensolutions define the optimal basis functions for the linear representation of Eq. (4). Therefore, its eigenfunctions (KL modes)  $\{\boldsymbol{\varphi}_k\}_{k=1}^{\infty}$  are orthogonal and form a complete basis for  $L^2_\rho(\mathcal{G})$ . Additionally, it may be proven that

$$\sigma^2 = \sum_{k=1}^{\infty} \lambda_k \quad (9)$$

where the eigenvalues  $\lambda_k$  (KL values) represent the variance resolved by the associated basis function  $\boldsymbol{\varphi}_k$ , through its component  $x_k$  in Eq. (4):

$$\lambda_k = \langle x_k^2 \rangle \quad (10)$$

Finally, the solutions  $\{\boldsymbol{\varphi}_k\}_{k=1}^{\infty}$  of Eq. (8) are used to define the reduced-dimensionality space for the shape modification. Define  $l$ ,  $0 < l \leq 1$ , as the desired level of confidence for the shape modification variability, the smallest  $N$  in Eq. (4) is selected, such as

$$\sum_{k=1}^N \lambda_k \geq l \sum_{k=1}^{\infty} \lambda_k = l\sigma^2 \quad (11)$$

with  $\lambda_k \geq \lambda_{k+1}$ .

It may be shown how the numerical solution of Eq. (8) via discretization of the shape domain and Monte Carlo (MC) sampling over design variables in  $\mathbf{u}$  yields the PCA of the discretized shape modification vector. Details of equations and numerical implementation are given in Diez et al. (2015). The block diagram for simulation-based shape optimization using geometry-based dimensionality reduction is shown in Figure 2.

### 2.2 Physics-Informed Formulation

Along with the shape modification vector  $\boldsymbol{\delta}$ , consider a distributed physical parameter vector  $\boldsymbol{\pi} \in \mathbb{R}^p$ ,  $p = 1, \dots, \infty$

(including, e.g., velocity, pressure, etc.) defined on a physical domain  $\mathcal{P} \in \mathbb{R}^n$  and a lumped physical parameter vector  $\boldsymbol{\theta} \in \mathbb{R}^q$ ,  $q = 1, \dots, \infty$  (including, e.g. resistance) on a domain  $\mathcal{Q}$  (see Figure 3). Note that  $\mathcal{Q}$  has a null measure and corresponds to an arbitrary point where the lumped physical parameter vector is virtually defined. Also note that, in general,  $\mathcal{D} \equiv \mathcal{G} \cup \mathcal{P} \cup \mathcal{Q}$  is not simply connected. Rather,  $\mathcal{G}$  may be a boundary of  $\mathcal{P}$ .

Consider now a combined geometry-based and physics-informed vector  $\boldsymbol{\gamma} \in \mathbb{R}^m$ , and for the sake of simplicity a set of coordinates  $\boldsymbol{\xi} \in \mathbb{R}^n$ , such that

$$\boldsymbol{\gamma}(\boldsymbol{\xi}, \mathbf{u}) = \begin{cases} \boldsymbol{\delta}(\boldsymbol{\xi}, \mathbf{u}) & \text{if } \boldsymbol{\xi} \in \mathcal{G} \\ \boldsymbol{\pi}(\boldsymbol{\xi}, \mathbf{u}) & \text{if } \boldsymbol{\xi} \in \mathcal{P} \\ \boldsymbol{\theta}(\boldsymbol{\xi}, \mathbf{u}) & \text{if } \boldsymbol{\xi} \in \mathcal{Q} \end{cases} \quad (12)$$

belongs to a disjoint Hilbert space  $L^2_\rho(\mathcal{D})$ , defined by the generalized inner product

$$\begin{aligned} (\mathbf{a}, \mathbf{b})_\rho &= \int_{\mathcal{D}} \rho(\boldsymbol{\xi}) \mathbf{a}(\boldsymbol{\xi}) \cdot \mathbf{b}(\boldsymbol{\xi}) d\boldsymbol{\xi} \\ &= \int_{\mathcal{G}} \rho(\boldsymbol{\xi}) \mathbf{a}(\boldsymbol{\xi}) \cdot \mathbf{b}(\boldsymbol{\xi}) d\boldsymbol{\xi} \\ &+ \int_{\mathcal{P}} \rho(\boldsymbol{\xi}) \mathbf{a}(\boldsymbol{\xi}) \cdot \mathbf{b}(\boldsymbol{\xi}) d\boldsymbol{\xi} \\ &+ \rho(\boldsymbol{\xi}_\theta) \mathbf{a}(\boldsymbol{\xi}_\theta) \cdot \mathbf{b}(\boldsymbol{\xi}_\theta) \end{aligned} \quad (13)$$

with associated norm  $\|\mathbf{a}\|_\rho = (\mathbf{a}, \mathbf{a})_\rho^{1/2}$ .

Again, considering all possible realizations of  $\mathbf{u}$ , the associated mean vector is

$$\langle \boldsymbol{\gamma} \rangle = \int_{\mathcal{U}} \boldsymbol{\gamma}(\boldsymbol{\xi}, \mathbf{u}) f(\mathbf{u}) d\mathbf{u} \quad (14)$$

where  $\langle \boldsymbol{\gamma} \rangle$  is a function of  $\boldsymbol{\xi}$ . The associated variance (which now considers a combined geometry-based and physics-informed design variability) equals

$$\sigma^2 = \langle \|\hat{\boldsymbol{\gamma}}\|^2 \rangle = \int_{\mathcal{U}} \int_{\mathcal{D}} \rho(\boldsymbol{\xi}) \hat{\boldsymbol{\gamma}}(\boldsymbol{\xi}, \mathbf{u}) \cdot \hat{\boldsymbol{\gamma}}(\boldsymbol{\xi}, \mathbf{u}) f(\mathbf{u}) d\boldsymbol{\xi} d\mathbf{u} \quad (15)$$

where  $\hat{\boldsymbol{\gamma}}(\boldsymbol{\xi}, \mathbf{u}) = \boldsymbol{\gamma}(\boldsymbol{\xi}, \mathbf{u}) - \langle \boldsymbol{\gamma} \rangle$  represents the physics-informed design modification vector.

Similarly to the previous case, the aim is to find an optimal basis of orthonormal functions, which will be used to construct a linear representation of  $\hat{\boldsymbol{\gamma}}$ :

$$\hat{\boldsymbol{\gamma}}(\boldsymbol{\xi}, \mathbf{u}) \approx \sum_{k=1}^N x_k(\mathbf{u}) \boldsymbol{\psi}_k(\boldsymbol{\xi}) \quad (16)$$

where by definition (Serani et al., 2019)

$$\boldsymbol{\psi}_k(\boldsymbol{\xi}) = \begin{cases} \boldsymbol{\varphi}_k(\boldsymbol{\xi}) & \text{if } \boldsymbol{\xi} \in \mathcal{G} \\ \boldsymbol{\chi}_k(\boldsymbol{\xi}) & \text{if } \boldsymbol{\xi} \in \mathcal{P} \\ \boldsymbol{\nu}_k(\boldsymbol{\xi}) & \text{if } \boldsymbol{\xi} \in \mathcal{Q} \end{cases} \quad (17)$$

and

$$x_k(\mathbf{u}) = (\hat{\boldsymbol{\gamma}}, \boldsymbol{\psi}_k)_\rho = \int_{\mathcal{D}} \rho(\boldsymbol{\xi}) \hat{\boldsymbol{\gamma}}(\boldsymbol{\xi}, \mathbf{u}) \cdot \boldsymbol{\psi}_k(\boldsymbol{\xi}) d\boldsymbol{\xi} \quad (18)$$

Similarly to Eq. 8 the solution is given by

$$\mathcal{L} \boldsymbol{\psi}_k(\boldsymbol{\xi}) = \int_{\mathcal{D}} \rho(\boldsymbol{\xi}') \langle \hat{\boldsymbol{\gamma}}(\boldsymbol{\xi}, \mathbf{u}) \otimes \hat{\boldsymbol{\gamma}}(\boldsymbol{\xi}', \mathbf{u}) \rangle \boldsymbol{\psi}_k(\boldsymbol{\xi}') d\boldsymbol{\xi}' = \lambda_k \boldsymbol{\psi}_k(\boldsymbol{\xi}) \quad (19)$$

where again  $\mathcal{L}$  is a selfadjoint integral operator whose eigen-solutions define the optimal basis functions for the linear representation of Eq. (16). Therefore, its eigenfunctions (KL modes)  $\{\boldsymbol{\psi}_k\}_{k=1}^\infty$  are orthogonal and form a complete basis for  $L^2_\rho(\mathcal{D})$ . After dimensionality reduction is performed, the geometric components  $\{\boldsymbol{\varphi}_k\}_{k=1}^N$  of the eigenvectors  $\boldsymbol{\psi}_k$  in Eq. (17) are used for the new representation of the shape modification vector.

Again, it may be shown how the numerical solution of Eq. (19) via discretization of shape and physics domains and MC sampling over design variables  $\mathbf{u}$  yields the PCA of the discretized shape and physical-parameters modification vector. Details of equations and numerical implementation may be found in Serani et al. (2017); Serani & Diez (2018); Serani et al. (2019). The block diagram for simulation-based shape

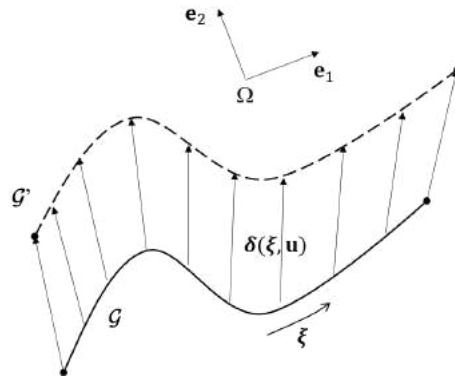


Figure 1: Scheme and notation for the current formulation, showing an example for  $n = 1$  and  $m = 2$ .

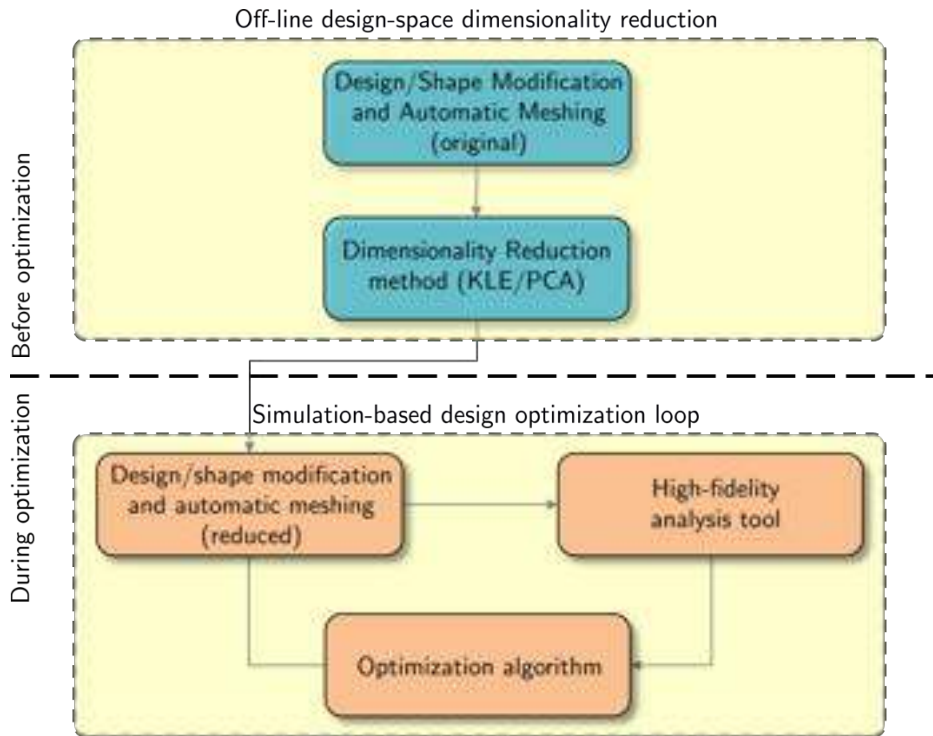


Figure 2: Block diagram for simulation-based shape optimization using geometry-based dimensionality reduction.

optimization using physics-informed dimensionality reduction is shown in Figure 4. For the sake of computational efficiency, the procedure includes low-fidelity analysis tools in the up-front dimensionality reduction, whereas high-fidelity analysis tools are devoted to drive the design optimization loop.

### 2.3 Extension to Parametric Model Embedding (PME)

A possible limitation to the use of KLE/PCA methods is that, if the dimensionality reduction procedure is fed only with information on the shape modification and physical parameters vector, KLE/PCA does not directly provide a way to return to the original design parameters from the so-called latent space (i.e., the reduced dimensionality representation of the original shape parameterization). Two criticalities ensue: (1) shape

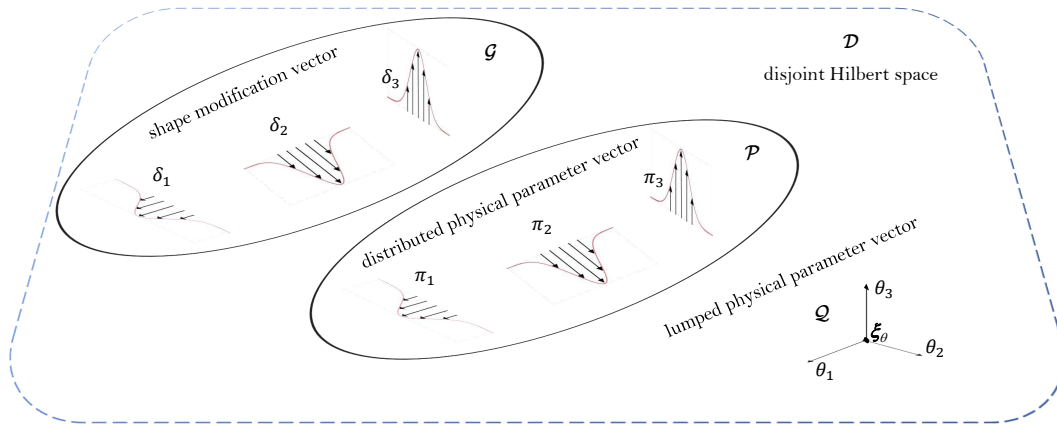


Figure 3: Domains for shape modification vector, distributed physical parameter vector, and lumped (or global) physical parameter vector in a disjoint Hilbert space.

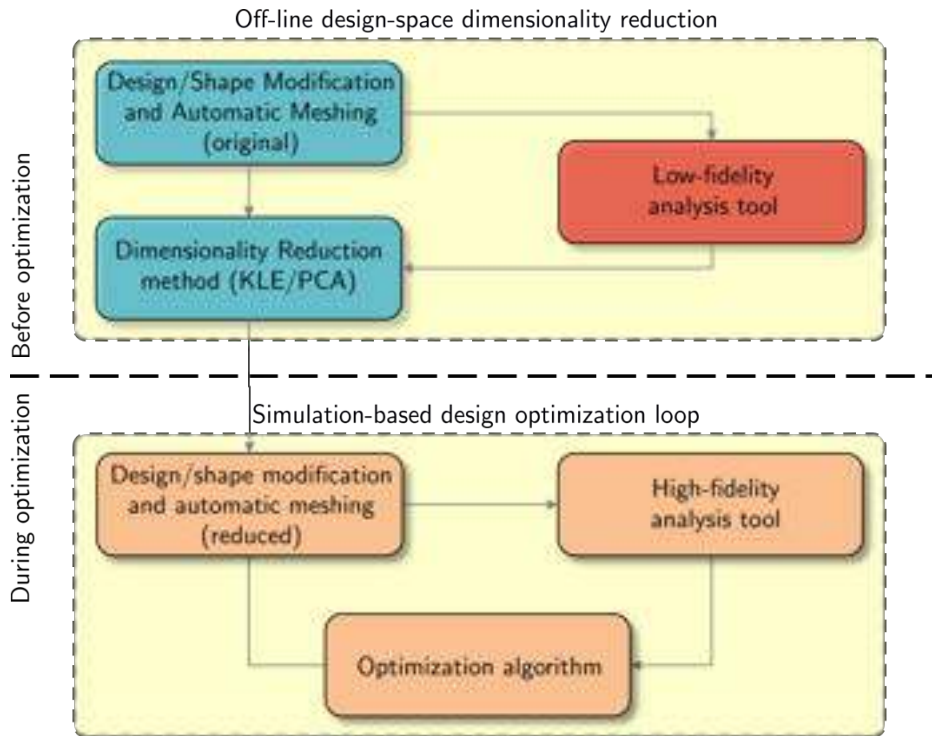


Figure 4: Block diagram for simulation-based shape optimization using physics-informed dimensionality reduction.

modification-based KLE/PCA obliges the user to implement a new shape modification method based on the KLE/PCA eigenfunctions/eigenvectors; (2) moreover, depending on the bounds applied to the reduced design variables, there is not guarantee that the shape produced using KLE/PCA eigenvectors actually belongs to the original design space, thus potentially resulting in design unfeasibilities.

For these reasons, a recent extension of the methodology was introduced by Serani & Diez (2022) to embed the parameters of the original shape parameterization (e.g., CAD/CAE models) in the reduced-dimensionality representation provided by KLE/PCA. The embedding relies on a formulation that is formally equivalent to using Eqs. 12 and 13, albeit at the discrete level. Specifically, the original model parameters are given a null weight in the generalized inner product. This allows to preserve the design variability structure based on the concept of geometric variance, and, at the same time, provide with a reduced-dimensionality representation of the shape parameterization that uses directly the original parameters, without the need for implementing shape modifications based on KLE/PCA eigenfunctions/eigenvectors. Detailed mathematical formulation with applications are provided by Serani & Diez (2022) and, for the sake of brevity, not repeated here.

### 3 EXAMPLE APPLICATION

KLE/PCA is applied to the shape reparameterization and hull-form optimization of the DTMB 5415 model, an open-

to-public naval combatant hull widely used as optimization benchmark in the ship hydrodynamic community (Grigoriopoulos et al., 2017).

The optimization problem pertains to the minimization of the total resistance in calm-water at  $Fr = 0.28$  (equivalent to 20 kn for the full-scale ship,  $L_{pp} = 142$  m), subject to fixed length between perpendiculars, vessel displacement greater or equal to the original,  $\pm 5\%$  of maximum variation of beam and draught, and dedicated volume for the sonar in the bow dome.

Hydrodynamic simulations are conducted using the code WARP (WAVE Resistance Program), developed at CNR-INM. Wave resistance computations are based on the linear potential-flow theory using Dawson (double-model) linearization (Dawson, 1977). The frictional resistance is estimated using a flat-plate approximation, based on the local Reynolds number (Schlichting & Gersten, 2000). Details of equations, numerical implementations, and validation of the numerical solver are given in Bassanini et al. (1994). Simulations are performed with two degrees of freedom (sinkage and trim) for the demi-hull, taking advantage of symmetry about the  $\xi_1\xi_3$ -plane. The computational domain for the free-surface is defined within  $0.5L_{pp}$  upstream,  $1.5L_{pp}$  downstream, and  $1L_{pp}$  sideways. For the shape optimization problem,  $180 \times 50$  grid nodes are used for the hull, whereas  $150 \times 50$  nodes are used for the free-surface.

The original design space for the shape modification is

formed by  $M = 10$  design variables, defined by the free-form deformation (FFD) method (Sederberg & Parry, 1986). Specifically, the demi-hull is embedded in a lattice of  $5 \times 3 \times 3$  nodes in the  $\xi_1 \xi_2 \xi_3$  reference system: only 10 nodes are active and can be moved in the beam ( $\xi_2$ ) direction only. Figure 5 shows an example of shape modification by a contour plot: the FFD lattice is represented by the black points, the active nodes are depicted with green circles, and the modified nodes are shown with blue diamonds.

Data for geometry-based KLE/PCA collects the shape modification vector  $\delta$  components. Physics-informed KLE/PCA data also includes heterogeneous/distributed and lumped physical parameters. Specifically, pressure distribution ( $p$ ), wave elevation ( $\eta$ ), and wave resistance coefficient ( $C_w$ ) are taken into account. These physical parameters are based on even-keel WARP solutions obtained with a quite coarse panel grid.

A hybrid global/local deterministic particle swarm optimization algorithm (Serani et al., 2015) is used, assuming a limited budget of function evaluations equal to 200. The optimization algorithm setup is taken from Serani et al. (2016b). For the sake of current example, two degrees of freedom WARP solutions obtained with a quite fine panel grid are used to drive the optimization loop.

KLE/PCA is trained by sets of  $S = 100, 1000, \text{ and } 10000$  MC samples and the variance resolved is presented in Figure 6. Specifically, Figure 6 shows the cumulative sum of the KL eigenvalues as percentage of the total variance, along with mean and 95% confidence interval evaluated by bootstrap analysis. The results are found convergent versus the number of samples. If at least the 95% of the original variance ( $\sigma^2$ ) is desired,  $N = 4$  reduced design variables are needed using geometry-based KLE/PCA, whereas physics-informed KLE/PCA requires  $N = 6$  variables. The corresponding KL modes for the shape modification are shown in Figures 7 and 8. It can be noted how the use of physical parameters affects the shape of the KL modes.

The optimization is performed with the original FFD and the two reduced design spaces. The optimization convergence is shown in Figure 9. The original design space ( $M = 10$ ) achieves a 7.6% reduction for the total resistance. Using geometry-based reduced design space ( $N = 4$ ) improves the algorithm convergence, achieving a better optimum with 8.4% objective improvement. Finally, the physics-informed reduced design space ( $N = 6$ ) provides the best optimum with 11.4% reduction for the total resistance. This means that, even if physics-informed KLE/PCA is not able to reduce the design space dimensionality as the geometry-based KLE/PCA is (six versus four design variables, respectively), using physical parameters in the dimensionality-reduction phase provides a more efficient and effective design space, leveraging the resulting physical significance of KL modes.

The optimal hull shapes, along with the contour of the shape modification, are shown in Figure 10. It can be noted how original FFD and geometry-based reduced design space op-

tima are quite similar, whereas the optimum obtained by the physics-informed reduced design space is significantly different, showing a wider bow dome. Finally, comparison of pressure distribution on the hull and wave elevation pattern produced by the parent and the optimal hull forms are given in Figures 11 and 12, respectively. The design obtained by the physics-informed reduced design space shows a better pressure recovery towards the stern compared to the other optima, along with a significant reduction of both transverse and diverging Kelvin waves.

#### 4 CONCLUDING REMARKS

The paper reviewed and discussed recent methods for design-space dimensionality reduction in global simulation-based shape optimization, based on the KLE. The approach moves from the assumption that, before running the design optimization procedure, the design problem is affected by epistemic uncertainty, being the optimal design not known a priori. Therefore, the design variable vector goes stochastic, opening the door to cross-fertilization with methods for stochastic processes, specifically aimed at dimensionality reduction such as the KLE.

KLE is formally equivalent to POD for flows/turbulence studies and reduces to the PCA of the discretized shape (and optionally physical parameters) modification vector. The formulations discussed here span from geometric only to physics informed. An example has been shown and discussed for the hydrodynamic optimization of a ship hull. The methodology goes beyond the current application and may be applied in all those areas where the design performance depends on the product shape (such as aerodynamics, heat transfer, acoustics, and aeroacoustics, etc.).

The geometry-based formulation has the evident advantage that no simulations are required before running optimization. Nevertheless, no physical information is used in the analysis and therefore no physical meaning is provided of what is physically resolved in the reduced-dimensionality design space and what is not. In other words, KL modes are not necessarily physically relevant.

The physics-informed formulation overcomes this limitation by including physical parameters provided by low-fidelity solvers. The resulting reduced-dimensionality representation of the shape modification vector is more efficient and effective than that provided by the geometry-based formulation, leveraging the physical significance of KL modes. Nevertheless, it is achieved at a higher computational cost as low-fidelity solvers need to be run during the design-space dimensionality reduction phase. Nevertheless, if the computational cost associated to low-fidelity solutions is orders of magnitude smaller than that associated to high-fidelity solutions used during the optimization phase, the physics-informed formulation is still very convenient.

A third and compromise option is to use geometrical parameters that are physically relevant, such as for instance air/hydrofoil sections global/integral parameters (Volpi et al.,

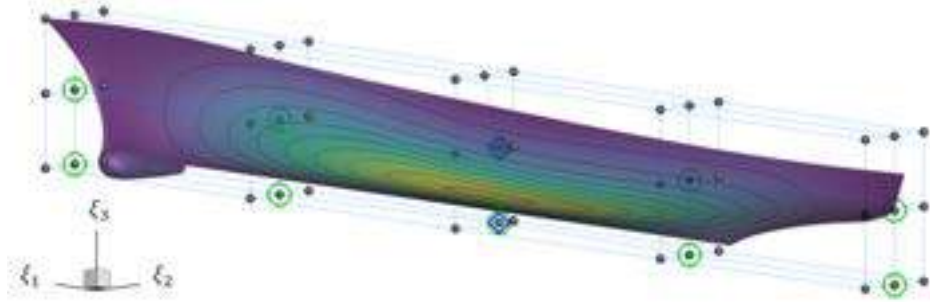
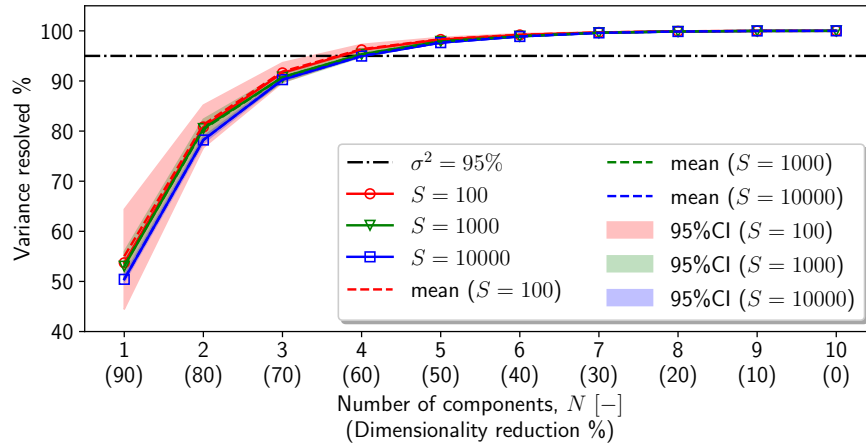
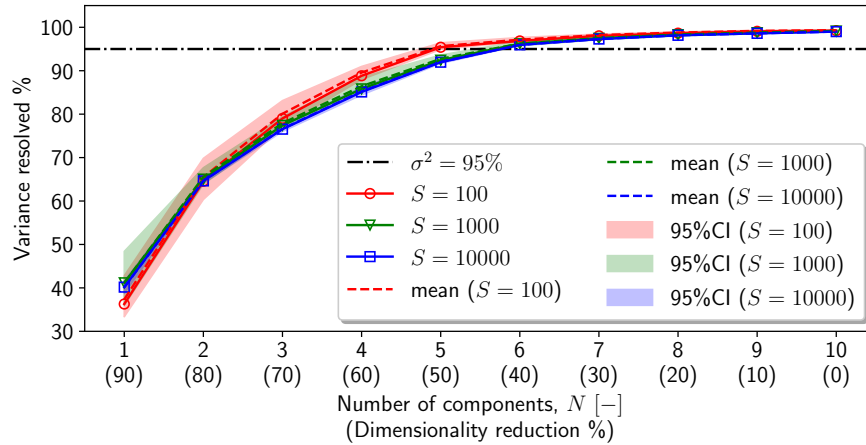


Figure 5: FFD shape modification example: black points are the FFD lattice nodes, green circle are the active nodes, and blue diamonds are the modified nodes in this example.



(a) Geometry-based



(b) Physics-informed

Figure 6: Variance resolved by the KL modes conditional to the number of MC samples ( $S$ ), along with mean value and confidence interval provided by the bootstrap method.

2018) or hulls sections/waterplane-area global/integral parameters (Khan et al., 2022). This would allow for con-

sidering physically related parameters (though by geometry only) without the need for running any physical-model solver

in the design-space dimensionality reduction phase, providing a reasonable compromise between geometry-based and physics-informed formulations.

A possible limitation to the use of KLE/PCA methods is that, if the dimensionality reduction procedure is fed only with information on the shape modification and physical/geometrical parameters, KLE/PCA does not directly provide a way to return to the original design parameters from the latent space. For these reasons, a recent extension of the methodology was introduced by Serani & Diez (2022) to embed the parameters of the original shape parameterization (e.g., CAD/CAE models) in the reduced-dimensionality representation provided by KLE/PCA, which can be very attractive in the industrial context.

It may be noted that the formulations discussed here rely on a linear dimensionality reduction approach and therefore a linear representation of the reduced-dimensionality shape-modification vector (linear subspace). If strongly nonlinear relationships exist between design variables, shape modification, and physical parameters, nonlinear dimensionality reduction methods may provide a more efficient and effective representation of the reduced-dimensionality shape-

modification vector, as discussed in D'Agostino et al. (2018); Serani et al. (2020).

In summary, theory and techniques for stochastic processes and dimensionality reduction in uncertainty modeling and quantification, such as KLE and its variants, have demonstrated their capability of providing a rigorous and powerful framework for design-space variability assessment and dimensionality reduction in global shape optimization. These allow for the efficient exploration of large design spaces in shape optimization, which, in turn, enables global multidisciplinary optimization under uncertainty.

#### ACKNOWLEDGMENTS

The authors are grateful to Drs. Woei-Min Lin, Elena McCarthy, and Salahuddin Ahmed of the Office of Naval Research and Office of Naval Research Global for their support through NICOP grants N62909-18-1-2033 and N62909-21-1-2042.

#### REFERENCES

Bassanini, P., Bulgarelli, U., Campana, E. F., & Lalli, F. (1994). The wave resistance problem in a boundary in-

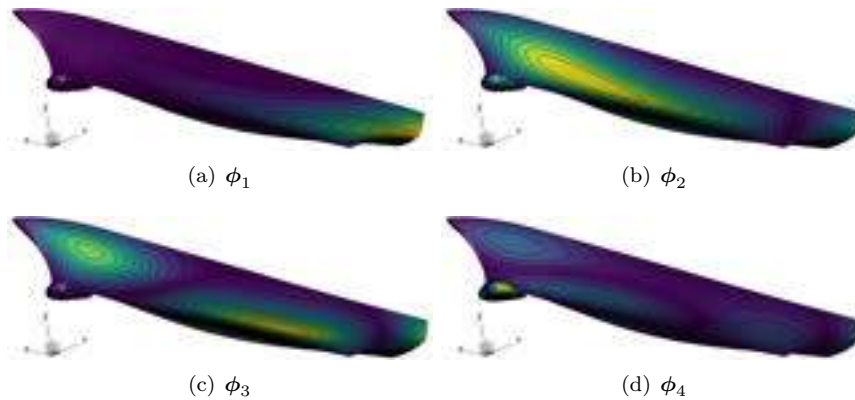


Figure 7: Geometry-based eigenvectors magnitude.

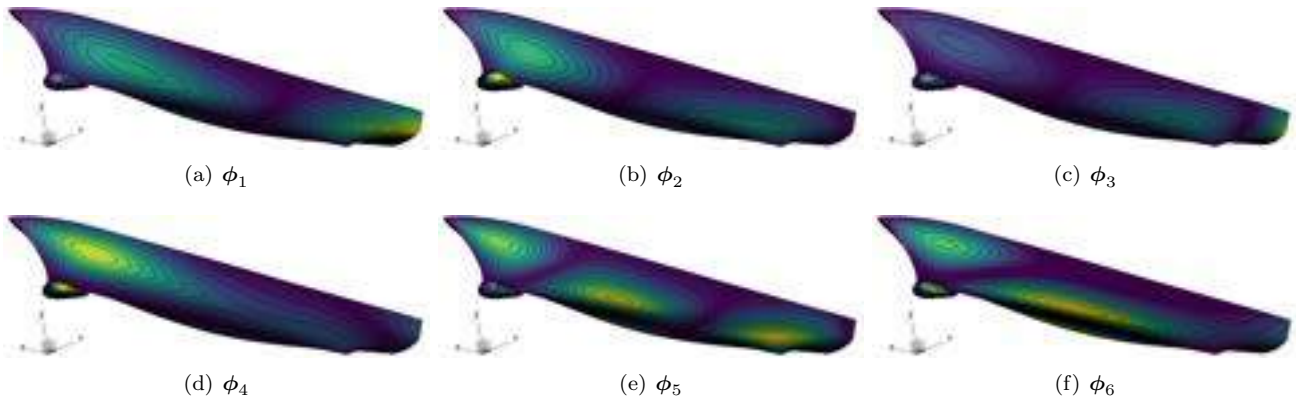


Figure 8: Physics-informed eigenvectors magnitude (shape modification component).

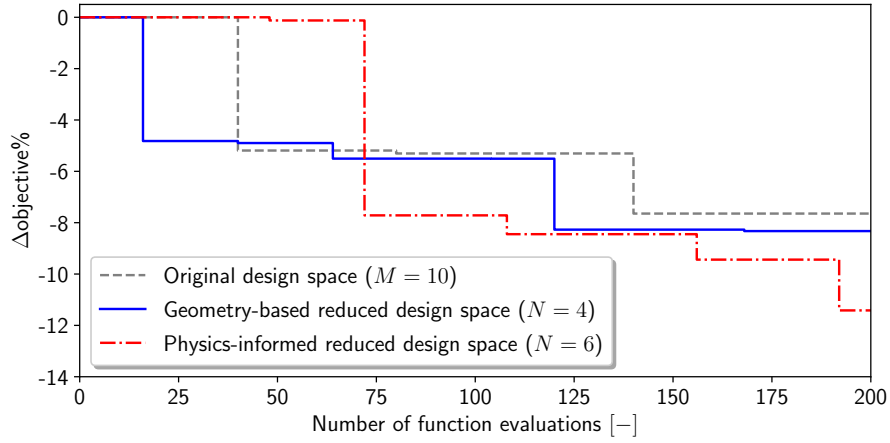


Figure 9: Optimization convergence.

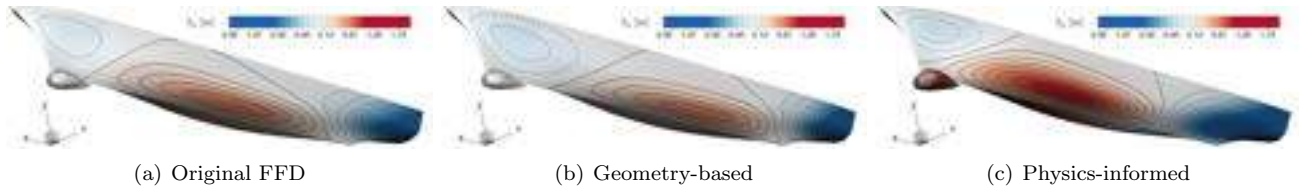


Figure 10: Optimal shapes for the the original and the reduced design spaces: shape modification in  $\xi_2$ -direction.

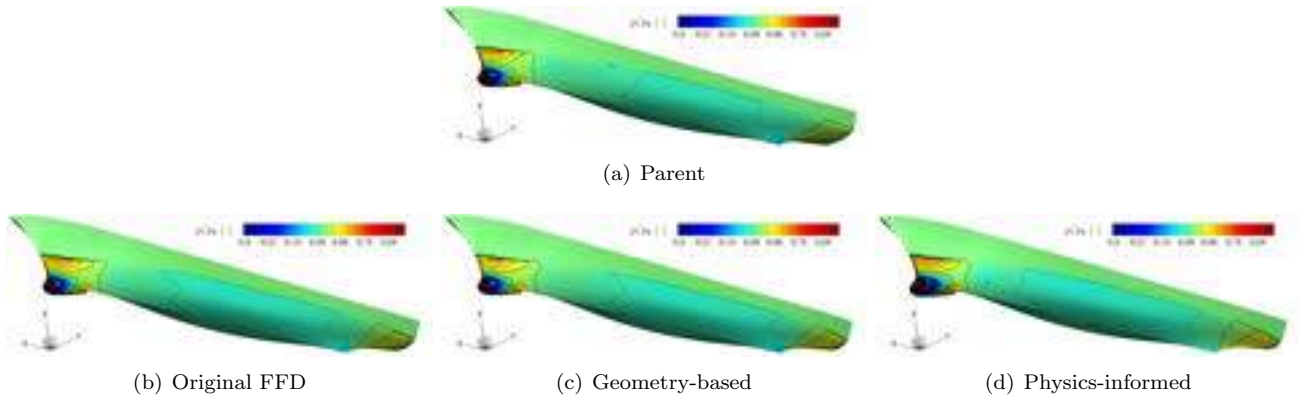


Figure 11: Comparison of the pressure field on the parent (a) and the optimal (b, c, d) hulls.

tegral formulation. Surveys on Mathematics for Industry, 4, 151–194.

Borzi, A., Schulz, V., Schillings, C., & Von Winckel, G. (2010). On the treatment of distributed uncertainties in pde-constrained optimization. GAMM-Mitteilungen, 33(2), 230–246.

Campana, E. F., Peri, D., Tahara, Y., & Stern, F. (2006). Shape optimization in ship hydrodynamics using compu-

tational fluid dynamics. Computer methods in applied mechanics and engineering, 196(1-3), 634–651.

Cinquegrana, D., & Iuliano, E. (2018). Investigation of adaptive design variables bounds in dimensionality reduction for aerodynamic shape optimization. Computers & Fluids, 174, 89–109.

D’Agostino, D., Serani, A., Campana, E. F., & Diez, M. (2018). Deep autoencoder for off-line design-space dimensionality reduction in shape optimization. In 2018

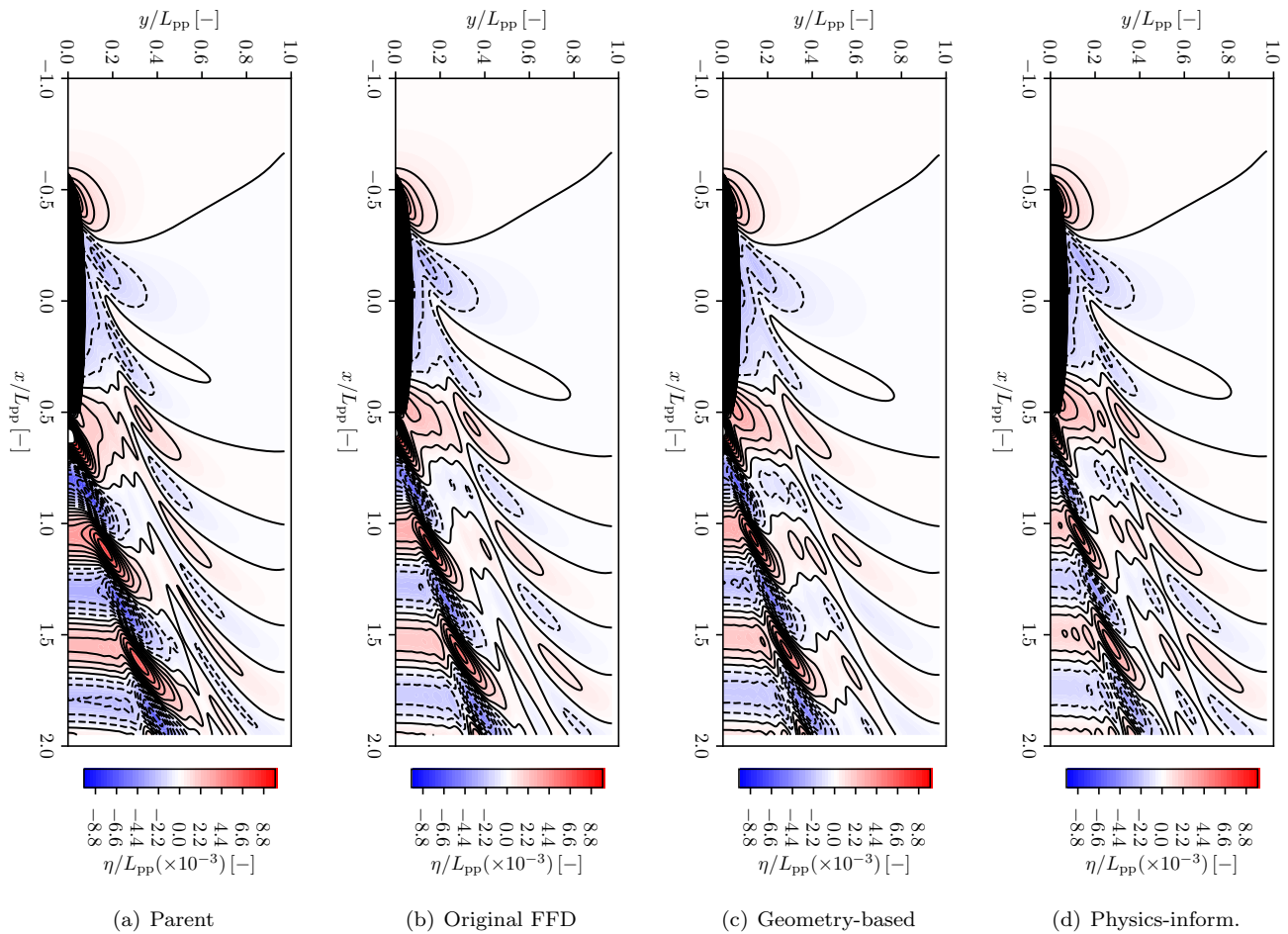


Figure 12: Comparison of the wave elevation pattern produced by the parent (a) and the optimal (b, c, d) hull shapes.

AIAA/ASCE/AHS/ASC Structures, Structural Dynamics, and Materials Conference, (p. 1648).

Dawson, C. W. (1977). A practical computer method for solving ship-wave problems. In Proceedings of the 2nd International Conference on Numerical Ship Hydrodynamics, (pp. 30–38). Berkeley.

Diez, M., Campana, E. F., & Stern, F. (2015). Design-space dimensionality reduction in shape optimization by Karhunen–Loève expansion. Computer Methods in Applied Mechanics and Engineering, 283, 1525–1544.

Diez, M., Campana, E. F., & Stern, F. (2018). Stochastic optimization methods for ship resistance and operational efficiency via cfd. Structural and Multidisciplinary Optimization, 57(2), 735–758.

D’Agostino, D., Serani, A., & Diez, M. (2020). Design-space assessment and dimensionality reduction: An off-

line method for shape reparameterization in simulation-based optimization. Ocean Engineering, 197, 106852.

Grigoropoulos, G., Campana, E., Diez, M., Serani, A., Goren, O., Sariöz, K., Danişman, D., Visonneau, M., Queutey, P., Abdel-Maksoud, M., et al. (2017). Mission-based hull-form and propeller optimization of a transom stern destroyer for best performance in the sea environment. In VII International Conference on Computational Methods in Marine Engineering MARINE2017.

Haftka, R. T., & Grandhi, R. V. (1986). Structural shape optimization-a survey. Computer Methods in Applied Mechanics and Engineering, 57(1), 91–106.

Harries, S., & Abt, C. (2019). Faster turn-around times for the design and optimization of functional surfaces. Ocean Engineering, 193, 106470.

Khan, S., Kaklis, P., Serani, A., & Diez, M. (2022). Geometric moment-dependent global sensitivity analysis without

- simulation data: application to ship hull form optimisation. Computer-Aided Design, (p. 103339).
- Le Maître, O., & Knio, O. M. (2010). Spectral methods for uncertainty quantification: with applications to computational fluid dynamics. Springer Science & Business Media.
- Lukaczyk, T., Palacios, F., Alonso, J. J., & Constantine, P. (2014). Active subspaces for shape optimization. In Proceedings of the 10th AIAA Multidisciplinary Design Optimization Specialist Conference, National Harbor, Maryland, USA, 13-17 January.
- Poole, D. J., Allen, C. B., & Rendall, T. C. (2015). Metric-based mathematical derivation of efficient airfoil design variables. AIAA Journal, 53(5), 1349–1361.
- Raghavan, B., Xiang, L., Breikopf, P., Rassineux, A., & Vilon, P. (2013). Towards simultaneous reduction of both input and output spaces for interactive simulation-based structural design. Comput. Methods Appl. Mech. Engrg., 265, 174–185.
- Robinson, G., & Keane, A. (2001). Concise orthogonal representation of supercritical airfoils. Journal of Aircraft, 38(3), 580–583.
- Samareh, J. A. (2001). Survey of shape parameterization techniques for high-fidelity multidisciplinary shape optimization. AIAA journal, 39(5), 877–884.
- Schillings, C., Schmidt, S., & Schulz, V. (2011). Efficient shape optimization for certain and uncertain aerodynamic design. Computers & Fluids, 46(1), 78–87.
- Schlichting, H., & Gersten, K. (2000). Boundary-Layer Theory. Springer-Verlag, Berlin.
- Sederberg, T. W., & Parry, S. R. (1986). Free-form deformation of solid geometric models. ACM SIGGRAPH computer graphics, 20(4), 151–160.
- Serani, A., Campana, E. F., Diez, M., & Stern, F. (2017). Towards augmented design-space exploration via combined geometry and physics based Karhunen-Loève expansion. In 18th AIAA/ISSMO Multidisciplinary Analysis and Optimization Conference (MA&O), AVIATION 2017, Denver, USA, June 5-9.
- Serani, A., D’Agostino, D., Campana, E. F., Diez, M., et al. (2020). Assessing the interplay of shape and physical parameters by unsupervised nonlinear dimensionality reduction methods. Journal of Ship Research, (pp. 1–15).
- Serani, A., & Diez, M. (2018). Shape optimization under stochastic conditions by design-space augmented dimensionality reduction. In 19th AIAA/ISSMO Multidisciplinary Analysis and Optimization Conference (MA&O), AVIATION 2018, Atlanta, USA, June 25-29.
- Serani, A., & Diez, M. (2022). Parametric model embedding. to appear in Computer Methods in Applied Mechanics and Engineering, arXiv preprint arXiv:2204.05371.
- Serani, A., Diez, M., Campana, E. F., Fasano, G., Peri, D., & Iemma, U. (2015). Globally convergent hybridization of particle swarm optimization using line search-based derivative-free techniques. In X.-S. Yang (Ed.) Recent Advances in Swarm Intelligence and Evolutionary Computation, vol. 585 of Studies in Computational Intelligence, (pp. 25–47). Springer International Publishing.
- Serani, A., Diez, M., Wackers, J., Visonneau, M., & Stern, F. (2019). Stochastic shape optimization via design-space augmented dimensionality reduction and rans computations. In AIAA SciTech 2019 Forum, (p. 2218).
- Serani, A., Fasano, G., Liuzzi, G., Lucidi, S., Iemma, U., Campana, E. F., Stern, F., & Diez, M. (2016a). Ship hydrodynamic optimization by local hybridization of deterministic derivative-free global algorithms. Applied Ocean Research, 59, 115 – 128.
- Serani, A., Leotardi, C., Iemma, U., Campana, E. F., Fasano, G., & Diez, M. (2016b). Parameter selection in synchronous and asynchronous deterministic particle swarm optimization for ship hydrodynamics problems. Applied Soft Computing, 49, 313 – 334.
- Sieger, D., Menzel, S., & Botsch, M. (2015). New Challenges in Grid Generation and Adaptivity for Scientific Computing, chap. On Shape Deformation Techniques for Simulation-Based Design Optimization, (pp. 281–303). Cham: Springer International Publishing.
- Toal, D. J., Bressloff, N. W., Keane, A. J., & Holden, C. M. (2010). Geometric filtration using proper orthogonal decomposition for aerodynamic design optimization. AIAA journal, 48(5), 916–928.
- Volpi, S., Diez, M., & Stern, F. (2018). Multidisciplinary design optimization of a 3d composite hydrofoil via variable accuracy architecture. In 2018 Multidisciplinary Analysis and Optimization Conference, (p. 4173).

# The Performance Prediction and Energy Saving Evaluation for the Retrofit of a Gate Rudder System on a General Cargo Vessel using CFD Procedures

**Kurt Mizzi<sup>1\*</sup>, Mariana Zammit Munro<sup>1</sup>, Ahmet Gurkan<sup>2</sup>, Batuhan Aktas<sup>2</sup>,  
Mehmet Atlar<sup>2</sup>, Noriyuki Sasaki<sup>2</sup>**

<sup>1</sup>Naval Architectural Services Ltd., Research, Development & Innovation Dept., Paola, Malta

<sup>2</sup>University of Strathclyde, Naval Architecture, Ocean and Marine Engineering, Glasgow, United Kingdom

**Abstract:** The path to climate neutrality by 2050 has incentivised policymakers to introduce regulatory measures and social pressures in the marine industry to accelerate the development of energy saving technologies and the optimisation of ship propulsion performance to minimise the consumption of fuel. The Gate Rudder System (GRS) is a novel energy saving and manoeuvring device that has successfully demonstrated the reduction of fuel consumption and emissions when installed on newbuilt ships that operate in coastal regions. The GATERS project, funded by the EC EU H2020 programme (ID: 860337), aims to demonstrate the retrofit application of the GRS on ships and is evaluating the retrofit on a general cargo vessel from a holistic point of view, including structure, installation, fabrication, experimental and virtual tank testing. The project brings together leading experts in computational fluid dynamics to identify and implement the best practices to accurately predict the performance of the Gate Rudder System using numerical procedures. This paper provides an overview of the different CFD methods, solvers and approaches that were utilised and fine-tuned to capture the benefits of the GRS and improve ship performance.

**Keywords:** Gate Rudder System, Virtual Tank Testing, CFD, Numerical Performance Prediction, Energy Saving.

## 1 INTRODUCTION

The Gate Rudder System (GRS) is an emerging technology in the marine industry that has initially proven a reduction in power requirements as well as improvements in manoeuvring performance, thus offering a solution to the industry for a remarkable reduction in fuel consumption and reduced environmental impact. To further demonstrate and exploit its "Retrofit" potential, technology experts, prime stakeholders, policymakers, and suppliers have come together to collaborate, investigate and study the technology further.

The aim of the GATERS project is to design, manufacture and install a retrofit Gate Rudder System (GRS) on a general cargo vessel and demonstrate the effectiveness of the retrofit technology through sea trials and voyage monitoring (GATERS 2021). Additional goals of the GATERS project are to exploit the potential feasibility, benefits and impact of retrofitting the Gate Rudder System (GRS) across the range of European Short Sea Shipping (SSS) operations or its implementation and impact through wider ship types at the concept exploration level, including the Oceangoing Shipping (OS) operations. The consortium consists of 18 partners across Europe, all having the necessary and complementary expertise to carry out the tasks, disseminate and exploit the project (EU 2021). The GATERS Innovation Action Project is sponsored by the EC H2020 Programme (ID: 860337) with an independent aim and objectives. The project has an official sub-license

agreement with Wartsila Netherlands BV to utilise the Gate Rudder Patent (EP 3103715) for specific retrofit projects of vessel sizes below 15000 dwt.

The consortium consists of a dedicated CFD team dedicated to the development of accurate numerical performance prediction procedures for the General Cargo vessel with the current conventional rudder as well as the retrofitted Gate Rudder.

This paper showcases the numerical modelling practices adopted by two of the partners, Naval Architectural Services Ltd. (NAS) and University of Strathclyde (USTRATH) with the aim of accurately predicting the performance of the Gate Rudder System whilst also demonstrating and exploiting the benefits of the technology.

The initial step of the investigation was to validate the different numerical methods by comparing results to experimental benchmark data. Once verified, the study then moved on to analysing the performance of the Gate Rudder System at various speeds at full-load condition. The results indicated average savings of around 7.90% for the different conditions.

## 2 BACKGROUND

Energy saving devices may be defined as mechanisms that reduce power demand by improving losses in the propeller-hull system (Terwisga 2013). The losses generally

\* Corresponding author e-mail: kurt.mizzi@nas.com.mt

considered are rotational and axial propeller energy losses, which, if reduced, also lead to lower carbon dioxide emissions – working towards the IMO strategy to reduce GHG emissions from shipping by at least 50% by 2050 compared to 2008 (Spinelli, et al. 2022).

The principle behind the energy saving device being investigated, the Gate Rudder System (GRS), is the presence of two asymmetric rudders at each side of the propeller with the functionality of a ducted propeller. The duct effect of the system provides increased propulsive efficiency and the ability to rotate both rudders, resulting in improved manoeuvrability and seakeeping properties (Sasaki, et al. 2018). Besides the economic advantages provided by the GRS, the safety and habitability of the ship are also improved. Regarding economic gain, the GRS allows for higher propulsive efficiency, an increase of cargo space and a reduction of ship length through the elimination of the conventional rudder. Safety is also improved as the GRS is superior to the conventional rudder in terms of stopping ability, manoeuvrability, berthing performance in crabbing mode and also through reduction of the ship's rolling motion. Moreover, considering the comfort of crew and passengers aboard, the GRS is beneficial as it reduces the propeller-induced noise and hence the system vibration (Turkmen, et al. 2016).

The original purpose of the GRS was to improve the manoeuvrability of Japanese coastal vessels that required tighter control of ships in their transverse motions at ports. The GRS was first applied on the coastal container "Shigenobu", and the vessel's performance was compared to that of her sister ship "Sakura", fitted with a conventional rudder system. The results obtained from sea trials indicated that Shigenobu was 14% more efficient at the design speed than Sakura. Moreover, it was found that the gain in service from employing the GRS can be as high as 30% in rough seas (Sasaki et al., 2020).

In recent years, several numerical and experimental studies have been carried out to determine the feasibility of the GRS. Turkmen et al. (2016) carried out a series of experiments at the Emerson Cavitation Tunnel in the UK to obtain open water propeller data, measure and compare the gate rudder forces with a conventional rudder system (Turkmen, et al. 2016). In conjunction with the model-scale experiments, CFD analysis were conducted to investigate the effect of the full-scale GRS on the flow field at the stern. The results showed that there was an increase in thrust by 10% when the gate rudder was located closer to the propeller plane (at 1.25R in comparison to 1.5R). Turkmen et al. (2016) also performed a cost effectiveness study, where the authors found that the Return on Investment (ROI) for the GRS installed on a new ship would be between 0.56 and 1.18 years, indicating a period of less than a year for most of the scenarios considered. The authors describe a new powering performance prediction technology, the "Fine powering performance prediction technology", that has been developed particularly for ship hulls incorporating Energy Saving Devices (ESDs), for instance, the GRS. The concept is based on the use of a

reasonably large model at a relatively high Reynolds number to capture the complex interaction between the model hull, propeller and rudder and more accurately extrapolate the results obtained. Turkmen et al. (2016) found that due to the favourable thrust of the gate rudder, resistance tests revealed a reduction in the resistance of about 1-3%, which is equal to the reduction in hull resistance in the absence of a conventional rudder. Moreover, self-propulsion tests with the GRS revealed 4-8% higher (1-t) value compared to the conventional rudder and open water data for the GRS also presented 15-25% higher (1-w) values (Turkmen, et al. 2016).

Further investigation of the GRS using CFD was conducted by Tacar et al. (2020), who compared experimental and virtual towing tank tests results for full load and sea trial load conditions, with the gate rudder, conventional rudder and with the bare hull (Tacar et al., 2020). Two model sizes were investigated, both experimentally and numerically, of dimensions 2 m and 5 m. For the CFD analysis, the full load condition was investigated, and the realisable k- $\epsilon$  turbulence model was used. The effective power of the GRS was estimated from the experiment, and the CFD simulations and the results were found to be very similar, with the difference between them amounting to just over 1%.

Tacar et al. (2020) performed an open water test for the GRS using the Moving Reference Frame (MRF) method for propeller modelling, which showed very good agreement with the experiment results. They found that as the ship speed increases, the advantageous effect of the GRS also increases, compared to the conventional rudder case at the sea trial condition (Tacar et al., 2020). Moreover, the authors state that at a service speed of 15 knots, the ship fitted with the GRS requires approximately 17% less brake power in comparison to that employing the conventional rudder system. Tacar et al. (2020) then proceeded to extrapolate the experimental model results to full scale using the ITTC 1978 method. The authors found that, with regard to scale effects, the smaller model size overpredicts, while the larger model underpredicts the power requirement, compared to sea trial measurements (Tacar et al., 2020).

ESDs are challenging to evaluate by means of model test results and also during sea trial measurements. Moreover, the issue of scaling arises and leads to improper extrapolation of model test results, causing uncertainties when determining the performance of such devices (Mizzi, et al. 2015). In particular, since ESDs are generally fitted within the boundary layer of the hull, direct extrapolation to full scale conditions is problematic due to the strong viscous effects occurring in the region (Mizzi, et al. 2017).

Moreso, for the GRS, the scale effect is also a topic of concern, as mentioned by Tacar et al. (2020) and further studied in depth by Sasaki et al. (2019), who explored the reasons behind this phenomenon and proposed a new correction procedure.

Sasaki et al. discovered that the resistance of the GRS measured in model tests was 5 to 10 times that of the full-scale results (Sasaki & Atlar, 2019). While the full-scale trials of Shigenobu presented 14% energy savings, the conventional prediction method did not present any gain for the GRS. The authors noted that in the model scale, the GRS experiences laminar flow over the appendages in the stern region, even with turbulence stimulators, as suggested by the ITTC 1978 procedure. Conventional rudders operate in the propeller slipstream, where the accelerated flow suppresses laminar flow separation and therefore do not experience this issue (Sasaki & Atlar, 2019). In fact, other studies have found that ESDs tend to be more efficient at full scale than model scale (Kawamura, Ouchi and Nojiri 2012), (Hansen, Dinham-Peren and Nojiri 2011).

Consequently, the scale effect of the GRS is significantly larger than that of the conventional rudder. Therefore, Sasaki et al. (2019) proposed a correction procedure based on the semi-empirical approaches supported by model and full-scale data. The recommendation by Sasaki et al. (2019) is to divide the measured propeller advance speed, based on the thrust identity, into two components – a different scaling method being applied to each component. However, the authors state that this study would greatly benefit from additional studies, incorporating CFD, systematic model tests and also full-scale trials (Sasaki & Atlar, 2019).

### 3 GEOMETRY

#### 3.1 Hull & Propeller

The target vessel is a multi-purpose 90m dry cargo ship of 5650 DWT that is equipped with a 5 bladed fixed pitch propeller. The original propeller was initially manufactured to be 3.6m but was later cropped to 3.42m following the sea trials. The hull and propeller characteristics can be found in Table 1 and Table 2.

A 6m hull model and corresponding model propeller were manufactured for experimental testing purposes. Towing tank tests were carried out at various speeds, both at full and trial draught conditions, in both towing and propelled arrangements. The tests were also replicated with the retrofitted Gate Rudder System that was designed and fine-tuned to the form of the vessel. The experimental data was then used as benchmark data for validation and verification purposes of the numerical methods.

**Table 1. Hull Characteristics**

Parameter	Symbol	Units	Ballast Load	Full Load
Length overall	$L_{OA}$	<i>m</i>	89.95	
Length between perp.	$L_{BP}$	<i>m</i>	84.95	
Breadth	<i>B</i>	<i>m</i>	15.4	
Draught (midship)	<i>T</i>	<i>m</i>	3.3	6.45
Draught (AP)	$T_A$	<i>m</i>	3.8	6.45
Draught (FP)	$T_F$	<i>m</i>	2.8	6.45
Displacement	$\Delta$	<i>t</i>	3607	7241
Block coefficient	$C_B$	--	0.818	0.84

**Table 2. Propeller Characteristics**

Parameter (Original / Modified)	Symbol	Unit	Value
Propeller Diameter	<i>D</i>	<i>m</i>	3.60 / 3.42
Blade Number	<i>Z</i>	--	5
Pitch Diameter Ratio	<i>P/D</i>	--	0.79
Blade area ratio	<i>BAR</i>	--	0.66 / 0.61
Skew	--	<i>mm</i>	26.05
Rake	--	<i>mm</i>	5.5

Both the hull and propellers were developed in 3D digital format. It was ensured that the geometry was developed to be free of errors to prevent any issues in the meshing process. Furthermore, the hull form characteristics were verified and compared to the hydrostatics from the stability book to ensure accuracy and precision.

#### 3.2 Gate Rudder System

Similarly, the Gate Rudder System was designed in a 3D format, as shown in Figure 1. This followed an in-house design procedure whereby the wake characteristics of the naked hull were initially analysed, and the Gate Rudder blades and propeller design fine-tuned to optimise the angle of attack of the wake flow on the Gate Rudder System.

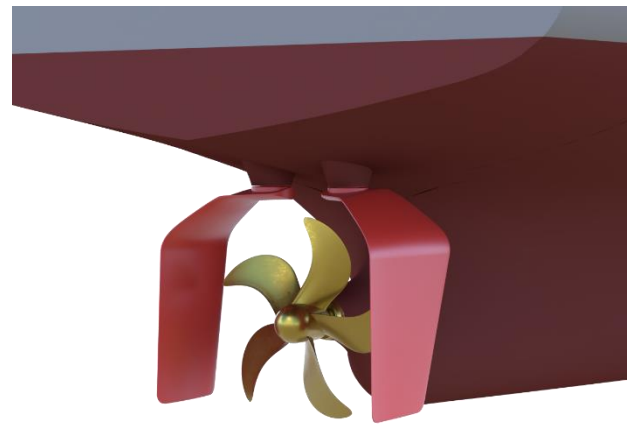


**Figure 1. Geometry**

#### 3.3 Ship Conditions

For this numerical study, the performance of the retrofitted GRS on the target vessel was analysed at 3 different speeds at full-load conditions. For each operating condition, the vessel was analysed in a naked hull condition (no appendages), towing condition (appendages and no propeller) and self-propelled condition (appendages and propeller).

### 4. METHODOLOGY

#### 4.1 Numerical Modelling

Both NAS and USTRATH adopted similar approaches for their numerical methods with key differences and models to provide a basis for investigation and discussion. Numerical details and differences are clearly highlighted in the following section.

Both entities used the commercial CFD solver, STAR-CCM+®, to model the multiphase flow using Unsteady Reynold Averaged Navier-Stokes (URANS) equations to simulate a three-dimensional environment. A Volume of Fluid (VOF) method was used to model the free surface effects. With regard to the turbulence model, NAS made use of the Reynolds Stress Model (RSM), whereas USTRATH made use of the realisable k-ε model.

All the studies were carried out in calm water conditions allowing the vessel to pitch or heave. For all the models, the all- $y^+$  wall treatment model was used with the appropriate blending of the prism layer cells to the near domain cells. This is a hybrid approach that allows high- $y^+$  wall treatment for coarse meshes and low- $y^+$  wall treatment for fine meshes. The high- $y^+$  wall treatment adopts the wall-function type approach which assumes that the near-wall cell lies within the logarithmic region of the boundary layer. The near-wall cell centroid must be situated in the logarithmic region of the boundary layer ( $y^+ > 30$ ). Meanwhile, the low- $y^+$  wall treatment is suitable only for low-Reynolds number turbulence models where the viscous sublayer is properly resolved. This method considers no explicit modelling assumptions and is generally used if the mesh is fine enough for  $y^+$  to be approximately 1 or less than 5. NAS have developed their mesh in such a way that that hull is treated using wall functions ( $y^+ > 30$ ) and the appendages, such as the Gate Rudder System, properly resolved with  $y^+$  values smaller than 5. Meanwhile, USTRATH have maintained a  $y^+$  lower than 1 on both the hull and appendages, as can be seen in Figure 2.

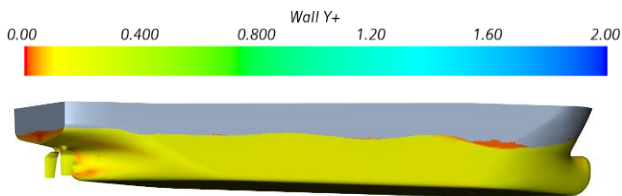


**Figure 2.  $y^+$  Distribution on Hull**

An implicit unsteady time marching scheme together with a Finite Volume Method (FVM) approach was carried out to treat temporal and spatial discretisation. The time step for all simulations were set to provide adequate convective courant numbers.

The accurate representation of ship geometry is very important as this dictates the flow behaviour. The surface mesh was generated using fine triangulated faces producing detailed geometry, and the volume mesh was developed using the automatic grid generation tool producing an unstructured grid. Mesh refinements have been applied at appropriate critical locations of high gradients to capture the flow behaviour accurately.

For all the simulations, a velocity flow field condition was specified at the inlet boundary and a pressure field for the outlet boundary. All the other boundaries were set with the appropriate physics. The ship geometry was specified with a non-slip wall allowing boundary layer generation. On the

other hand, the bottom boundary was placed far enough below the water level to avoid any shallow water effects. Wave damping was also applied to the inlet, outlet and side boundaries, preventing wave reflections.

Furthermore, the propeller behaviour was simulated using the virtual disk feature integrated within Star-CCM+®, commonly known as the actuator disk that makes use of a user-defined momentum source method. More specifically, the body force propeller method was utilised to simulate the propeller's action. This model approach generates a momentum source considering the propeller's geometrical and open water performance characteristics. The distribution of the axial and tangential forces of the propeller and its effect on the flow is calculated. The integration of these forces over the disk gives the thrust and torque of the propeller, which are available for coupling with the hull.

Since the actuator disk does not consider the physical model of the propeller, propeller induced velocities are not accounted for. To tackle this matter, an expert property known as the "Induced Velocity Correction" can be enabled that essentially follows a predictor corrector approach that modifies the local advance ratio and source terms as described in (Neitzel, et al. 2015).

The Body Force Propeller Method requires the definition of the inflow specification of the virtual disk, which in our case, is calculated from the flow field of the vessel. The virtual disk model uses the inflow information for the computation of the advance ratio that is then used to determine the operating point from the propeller open water characteristics curve. In order to establish the self-propulsion point of the vessel such that there is no acceleration/deceleration, the operating point is defined by indicating that the propeller thrust needs to be equal to the ship resistance. The operating point of the propeller is automatically varied until this condition is met.

#### **4.2 Verification & Validation**

In order to showcase and justify consistency and reliability of the numerical solver, verification and validation procedures were carried out. The validation and verification studies involved carrying out a mesh refinement study for the conditions with the highest loads and speeds for the model scale condition assumed to be 1:14 of the full-scale ship. Results were processed to ensure validation and verification and tabulated in the standard format/template to allow easy comparison between NAS and USTRATH.

The verification studies were carried out to demonstrate and ensure the capability of the numerical models using the Grid Convergence Index (GCI) that is based on the Richards Extrapolation (L. F. Richardson 1911, Richardson and Gant 1927) to calculate the discretisation error estimates as described by Celik et al. (2008).

The apparent order of the method,  $p$ , is calculated using Eqs. (1) to (3), where  $r_{21}$  and  $r_{32}$  are refinement factors,  $\phi_k$  is the CFD output parameter (resistance, thrust, torque and RPM) and  $\varepsilon_{21}$  and  $\varepsilon_{32}$  represent the difference between the results obtained from grids 1 (fine) and 2, and 2 and 3 (coarse), respectively. For this study, the refinement ratios were selected to be  $\sqrt{2}$  ( $r_{21}$ ,  $r_{32}$ ) for NAS and 2.3 ( $r_{21}$ ) and 1.7 ( $r_{32}$ ) for USTRATH.

$$p = \frac{1}{\ln(r_{21})} |\ln|\varepsilon_{32}/\varepsilon_{21}| + q(p)| \quad (1)$$

$$q(p) = \ln\left(\frac{r_{21}^p - s}{r_{32}^p - s}\right) \quad (2)$$

$$s = 1 \cdot \text{sign}\left(\frac{\varepsilon_{32}}{\varepsilon_{21}}\right) \quad (3)$$

The extrapolated values are obtained by Eq. (4).

$$\phi_{ext}^{21} = \frac{(r_{21}^p \phi_1 - \phi_2)}{(r_{21}^p - 1)} \quad (4)$$

The approximate and extrapolated errors are calculated using Eqs. (5) and (6), and the Grid Convergence Index between the two finest grids ( $GCI_{21}$ ) is given by Eq. (7).

$$e_a^{21} = \left| \frac{\phi_1 - \phi_2}{\phi_1} \right| \quad (5)$$

$$e_{ext}^{21} = \left| \frac{\phi_{ext}^{12} - \phi_1}{\phi_{ext}^{12}} \right| \quad (6)$$

$$GCI_{fine}^{21} = \frac{1.25 e_a^{21}}{r_{21}^p - 1} \quad (7)$$

Since the angle of attack of the flow to the gate rudder profile is considered crucial to the performance of the technology, NAS has also investigated the accuracy of their numerical method when it comes to wake prediction by comparing it with the experimental wake data. The velocities inside the wake were first processed to initially compare the contours and then compare the velocity distribution along different radial profiles to produce the wake plots for comparison and analysis.

#### 4.3 Computational Set up

The resource and computational infrastructure set-up is very similar for both partners (NAS and USTRATH), whereby the pre-processing and simulation set-up were configured on office computers using the Star-CCM+® software. In order to run the simulations, due to the high computational requirements, both partners make use of a High-Performance Computer (HPC) cluster to have access to more nodes and cores that can be utilised simultaneously. The information is uploaded onto the HPC via remote access and runs via a scheduler. The computational set-up is portrayed in Figure 3.

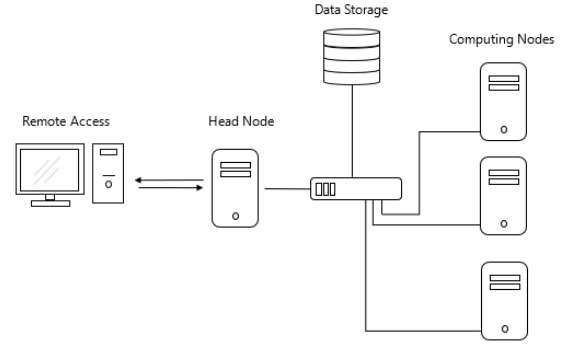


Figure 3. Computational Set-up

## 5. RESULTS & DISCUSSION

### 5.1 Verification & Validation

#### Verification

The GCI was used as a metric of comparison between the three grids of varying grid densities. Table 3 displays the  $GCI^{21}$  values for comparison between the turbulence models employed by USTRATH and NAS for the simulations analysing the GRS at full-load draught, in towing and self-propelled conditions. It should be noted that the simulations performed by USTRATH, used the realisable k- $\varepsilon$  model, while NAS used the RSM, both running the condition of  $Fr = 0.225$ , equivalent to the speed condition of 13 knots.

Table 3. Verification Study - Turbulence Model Comparison

	<i>Realisable k-<math>\varepsilon</math></i>	<i>RSM</i>
	$GCI^{21}$ %	
<b><math>R_T</math></b>	0.33	0.07
<b><math>T</math></b>	0.33	0.54
<b><math>Q</math></b>	0.28	0.45
<b><math>rps</math></b>	0.09	0.04

As presented in Table 3, for the resistance in towing condition ( $R_T$ ), the RSM and realisable k-epsilon turbulence models both produced converged results with  $GCI^{21}$  values of 0.07% and 0.33% respectively. With regards to the parameters measured in self-propelled conditions ( $T$ ,  $Q$ ,  $rps$ ), both the realisable k-epsilon model and RSM turbulence produced converged results, with the  $GCI^{21}$  values ranging from 0.04% to 0.54% for the various parameters.

The fine mesh configurations for both numerical models, featured significantly high cell numbers requiring substantial computational power. Therefore, it was not considered feasible to carry out the study using such mesh sizes. Since the medium mesh configurations produced very similar results to the fine mesh models, it was decided, by both partners, to carry out the validation comparison and GRS impact study using the medium grid size characteristics.

**Validation**

For validation with experimental (EFD) results, the percentage error between the EFD and CFD results were computed for the simulations analysing the GRS at full-load draught, in towing and self-propelled conditions. As portrayed in Table 4, for the resistance in towing condition ( $R_T$ ), the realisable  $k-\epsilon$  model produced more accurate results in comparison to experimental data, with a percentage error of 0.15%. However, for the parameters measured in self-propulsion conditions ( $T$ ,  $Q$ ,  $rps$ ), the RSM and realisable  $k-\epsilon$  model yielded similar results with values ranging from 1.43% to 3.76% across the different parameters.

In summary, the verification study produced satisfactory results that in most cases reflected monotonic convergence for both the realisable  $k-\epsilon$  and RSM turbulence models. Moreover, the validation study for both turbulence models revealed good agreement with experimental results.

**Table 4. Validation Study - Turbulence Model Comparison**

	<i>Realisable <math>k-\epsilon</math></i>	<i>RSM</i>
	<i>Error %</i>	
$R_T$	0.15	2.79
$T$	3.42	2.88
$Q$	3.76	3.62
$rps$	1.43	2.29

**5.2 Wake Validation**

*Wake Contours*

The towing simulation with GRS computed with the RSM turbulence model was further post-processed to validate and compare the wake behaviour at the propeller plane position with the available EFD data. As displayed in Figure 4, at first impression, the wake behaviour is similar. However, the CFD output indicates a symmetrical wake, whereas the experimental wake is not symmetrical. The matter is currently being investigated.

**Experimental Processed Data**

**CFD Output (NAS)**

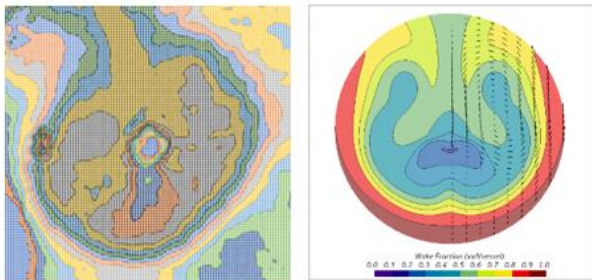


**Figure 4. Wake Contour Comparison**

The analysis then proceeded to compare the velocity distribution of the wake, between the CFD (RSM model) and the EFD tests, along different radial profiles at the propeller plane that led to the development of wake plots, as displayed in Tables 5, 6 and 7.

In general, one can notice the symmetrical behaviour of the numerical  $V_x$  wake plots in contrast to the experimental wake behaviour. Trends in wake distribution and velocity profile in the  $x$ -direction are sufficiently accurate except near the  $180^\circ$  region (see Table 5). Trends in  $V_y$  wake distribution and velocity profile in the  $y$ -direction are sufficiently similar to the experimental data. While not conclusive, CFD tends to underpredict the velocity in the  $y$ -direction (see Table 6). At the same time, the trends in  $V_z$  wake distribution and velocity profile in the  $z$ -direction are sufficiently similar to the experimental data, particularly at higher radii (see Table 7).

*Wake Plots*

**Table 5. Wake Profile Comparison -  $V_x$**

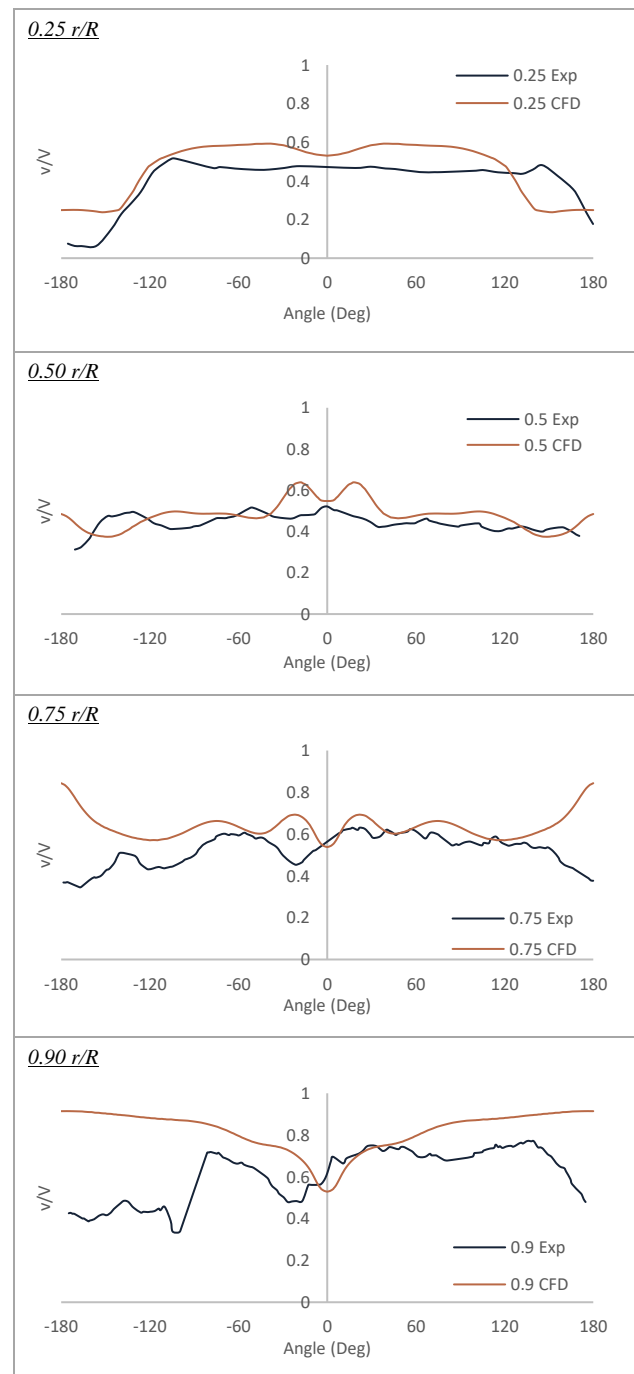


**Table 6. Wake Profile Comparison -  $V_y$**

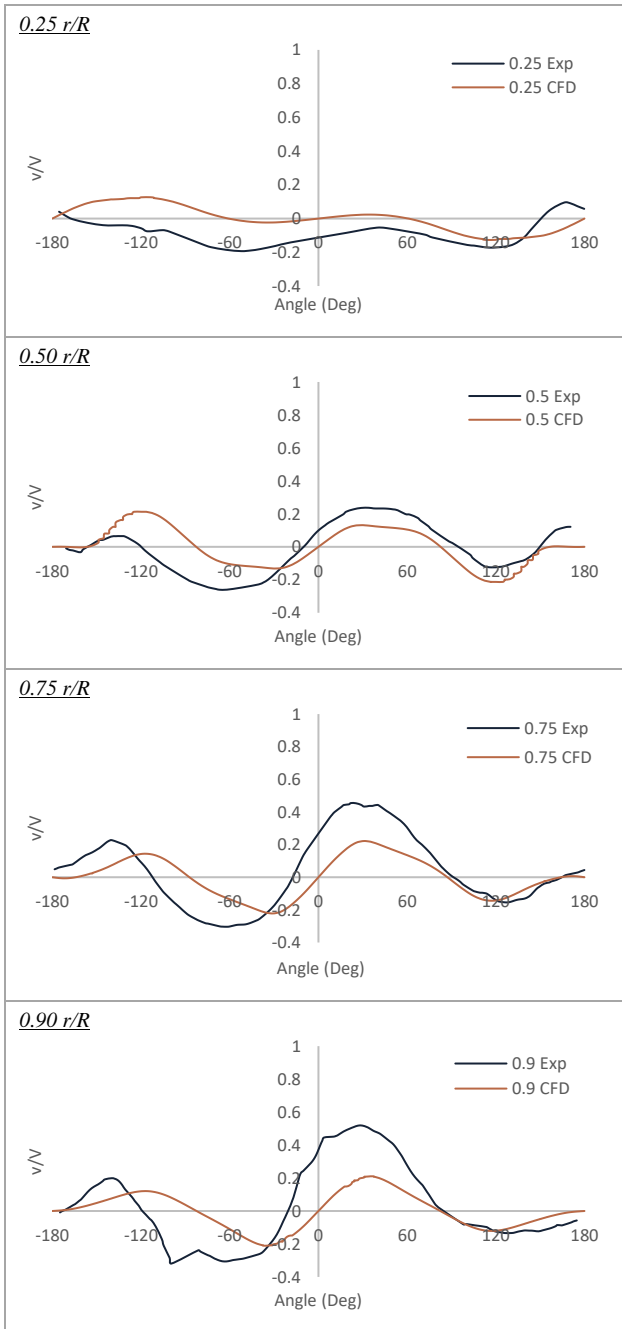
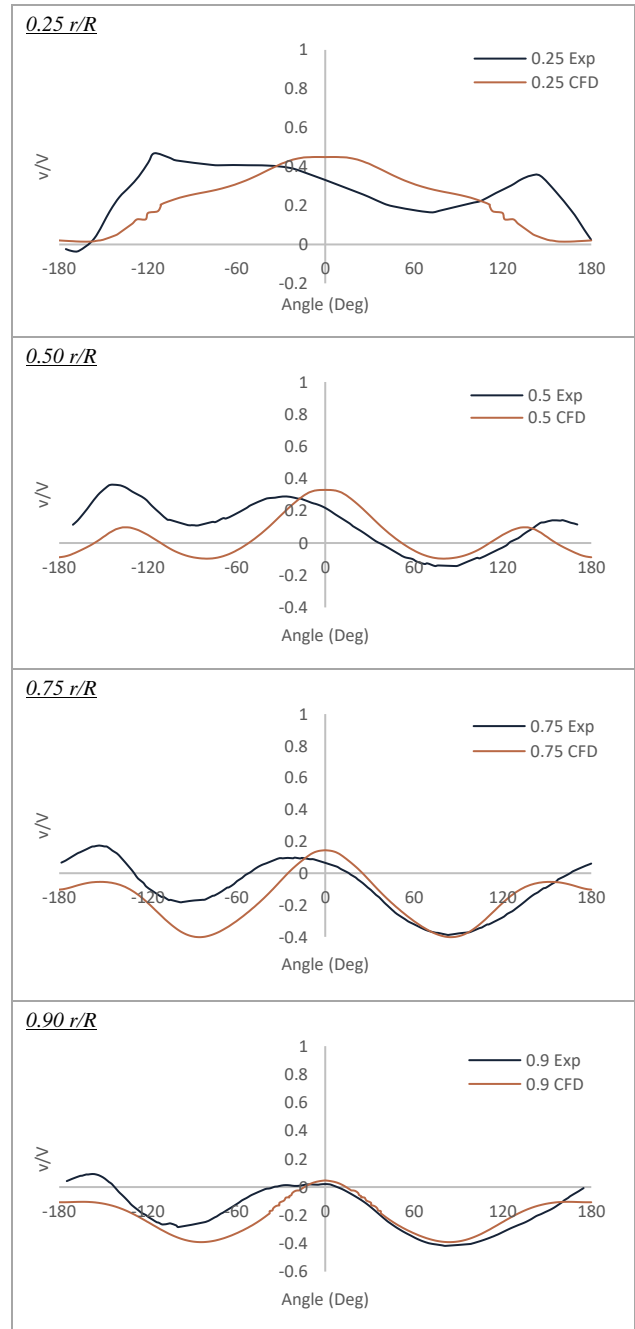


**Table 7. Wake Profile Comparison -  $V_z$**



**5.3 Gate Rudder Performance**

Once the numerical models had been validated and verified for both entities respectively, the same models were then used to compute and predict the performance of the target ship with the conventional rudder system (CRS) as well as the gate rudder system (GRS) at three different speeds (11kts, 12kts and 13kts) at full-load condition. As shown in Figures 5 and 6, it is further reassuring that the performance predictions for the effective power ( $P_E$ ) as well as the delivered power ( $P_D$ ) that were conducted by both partners for the three speeds, are exhibiting similar results and trends. It is evident from the effective power ( $P_E$ ) curves in Figure 5 that the benefits of the GRS over CRS in towing conditions are minor.

NAS results have indicated an average 1% effective power improvement across the three different speeds whilst USTRATH results indicate an average improvement of 0.70%. This is expected as the GRS requires the action of the propeller to exploit its benefits. This is clearly demonstrated in the delivered power ( $P_D$ ) curves (Figure 6), that indicate an average power improvement of 8.26% across the three speeds by NAS and 7.35% by USTRATH.

The measured data for Resistance, Thrust, Torque and RPM were further processed to compute and compare the propulsive efficiency parameters between the conventional rudder condition as well as the gate rudder system to better understand the reason behind the benefits of the GRS. Results have been tabulated in Table 8.

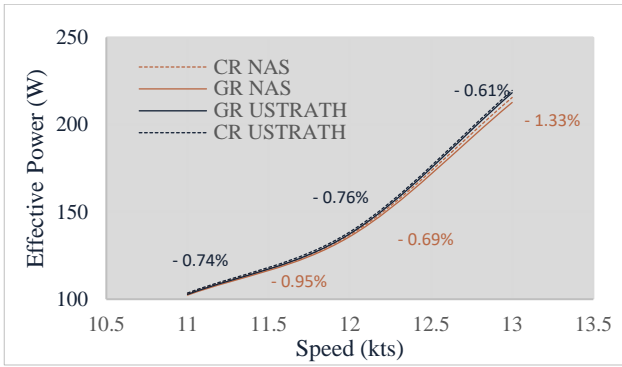


Figure 5. Effective Power Prediction

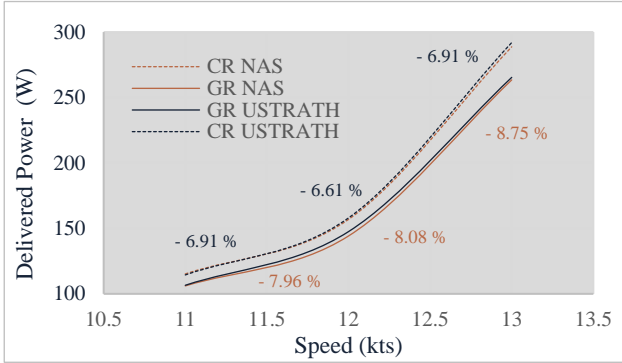


Figure 6. Delivered Power Prediction

Whilst the relative rotative efficiency ( $\eta_R$ ) is similar between both rudder types; the hull efficiency is lower for the hull with GRS. This may be explained by the reduction in wake fraction ( $w_i$ ) across the three different speeds, which is not offset by the decrease in the thrust deduction fraction ( $t$ ), which leads to a net reduction of hull efficiency.

The Gate Rudder blades produce a thrust (as opposed to the resistance produced by the conventional rudder) in the propelled condition. The result of this added thrust is a reduction in the total ship resistance ( $R_{sp}$ ), and hence the thrust requirement ( $T$ ) by the propeller is lower, leading to a lower thrust deduction fraction ( $t$ ). Since the propeller is required to produce a lower thrust value, it needs to operate at different operating points and higher advance ratios ( $J$ ). Assuming that the advance velocity is similar for both rudder scenarios, one would expect a reduced rpm value ( $n$ ) for the GRS condition to produce a higher  $J$  value. However, the GRS conditions have produced slightly higher propeller rotation measurements. Therefore, this implies that the advance velocity ( $V_a$ ) is different between

the conditions. As previously stated,  $1-w_i$  is higher across the three speeds for the GRS conditions. This implies that the presence of the Gate Rudder imparts an acceleration to the flow inside the propeller plane. The loss in hull efficiency ( $\eta_H$ ) by the GRS conditions, is however, compensated by the enhanced open water efficiency ( $\eta_o$ ). This is due to the higher advance ratio of the propeller as can be seen in Figure 7 for one of the speeds.

As seen in Table. 8, the product of all three efficiencies ( $\eta_R$ ,  $\eta_H$ ,  $\eta_o$ ) yields the propulsive efficiency ( $\eta_D$ ), indicating a higher efficiency of around 7% across the three speeds (between both NAS and USTRATH) for the GRS retrofitted hull as opposed to the CRS conditions. This improvement, together with the reduction in effective power (PE), leads to the benefits in delivered power (PD) that were previously stated.

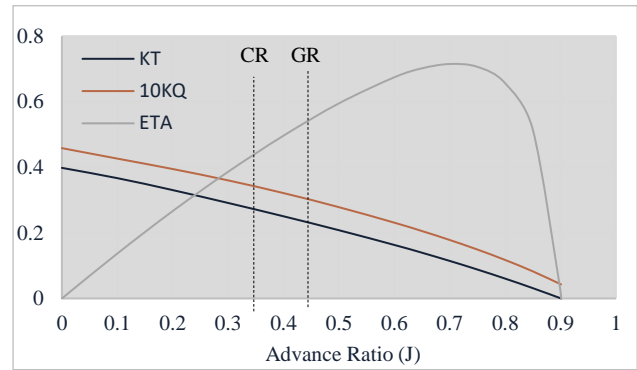


Figure 7. Propeller Open Water Data

#### Local Flow Analyses

Table 9 presents the hydrodynamic forces (i.e., resistance and/or thrust) measured on the hull and rudder(s) components, both in towing and self-propelled conditions, for the RSM numerical models. A positive (+) force indicates resistance, while a negative (-) force indicates a thrust. The percentages indicate the magnitude of the respective forces in proportion to the total force on the hull and rudder(s).

As shown in Table 9, in the towing condition, the Gate Rudder blades produce a minor resistance force, an average of 1.37% of the total resistance across the three speeds. This is very similar to the resistance produced by the conventional rudder at an average of 1.76% of the total resistance across the three speeds. However, in the self-propelled condition, since the propeller action accelerates the flow and hence alters the angle of attack of the flow favourably on the rudder blades, the Gate Rudder blades

Table 8. Propulsive Efficiency Parameters

		NAS									USTRATH							
		$V_s$	$\eta_o$	$w$	$t$	$\eta_H$	$\eta_r$	$\eta_D$	$P_E$	$P_D$	$\eta_o$	$w$	$t$	$\eta_H$	$\eta_r$	$\eta_D$	$P_E$	$P_D$
		$m/s$	--	--	--	--	--	--	W	W	--	--	--	--	--	--	W	W
CRS	11	0.48	0.48	0.24	1.45	1.00	0.70	103	115	0.49	0.47	0.24	1.43	1.00	0.70	104	114	
	12	0.48	0.47	0.25	1.41	1.00	0.68	137	157	0.49	0.46	0.24	1.41	1.00	0.69	139	158	
	13	0.45	0.45	0.23	1.40	1.00	0.63	216	289	0.46	0.44	0.23	1.37	1.00	0.62	220	292	
GRS	11	0.59	0.32	0.14	1.27	1.00	0.75	102	106	0.60	0.30	0.13	1.24	1.00	0.74	103	107	
	12	0.59	0.31	0.13	1.26	1.00	0.74	136	144	0.60	0.28	0.13	1.22	1.00	0.73	137	148	
	13	0.55	0.29	0.15	1.21	1.00	0.67	213	263	0.56	0.27	0.12	1.21	1.00	0.68	218	265	

**Table 9. Comparison of Simulated Forces on the Hull and Rudder(S)**

	Towing				Self-Propulsion				
	V <i>kts</i>	Hull <sub>T</sub> <i>N</i>	GRS <sub>T</sub> <i>N</i>	RT <sub>T</sub> <i>N</i>	Hull <sub>SP</sub> <i>N</i>	GRS <sub>SP</sub> <i>N</i>	RT <sub>SP</sub> <i>N</i>	FD <i>N</i>	T <i>N</i>
Gate Rudder System	11	66.602	1.09	67.692	79.76	-3.65	76.11	15.41	60.7
		98.39%	1.61%	100%	104.80%	-4.80%	100%	--	--
	12	81.17	1.2	82.37	96.31	-4.45	91.86	17.4	74.46
		98.54%	1.46%	100%	104.84%	-4.84%	100%	--	--
	13	117.785	1.255	119.04	141.9705	-5.92	136.05	20.76	115.29
		98.95%	1.05%	100%	104.35%	-4.35%	100%	--	--
Conventional Rudder	11	67.04	1.3	68.34	83.963	1.667	85.63	15.02	70.61
		98.10%	1.90%	100%	98.05%	1.95%	100%	--	--
	12	81.35	1.59	82.94	102.823	1.967	104.79	18.23	86.56
		98.08%	1.92%	100%	98.12%	1.88%	100%	--	--
	13	118.86	1.78	120.64	149.59	1.77	151.36	18.45	132.91
		98.52%	1.48%	100%	98.83%	1.17%	100%	--	--

then produce thrust at an average of 4.7 % of the total resistance across the three speeds. In contrast, with an active propeller, the conventional rudder still produces roughly 1.7% of the total resistance across the three speeds. The results further indicate that the presence of the GR in propelled condition augments the hull resistance favourably, indicating that the Gate Rudder has a positive influence on the pressure resistance of the hull. Also, as seen in Figure 8, most of the GR geometry produces a thrust in propelled condition except for the horizontal part of the rudder blade at the top producing detrimental performance (i.e. resistance). It is interesting to note that a similar thrust was produced by both blades (PS & SB) even if the propeller's rotational action is not entirely symmetrical.

**5.4 Propeller Treatment**

Further analyses were carried out by USTRATH to analyse the impact of the numerical propeller treatment methodology on the performance of the GRS. In this particular case, a study was carried out to analyse and compare the difference in GRS performance when using the virtual disk (VD) approach in comparison to the sliding

mesh (SM) approach in full-scale conditions. As can be seen in Figure 9, the average rudder forces are similar for both approaches. However, with the rigid body (SM), it can be stated that rudder force characteristics are sensitive to the propeller rotation direction. The rudder forces on the port side are higher since the interaction with the propeller is enhanced due to the related flow vector field.

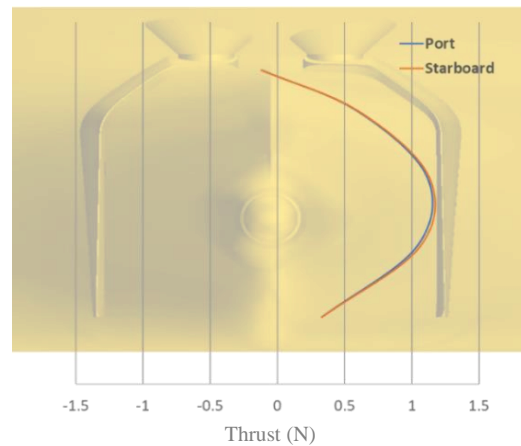


**Figure 8. Thrust Blade Profile**

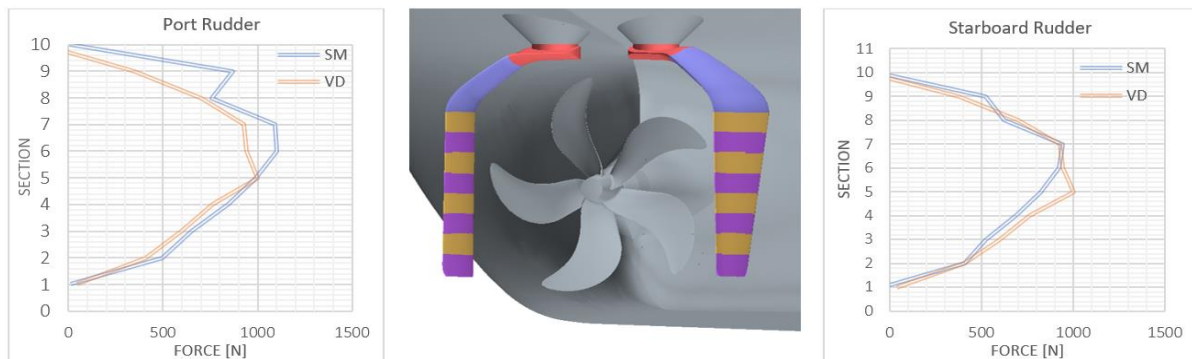


**Figure 9. SM vs VD Propeller Treatment Comparison.**

## 6. CONCLUSION

This paper presents the joint effort of two partners of the GATERS project, NAS and USTRATH, who successfully demonstrate the benefits of the Gate Rudder System (GRS) technology using CFD procedures by adopting and investigating different numerical modelling practices. In particular, model scale simulations were carried out using two different turbulence models, and the results obtained were successfully verified and validated. In summary, for most of the CFD simulations, the GCI reflected monotonic convergence, indicating sound results for all conditions. Moreover, the CFD results provided good agreement with experimental data for all conditions.

The numerical performance predictions of the GRS behaviour outlined in this study are in line with similar published literature, which show that the Gate Rudder System is beneficial, particularly due to the reason that the rudder blades produce a thrust and accelerate the wake flow in the propeller plane region thus leading to reduced power demand and fuel consumption. Future work for the GATERS project includes a study, similar to the one outlined in this paper but at full-scale conditions to determine the performance of this GRS in ship-scale conditions.

## ACKNOWLEDGEMENTS

This paper is based on the activities conducted in the collaborative European project GATERS which is an Innovation Action Project funded by the EC H2020 Programme (ID: 860337) with the independent aim and objectives. The project has an official sub-license agreement with Wartsila Netherlands BV to utilise the Gate Rudder Patent (EP 3103715) at specific retrofit projects of vessel sizes below 15000 DWT.

## REFERENCES

- Celik, I. B., Ghia, U., Roache, P. J., Freitas, C. J., Coleman, H., & Raad, P. E. (2008). 'Procedure for estimation and reporting of uncertainty due to discretization in CFD applications'. *Journal of Fluids Engineering-Transactions of the ASME* 078001-078001-4 , 130(7).
- EU. (2021). *Horizon 2020 - GATE Rudder System as a Retrofit for the Next Generation Propulsion and Steering of Ships*. Retrieved from Horizon Collaboration Network: <https://cordis.europa.eu/project/id/860337>
- GATERS. (2021). *Gaters Project*. Retrieved from <https://www.gatersproject.com/>
- Hansen, H., Dinham-Peren, T., & Nojiri, T. (2011). Model and full scale evaluation of a 'Propeller Boss Cap Fins' device fitted to an Aframax tanker. *Second International Symposium on Marine Propulsors*. Hamburg.
- Kawamura, T., Ouchi, K., & Nojiri, T. (2012). 'Model and full scale CFD analysis of propeller boss cap fins (PBCF)'. *J. Mar. Sci. Technol.*
- Mizzi, K., Demirel, Y. K., Banks, C., Turan, O., Kaklis, P., & Atlar, M. (2017). 'Design optimisation of Propeller Boss Cap Fins for enhanced propeller performance'. *Applied Ocean Research*, 210-222.
- Mizzi, K., Kim, M., Turan, O., & Kaklis, P. (2015). 'Issues with energy saving devices and the way forward'. *Shipping in Changing Climates Glasgow*. Glasgow.
- Neitzel, J., Pergande, M., Berger, S., & Abdel-Maksoud, M. (2015). 'Influence of the Numerical Propulsion Modelling on the Velocity Distribution behind the Propulsion Device and Manoeuvring Forces'. *Fourth International Symposium on Marine Propulsors*. Austin, Texas.
- Richardson, L. F. (1911). 'The approximate arithmetical solution by finite differences of physical problems involving differential equations, with an application to the stresses in a masonry dam'. *Transactions of the Royal Society of London*, 210(459-490).
- Richardson, L. F., & Gant, J. A. (1927). 'The deferred approach to the limit'. *Transactions of the Royal Society of London*, 226(636-646).
- Sasaki, N., & Atlar, M. (2019). 'Scale Effect of Gate Rudder'. *Sixth International Symposium on Marine Propulsors*. Rome.
- Sasaki, N., Kuribayashi, S., Atlar, M., & Steam Co, K. (2018). 'Gate Rudder'. *INT-NAM2018: 3rd International Symposium on Naval Architecture and Maritime*. Istanbul.
- Sasaki, N., Kuribayashi, S., Fukazawa, M., & Atlar, M. (2020). 'Towards a realistic estimation of the powering performance of a ship with a gate rudder system'. *Journal of Marine Science and Engineering*.
- Spinelli, F., Mancini, S., Vitiello, L., De Carlini, M., & Bilandi, R. N. (2022). 'Shipping Decarbonization: An Overview of the Different Stern Hydrodynamic Energy Saving Devices'. *Journal of Marine Science and Engineering (JSME)*.
- Tacar, Z., Sasaki, N., Atlar, M., & Korkut, E. (2020). 'An investigation into effects of Gate Rudder® system on ship performance as a novel energy-saving and manoeuvring device'. *Ocean Engineering*.
- Terwisga, T. (2013). 'On the working principles of energy saving devices'. *3rd International Symposium on Marine Propulsors*. Tasmania, Australia.
- Turkmen, S., Carchen, A., Sasaki, N., & Atlar, M. (2016). 'A New Energy Saving Twin Rudder System-Gate Rudder'.

## Computational optimization of the ship hull shape by constrained transformation of the longitudinal volume distribution

Marek Kraskowski<sup>1</sup>

<sup>1</sup>Maritime Advanced Research Centre, Gdańsk, Poland

**Abstract:** The paper presents a proposal of a formalized approach to the hull shape optimization in respect of total resistance by fine-tuning of its longitudinal volume distribution. An algorithm for automated modification of the hull is presented, allowing for varying the sectional area distribution with negligible influence on resulting displacement. CFD RANS solver STAR-CCM+, coupled with CAD software NX were used for searching of the optimal volume distribution of selected parent shape in respect of total resistance. The bow part and the aft part were optimized separately. The resulting resistance of the selected optimal shapes was then verified by means of scale model tests realized in the towing tank of Maritime Advanced Research Centre (CTO) S.A. Noticeable gain in total resistance was achieved and confirmed by experimental tests. The proposed approach seems a promising method for relatively quick parametric optimization of the designed hull shapes; it is also applicable for generic CFD optimization studies.

**Keywords:** parametric optimization, CFD, model tests, resistance, wave pattern

### 1 INTRODUCTION

The trends observed in modern research focused on experimental and computational ship hydromechanics reflect new possibilities provided by advanced software, high-performance computers and advanced control systems applied in experimental setups. The examples of state-of-the-art experimental techniques are presented e.g. by Lu et al. [1] and Bielicki [2]. In computational fluid dynamics, the focus is e.g. on simulating fully nonlinear dynamics [3] and on effective shape optimization [4]. Especially when it comes to computational analyses, last two decades have witnessed a revolution in the feasibility of CFD analyses in engineering applications. While in the early 2000's the viscous flow analyses were carried out mainly by full-time researchers, for relatively simple objects and with the use of coarse block-structured meshes, at present, the objects of arbitrary complexity can be easily analysed by engineers. This progress was possible mainly due to growing possibilities of computers, development of automated unstructured meshing, as well as development in handling complex geometries and user-friendly graphic interfaces. The attempts on formalized optimization of analyzed geometries were also made from the very beginning of the solvers development. Initially, the multi-variant analyses were possible with the use of potential codes [5] and for 2D cases [6]. Later on, growing power of the computers and efficiency of CAD software allowed for parametric optimization of actual 3D geometries with the use of RANS solvers. An

example of effective optimization of the parametrized hull shape was presented e.g. by Gundelach [7]. His approach to hull modelling can be referred to as Fully Parametric Model (FPM), in which the CAD surface is based on Non-Uniform Rational B-Spline (NURBS) curves surfaces defined from scratch. A foundation for this approach was prepared e.g. by Nowacki [8] and Harries [9,10]. Examples of successful application of fully parametric models for hull shape optimization were presented e.g. by Biliotti et al. [11], Han et al. [12] and Brenner et al. [13]. In order to make the optimization process more efficient, surrogate models are also being used (Feng et al., [14]. However, parameterization of the free form shape like ship hull usually requires careful selection of the regions to be modified and advanced coding, which makes the CAD preparation so time-consuming that this approach not very feasible in engineering practice. An alternative approach is the *a posteriori* transformation of an existing CAD file, which makes the possibilities of modifications strongly limited, but the parameterization itself can be realized relatively fast [15]. Examples of such an approach are presented e.g. by Peri and Campana [16], Perez and Clemente [17] and Choi [18]. This paper also presents a variant of this approach; the optimization is focused on finding the optimum balance between the angle of waterplane ends and the fairness of the shoulders. This kind of optimization is applicable for fine-tuning of the pre-optimized shapes with no major faults. An example of application of proposed approach to selected shape and experimental verification of the results are presented.

## 2 PARENT HULL SHAPE

The presented analyses were carried out for the INSEAN 7000 DWT Tanker. Its shape is presented in Fig. 1. Its basic features are presented in table 1.

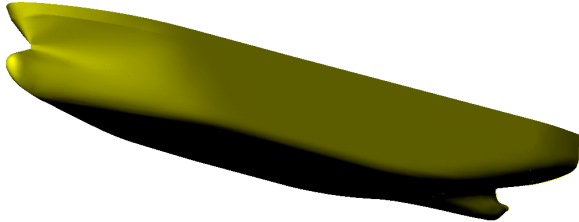


Fig. 1 Parent hull shape

Table 1. Basic features of the parent hull shape

Length between perpendiculars	$L_{PP}$ [m]	94.00
Breadth	$B$ [m]	15.40
Draught	$T$ [m]	6.00
Displacement	$\nabla$ [m <sup>3</sup> ]	6827
Wetted surface area	$S$ [m <sup>2</sup> ]	2249
Block coefficient	$C_B$ [-]	0.786
Design speed	$V$ [kn]	14
Froude number	$F_n$ [-]	0.237

## 3 POSSIBLE APPROACHES TO SHAPE PARAMETERIZATION

Parameterization of the CAD geometry consists in defining the dependencies between location of points, angles of curves etc. by introducing the expressions, so that changing the value of one or more global variables modifies whole geometry. This can be explained by simple example of a cube. If the properties of this solid are not known, its unequivocal definition in Cartesian coordinate system requires specification of 24 figures, i.e. three coordinates of each of 8 corners of the cube. However, if we know the dependencies between the coordinates of the cube corners, we can define and modify its geometry by giving just one figure, i.e. the length of the side.

Two important observations can be made on the basis of this example:

- although the modification of the parameterized geometry is very fast, much more work is required to prepare the CAD definition due to the need of defining the dependencies between selected geometric features of the object;

- parametric definition of the object loses the flexibility in introducing the modifications; e.g. changing the form of the regular cube into arbitrary cuboid is not possible with parametric definition, while it is straightforward with standard definition.

Several attempts on effective hull form parameterization were made; it was found that two general approaches can be distinguished:

1. Building the parameterized hull definition from scratch, i.e. defining points, curves and surfaces so as to match the required basic shape, and then defining the dependencies between location of the points, curve angles etc. to enable efficient modifications.
2. Defining the control points and planes so as to control the surface provided in the form of CAD exchange file, e.g. IGES, and then defining the dependencies between location of control points and planes to enable efficient modifications.

Pros and cons of described approaches can be easily pointed out - assuming that the task to be realized consists in optimizing the initial proposal of the shape provided by the customer.

1. Building the parameterized definition from scratch.

Advantages:

- + allows much more accurate control of the details of the geometry;
- + provides full flexibility in deciding which regions will be modified and how;

Disadvantages

- when the definition is relatively simple, i.e. based on small number of points and curves, it is hardly possible to match accurately the required basic shape;
- on the other hand, if the shape is to be reproduced accurately, the complexity of the definition increases dramatically, which makes it less useful in introducing modifications;
  - defining the hull from scratch always requires relatively long time, while fast exchange of proposals is especially important at early stage of the contract.

2. Defining the control points and planes allowing transformations of existing shape.

Advantages:

- + full match between basic shape and its parameterized definition
- + the process of parametrization is fast and easy

Disadvantages

- considerably limited control of the details of the geometry.

An attempt on both approaches was made. The results are presented in the following sections.

#### 4 HULL PARAMETERIZATION

As mentioned in the introduction, the selected approach is based on the a-posteriori transformation of existing hull surface definition; an attempt on modelling the shape with fully parametric definition turns out to be inefficient - it is either very hard to obtain required consistency with parent shape, or the definition becomes extremely complex. Parametric transformation of the existing geometry was realized using the Global Shaping feature of the NX software. NX CAD is a very generic environment designed for integrated computer aided engineering. It contains CAD, CAM, CFD, FEM and other tools; in presented work, only the CAD module is used. The Global Shaping is a feature dedicated for manipulating the features of the object imported as an external geometry file. The method of the transformation is explained on the basis of Fig. 2. It can be described as a formalized global shaping.

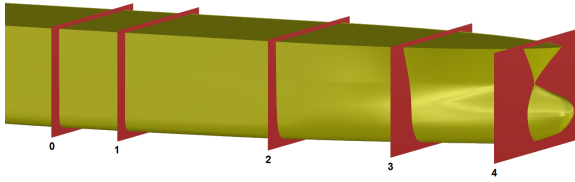


**Fig. 2 Transformation with the use of control planes**

Arbitrary number of control points is assigned to the transformed region. In presented case, the transformation is applied to the region between the midship section and the fore perpendicular. The location of the ones located at the ends of the region (0 and 3 in presented case) remains unchanged. All the control points located between them (1-2) can be shifted arbitrarily, which results in continuous shift of the hull sections in the region between points 0 and 3. The resulting shift of individual sections relative to their initial position is evaluated using the Bézier curve formulation. This formulation is explained in detail below.

Let us define the vector of initial locations of control points:

$$X_{BASE} = [x_0 \quad x_1 \quad x_2 \quad x_3 \quad x_4]$$

The transformation is realized by shifting the control points to new locations:

$$X_{TR} = [x_{0\_TR} \quad x_{1\_TR} \quad x_{2\_TR} \quad x_{3\_TR} \quad x_{4\_TR}]$$

In presented case,  $x_0 = x_{0\_TR}$  and  $x_4 = x_{4\_TR}$ , however, in generic case, this does not necessarily hold true.

The difference between initial and transformed location of the control points is denoted as:

$$\Delta X = X_{BASE} - X_{TR} = [\Delta x_0 \quad \Delta x_1 \quad \Delta x_2 \quad \Delta x_3 \quad \Delta x_4]$$

Our goal is to evaluate the shift of arbitrary point located between  $x_0$  and  $x_4$  based on the values of  $\Delta X$ . For this purpose, let us introduce the parameter  $t \in [0,1]$  and parametrize the length of the transformed region, so that  $x_0$  corresponds to  $t = 0$  and  $x_4$  corresponds to  $t = 1$ . The shift of arbitrary point between  $x_0$  and  $x_4$  is evaluated using the formula:

$$dx(t) = \sum_{i=0}^n \Delta x_i B_i^n(t) \quad (1)$$

where  $B_i^n(t)$  are so-called Bernstein polynomials [9] defined as:

$$B_i^n(t) = \begin{cases} \binom{n}{i} t^i (1-t)^{n-i} & \text{for } i = 0, \dots, n \\ 0 & \text{for } i < 0, i > n \end{cases} \quad (2)$$

Let us now present an example of shape transformation based on 4 control points ( $n=3$ ). The graph below (Fig. 3) shows the form of Bernstein polynomials for  $i=0, \dots, 4$ .

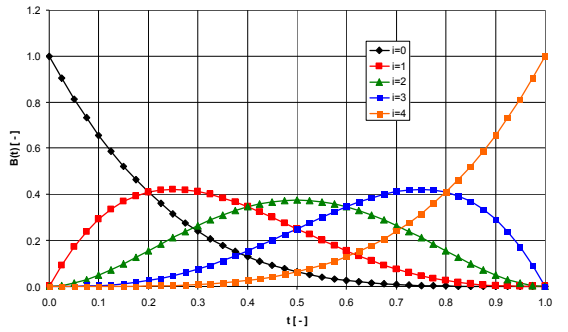


**Fig. 3 Bernstein polynomials**

Formulation of the transformation results in the fact that the location of the control points has no influence on the transformation result - it is only the number of control points which affects the transformation form. The control points are thus evenly distributed along the modified region, which results from technical requirements of the applied NX software (we use midship as zero point and fore perpendicular as end point,  $x=47$  m):

$$X_{BASE} = [0 \quad 11.75 \quad 23.50 \quad 35.25 \quad 47]$$

We then introduce the following transformation based on single parameter  $p$  (values of vector  $\Delta X$ ):

$$\Delta X = [0 \quad -p \quad -p \quad a \cdot p \quad 0] \quad (3)$$

The result of shifting three control points according to (3) on the transformation of the sectional area curve of the bow part is shown in Fig. 4 (modified - red). The contribution of subsequent control points as well as resulting shift  $dx$  is presented in the second graph.

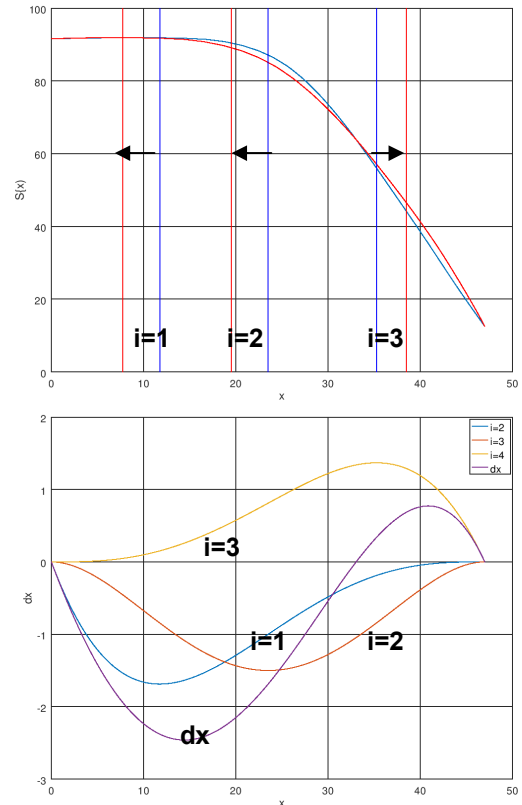


**Fig. 4 Using Bernstein polynomials for shape transformation**

The coefficient  $a$  is a constant used to calibrate the transformation procedure so as the displacement volume remains constant within considered range of variation of parameter  $p$ . The range of  $p$  is limited by the software requirements, i.e. the control planes must not swap their places along the hull after transformation; in other words. if the  $x$  coordinate of plane  $i$  is larger than the  $x$  coordinate of plane  $i-1$  before transformation, it must still be larger after transformation (this is not a limitation of the formulation itself). On the other hand, the transformed shape for extreme values of parameter  $p$  must still fit the ship shape canon, however, this criterion has no mathematical formulation, it is only based on designer's experience and intuition. The procedure of selection of the range of  $p$  and value of  $a$  can be described as follows:

- select an interval (usually symmetrical) of parameter  $p$  meeting the mentioned criteria; in presented example the range is from -4 to 4;
- set the value of  $p$  to minimum of the assumed interval and set the value of  $a$  to 1;
- use the trapezoid rule to integrate the sectional area curve and compare the displacement volume before

and after the transformation; vary the coefficient  $a$  to obtain a match;

- repeat the procedure for maximum value of parameter  $p$ , using the value of  $a$  found in previous step; in presented example, a match was achieved without further iterations.

Using a MATLAB routine for transformation and integration allows to find the correct value of  $a$  in just a few steps in a guess-and-check manner. In presented example, constant value of  $a$  allows to maintain constant displacement with the accuracy of  $0.2\text{m}^3$  i.e. 0.006%.

The longitudinal centre of buoyancy (LCB) of the ship is not directly controlled in described procedure. In presented example, changing the parameter  $p$  between -4 and 4 results in shifting the centre of volume of the fore part by 0.113m, which results in shifting the LCB of the ship by 0.057m (0.06% of  $L_{pp}$ ). If such a change in LCB is acceptable, as assumed in presented study, the fore part and the aft part can be optimized independently. If not, the aft part must be transformed in parallel with the fore part so as to compensate any change in LCB. The example of resulting modifications of the sectional area curve for extreme values of parameter  $p$  are presented in Fig. 5.

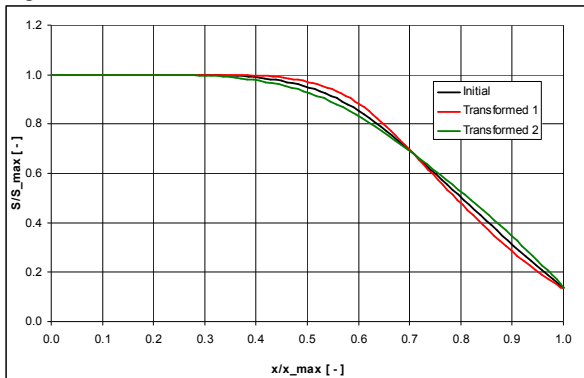


Fig. 5 Considered range of modifications of the longitudinal volume distribution

The described method of parametrized hull transformation is quite similar to the well known Lackenby transformation ([20]) in the sense that existing hull sections are moved to new locations. The features of the method, in comparison with the studies presented by cited authors, are as follows:

- shape controlled by just one parameter;
- applied constraints imply that all the modifications generated during the optimization process are allowable (constant displacement volume);
- very small number of cases to be analysed in order to find the optimum.

The method is also easy to implement in the commercial NX software used in presented study. On

the other hand, its drawback is that at the moment it is dedicated to optimize a single geometric feature of the hull.

## 5 COMPUTATIONAL MODEL

The resistance for subsequent variants of the parent shape was computed with the use of STAR-CCM+ solver. The computations were carried out at full scale. The CFD solver was coupled with the CAD software NX, and the computational procedure was executed in the following manner:

- a table of required range of parameter  $p$  to be analysed was pre-defined and imported to the CFD solver;
- the CFD solver manages the process by sending the command to CAD software at the beginning of each analysis, to execute another modification;
- the modified shape is imported to CFD solver, which executes remeshing and analysis.

This procedure is presented in the form of flowchart in Fig. 6.

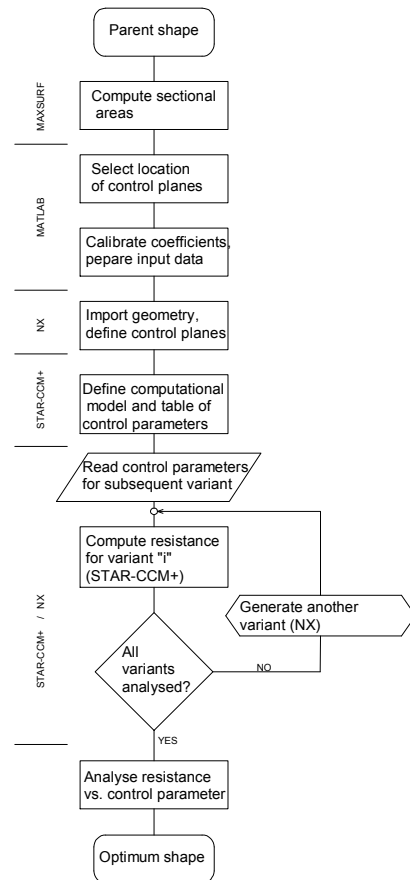
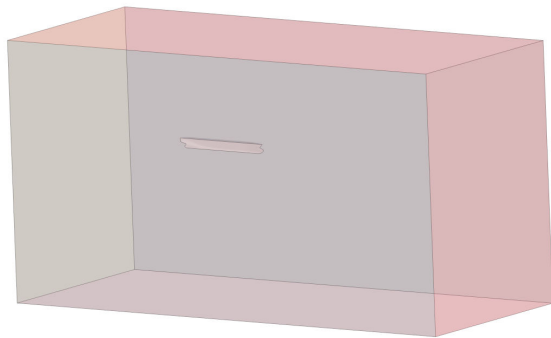


Fig. 6 Optimization procedure - flowchart

As the low computational time is of high priority, and the focus was primarily on differences in resistance rather than absolute values of the resistance, relatively coarse mesh was used and the dynamic trim and sinkage were neglected. Initial trim and draught were adjusted based on the computations for the parent shape, and remained unchanged for all other variants, assuming that their variation will be small due to constant displacement and LCB. The number of mesh cells for optimization process was  $1.9 \cdot 10^6$ . It was confirmed by computations for variable mesh density that increasing the number of cells above this value does not influence the tendencies revealed in the optimization process. The boundaries of the rectangular domain were located follows: inlet - 2L upstream of the bow, outlet - 2L downstream of the stern, bottom - 2L below the hull base line, top 1L above the hull base line, lateral wall - 2L from the hull symmetry, where L is the ship length overall. The computational domain is presented in Fig. 7.



**Fig. 7 Computational domain size**

The types of boundary conditions are as follows:

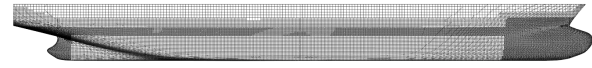
- upstream, top, bottom and side walls of the domain: prescribed velocity components and volume fraction of water;
- downstream: prescribed pressure;
- hull: no-slip wall.

The wave damping zone was used in the region close to the domain boundaries in order to speed up the convergence by preventing the wave reflections inside the domain.

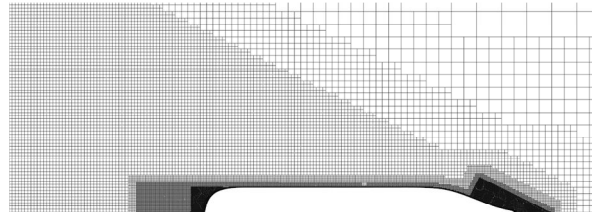
The settings of the computational model were as follows:

- free surface treatment: multiphase flow (Volume of Fluid);
- implicit unsteady model;
- turbulence model: k-epsilon;
- time step: 0.02s;
- 5 outer iterations per time step.

The visualizations of the mesh is presented in Fig. 8 and Fig. 9.

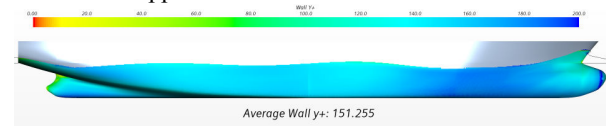


**Fig. 8 Computational mesh - hull surface**



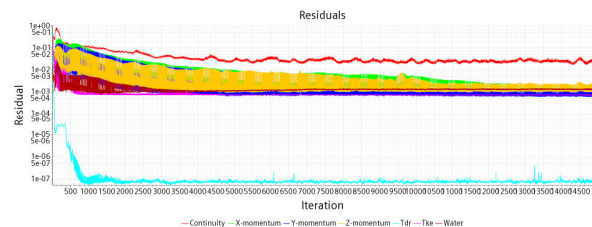
**Fig. 9 Computational mesh - free surface region**

The resulting  $y^+$  values on the hull surface are presented in Fig. 10. Relatively large values of  $y^+$  (above 100) enforce the application of wall functions.

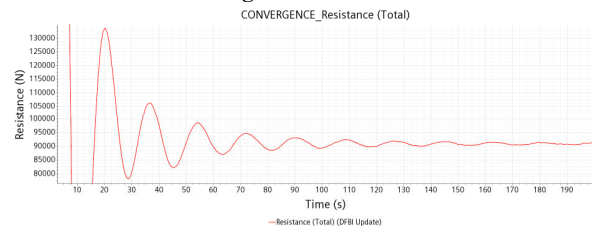


**Fig. 10 Wall  $y^+$  on the hull surface**

Convergence of the continuity equations and convergence of the resistance value for selected case is presented in Fig. 11 and Fig. 16, respectively.



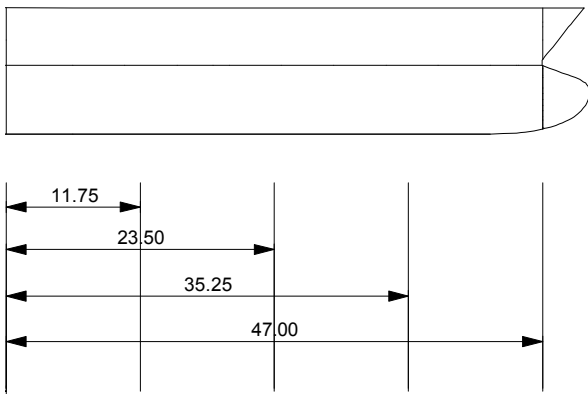
**Fig. 11 Residuals**



**Fig. 12 Convergence of the resistance**

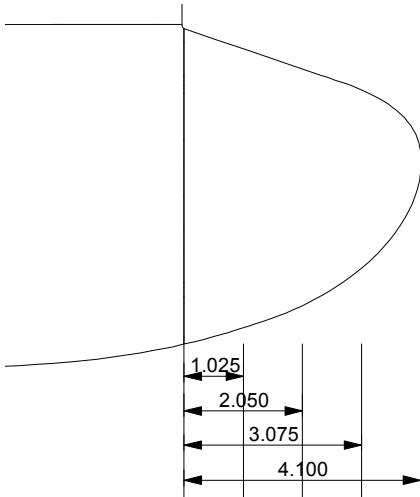
## 6 RESULTS OF BOW PART OPTIMIZATION

The bow part optimization in respect of resistance was carried out in two steps. The first one was the optimization of the longitudinal volume distribution between the midship section and the fore perpendicular; the second one was the optimization of the bow bulb length. Location of the control points for the optimization of longitudinal volume distribution is presented in Fig. 13 (three variable control points).



**Fig. 13 Location of the control points for the bow part**

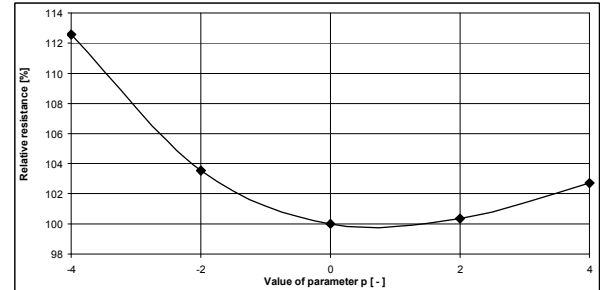
Location of the control points for the optimization of bow bulb length is presented in Fig. 14.



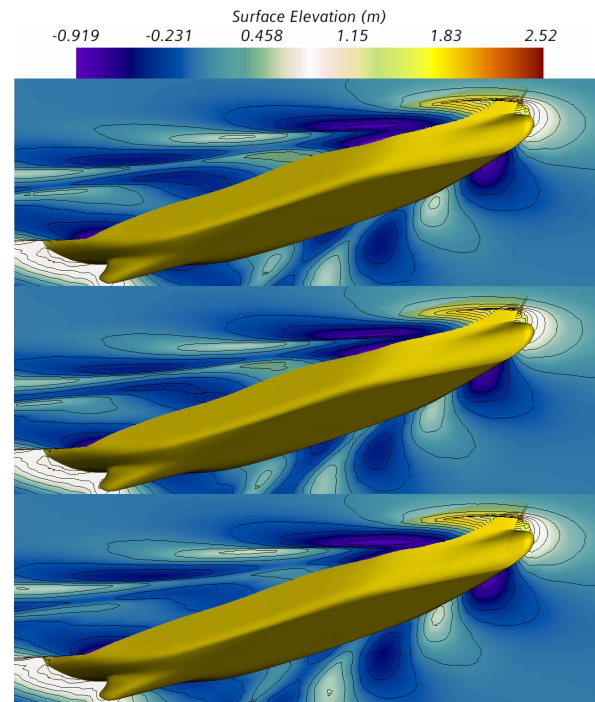
**Fig. 14 Location of the control points for the bow bulb**

The search for optimum longitudinal volume distribution started with quick analysis of global tendency; five values of parameter  $p$  were used to generate the population of shapes: -4, -2, 0, 2 and 4 (5 variants),

where  $p = 0$  corresponds to parent shape. The resulting relative resistance value are presented in Fig. 15.



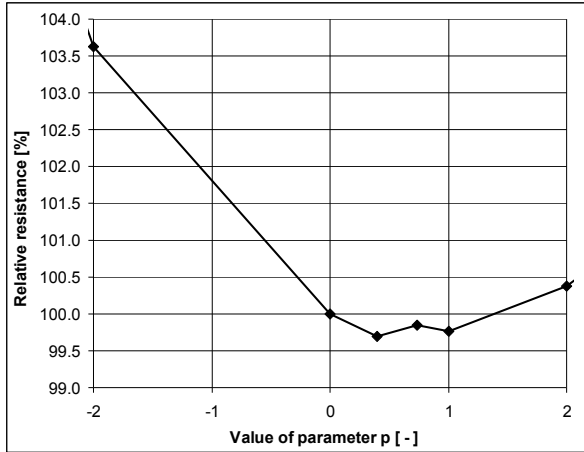
**Fig. 15 Relative resistance for five variants of the bow part**  
 The influence of the modifications on the bow pattern for two extreme variants and for the optimal one is presented in Fig. 16.



**Fig. 16 Optimization of the bow part - wave pattern; lowest waterplane entrance angle (top), optimum (middle) and fairest shoulder (bottom)**

The quantitative results show that the computer resistance is lowest for the parent shape, i.e. no improvement was achieved in first attempt. However, the shape of the curve suggests that the actual minimum of the resistance should be expected for the value of parameter  $p$  between 0 and 2. Thus, the computations were continued for three more variants of the hull shape,

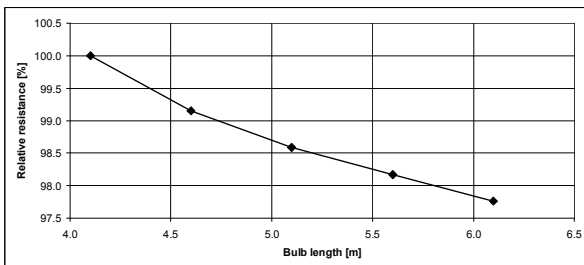
corresponding to the values of parameter  $p$  equal to 0.4, 0.74 and 1.0. The results are presented in Fig. 17.



**Fig. 17 Analysis of relative resistance for refined range of parameter  $p$**

Some slight reduction of resistance was observed, however, it is almost negligible (app. 0.25%).

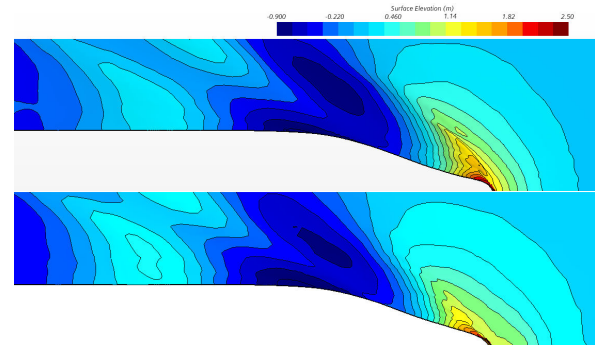
Next step of the optimization of the bow part was the optimization of the bulb length. The length was changed within the range 4.1m - 6.1m (upper limit was selected arbitrarily). In case of a bulb optimization, the influence of its size on total displacement volume was neglected; the actual increase of volume for longest bulb is 16m<sup>3</sup>, which corresponds to 0.2% of total volume of parent shape. A change in LCB also occurs, equal to 0.12% of  $L_{PP}$ . Location of the control points presented in Fig. 14 was changed proportionally, i.e. the bulb was transformed by uniform "stretchnig". 5 variants of the bulb were analysed. The resulting relative resistance values are presented in Fig. 18 (100% now corresponds to initial bulb length).



**Fig. 18 Relative resistance as a function of bulb length**

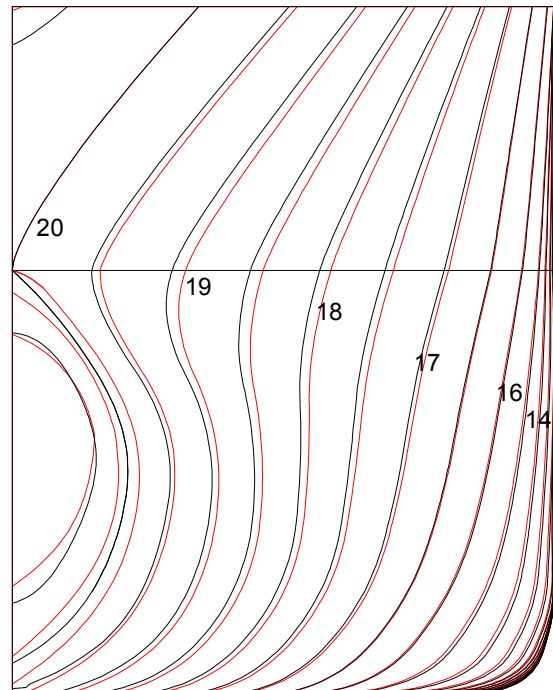
As can be seen, the resistance decreases monotonically with increasing bulb length. The total achieved reduction of resistance due to optimization of the bow part is 2.54%, which is noticeable from the point of view of fuel consumption.

The influence of the bow bulb modifications on the wave pattern are presented in Fig. 19.



**Fig. 19 Optimization of the bow bulb - wave pattern; initial bulb (top) vs. optimized bulb (bottom)**

Comparison between the bow parts of the parent shape and the optimized one is presented in Fig. 20.



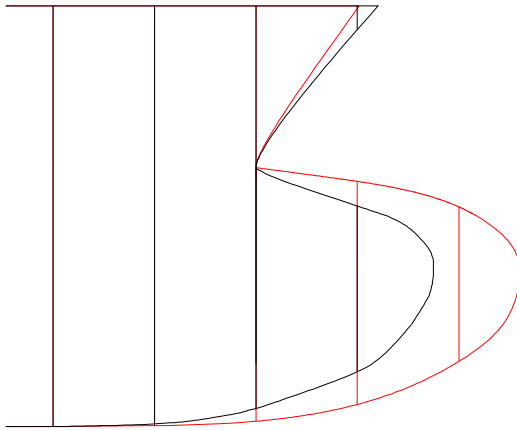


**Fig. 20** Bow part - parent shape (black) vs. optimized one (red)

## 7 RESULTS OF STERN PART OPTIMIZATION

Optimization of the stern part consisted only in the optimization of the longitudinal volume distribution. Location of the control points is presented in Fig. 21 (four variable control points).

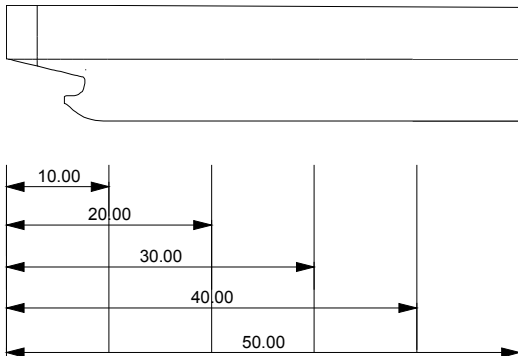


**Fig. 21** Location of the control points for the stern part

In case of stern part, there are four intermediate control points. The values of the vector

$$\Delta X = [0 \quad -p \quad -p \quad a \cdot p \quad a \cdot p \quad 0]$$

The considered values of parameter  $p$  were: -3, -1, 0, 1, 3, 5 and 6 (7 variants), where  $p = 0$  corresponds to parent shape. The relative resistance for resulting hull shape variants is presented in Fig. 22.

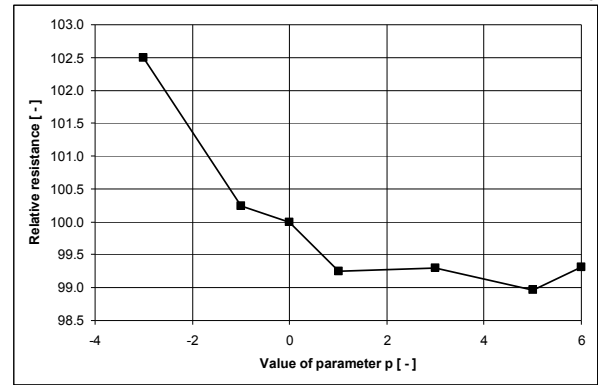


**Fig. 22** Relative resistance for seven variants of the stern part

In case of stern, total resistance was reduced by 1.03%, according to CFD results. The influence of the stern part modifications is presented in Fig. 23.

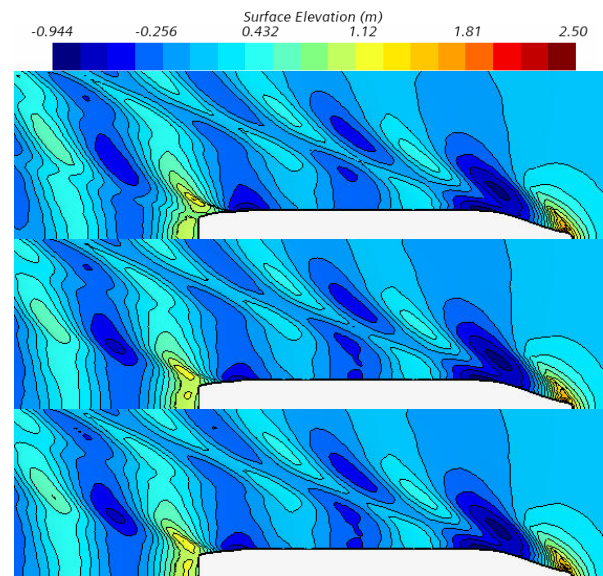


**Fig. 23** Optimization of the bow part - wave pattern; lowest waterplane entrance angle (top), optimum (middle) and fairest shoulder (bottom)

Comparison between the aft parts of the parent shape and the optimized one is presented in Fig. 24

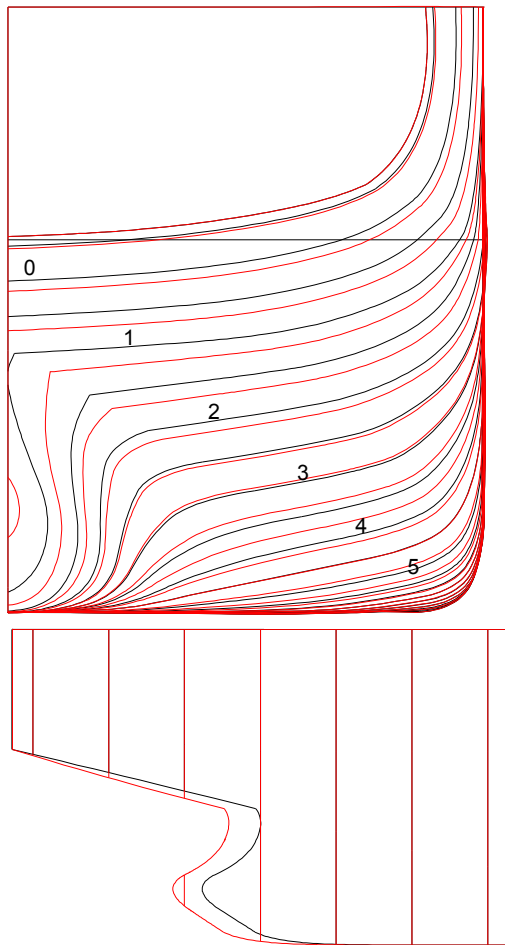


Fig. 24 Aft part - parent shape (black) vs. optimized one (red)

## 8 Results of experimental verification

The experiments were carried out in the towing tank of CTO S.A., for the model built at scale 17.035. The model was done in two parts, so that the influence of bow part optimization and stern part optimization could be verified separately. Three configurations were thus tested:

- initial bow + initial stern
- optimized bow + optimized stern
- optimized bow + optimized stern.

The model during the experiment is presented in Fig. 25.

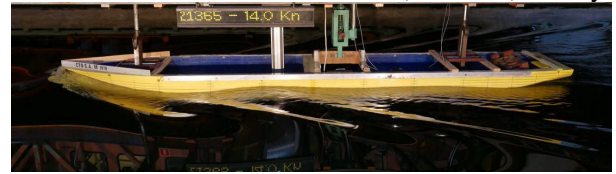


Fig. 25 Model tests

The resulting resistance (direct results of model tests) are presented in Fig. 26.

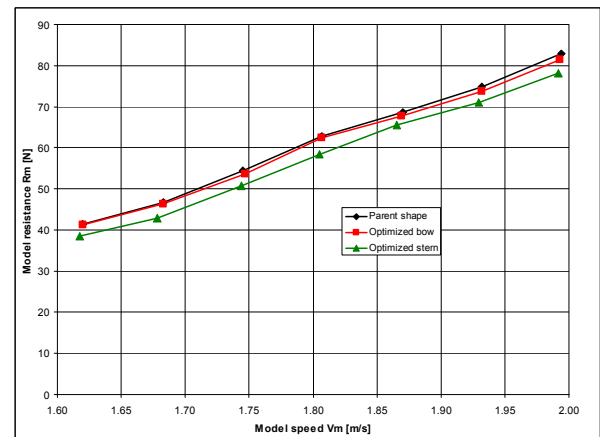


Fig. 26 Results of model tests

Quantitative comparison for the design speed of 14 knots between the full scale resistance extrapolated from model tests and computed with CFD is presented in Tab. 2.

Table 2 Comparison between model tests and CFD

	Experiment		CFD	
	Resist. [kN]	Reduct. [%]	Resist. [kN]	Reduct. [%]
Orig. bow/orig. aft	211.4	-	183.4	-
Optim. bow/orig. aft	207.9	1.7	178.7	2.5
Optim. bow/orig. aft	200.8	5.0	176.8	3.6

General underestimation of the total resistance in CFD computations can be observed, which is explained primarily by neglecting the dynamic trim and sinkage in CFD. Besides that, the results of resistance

measurements show different values of the gain in total resistance due to optimization, however, the tendency observed in CFD computations was confirmed.

## 9 SUMMARY

The paper proposes an approach to parametric optimization of the ship hull in respect of resistance, based on a posteriori transformation of existing CAD file. The transformation is realized so that the volume of the submerged part remains unchanged. The optimization is realized by coupling the CFD solver STAR-CCM+ with the CAD software NX. A prescribed set of parameters is considered, and the resulting modifications are compared in respect of total resistance. The bow part and the stern part were optimized separately. The conclusions are as follows:

- the parent shape is already quite well optimized, so only small reduction of resistance could be achieved;
- however, some reduction of resistance was obtained both for the bow part and for the stern part (in case of bow part, the reduction of resistance was achieved mainly by bow bulb elongation);
- the values resulting from model tests are not consistent with the values obtained from CFD, however, correct tendency was shown with CFD computations;
- the possibility of modification with presented method is strongly limited, but, on the other hand, it can be applied quite fast and the optimization process is relatively short as the optimum can be found for small number of variants.

Further work should include taking into account the following issues:

- introducing the constraints in the stern shape transformation, so that the propeller space remains unchanged;
- verification of the influence of stern shape transformation on propulsive and cavitation characteristics, based on a study similar to the one presented e.g. by Zhang et al. [21].

## ACKNOWLEDGEMENT

The research was financed by the National Centre for Research and Development of the Republic of Poland, within the framework of the Esthetics project (POLTUR3/ESTHETICS/1/2019).

## BIBLIOGRAPHY

1. Y. Lu, J. Wu, W. Li & Y. Wu "A new six-dof parallel mechanism for captive model test", *Polish Maritime Research*, No. 3 (107), Vol. 27; pp. 4-15, 2020, DOI: 10.2478/pomr-2020-0041 27
2. S. Bielicki, "Prediction of ship motions in irregular waves based on response amplitude operators evaluated experimentally in noise waves", *Polish Maritime Research*, No. 1(109), Vol. 28, pp. 16-27, 2021, DOI: 10.2478/pomr-2021-0002
3. Q. Wang, P. Yu, B. Zhang, G. Li, "Experimental Study and Numerical Simulation of the Water Entry of a Ship-Like Symmetry Section with an Obvious Bulbous Bow", *Polish Maritime Research*, No. 3(111), Vol. 28, pp. 16-34, 2021, DOI: 10.2478/pomr-2021-0031
4. A. Karczewski, M. Kunicka, "Influence of the Hull Shape on the Energy Demand of a Small Inland Vessel with Hybrid Propulsion", *Polish Maritime Research*, No. 3(111), Vol. 28, pp. 16-34, 2021, DOI: 10.2478/pomr-2021-0032
5. H.C. Raven, "A solution method for the nonlinear ship wave resistance problem", Ph.D. dissertation, Delft Univ. Techn., 1996
6. A. Stück, "Adjoint Navier-Stokes Methods for Hydrodynamic Shape Optimisation", Ph.D. dissertation, Technische Universität Hamburg-Harburg, 2012
7. M. Gundelach, "Sketched Parametric Modeling in CFD Optimization", Master thesis, Feb/2017, University of Rostock, Germany
8. H. Nowacki, D. Liu, X. Lü, "Fairing bézier curves with constraints", *Computer Aided Geometric Design*, 7(1-4), 43-55 (1990)
9. S. Harries, "Parametric Design and Hydrodynamic Optimization of Ship Hull Forms", Mensch-und-Buch-Verlag, Berlin (1998)
10. S. Harries, C. Abt, "Parametric curve design applying fairness criteria", International Workshop on Creating Fair and Shape-Preserving Curves and Surfaces (1998)

11. I. Biliotti, S. Brizzolara, M. Viviani, G. Vernengo, D. Ruscelli, M. Galliussi, D. Guadalupi, A. Manfredini, "Automatic parametric hull form optimization of fast naval vessels", Proceedings of the Eleventh International Conference on Fast Sea Transportation (FAST 2011) (2011)
12. S. Han, Y.-S. Lee, Y.B. Choi: "Hydrodynamic hull form optimization using parametric models", Journal of Marine Science and Technology, 17(1), 1–17(2012), DOI: 10.1007/s00773-011-0148-8
13. M. Brenner, V. Zagkas, S. Harries, T. Stein, "Optimization using viscous flow computations for retrofitting ships in operation", Proceedings of the 5th International Conference on Computational Methods in Marine Engineering, MARINE (2013)
14. Y. Feng, O. el Moctar, T.E. Schellin, "Parametric Hull Form Optimization of Containerships for Minimum Resistance in Calm Water and in Waves", Journal of Marine Science and Application 20, 670–693 (2021). DOI: 10.1007/s11804-021-00243-w
15. G. Vernengo, D. Villa, S. Gaggero, M. Viviani, "Interactive design and variation of hull shapes: pros and cons of different CAD approaches", *International Journal on Interactive Design and Manufacturing*, 14, pp. 103-114, 2020 DOI: 10.1007/s12008-019-00613-3
16. D. Peri, E.F. Campana, "Multidisciplinary design optimization of a naval surface combatant", Journal of Ship Research 47(1), 1–12 (2003), DOI: 10.5957/jsr.2003.47.1.1
17. F. Perez, J.A. Clemente, "Constrained design of simple ship hulls with b-spline surfaces", Computer Aided Design 43(12), 1829–1840 (2011), DOI:10.1016/j.cad.2011.07.008
18. H.J. Choi, "Hull-form optimization of a container ship based on bell-shaped modification function", International Journal of Naval Architecture and Ocean Engineering 7(3), 478–489 (2015), DOI: 10.1515/ijnaoe-2015-0034
19. G. G. Lorentz, "Bernstein Polynomials", University of Toronto Press, 1953
20. H. Lackenby, "On the systematic geometrical variation of ship forms", Trans. INA 92, 289–315 (1950)
21. Y. Zhang, X. P. Wu, M. Y. Lai, G. P. Zhou & J. Zhang, "Feasibility Study of Rans in Predicting Propeller Cavitation in Behind-Hull Conditions", *Polish Maritime Research*, No. 4(108), Vol. 27, pp. 26-35, 2020, DOI: 10.2478/pomr-2020-0063

## A Systematic Optimisation on the Energy Saving Devices for Ship, in Particular, Combination of Pre-Swirl Stator (PSS) and Duct

Selahattin Özsayan<sup>1</sup>, Çağrı Aydın<sup>1</sup>, Çağatay Sabri Köksal<sup>1\*</sup>, Emin Korkut<sup>1</sup>

<sup>1</sup>Istanbul Technical University, Faculty of Naval Architecture and Ocean Engineering, 34469 Maslak-Istanbul, Turkey

**Abstract:** The use of energy-saving devices (ESD) increases the propulsive efficiency of the ships and hence reduces fuel consumption. In this study, various pre-swirl stator (PSS) and duct configurations were investigated in terms of their influences on propulsive efficiency of 7000DWT INSEAN Tanker. The resistance and propulsion tests of the original form and the bow optimised form were performed without and with ESDs in Ata Nutku Ship Model Testing Laboratory. In the simulations, unsteady, incompressible RANS equations were solved by using the STAR-CCM+ software for the computations. In order to calculate the turbulence field and hence model the Reynolds stresses, which arise in RANS equations after the averaging operation as additional unknowns, the SST k- $\omega$  turbulence model, which is a robust two-equation eddy-viscosity turbulence model, was employed. The validation study was conducted on the results of resistance and self-propulsion simulations. In the experimental and numerical studies, a 7000DWT INSEAN Tanker model and a stock propeller were used. The optimum duct design and the effect of interaction were examined. A series of combinations for the duct and the Pre-Swirl Stator (PSS) geometries was studied to obtain the optimum propulsive efficiency at the design speed by the combination of the duct and PSS. The results indicate that ESD increases the ship resistance, whilst the propulsive efficiency varies depending on the duct and PSS interaction and design parameters.

**Keywords:** Optimisation, Energy Saving Device (ESD); Duct; Pre-Swirl Stator (PSS).

### 1 INTRODUCTION

Energy-saving devices (ESD) improve the flow characteristics (Mewis et al., 2011) and can be classified considering their locations or working principles. Ducts can be classified as an energy-saving device, and types include Schneekluth (1989) duct, Mewis's (2009) duct, Becker-Mewis's (2013) duct, Mitsui Integrated Duct Propeller (MDIP) and Hitachi Zosen Nozzle (HZN). Ducts reduce the risk of cavitation on propellers and improve the ship's propulsion performance and manoeuvrability (Kitazawa et al., 1982). Pre-swirl stator (PSS) can be introduced as another type of energy-saving device. PSS is positioned on the upstream side of the propeller and used to recover the rotational energy losses. The purpose of the PSS devices is to increase propeller efficiency and enhance the wake (Simonsen et al., 2012). In this study, various pre-swirl stator and duct configurations were investigated in terms of their effects on propulsive efficiency. In the design of pre-swirl stators, the optimum case in the study of Tacar and Korkut (2018) was considered. The axial position of the PSS and the parameters of the duct contraction angle ( $\theta_x$ ), diameter ( $D_D$ ) and distance ( $d_x$ ) to the propeller plane were investigated systematically. In the numerical studies, the Cartesian Cut-Cell mesh type was used. The mesh size of the ship's stern area has been improved, including the ESD. The free surface effect was included in the simulations.

The main objective of this study is to improve the flow characteristics at the propeller plane and increase the quasi propulsive coefficient, QPC by the use of combination of

duct with PSS. Another objective of the study is to try to get some insight into the phenomenon.

In the following sections of the paper the details of the ship and propeller geometry are given in Section 2. In Section 3 the numerical study is explained and the design parameters and the design matrix are given in Section 4. The results are presented and discussed in Section 6. Finally the conclusions obtained from the study are given in Section 7.

### 2 EXPERIMENTAL STUDY

Resistance and self-propulsion tests were carried out in the Ata Nutku Ship Model Testing Laboratory of Istanbul Technical University. The towing tank of the laboratory is 160 m long, 6 m wide and 3.4 m deep and equipped with a manned carriage, which is able to achieve a speed of up to 6 m/s.

#### 2.1 Model Test Procedure

##### 2.1.1 Resistance Tests

The resistance tests were performed with a single-component electronic resistance dynamometer (OPN500) and ship model (Figure 1). According to the recommendation of ITTC (2017a), resistance tests were first carried out at varying speeds for the bare hull (rudder included) and then repeated with the ESDs (Figure 2a).

The model was tested only free to trim and sink in calm water. Dynamic trim and sinkage were measured using an inclinometer and distance sensor, respectively. Carriage speed, resistance, trim, sinkage, and water temperature were recorded during the experiments. The model ship resistance was collected for the various speeds, and form

\* Corresponding author e-mail: koksalcag@itu.edu.tr

factor analysis was performed by the Prohaska method considering the low speeds ( $0.1 < Fr < 0.2$ ).



**Figure 1:** Resistance tests with a single-component electronic resistance dynamometer (OPN500).

### 2.1.2 Self-Propulsion Tests

The self-propulsion tests were performed with a stock propeller (ANP-12), an electric motor, a propeller dynamometer (Cussons Technology R25), a single component electronic resistance dynamometer (OPN500), shafts and bearings installed in the ship model.

The propulsion tests were carried out at two different speeds (14 and 15 knots) without ESDs and at design speed (14 knot) with ESDs (Figure 2b). Idle thrust and torque measurements were also performed before the self-propulsion tests. According to the recommendation of ITTC (2017b), experiments were carried out at three different rate of revolutions ( $n$ ) for each speed in order to determine the self-propulsion point (load varying or constant speed method). The external force ( $F_D$ ) was calculated as in the Equation 1 according to ITTC (2014).

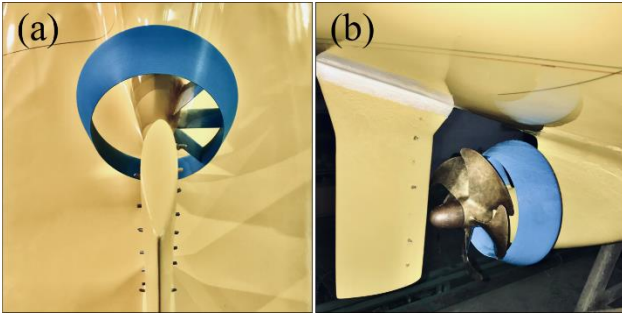


**Figure 2:** A view of ESDs on the stern form, a) w/o, b) w propeller.

$$F_D = 0.5\rho_M S_M V_m [(1+k)(C_{FM} - C_{FS}) - \Delta C_F] \quad (1)$$

where  $\rho_M$  is the density of water,  $S_M$  is the wetted surface area of model,  $V_M$  is the model or carriage speed,  $(1+k)$  is the form factor,  $C_F$  is the frictional resistance coefficient and  $\Delta C_F$  is the roughness allowance.

The thrust deduction factor is calculated as follows.

$$t = \frac{T_M + F_D - R_{TM}}{T_M} \quad (2)$$

where  $T_M$  is the measured thrust and  $R_{TM}$  is the total resistance of the towed model at the corresponding speed.

The thrust identity method was used in order to obtain the propulsive factors. The wake fraction ( $w_{TM}$ ), hull efficiency ( $\eta_H$ ), relative rotative efficiency ( $\eta_R$ ) and propulsive efficiency ( $\eta_D$ ) are calculated as follows.

$$w_{TM} = \frac{V_M - V_{AM}}{V_M} \quad (3)$$

where  $V_{AM}$  is the advance velocity of the model.

$$\eta_H = \frac{1-t}{1-w_{TM}} \quad (4)$$

$$\eta_R = \frac{K_{QM}}{K_{Q0}} \quad (5)$$

where  $K_{QM}$  is the measured torque coefficient and  $K_{Q0}$  is the read off value from the open water curves for the corresponding  $J$  values.

$$\eta_D = \eta_H \eta_0 \eta_R \quad (6)$$

### 2.2 Test Cases

In the experimental and computational studies, a 7000 DWT chemical tanker model designed for the EU-STREAMLINE project and ITU stock propeller, ANP-12, was used. This wooden model with a scale of 1/22.65 was built in the workshop of the Ata Nutku Ship Model Testing Laboratory (Figure 3). ANP-12 model propeller is 5-bladed, right-handed and fixed-pitch type (Figure 4). The ship model and stock propeller characteristics are given in Table 1 and 2, respectively.

**Table 1:** Characteristics of the ship in model and full-scale.

Parameters	Symbol	Ship	Model
Scale	$\lambda$	1	22.65
Length (PP)	$L_{PP}$ (m)	94.00	4.150
Length (WL)	$L_{WL}$ (m)	96.75	4.272
Breadth at WL	$B_{WL}$ (m)	15.41	0.681
Draft at FP	$T_F$ (m)	6.01	0.265
Draft at AP	$T_A$ (m)	6.01	0.265
Displacement	$\nabla$ (m <sup>3</sup> )	6820.6	0.587
Wetted Surface	$S$ (m <sup>2</sup> )	2297.5	4.478
Block coefficient	$C_B$	0.76	0.762
Propeller diameter	$D_P$ (m)	3.85	0.170
Service speed	$V_S$ (knot-m/s)	14.00	1.513
Froude number	$Fr$	0.23	0.23

**Table 2:** ANP-12 model propeller characteristics.

Parameters	Symbol	ANP-12
Diameter	$D$ (m)	0.17
Chord length at $r/R=0.7$	$c_{0.7}$ (m)	0.058
Pitch ratio at $r/R=0.7$	$P_{0.7}/D$	1.222
Blade area ratio	$A_E/A_0$	0.85
Type of propeller	-	FPP
Material	-	Bronze

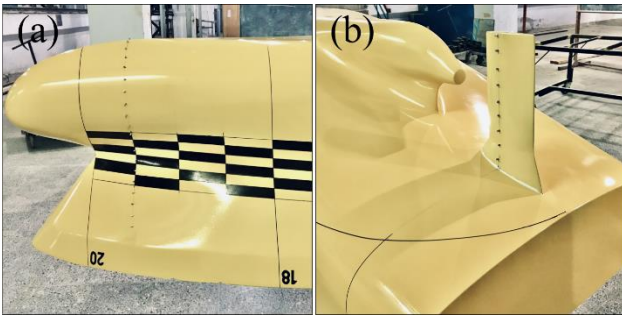


**Figure 3:** A view of the tanker model, a) bow, b) stern.

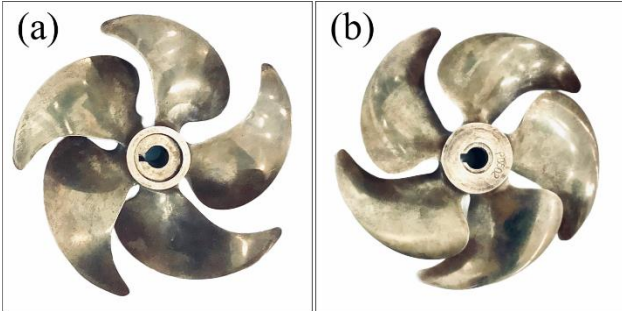


**Figure 4:** ANP-12 stock propeller.

The test matrix for resistance and self-propulsion tests are given in Table 3 and Table 4, respectively.

**Table 3:** Resistance test matrix.

Test No.	Test	Loading	Speed (knot)
M439-01	Bare hull	Full load	6-16
M439-02	w ESD	Full load	11-15

**Table 4:** Self propulsion test matrix.

No	V <sub>S</sub> (knot)	V <sub>M</sub> (m/s)	n (w/o ESD)	n (w ESD)
v1n1	14	1.513	7.5	8.8
v1n2	14	1.513	8.5	9.5
v1n3	14	1.513	10.5	10.1
v2n1	15	1.621	9.0	-
v2n2	15	1.621	10.5	-
v2n3	15	1.621	12.0	-

### 3 NUMERICAL STUDY

#### 3.1 Methodology

In the simulations, unsteady, incompressible RANS equations (Wilcox, 2006) were solved. STAR CCM+ software package was used for the computations. In order to calculate the turbulence field, and hence model the Reynolds stresses, which arise in RANS equations after the averaging operation as additional unknowns, the SST  $k-\omega$  turbulence model (Menter, 1994) which is a widely used and robust two-equation eddy-viscosity turbulence model was employed. The model combines the  $k-\omega$  turbulence model and  $k-\epsilon$  turbulence model such that the  $k-\omega$  is used in the inner region of the boundary layer and switches to the  $k-\epsilon$  in the free shear flow regions. When applying this turbulence model, two additional transport equations for turbulence kinetic energy and turbulence dissipation should be solved. The RANS and aforementioned turbulence transport equations were solved by finite volume technique with a segregated algorithm (Blazek, 2001; Versteeg and Malalasekera, 2007). For the pressure-velocity coupling, a standard pressure-correction

procedure, SIMPLE, was applied (Patankar and Spalding, 1972). The second-order upwind scheme were used to discretise the convective acceleration terms, while the viscous terms were dealt with the second-order central difference scheme (Pletcher et al., 2013). In addition, VOF (Volume of Fluid) method is adopted to model the free surface of the water (Hirt and Nichols, 1981). The tracking of the free surface was performed with a second-order scheme. The convergence of the solution at each time step was checked by the examination of the variation of the primitive variables, such as velocity and pressure, in addition to the scaled residuals of the equation systems.

#### 3.2 Computational Domain and Mesh Topology

A relatively large computational domain was used in this study in order to avoid the possible reflections from the boundaries. The boundaries of the domain are placed at a distance of 2L, 4L, 3L, 1.5L and 3L, respectively, from the ship model, considering the inlet, outlet, sides, upper and lower limits. In the mesh structure, tetrahedral and prism cells are used, with hexahedral cells being dominant. The height of the first cell from the wall was calculated to remain below the dimensionless  $y^+$  value of 1 for the ESD and propeller, however, hull was modelled with  $y^+$  of around 50 in order to reduce the overall cell count. Volumetric and surface improvements have been made on the ship's surface, skeg and around the ship. At the same time, non-isotropic mesh refinement has been applied around the ship's draught and throughout the entire volume in order to resolve the waves on the free surface. Overall mesh structure is given on Figure 5. For the self-propulsion simulations, a separate rotational domain was created which connected to the static domain with a sliding interface. In this domain, polyhedral cells were used in order to better capture the flow characteristics with more faces aligned with the rotating movement of the fluid. The mesh for the ESD and propeller can be seen on Figure 6.

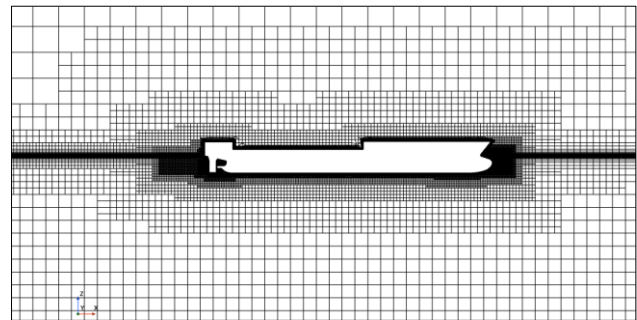


**Figure 5:** Overall mesh topology.

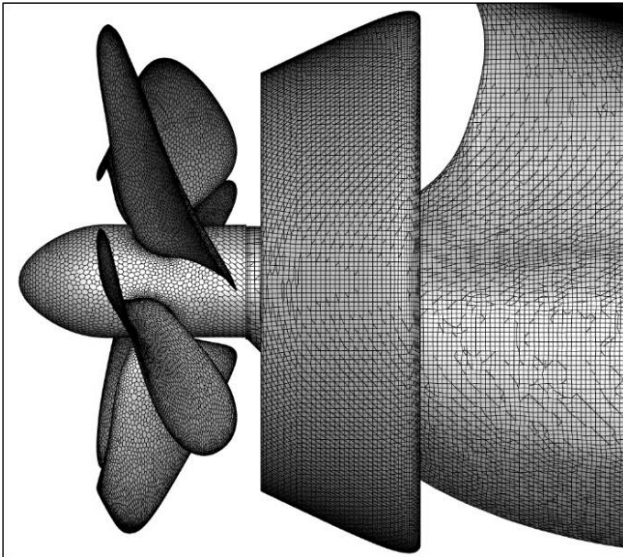


**Figure 6:** Mesh topology of ESD and propeller.

#### 4 DESIGN AND OPTIMISATION OF ESD

In the study, the combination of the duct and pre-swirl stator (PSS) was studied on resistance and propulsive efficiency at design speed for INSEAN 7600DWT Tanker model (Figure 7). When duct and PSS are considered separately, the cord length, diameter, profile type, opening/contraction angle and distance from the propeller plane for the duct; and the number of blades, diameter, cord length, axial location, profile type, angular blade position, and blade pitch angle for the PSS are essential parameters that affect the propulsive efficiency. In addition, these systems interact with each other in the combination of duct and PSS.

In the optimisation study, optimum duct design and interactions of the systems were studied. The PSS's optimum design was obtained from the study of Tacar and Korkut (2018). Accordingly, the optimum PSS is the 3-bladed stator (without SC blade) with a blade pitch angle of  $-8^\circ$  and blade type NACA0012 (Figure 8).

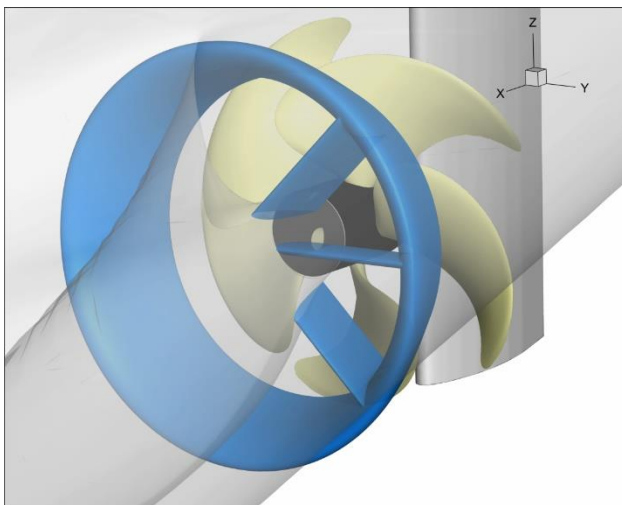


**Figure 7:** The combination of the duct and PSS.

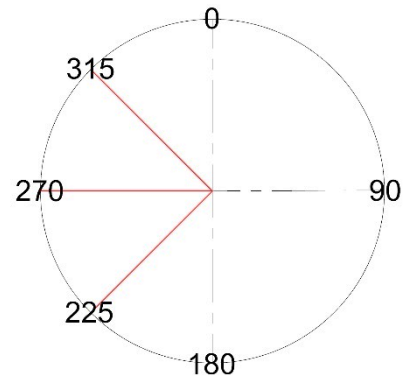


**Figure 8:** Blade angular position of PSS.

NACA4420 type profile was used for duct design (Furcas et al, 2019). In the optimization study, the effects of the opening/contraction angle of the duct ( $\Theta_x$ ), the duct diameter ( $D_D$ ) and the distance of the duct to the centre of the propeller ( $d_x$ ) were systematically investigated. Other parameters were kept constant. A total of 24 cases were generated with the duct diameter of  $D_D=0.7-0.8D_P$ , with the opening/contraction angle of the duct  $\Theta_x=17.5-22.5^\circ$  and with the distance of the duct to the propeller centre  $d_x=0.25-0.3D_P$ . The cord length of the duct was determined as  $0.33D_P$  considering the stern form of the ship. Optimisation studies were carried out by combining the duct with the optimum PSS design. The investigated parameters are shown in Figure 9 on the stern form of the ship and the optimization matrix is given in Table 5.

**Table 5:** Optimization matrix for ESDs design.

No	$\Theta_x$ ( $^\circ$ )	$d_x/D_P$	$D_D/D_P$
1	17.5	0.250	0.700
2	17.5	0.250	0.750
3	17.5	0.250	0.800
4	17.5	0.275	0.700
5	17.5	0.275	0.750
6	17.5	0.275	0.800
7	17.5	0.300	0.700
8	17.5	0.300	0.750
9	17.5	0.300	0.800
10	20	0.250	0.700
11	20	0.250	0.750
12	20	0.250	0.800
13	20	0.275	0.700
14	20	0.275	0.750
15	20	0.275	0.800
16	20	0.300	0.700
17	20	0.300	0.750
18	20	0.300	0.800
19	22.5	0.250	0.700
20	22.5	0.250	0.750
21	22.5	0.250	0.800
22	22.5	0.275	0.700
23	22.5	0.275	0.750
24	22.5	0.275	0.800

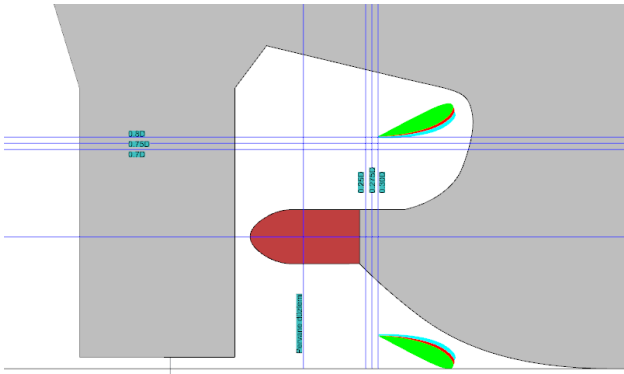


Figure 9: A view of duct parameters on the stern form.

## 5 VERIFICATION AND VALIDATION

In order to check whether the computational results were independent of the grid density, some additional computations were carried out with four different mesh densities for both open water and resistance simulations. A basic grid structure “coarse” was initially generated with the mesh generation technique described. The “medium”, “fine” were then obtained by systematically increasing the mesh resolution at each direction of the coordinate system by a factor of approximately  $\sqrt[3]{2}$ , hence the total cell number in the domain, excluding the boundary layer which was kept constant, was nearly doubled in each step. Negligible difference between the mesh “medium” and “fine” points out that the medium mesh is suitable to carry out further simulations for both open water and resistance cases. The uncertainty analysis of the numerical discretisation was performed by using the Grid Convergence Index (GCI) method (Roache, 1998). The procedure is explained in detail in Çelik et al. (2008). The resulting GCI value of the open water and resistance cases for the medium meshes were 0.27% and 0.72% respectively, which implies the general numerical uncertainty in these simulations. Table 6 and Table 7 show the procedure of the GCI calculations for open water and resistance simulations, respectively.

Table 6: GCI results for open water.

Mesh type	fine	medium	coarse
No of cells	6.7E+06	5.1E+06	3.9E+06
$r_{21}$	1.26		
$r_{32}$		1.26	
$\Phi$	0.3989	0.3995	0.4007
$\epsilon_{21}$	5.67E-04		
$\epsilon_{32}$		1.16E-03	
$p$	2.202		
$\Phi_{ext}^{21}$	0.398		
$e_a^{21}$	0.001		
$GCI_{fine}^{21}$		0.27%	

A validation study was conducted for the resistance and self-propulsion simulations in order to determine the validity of the results. For the resistance cases, two separate validation studies were conducted for the original and bow optimised hull forms. Figure 10 and Figure 11 indicates a good agreement between CFD and experimental results for both hull forms where maximum differences of 2.0% and 3.2% were found for original and optimised hull forms, respectively.

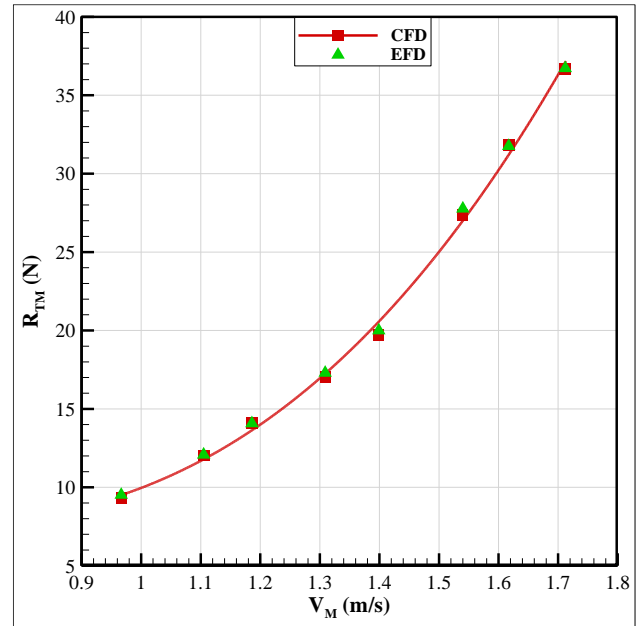


Figure 10: Resistance test results in model scale (original form).

Table 7: GCI results for resistance.

Mesh type	fine	medium	coarse
No of cells	4.59E+06	2.77E+06	1.60E+06
$r_{21}$	1.26		
$r_{32}$		1.26	
$\Phi$	4.701E-03	4.754E-03	4.905E-03
$\epsilon_{21}$	5.337E-05		
$\epsilon_{32}$		1.502E-04	
$p$	4.735		
$\Phi_{ext}^{21}$	0.005		
$e_a^{21}$	0.011		
$GCI_{fine}^{21}$		0.715%	

Two different velocities of  $V_M=1.49$  m/s and  $V_M=1.61$  m/s were used for the validation of the self-propulsion simulations. For the SP cases, the temporal discretisation was adjusted so that the propeller was rotated 1 degree per time-step as per ITTC recommendations. For both velocities, an ambitious agreement between CFD and experiments was obtained for a number of parameters in which the results are given in Table 8 and Table 9.

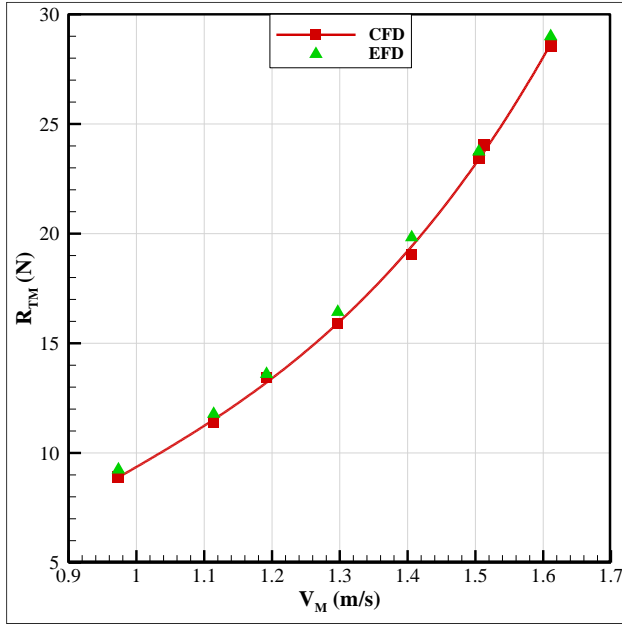
The overall results of the validation cases indicate that the methodology of the numerical study is suitable to use for the rest of the simulations.

Table 8: Self-propulsion results at  $V_M=1.49$  m/s (original form).

Parameters	CFD	EFD	% Diff.
$V_M$ (m/s)	1.49	1.49	-
$n$ (rps)	9.469	9.577	-1.1
$K_{TM}$	0.295	0.289	2.1
$J_0$	0.689	0.698	-1.3
$K_{Q0}$	0.054	0.054	0.0
$\eta_0$	0.597	0.602	-0.8
$1-w_{TM}$	0.742	0.761	-2.5
$t$	0.199	0.195	2.1
$\eta_H$	1.080	1.057	2.2
$\eta_R$	1.049	1.063	-1.3
$\eta_D$	0.676	0.677	-0.1

**Table 9:** Self-propulsion results at  $V_M=1.61$  m/s (original form).

Parameters	CFD	EFD	% Diff.
$V_M$ (m/s)	1.61	1.61	-
$n$ (rps)	10.805	10.782	0.2
$K_{TM}$	0.307	0.312	-1.6
$J_0$	0.668	0.658	1.5
$K_{Q0}$	0.056	0.057	-1.8
$\eta_0$	0.585	0.579	1.0
$1-w_{TM}$	0.760	0.748	1.6
$t$	0.228	0.238	-4.2
$\eta_H$	1.016	1.020	-0.4
$\eta_R$	1.030	1.069	-3.6
$\eta_D$	0.612	0.631	-3.0



**Figure 11:** Resistance test results in model scale (bow opt).

## 6 RESULTS AND DISCUSSION

Comparison of the self-propulsion analyses results between original and bow optimised forms is given in Table 10, where the maximum difference is found to be the thrust deduction, which is a reduction of 14.1% for the latter. Therefore, it was found that the bow optimisation is mostly effecting the thrust deduction value.

**Table 10:** Comparison of self-propulsion analyses results of original and bow optimised forms.

Parameters	Bow opt	Original	% Diff.
$V_M$ (m/s)	1.49	1.49	-
$n$ (rps)	9.349	9.469	-1.3
$K_{TM}$	0.286	0.295	-3.1
$J_0$	0.705	0.689	2.3
$K_{Q0}$	0.053	0.054	-1.9
$\eta_0$	0.606	0.597	1.5
$1-w_{TM}$	0.750	0.742	1.1
$t$	0.227	0.199	14.1
$\eta_H$	1.030	1.080	-4.6
$\eta_R$	1.092	1.049	4.1
$\eta_D$	0.682	0.676	0.9

The resistance and self-propulsion analyses were performed for the cases given in Table 5 and the results of the resistance analysis and self-propulsion analyses are given in Table 11, Table 12 to Table 14, respectively.

**Table 11:** Resistance analyses results and the comparison of the cases that with and without ESD.

Case	$R_{TM}$ (N)	% Diff.	Case	$R_{TM}$ (N)	% Diff.
1	25.611	6.5	14	26.360	9.6
2	26.114	8.5	15	26.591	10.5
3	26.209	8.9	16	25.952	7.9
4	25.592	6.4	17	26.231	9.1
5	26.103	8.5	18	26.581	10.5
6	26.292	9.3	19	26.398	9.7
7	25.710	6.9	20	26.813	11.5
8	26.161	8.8	21	27.010	12.3
9	25.914	7.7	22	26.334	9.5
10	26.074	8.4	23	27.048	12.4
11	26.204	8.9	24	27.147	12.9
12	26.733	11.1	w/o ESD	<b>24.055</b>	-
13	25.890	7.6			

As far as the resistance values are concerned, the resistance increases for all the cases compared to that of the original form without any ESDs. The increase in the resistance characteristics is more significant as the duct diameter ( $D_D$ ) and opening/contraction angle ( $\theta_x$ ) increase when the  $d_x$  is fixed. However, the increase of resistance is almost unchanged when only the distance to the propeller centre ( $d_x$ ) is varied.

The propulsion analyses results for the opening/contraction angle of  $17.5^\circ$ ,  $20.0^\circ$ ,  $22.5^\circ$  are shown in Table 12, Table 13 and Table 14, respectively. The propulsive efficiency ( $\eta_D$ ) is maximum for the opening/contraction angle of  $17.5^\circ$  when the duct diameter is  $0.75D_p$  for all the cases. As the duct is closest to the centre of the propeller, the propulsive efficiency increases for all duct diameters.

**Table 12:** Effect of duct the duct diameter ( $D_D$ ) and the distance ( $d_x$ ) on propulsion parameters for  $\theta_x=17.5^\circ$ .

Case	$n$ (rps)	$J_0$	$K_{Q0}$	$\eta_0$	$1-w_{TM}$	$t$
1	9.467	0.609	0.060	0.547	0.648	0.294
2	9.305	0.586	0.062	0.531	0.613	0.276
3	9.373	0.584	0.062	0.529	0.615	0.285
4	9.383	0.595	0.061	0.537	0.627	0.298
5	9.423	0.595	0.061	0.537	0.630	0.284
6	9.524	0.594	0.062	0.536	0.635	0.294
7	9.354	0.593	0.062	0.536	0.624	0.291
8	9.410	0.587	0.062	0.532	0.621	0.289
9	9.418	0.582	0.062	0.528	0.616	0.306
w/o ESD	<b>9.523</b>	<b>0.703</b>	<b>0.053</b>	<b>0.605</b>	<b>0.752</b>	<b>0.244</b>

**Table 12:** Effect of duct the duct diameter ( $D_D$ ) and the distance ( $d_x$ ) on propulsion parameters for  $\theta_x=17.5^\circ$  (cont.).

Case	$\eta_H$	$\eta_R$	$\eta_D$	Diff. $\eta_D$ (%)
1	1.090	1.187	0.708	5.51
2	1.182	1.214	0.762	13.54
3	1.163	1.211	0.745	11.10
4	1.119	1.177	0.708	5.48
5	1.136	1.177	0.719	7.10
6	1.112	1.137	0.678	1.04
7	1.137	1.132	0.690	2.90
8	1.145	1.162	0.708	5.47
9	1.128	1.166	0.694	3.47
w/o ESD	<b>1.006</b>	<b>1.102</b>	<b>0.671</b>	

For the opening/contraction angle of 20°, when the distance of the duct from the centre of the propeller is 0.25D<sub>P</sub>, the propulsive efficiency increases as the duct diameter increases.

**Table 13:** Effect of duct the duct diameter (D<sub>D</sub>) and the distance (d<sub>x</sub>) on propulsion parameters for  $\Theta_x=20^\circ$ .

Case	n (rps)	J <sub>0</sub>	K <sub>Q0</sub>	$\eta_0$	1-w <sub>TM</sub>	t
10	9.510	0.595	0.061	0.537	0.635	0.299
11	9.411	0.577	0.063	0.524	0.610	0.299
12	9.320	0.556	0.064	0.508	0.582	0.289
13	9.370	0.571	0.063	0.520	0.602	0.311
14	9.455	0.570	0.063	0.519	0.606	0.307
15	9.437	0.558	0.064	0.510	0.592	0.308
16	9.446	0.574	0.063	0.522	0.610	0.316
17	9.332	0.554	0.064	0.507	0.581	0.310
18	9.426	0.552	0.065	0.506	0.585	0.314
w/o ESD	<b>9.523</b>	<b>0.703</b>	<b>0.053</b>	<b>0.605</b>	<b>0.752</b>	<b>0.244</b>

**Table 13:** Effect of duct the duct diameter (D<sub>D</sub>) and the distance (d<sub>x</sub>) on propulsion parameters for  $\Theta_x=20^\circ$  (cont.).

Case	$\eta_H$	$\eta_R$	$\eta_D$	Diff. $\eta_D$ (%)
10	1.104	1.142	0.677	0.85
11	1.149	1.216	0.732	9.16
12	1.223	1.249	0.776	15.71
13	1.146	1.192	0.711	5.89
14	1.144	1.151	0.684	1.94
15	1.168	1.181	0.704	4.96
16	1.122	1.124	0.659	-1.83
17	1.187	1.234	0.743	10.71
18	1.174	1.159	0.688	2.55
w/o ESD	<b>1.006</b>	<b>1.102</b>	<b>0.671</b>	

The propulsive efficiency ( $\eta_D$ ) for the opening/contraction angle of 22.5° is maximum when the duct diameter is 0.75D<sub>P</sub> for all cases.

**Table 14:** Effect of duct the duct diameter (D<sub>D</sub>) and the distance (d<sub>x</sub>) on propulsion parameters for  $\Theta_x=22.5^\circ$ .

Case	n (rps)	J <sub>0</sub>	K <sub>Q0</sub>	$\eta_0$	1-w <sub>TM</sub>	t
19	9.443	0.556	0.064	0.509	0.590	0.318
20	9.349	0.535	0.066	0.493	0.562	0.311
21	9.367	0.512	0.068	0.474	0.539	0.330
22	9.474	0.552	0.065	0.505	0.587	0.330
23	9.402	0.533	0.066	0.491	0.563	0.313
24	9.393	0.512	0.068	0.474	0.541	0.328
w/o ESD	<b>9.523</b>	<b>0.703</b>	<b>0.053</b>	<b>0.605</b>	<b>0.752</b>	<b>0.244</b>

**Table 14:** Effect of duct the duct diameter (D<sub>D</sub>) and the distance (d<sub>x</sub>) on propulsion parameters for  $\Theta_x=22.5^\circ$  (cont.).

Case	$\eta_H$	$\eta_R$	$\eta_D$	Diff. $\eta_D$ (%)
19	1.155	1.135	0.667	-0.60
20	1.225	1.273	0.768	14.48
21	1.244	1.119	0.660	-1.63
22	1.141	1.125	0.649	-3.31
23	1.220	1.161	0.696	3.69
24	1.242	1.129	0.665	-0.87
w/o ESD	<b>1.006</b>	<b>1.102</b>	<b>0.671</b>	

As the effect of the opening/contraction angle is examined, the propulsive efficiency reduces for all the cases (except case 12 and 20) when the opening/contraction angle increases. The analysis of the results indicates that the case 12 ( $\Theta_x=20$ , D<sub>D</sub>=0.8D<sub>P</sub> and d<sub>x</sub>=0.25D<sub>P</sub>) is the optimum

combination of duct with the PSS. The optimum duct and PSS combination were manufactured and the resistance and propulsion tests were carried out for the ship model with the optimum ESDs. Table 15 shows the comparison of self-propulsion results between CFD and the experiment. Again, there is a good agreement between the CFD and the experiment results.

**Table 15:** Self propulsion results at V<sub>M</sub>=1.513 m/s (Case 12).

Case	CFD	EFD	% Diff.
n (rps)	9.320	9.413	-1.0
K <sub>TM</sub>	0.370	0.366	1.1
J <sub>0</sub>	0.556	0.559	-0.5
K <sub>Q0</sub>	0.064	0.064	0.0
$\eta_0$	0.508	0.511	-0.6
(1-w <sub>TM</sub> )	0.582	0.591	-1.5
t	0.289	0.273	5.9
$\eta_H$	1.223	1.229	-0.5
$\eta_R$	1.249	1.206	3.6
$\eta_D$	0.776	0.757	2.5

## 7 CONCLUSIONS

Numerical and experimental studies have been performed to investigate the effects of the combination of a pre-swirl stator and a duct on the propulsive efficiency for a 7000 DWT tanker model. A series of combinations for the duct and the PSS were considered to obtain the maximum propulsive efficiency. Consequently, ESD increases the ship resistance, whilst the propulsive efficiency is considerably sensitive to the design parameters and hence the interaction of the duct and PSS. As a further study, extrapolation methods on the PSS should be investigated by ITTC procedures and full-scale simulations.

## ACKNOWLEDGEMENT

The research presented in this paper is supported by the TUBITAK - The Scientific and Technological Research Projects Funding Programme with Project No: 218M487.

## REFERENCES

- Blazek, J. (2001). 'Computational Fluid Dynamics: Principles and Applications'. Elsevier, Oxford, UK.
- Çelik, İ., Ghia, U., Roache, P., Fretias, C.J., Coleman, H., Raad, P.E. (2008). 'Procedure for estimation and reporting of uncertainty due to discretization in CFD applications'. J. Fluid Eng. 130 (7).
- Furcas, Francesco, Stefano Gaggero, and Diego Villa. 'Duct-type ESD: a design application using RANSE-based SBDO'.
- Guiard, T., Leonard, S. (2013). 'The Becker Mewis Duct®-Challenges in Full-Scale Design and new Developments for Fast Ships', In 3rd international symposium on marine propulsors.
- Hirt, C.W., Nichols, B.D. (1981). 'Volume of fluid (VOF) method for the dynamics of free boundaries'. J. Comput. Phys. 39, 201–225.
- ITTC Recommended Procedures and Guidelines. (2014). 'Propulsion\Bollar Pull Test. 7.5-02-03-01.1'.

- ITTC Recommended Procedures and Guidelines. (2017a). 'Resistance Test Procedure. 7.5-02-02-01'.
- ITTC Recommended Procedures and Guidelines. (2017b). 'Propulsion\Bollar Pull Test. 7.5-02-03-01.1'.
- ITTC Recommended Procedures and Guidelines. (2021). 'Open Water Test Procedure. 7.5-02-03-02.1.'
- Kitazawa, T., Hikino, M., Fujimoto, T., Ueda, K. (1982). 'Increase in the propulsive efficiency of a ship by a nozzle installed just in front of a propeller', In Journal of the Kansai Society of Naval Architects, 184, 73-78.
- Menter, F. R. (1994). 'Two-equation eddy-viscosity turbulence models for engineering applications'. AIAA journal, 32(8), 1598-1605.
- Mewis, F. (2009). 'A novel power-saving device for full-form vessels', In First International Symposium on Marine Propulsors, SMP.
- Mewis, F., Guiard, T. (2011). 'Mewis duct–new developments, solutions and conclusions', In Second International Symposium on Marine Propulsors.
- Patankar, S.V., Spalding, D.B. (1972). 'A calculation procedure for heat, mass and momentum transfer in three-dimensional parabolic flows'. Int. J. Heat Mass Tran 15, 1787–1806.
- Pletcher, R.H., Tannehill, J.C., Anderson, D.A. (2013). 'Computational Fluid Mechanics and Heat Transfer', third ed. CRC Press. Florida, USA.
- Roache, P.J., (1998). 'Verification and Validation in Computational Science and Engineering'. Hermosa Publishers. New Mexico, USA.
- Schneekluth, H. (1989). 'The wake equalising duct', In International Maritime and Shipping Conference, 103, 147-150.
- Simonsen, C. D., Nielsen, C., Klimt-Møllenbach, C., Holm, C. R., Minchev, A. (2012). 'CFD based investigation of potential power saving for different rudder types, positions and pre-swirl fins', FORCE Technology.
- Tacar, Z., Korkut, E. (2018). 'Parametric Study of a Pre-swirl Stator for a Tanker', A. Yücel Odabaşı Colloquium Series, 3rd International Meeting-Progress in Propeller Cavitation and its Consequences.
- Versteeg, H. K., & Malalasekera, W. (2007). 'An introduction to computational fluid dynamics: the finite volume method'. Pearson education.
- Wilcox, D. C., (2006). 'Turbulence Modeling for CFD', third ed. DCW Industries. California, USA.

## Assessing the Performance of Kriging and Artificial Neural Network in Simulation-based Design Optimization

Hayriye Pehlivan Solak<sup>1\*,2</sup>, Devrim Bülent Danışman<sup>1</sup>, Ömer Gören<sup>1</sup>

<sup>1</sup>Istanbul Technical University, Faculty of Naval Architecture and Ocean Engineering, 34469 Maslak-Istanbul, Turkey

<sup>2</sup>LHEEA, Res. Lab. in Hydrodynamics, Energetics and Atmospheric Environment, Centrale Nantes, 44321 Nantes Cedex 3, France

**Abstract:** Surrogate modeling strategies are widely used in design processes, as they possess many advantages in engineering optimization especially in hull form optimization. The present study is focused on the aft form optimization where the viscous effects become dominant. It is necessary to solve this problem within a reasonable amount of time which makes the implementation of surrogate modeling techniques inevitable. The present study discusses application-oriented comparison of Kriging with a prominent surrogate model of Artificial Neural Network with respect to their learning performances in terms of RMS error, correlation coefficient and required number of training points by means of high-fidelity solvers. The optimization study is then carried out for minimum viscous resistance of a given ship by Genetic Algorithm. When the results are compared by numerical simulation, it is shown that at least 5% reduction in viscous resistance is attainable by means of Kriging surrogate model. Besides the numerical comparisons for initial and optimized hull forms and comparisons between Kriging and ANN models; the resistance gain is also validated by a series of model scale experiments.

**Keywords:** Kriging, ANN, simulation-based design optimization, SBDO.

### 1 INTRODUCTION

Surrogate models, meta-models or known as models of models are used for approximating the single or multi-variate system of inputs/outputs based on a limited set of computational data points. Surrogate strategies are implemented for different purposes such as recovering missing data, filtering out noise from simulation outcomes, combining the results from different fidelity levels of sources, or as presented here, considered models are used for replacing the expensive simulations with black-box functions.

Surrogate strategies are widely used for engineering design optimization problems due to their computational efficiency by decreasing the need for excessive number of simulations that needs to be completed in design phase. Especially in ship hydrodynamics, design optimization studies are based on time demanding high-fidelity computer simulations. Particularly aft form design has its own difficulties, as the flow in this region of the hull is dominated by viscous effects which makes high-fidelity computer simulations inevitable. Therefore, the surrogate strategies have paramount importance in this specific simulation-based design optimization (SBDO) field.

Today, the motivation behind using surrogates in SBDO problems – by substituting the time-consuming flow simulations with analytical approximating functions based on relatively smaller training set of data – have produced different types of methods. According to the expectation from the meta-model, accuracy or robustness etc. surrogate model performances can significantly vary in terms of required training data or ability to capture the response of

the problem. Obviously, surrogate models have different deficiencies depending on their modelling characteristics may cause problem dependent surrogate performances. Therefore, a unique metamodel technique could not developed which can be applied with the same efficiency in any kind of engineering problem. Thus, many research groups investigating the implementation limits of widely used strategies or they are trying either to tuning parameters of the methods that is currently in use or introduce new surrogate models (Volpi 2015, Peri 2012).

Current literature has different surrogate strategies such as Kriging, Artificial Neural Network, radial basis functions or response surface methodology that are widely used in engineering problems as powerful prediction tools. In the present study, Kriging and -the most trending method- Artificial Neural Network (ANN) in machine learning are chosen for assessing their learning performance for a challenging aft form optimization problem. Accordingly, the study presented here compares Kriging and ANN learning performances for the aft form optimization problem by investigating the models' drawbacks in terms of their exploration ability. Additionally, the present approach has a different point of view from the recent hull form optimization studies (Scholcz 2017), which employs a point-based surface transformation instead of using global shift of cross-sections for hull form variations. Thus, the most important output of the study was being able to find and eliminate the problem of local flow separation, by the advantage of focusing on a local design patch.

To summarize; from recent studies, one can easily admit that Kriging technique is still developing by many research

\* Corresponding author e-mail: pehlivanha@itu.edu.tr

groups from all around the world (He et al 2018, Chen 2019). Those development studies are rather concentrated on the sampling types (Rumpfkeil et al 2011), on the tuning parameter exploration such as variogram adaptation (Peri 2015) or on adding some descriptive new information into the algorithm such as gradient/hessian enhanced types (Bouhlef et al 2019). Since Kriging has many advantages, such as being a proper approach to multi-dimensional problems and its prediction capability as compared to other metamodeling techniques and being able to produce error estimates, it is selected for current SBDO implementation study.

The second approach, ANN, is derived based on neurons inspired from human brain which uses functions as a means of a logical decision tools. According to related literature, ANN is shown to be a method that uses less computational sources (Sun and Wang 2019). In addition, ANN regarded as easy-to-implement except assigning appropriate parameters for the selected problem. ANN methodology is used in variety of fields in engineering from chemical processes (McBride et al 2019) to geometry design optimization or aerospace applications (Azizi et al 2013). Since the ANN has user defined parameters such as selecting the activation, construction of the architecture type or the learning rate that makes the meta-model regarded as easy to implement, but causes a drawback for having a structured implementation framework. Therefore, finding best composition of parameters to these user defined selections – which is the case for every possible SBDO problem – is indeed a challenging task to arrive at a high performance result every time. Therefore, ANN should be rigorously investigated in terms of accuracy and robustness that is currently under investigation.

In this study Kriging code is implemented via using references Jones (2001) and Forrester et al (2008) whereas ANN is implemented by using MATLAB neural net toolbox to train neural net fitting for the same DoE (Design of Experiments) set of hull form variations. Accordingly, single fidelity Kriging and ANN meta-models are subjected to determine the optimum hull form in terms of viscous resistance by using Genetic Algorithms (GA). Then, optimal hull forms are compared via numerical simulation tools and best optimal hull form is subjected to a series of model experiments: resistance, wake measurements and flow visualization tests respectively. It is seen from both numerical and experimental comparisons that; Kriging surrogate modeling is captured the relation between the hull form variations and resistance better than the ANN by achieving 5% reduction in total resistance and provided better flow characteristics for the aft region of the flow.

The remainder of the paper is structured as follows: The next section introduces confronted surrogate models; Kriging and ANN. Then, DoE and surrogate model results are demonstrated. The optimization results followed by the initial and optimized hull form comparisons by numerical

and experimental means. Finally, our conclusions with future work comments are presented.

## 2 METHODS

Surrogate model strategy for a simulation-based design optimization problem can be summarized as in Figure 1.

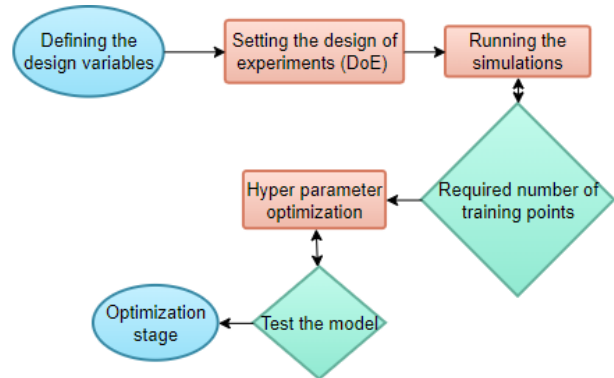


**Figure 1.** A typical flow chart for surrogate modeling

At the first stage the problem parameters must be defined. For the present study, this stage corresponds to defining the selected hull form geometry parameters to be optimized. The next stage is creating DoE to train the surrogate model by running the simulations for corresponding geometries - namely variant hull forms-. When a certain amount of training point data is reached, the assigned surrogate model can be implemented to explore the relation between system of inputs and outputs. Correspondingly, according to the methodology employed, meta-models' parameters adapt itself to explore input-output relationship known as hyper-parameter optimization. To evaluate the performance of the meta-model a certain number of data must be available to test the model (which is not used in meta-model training stage) otherwise switching to optimization stage before the mathematical behavior of the response has not captured yet, global optimum might be quite deceptive. Finally, by means of the optimization tool adopted arrives at the corresponding optimal solution.

In the present study, the realization of this typical flow chart is presented and compared for the two meta-models; Kriging and ANN. Firstly, the two surrogates are summarized with their essential characteristics.

### 2.1 Kriging

Kriging was originally developed in geostatistics by Danie G. Krige (1951). The mathematical basis for Krige's idea was then developed by Matheron (1963). Following Matheron, Kriging meta-models were applied to the input/output data sets of deterministic simulation models.

Kriging is mostly presented as a way of 'modelling the function as a realization of a stochastic process'. The reason is, if we want to make a guess at a point  $x$  in the domain before sampling any point, the prediction will have an uncertainty. Modelling this uncertainty resembles a random variable  $Y(x)$  that is normally distributed with the mean,  $\mu$ , and the variance,  $\sigma^2$ , (Jones 2001). This means that the function has a value  $\mu$  which varies between  $\pm\sigma$ . This implies that closer data points will tend to have nearly

the same function values,  $y(x_i)$ ,  $y(x_j)$ , where  $x_i$  and  $x_j$  are data points. In other words, this interpolation technique assumes correlation between closer observed data as can be statistically modelled in the following expression.

$$cor[Y(x_i), Y(x_j)] = exp(-\sum_{\ell=1}^d \theta_{\ell} |x_{i\ell} - x_{j\ell}|^{p_{\ell}}) \quad (1)$$

Expression (1) has an intuitive property that if  $x_{i\ell} = x_{j\ell}$  then the correlation is 1, and as  $\|x_{i\ell} - x_{j\ell}\| \rightarrow \infty$  the correlation tends to 0 for each d (number of dimensions). The interpolation parameter  $\theta_{\ell}$  are related with correlation change by moving in the  $\ell^{th}$  coordinate direction and if this parameter tends to have greater values, function values change rapidly even if the distances between the data points are small. The  $p_{\ell}$  makes the model smooth when it is near 2. On the one hand, the additional parameters in (1) make the model more complex, but, on the other hand, they enhance the accuracy and capability of the prediction. The uncertainty of the function values at, n, number of sample points by using a random vector can be written as:

$$Y = \begin{pmatrix} Y(x_1) \\ \vdots \\ Y(x_n) \end{pmatrix} \quad (2)$$

and covariance matrix is equal to;

$$Cov(Y) = \sigma^2 \mathbf{R} \quad (3)$$

where  $\mathbf{R}$  vector is a  $n \times n$  matrix which is represented in (1) with (i,j) element. Covariance is a measure of the correlation between two or more sets of random variables which one can derive correlation from covariance as;  $cor(X, Y) = cov(X, Y) / (\sigma_x \sigma_y)$ , where  $\sigma_x$  and  $\sigma_y$  are standard deviations of X and Y. The distribution of observed values determines the variation by moving different coordinate directions which depends on the model parameters as;  $\sigma^2$ ,  $\theta_{\ell}$  and  $p_{\ell}$ . For the estimation of those parameters, maximum likelihood estimation is used. The likelihood estimation can be written - by using the observed values represented by  $\mathbf{y}$  as:

$$\frac{1}{(2\pi\sigma^2)^{n/2} |\mathbf{R}|^{1/2}} exp\left(-\frac{(\mathbf{y}-1\hat{\mu})^T \mathbf{R}^{-1} (\mathbf{y}-1\hat{\mu})}{2\sigma^2}\right) \quad (4)$$

To simplify the likelihood estimation, we maximize (4) by taking its natural logarithm and derivative;

$$-\frac{n}{2} \log(\sigma^2) - \frac{1}{2} \log(|\mathbf{R}|) - \left(\frac{(\mathbf{y}-1\hat{\mu})^T \mathbf{R}^{-1} (\mathbf{y}-1\hat{\mu})}{2\sigma^2}\right) \quad (5)$$

and end up with the optimal values of  $\hat{\mu}$  and  $\hat{\sigma}^2$  as functions of  $\mathbf{R}$ ;

$$\hat{\mu} = \frac{\mathbf{1}^T \mathbf{R}^{-1} \mathbf{y}}{\mathbf{1}^T \mathbf{R}^{-1} \mathbf{1}} \quad (6)$$

$$\hat{\sigma}^2 = \frac{(\mathbf{y}-1\hat{\mu})^T \mathbf{R}^{-1} (\mathbf{y}-1\hat{\mu})}{n} \quad (7)$$

Then substituting (6) and (7) into the Eq. (5) gives the concentrated log-likelihood function – ignoring the constant term – as:

$$-\frac{n}{2} \log(\hat{\sigma}^2) - \frac{1}{2} \log|\mathbf{R}| \quad (8)$$

$p_{\ell}$  is specified as 2 – as described above – and  $\theta_{\ell}$  is searched according to the procedure given in Jones (2001).

Now, the same procedure is applied to a pseudo observation which means a new point added to the previous data set for a new estimation. The estimator will be derived by evaluating the quality of the new estimation which means again maximizing the likelihood function with the model parameters obtained so far. By adding (n+1)<sup>th</sup> observation to the data as  $(\mathbf{x}^*, y^*)$  – new point  $\mathbf{x}^*$  and estimated  $y^*$  – to get the augmented likelihood function,  $\tilde{\mathbf{y}} = (\mathbf{y}^T, y^*)^T$ , and  $\mathbf{r}$  denoting the vector of correlations of  $Y(\mathbf{x}^*)$  with the  $Y(x_i)$  for  $i=1, \dots, n$ ;

$$\mathbf{r} = \begin{pmatrix} cor[Y(\mathbf{x}^*), Y(x_1)] \\ \vdots \\ cor[Y(\mathbf{x}^*), Y(x_n)] \end{pmatrix} \quad (9)$$

The correlation matrix for the augmented data  $\tilde{\mathbf{R}}$ ;

$$\tilde{\mathbf{R}} = \begin{pmatrix} \mathbf{R} & \mathbf{r} \\ \mathbf{r}^T & 1 \end{pmatrix} \quad (10)$$

and by using (10) in the concentrated likelihood function and solving the equation – again by maximizing the relation by taking derivatives and setting it to zero – for the new  $y^*$  which gives us the standard Kriging predictor as:

$$\hat{y}(\mathbf{x}^*) = \hat{\mu} + \mathbf{r}^T \mathbf{R}^{-1} (\mathbf{y} - \mathbf{1}\hat{\mu}) \quad (11)$$

## 2.2 Artificial Neural Network

Artificial Neural Network (ANN) is a widely used methodology not only in the field of surrogate modeling for engineering design optimization, but also various fields such as pattern recognition, identification or classification problems, control systems and many more (Matlab - Neural Network Toolbox). ANN was derived by inspiration from biological nervous system. The principal resembles to a neuron pattern which acts as a network to transfer information.

A typical neuron is depicted in Figure 2. The training stage within this network system conducted by functions via tuning the weight parameters. As resembles to a real nervous system, neural network functions determined by the relation between the connections. Each system of equation within network is called as neuron. A layer is results from two or more neurons and combining layers compose a particular network. The network is trained based on the comparison between input and target value.

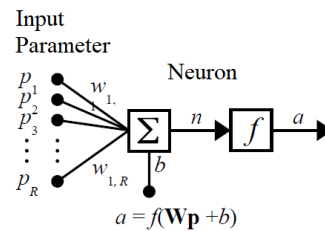
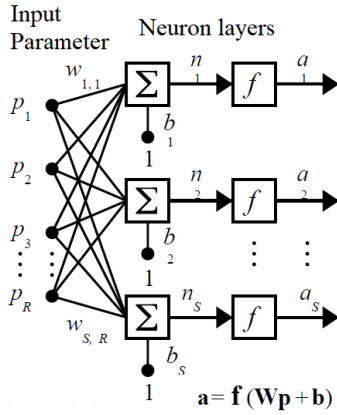


Figure 2. A typical neuron within ANN (Demuth et al 1992).

In Figure 2, scalar input parameters, p, is transmitted through a connection that is multiplied by a weighting

coefficient,  $w$ , and added a scalar bias,  $b$ . These values correspond to the net input argument,  $n$ , of the transfer function,  $f$ , which then turned to an output value,  $a$ . Here,  $w$  and  $b$  values are adjustable parameters of the transfer function. As stated above, a neural network composed of layer of neurons. In Figure 3, a layer of neuron is demonstrated.



**Figure 3.** A typical layer of neurons (Demuth et al 1992).

In Figure 3, the elements of input vector is connected to a neuron as an input through the weighting matrix and the neuron collects all connections weighting and bias to convert information to the corresponding scalar. Neuron layer outputs conforms a column vector. In a network of layers except input weighting, there is weighting of neuron layers that connects neurons to each other. In addition, a network may consist multiple layers of neurons that each has a weighting matrix and Figure 3 is a unit of such multiple layers of neurons.

In this study, for the hull form optimization problem, the design variables are the inputs of learning stage which is received by the first layer of the network to be processed and multiplied by a weighting factor. The information is transferred to the next layers and turned to the output value at the last neuron. Assigning the hidden layer and neuron number must be defined by the user and a layer constrained to have the same value neither the number of its inputs nor its neurons. In a network system, layers can be assigned for different roles as output layer determines the result of the system and all other layers are known as namely hidden layers. The motivation behind using multiple layers is to create more powerful architectures by assigning different activation functions for different layers. Defining a powerful architecture, however, is problem dependent procedure which is one of the drawbacks of the ANN.

In the present study, Matlab Neural Network Toolbox (nftool) is implemented for static sampling, to find the relation between the control points and corresponding resistance results. Input parameters and corresponding output vector are used for training the network to find an approximating function in between inputs and outputs. Presently, Levenberg-Marquardt algorithm is used because

of Hessian matrix calculation approximation makes the method fastest for training moderate sized feedforward neural networks. As mentioned previously, both metamodel strategies are trained with same set of DoE.

The selected metamodels are tested with respect to Root Mean Square Error (RMSE) and correlation coefficient ( $r$ ).

$$RMSE = \sqrt{\frac{\sum_{i=0}^{n_t} (y^{(i)} - \hat{y}^{(i)})^2}{n_t}} \quad (12)$$

$$r^2 = \left( \frac{cov(y, \hat{y})}{\sqrt{var(y) var(\hat{y})}} \right)^2 \quad (13)$$

RMSE in (12) and the correlation coefficient in (13) provide a quantitative measure of model accuracy also is useful to have a numerical understanding of the quality of the surrogate model.

#### 4 DESIGN OF EXPERIMENTS

The design of experiments was accomplished by a two-step process which contains a hull form transformation procedure and a sensitivity analysis to properly locate the control points defining the surface patch of the optimization region. The geometry of the proposed hull form can be seen in Figure 4. Main particulars of the hull form in model scale are given in Table 1.

**Table 1:** General specifications of the hull form.

Main properties	Symbol	Value
Scale	$\lambda$	21.0
Length	$L_{PP}$ (m)	4.14
Breadth	$B$ (m)	0.71
Draft	$D$ (m)	0.29
Displacement	$\nabla$ (m <sup>3</sup> )	0.69

The hull form used in this study is not a well-known benchmark form, but a form with problematic flow characteristics understood from viscous flow analysis.

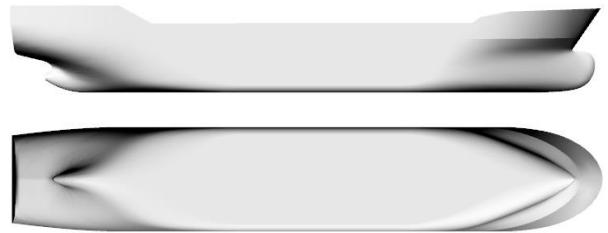


**Figure 4.** 3D view of initial hull form.

#### 4.1 Hull Form Transformations

To obtain the DoE, as being one of the cubic interpolation techniques Akima (1970) is employed. This method is a continuously differentiable interpolation, built from piecewise third order polynomials and applicable to successive intervals of the given points. Therefore, this method is chosen to obtain the hull form variations (Diez et al. 2015).

#### 4.2 RANS Computations

The governing equations are the continuity equation;

$$\frac{\partial u_i}{\partial x_i} = 0 \quad (14)$$

and the Navier-Stokes equations approximated by the RANS equations for the steady, three-dimensional, incompressible flow:

$$\frac{\partial(U_i U_j)}{\partial x_j} = \frac{1}{\rho} \frac{\partial P}{\partial x_i} + \frac{\partial}{\partial x_j} \left[ \nu \left( \frac{\partial U_i}{\partial x_j} + \frac{\partial U_j}{\partial x_i} \right) \right] - \frac{\partial u'_i u'_j}{\partial x_j} \quad (15)$$

P demonstrates the mean pressure,  $\rho$  the density and  $\nu$  the kinematic viscosity of the fluid where the velocity  $U$  can be decomposed into mean velocity  $\bar{U}_i$  component and fluctuating velocity part as in (16),

$$U_i = \bar{U}_i + u'_i \quad (16)$$

The k- $\epsilon$  turbulence model is applied to simulate the turbulent flow around the hull. This turbulence model is applicable when there are no high-pressure changes along the hull and quite economical in terms of CPU time (Farkas et al 2017), compared to, for example, the SST turbulence model, which increases the required CPU time by nearly 25% (Querard et al 2008). During the analyses, Reynolds stress tensor is calculated as in (17);

$$\overline{u'_i u'_j} = -\nu_t \left( \frac{\partial U_i}{\partial x_j} + \frac{\partial U_j}{\partial x_i} \right) + \frac{2}{3} \delta_{ij} k \quad (17)$$

Here,  $\nu_t$  is the eddy viscosity and expressed as  $\nu_t = C_\mu k^2 / \epsilon$  while  $C_\mu$  is an empirical constant ( $C_\mu = 0.09$ ).  $k$  is the turbulent kinetic energy and  $\epsilon$  is the turbulent dissipation rate. Also, transport equations are solved for  $k$  (18) and  $\epsilon$  (19):

$$\frac{\partial k}{\partial t} + \frac{\partial(k U_j)}{\partial x_j} = \frac{\partial}{\partial x_j} \left[ \left( \nu + \frac{\nu_t}{\sigma_k} \right) \frac{\partial k}{\partial x_j} \right] + P_k - \epsilon \quad (18)$$

$$\frac{\partial \epsilon}{\partial t} + \frac{\partial(\epsilon U_j)}{\partial x_j} = \frac{\partial}{\partial x_j} \left[ \left( \nu + \frac{\nu_t}{\sigma_\epsilon} \right) \frac{\partial \epsilon}{\partial x_j} \right] + C_{\epsilon 1} P_k \frac{\epsilon}{k} - C_{\epsilon 2} \frac{\epsilon^2}{k} \quad (19)$$

where comprehensive explanations can be found in (Wilcox 2006).

The solver uses a finite volume method which discretizes the governing equations. A second order convection scheme was used for the momentum equations and a first order temporal discretization was used. The flow equations were solved in a segregated manner. The continuity and momentum equations were linked with a predictor-corrector approach. The pressure field is solved by using SIMPLE algorithm which is based on pressure-velocity coupling. All governing equations are discretized using a cell based finite volume method and the advection terms are discretized with a first-order upwind interpolation scheme.

Table 2: Total resistance results for different number of cells.

Mesh	N. of Cells	Viscous Resistance [N]
Finer	4.64E+06	5.991
Fine	2.37E+06	5.972
Medium	1.21E+06	5.945

The computational domain was discretized by three-dimensional finite volume cells and appropriate mesh structure was created around the hull using hexahedral elements and trimmer meshing was applied. Systematic

studies were then performed to carry out a grid sensitivity study and to predict the numerical uncertainties. For this purpose, three different types of mesh refinements were tested given in Table 2. A mesh refinement factor was chosen as  $\sqrt{2}$ . According to the grid sensitivity results (Pehlivan Solak 2020) fine mesh is assigned for creating the DoE as seen from the Figure 5. In the figure bow and aft form represented apart from each other just to focus how mesh refinements change closer to the hull surface.

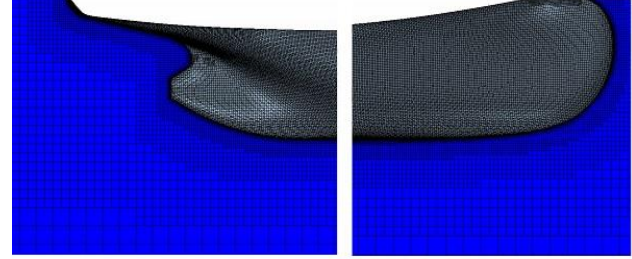


Figure 5. Mesh discretization on and around the hull surface.

Subsequently, double-body, fully turbulent viscous flow computations were performed for all the variant hull forms. The usage of double-body model is preferred since the present study particularly aims at obtaining optimal forms for minimum viscous resistance. Thus, the investigation of wave resistance is excluded from the metamodeling and from the optimization procedure to see the net viscous pressure effect of the variant hull forms.

The computation time was about an hour approximately for one case via using computational fluid dynamics software CD-Adapco's Star-CCM<sup>+</sup> with Intel Xeon i7 2.4GHz CPU with 64 GB of RAM. Three residuals monitored for convergence: continuity, forces acting on the hull and velocity values. The convergence criteria is selected as 0.0001 for all these residuals for all hull variant analysis.

### 4.3 DoE sensitivity analysis

Firstly, sensitivity analysis was carried out to determine the location of the control points defining the surface patch of the optimization region. We sought for the points of which their small variations end up with greater resistance changes. The main idea in the selection procedure of control points via sensitivity analysis is based on the approach that the search is made to figure out the control points having significant effects on viscous resistance when small geometric variations are applied transverse-wise. Then the location of control points is rearranged in a way that they concentrated around the points having greater changes (sensitivity) in resistance due to small changes in transverse-wise variation. The initial and revised placement of the control points shown in Figure 6.

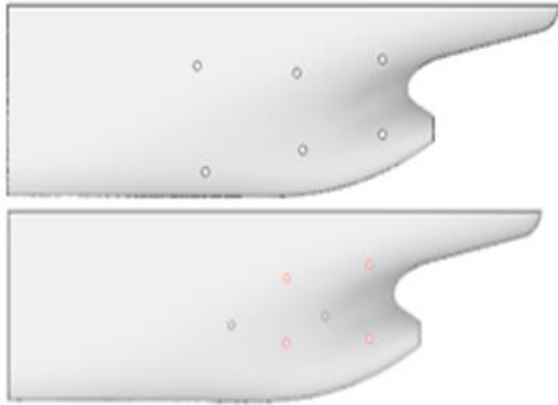


**Figure 6.** Initial placement of control points (top); revised placement of control points according to sensitivity analysis (bottom).

As a next step; using the 6 control points, a set of design of experiments were created by randomly varying their half-breadths  $\pm 10\%$ , which contains 280 number of hull variants non-dimensionalized with respect to initial hull form given in Figure 7. This figure includes all results of the design-of-experiments-study obtained by the computational evaluation of the variant hull forms.

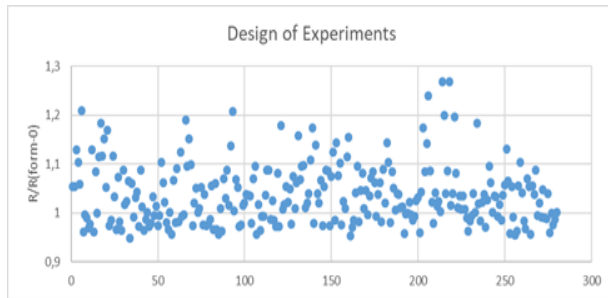


**Figure 7:** Non-dimensionalized design of experiments

#### 4.4 Meta-model Performance Assessment

The training output of Kriging is given in Table 3. It is seen from the results that, the accuracy of the meta-model increases significantly in between 100-140. Then, increasing the training data has positive effect at first but afterwards model accuracy shows stable behavior when compared to the effect of first incrementation of training sample. According to the related literature, this behavior may imply that model reached a certain level of training and adding more data could not improve the accuracy (Forrester et al 2008). When the correlation coefficient is greater than the 0.8 the meta-model is assumed to be satisfactory (Jones 2001). Kriging results show expected performance in terms of increasing learning ability that can be referred from correlation coefficient and better exploration for response of the problem that is directly related with the RMSE of the different surrogates.

Table 3: Training the meta-model Kriging and its results.

Total # of Points	Training Data	Test Data	Correlation Coefficient	RMSE
120	100	20	0.4004	0.2395
165	140	25	0.7524	0.1698
200	170	30	0.7938	0.1141
280	240	40	0.8185	0.1561

The performance of ANN is presented in Table 4 by using the same set of training and test data points. It can be concluded from the results that at the first attempt with 100 training data point, ANN could not provide a satisfactory learning level which may imply that for the same set of DoE ANN needed more training data points to reach same level of model accuracy. When the number of training points increased from 100 to 140, it appears that the model accuracy is affected negatively. When the number of training data points is increased, the results show similar performance with those of Kriging. With regards to the maximum level of training data, it is seen that correlation coefficient is slightly less than Kriging by providing smaller global error for the meta-model. One may also conclude that added training data (the bottom row in Table 4) may belong to unexplored regions in DoE so that RMSE increased for the last (bottom row) ANN meta-model.

Table 4: Training the meta-model ANN and its results.

Total # of Points	Training Data	Test Data	Correlation Coefficient	RMSE
120	100	20	0.3047	0.1062
165	140	25	0.2641	0.0594
200	170	30	0.6925	0.0295
280	240	40	0.8141	0.0377

The performances of ANN meta-models are presented in Figure 8 for 100, 140, 170 and 240 training points respectively, to show that how much are those test data points away from being accurate according to the trained meta-model. From Figure 8 for the 1<sup>st</sup> and 2<sup>nd</sup> plot, it is understood that the predicted and real results are widely scattered, which means that training should be continued with more additional data points. Afterwards, when learning is improved by additional training data to the model, predicted results became more accurate with less scattered behavior.

## 5 OPTIMIZATION

Selected model is restricted the transverse-wise variations within  $\pm 10\%$  of the original offsets. The optimization process for minimum viscous resistance is performed by genetic algorithm (GA). GA solver, utilized from the Matlab library in the present study, is a commonly used optimization solver based on genetic algorithms (Chipperfield and Fleming, 1995). The basic components common to almost all genetic algorithms are; a fitness function for optimization, a population of chromosomes, a

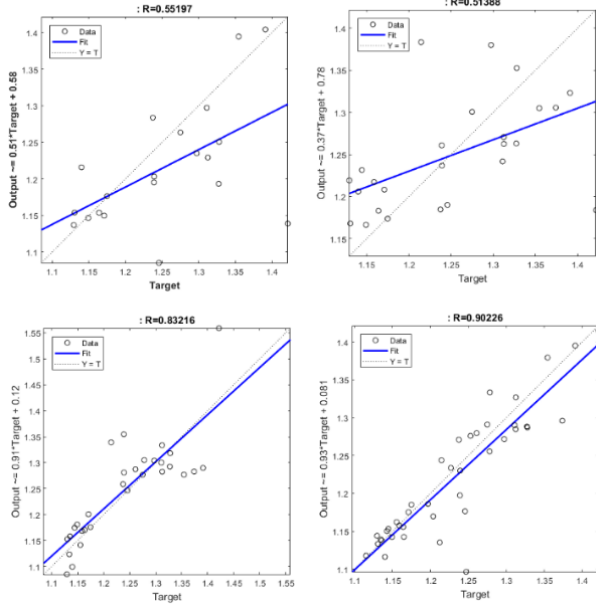


Figure 8: Learning performance of ANN surrogate model.

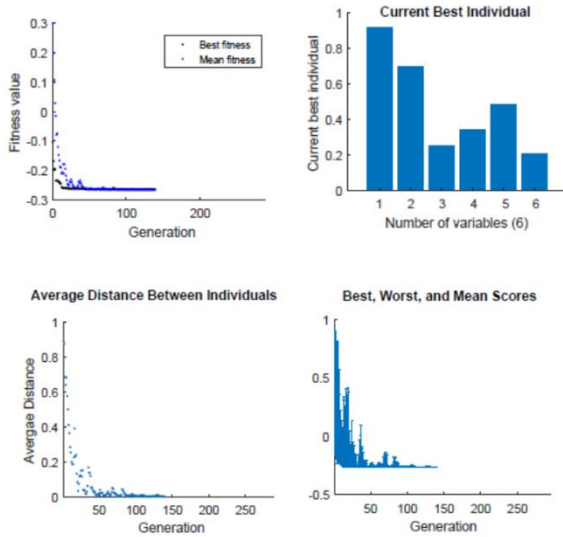


Figure 9: Optimization performance of Kriging surrogate model.

selection of which chromosomes will reproduce, crossover to produce next generation of chromosomes and random mutation of chromosomes in new generation (Mitchell, 1995). In the genetic algorithm, the evolution begins with a population of randomly generated individuals. In each generation, the fitness of every individual in the population is evaluated; multiple individuals are selected from the current population according to fitness and modified to form a new population. Then, new population is used in the next iteration stage of the algorithm. The algorithm terminates by achieving the maximum number of generations or by exceeding a satisfactory fitness level for the population. The present optimization study started with a set of data,  $x_1$  to  $x_6$ , which corresponds to multidimensional design input of each variant hull form,

with observed responses,  $R_V$  (presently the viscous resistance). The lower bound is 0.9 and the upper bound 1.1 for  $x_1$  to  $x_6$  that we restrict the variation of points  $\pm 10\%$  by the width of the hull model. Then the metamodelling stage started to find an expression for a predicted value at a new point  $(x_1^*, x_2^*, \dots, x_6^*)$ .

The outcome of the optimization procedure for both the surrogate strategies are presented in Table 5 and Table 6 for 100, 140, 170 and 240 data, respectively. The matrix content in Tables 5 and 6 represents the non-dimensionalized offsets by the original half-breadths.

Table 5: Optimized control points (Kriging).

$x_1$	$x_2$	$x_3$	$x_4$	$x_5$	$x_6$
1.0297	0.0724	0.9486	0.9483	0.9440	0.9714
0.9514	0.9728	0.9700	0.9377	0.9341	0.9500
0.9514	1.000	0.9729	0.9257	0.9372	0.9330
1.0882	1.0370	0.9517	0.9740	0.9986	0.9465

Table 6: Optimized control points (ANN).

$x_1$	$x_2$	$x_3$	$x_4$	$x_5$	$x_6$
1.1000	0.9468	1.1000	1.0497	0.9731	1.1000
1.0907	1.1000	1.0637	0.9163	1.0614	1.0242
0.9427	1.0612	0.9933	0.9525	0.9278	0.9440
1.0137	0.9364	0.9884	0.9738	0.9444	0.9042

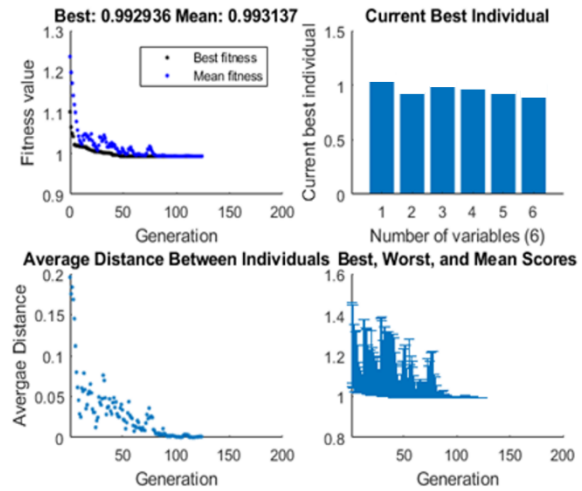


Figure 10: Optimization performance of ANN surrogate model.

In the present GA optimization; the population type is taken as double vector, the population size is selected as 50. The other main parameters are the number of generations, taken as 100, and the tournament size, taken as 5. In Figure 9 and Figure 10, GA performances based on Kriging and ANN, respectively, are presented. The convergence of optimum point is presented relative to the generation in terms of fitness value, average distance between individual and best scores of attempts. In addition, the predicted optimum is depicted as current best individual. Since the Kriging is performed for normalized values of the DoE variation, obtained optimal control point values seem diverse in Figure 9 compared to ANN. But, in

\* Corresponding author e-mail: pehlihanha@itu.edu.tr

Table 5 and in Table 6 optimized control point values are presented in non-normalized form. Therefore, the variation of control points for optimized hull forms can be directly compared from these tables.

**Table 7:** Predicted optimum hull form resistance values for different meta-models.

Train Data	Kriging		ANN	
	Viscous Res. (%)	Viscous Res. [N]	Viscous Res. (%)	Viscous Res. [N]
100	7	1.0986	15	1.0017
140	11	1.0513	14	1.0051
170	11	1.0478	9	1.0716
240	12	1.0367	16	0.9929

According to the figures obtained from the optimizer, the predicted resistance gains are presented in Table 7 in percentages and as absolute values of viscous resistances. From these comparisons, when the maximum available data point is used in the meta-models the resistance gains are said to be similar.

However, post-optimization CFD analyses show that the resistance reduction (in viscous resistance) attained by the optimal form, by means of Kriging, is about 5% instead of 12 %. In addition, when ANN outcome is investigated by CFD, the resistance gain is obtained as 4.3% instead of 16% as given in Table 7. The results of CFD computations are compared in Table 8, when the maximum number of training data is considered for the optimal forms.

**Table 8:** CFD results for optimized hull forms.

	Predicted		Resistance gain (%)
	Vis. Res. [N]	CFD [N]	
Form0	1.1800		
Kriging	1.0367	1.1209	5.01
ANN	0.9929	1.1259	4.30

It is important to discuss the possible reasons behind the results given in Tables 7 and 8. First of all, for the results presented in Table 7, Kriging provided more accurate meta-model, but ANN shows uncorrelated behavior as the number of training data increases. This may remind us that the nonlinear transfer functions used in ANN may produce many local minima as that may cause the optimization to be trapped in this deceptive local minimum instead of a global one. Even reinitializing the training process may not prevent trapping in a local minimum. The reinitializing process should be renewed several times since finding correct weight parameters for the network strictly related with assigned parameters. The reinitialization process conducted three times for this study to observe the converged optimal is same in sequential trainings.

Since, Kriging able to attain 5% resistance gain according to the simulation results, indicative visualizations are presented for the optimal form obtained by means of Kriging. In Figure 11, geometrical comparison of initial and optimized hull forms are given. Black lines represents

initial hull form and red lines constitutes for the optimal hull form in Figure 11. Since, there is no geometrical fairing criteria is implemented, the optimized hull form has some undulations particularly in WL6.

The comparison of the streamlines on the hull for initial (Form0) and optimal (Kriging) hull forms surface is presented in Figure 12.

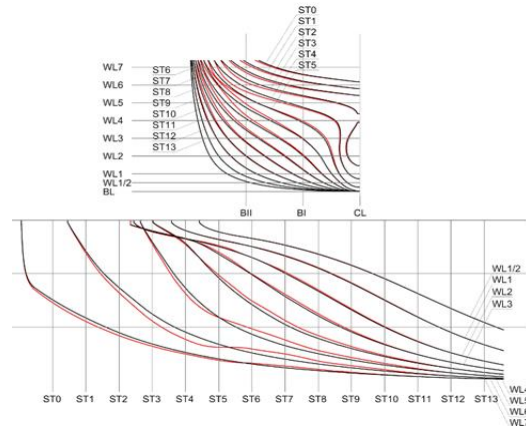


**Figure 11:** Geometrical comparison of initial and optimized hull forms.

Figure 12 validates the fact that using Kriging meta-model is able to offer considerably improved aft form hydrodynamics point of view. In addition, in Figure 13, it is seen that axial velocity is slightly increased which improves the flow characteristics in the aft region.

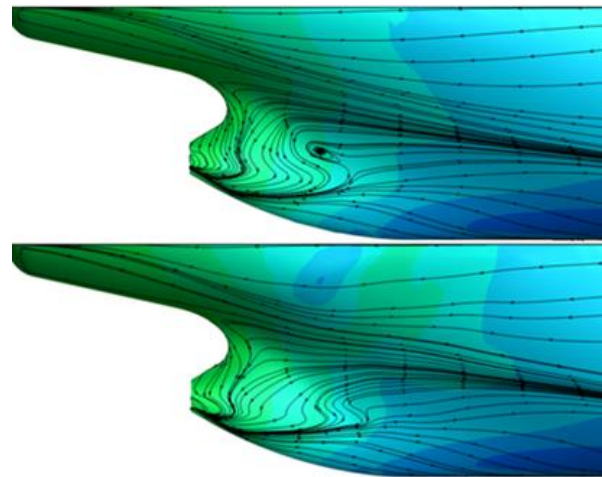


**Figure 12:** Comparison of the streamlines on the hull surface (Top: Form0 Bottom: optimal form.)

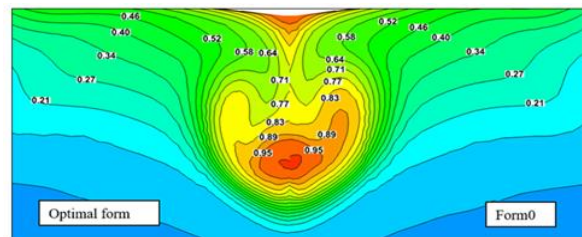


**Figure 13:** Nominal wake comparison for initial (right) and optimal (left) hull forms.

## 6 EXPERIMENTAL COMPARISONS

The optimal hull from which is obtained by means of the Kriging meta-model is subjected to experimental analyses to validate the computational work. The experiments are conducted at ITU Ata Nutku Ship Model Testing Laboratory. Accordingly, the initial hull form is produced in model scale as the main characteristics are presented in Table 1.



**Figure 14:** Revision made for the optimal aft form.

Initial hull form is first subjected to a set of experiments; resistance, wake measurements and flow visualization tests which are presented here respectively. After initial hull form experiments, the model is modified according to the optimal hull form from Kriging meta-model. The modified region on the model can be seen in Figure 14.

Firstly, resistance experiments are conducted and results are depicted in Figure 15 in model scale. It is seen that the proposed hull form obtained from Kriging meta-model is better than the initial hull form and gives a less total resistance around 5 % at the design speed of 1.08 m/s in model scale. This means that – as the gain in viscous resistance is about 5 % as calculated by CFD – the optimal form help also to reduce the wave resistance to reach 5% total resistance reduction. This observation poses an open discussion, hence wave resistance is not considered in the optimization process – because DoE based on the only double-body viscous flow computations.

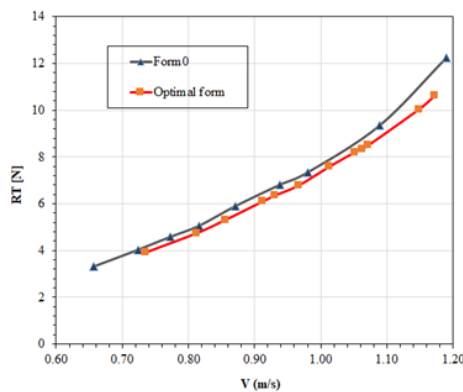


**Figure 15:** Resistance test results for initial and optimized hull forms.

In addition, wake measurement results are presented in Figure 16. In this figure significant flow improvement is observed from the comparison of wake measurements in the propeller plane.

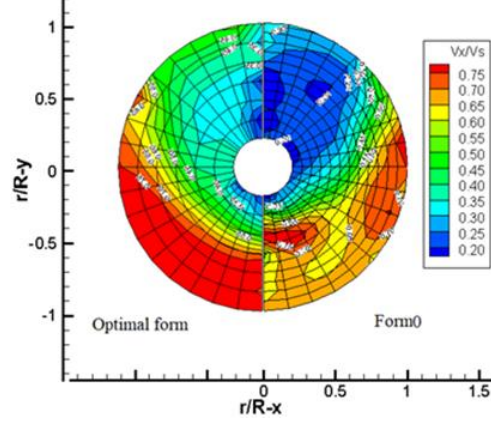


**Figure 16:** Wake resistance comparison for initial (right) and optimal (left) hull forms.

Moreover, flow visualization test by means of tufts is conducted at the service speed 1.08 m/s model scale) which is compared for optimal and initial hulls in Figure 17. The problematic region pointed out in the top figure is almost resolved in the optimal form.

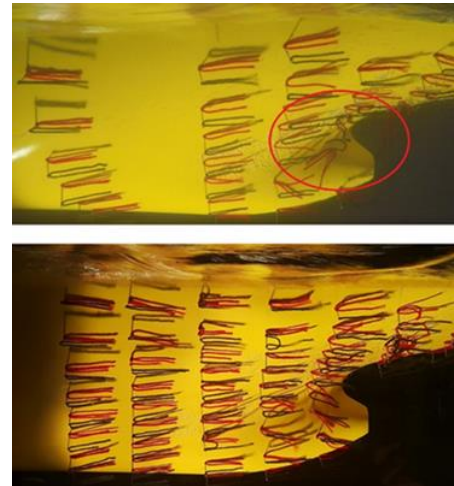


**Figure 17:** Wake resistance comparison for initial (top) and optimal (bottom) hull forms.

## 7 CONCLUSIONS

Taking all numerical and experimental results into account, Kriging provided slightly better results based on the metrics treated in the present study. It can be concluded that Kriging is a convenient interpolation model for multidimensional hull form optimization problem. The methodology presented here, proved its usefulness as a tool in hull form optimization/improvement studies, as it is able to almost eliminate the flow irregularity and reduce viscous resistance. For the same training data Kriging appears to offer slightly better optimal form and less difference between meta-model outputs and CFD results; a conclusion which needs further research regarding with variability in uncertainties inherent in meta-models depending on the nature of the problems tackled.

**ACKNOWLEDGEMENTS**

Authors would like to acknowledge the financial support by TUBITAK (The Scientific and Technological Research Council of Turkey) for the ESTHETICS (Energy Saving Techniques for Energy Efficient Vessels and Emission Reduction towards Green Shipping) project (No. 218M487) jointly carried out with CTO of Poland.

**REFERENCES**

- Akima, H. (1970). A New Method of Interpolation and Smooth Curve Fitting Based on Local Procedures. *J. ACM*, **17**(4), 589-602.
- Bouhleb, A. M., Martins, J. R. R. A. (2019). Gradient-enhanced kriging for high-dimensional problems. *Engineering with Computers*, **35**, 157-173.
- Chen, L., Qiu, H., Gao, L., Jiang, C., Yang, Z. (2019). A screening-based gradient enhanced Kriging modeling method for high-dimensional problems. *Applied Mathematical Modelling*, **69**, 15-31.
- Chipperfield, A. J., Fleming, P. J. (1995). The MATLAB genetic algorithm toolbox. 10-10.
- Demuth, H., Beale, M., & Hagan, M. (1992). Neural network toolbox. For Use with MATLAB. The MathWorks Inc, 2000.
- Diez, M., Serani, A., Campana, E. F., Goren, O., Sarioz, K., Danisman, D. B., Grigoropoulos, G., Aloniati, E., Visonneau, M., Queutey, P., Stern, F. (2015). Multi-objective Hydrodynamic Optimization of the DTMB 5415 for Resistance and Seakeeping. *FAST, 13<sup>th</sup> USA*.
- Diez, M., Serani, A., Campana, E.F., Volpi, S., Stern, F. (2016). Design-space dimensionality reduction for single and multi-disciplinary shape optimization. *17<sup>th</sup> AIAA/ISSMO MAO Conference*.
- Farkas, A., Degiuli, N., Martić, I. (2017). Numerical simulation of viscous flow around a tanker model. *Brodogradnja*, **68**(2), 109-125.
- Forrester, A. I. J., Sobester A., Keane, A. J. (2008). *Engineering Design via Surrogate Modelling*. John Wiley & Sons, United Kingdom.
- G. Sun, S. Wang, (2019). A review of the artificial neural network surrogate modeling in aerodynamic design, Proceedings of the Institution of Mechanical Engineers, Part G: *Journal of Aerospace Engineering*, **233** (16).
- He, W., Xu, Y., Zhou, Y., Li, Q. (2018). A novel improvement of Kriging surrogate model, *Aircraft Engineering and Aerospace Technology*.
- Jones, D. R. (2001). A taxonomy of global optimization methods based on response surfaces. *J. of Global Optimisation*, **21**, 345–383.
- K. McBride, K. Sundmacher (2019). Overview of Surrogate Modeling in Chemical Process Engineering, *Chem.-Ing.-Tech.* **91**, 228–239.
- Krige, D.G. (1951). A statistical approach to some basic mine valuation problems on the Witwaterstrand. *Journal of the Chemical, Metallurgical and Mining Engineering Society of South Africa*, **52**(6), 119-139.
- M.A. Azizi Oroumieh, S. Mohammad Bagher Malaek, M. Ashrafzaadeh, S. Mahmoud Taheri, (2013). Aircraft design cycle time reduction using artificial intelligence, *Aerosp. Sci. Technol.* **26** (1) 244–258
- Matheron, G. (1963). Principles of geostatistics. *Economic Geology*, **58**, 1246-1266.
- Mitchell, M. (1995). Genetic Algorithms: An Overview. *Complexity*, **1**(1), 31-39.
- Pehlivan Solak, H. (2020). Multi-dimensional surrogate based aft form optimization of ships using high fidelity solvers, *Brodogradnja*, **71**(1).
- Peri, D. (2012). Automatic tuning of metamodels for optimization. *12<sup>th</sup> (COMPIT)*, 51-62, Cortona.
- Peri, D. (2015). Improving predictive quality of kriging metamodel by variogram adaptation. *VI MARINE*, Italy.
- Rumpfkeil, M., Yamazaki, W., Mavripilis, D. (2011). A dynamic sampling method for Kriging and Co-Kriging surrogate model. 49th AIAA Aerospace Sciences Meeting Including the New Horizons Forum and Aerospace Exposition, Orlando, Florida.
- Querard, A.B.G., Temarel, P., Turnock, S.R. (2008). Influence of viscous effects on the hydrodynamics of ship-like sections undergoing symmetric and anti-symmetric motions, using RANS. *OMAE*, Portugal.
- Scholcz, T. P., Gornicz, T., & Veldhuis, C. (2015). Multi-objective hull-form optimization using Kriging on noisy computer experiments. MARINE VI (pp. 1064-1077). CIMNE.
- Wilcox, D.C. (2006). *Turbulence Modeling for CFD*. D.C.W. Industries, USA.

## Power efficient thrust allocation algorithms in design of dynamically positioned ships

Agnieszka Piekło<sup>1,2,\*</sup>, Anna Witkowska<sup>2</sup>, Tomasz Zubowicz<sup>2</sup>

<sup>1</sup>Maritime Advanced Research Centre, Gdańsk, Poland

<sup>2</sup>Faculty of electrical and control engineering, Gdansk University of Technology, Gdańsk, Poland

**Abstract:** Assessment of power consumption on a Dynamically Positioned (DP) ship in the early design stage can assist crucial design choices. The study presents a comparison between two algorithms of optimal thrust allocation in a propulsion system for an over-actuated DP ship. Applied algorithms were Quadratic Programming (QP) and Non-dominated Sorting Genetic Algorithm II (NSGAI). Based on both approaches, tools were developed for ship design purposes. Based on a case study, QP optimization is more suited for universal use and fast analysis of many designs. With adequate optimization of NSGAI parameters, this algorithm can be effective for DP simulations at specified weather conditions. This is due to the possibility of application of original functions describing the DP problem, which is not possible in the case of QP optimization, where the problem needs to be simplified.

**Keywords:** Dynamic Positioning, Thrust allocation, Optimization algorithms

### 1 INTRODUCTION

Dynamic Positioning (DP) is a ship's operational state in which the ship maintains its position and heading only through its propulsion system in a variety of environmental conditions. Thrusters control inputs: propeller revolutions (corresponding to power) and orientation angle are automatically and dynamically controlled by the DP control system with the aim of stabilizing and high disturbance rejection.

For a given environmental condition and ship's heading the stabilizing task will result in a specific power distribution among thrusters and total power consumption on the ship. Since the power on each thruster and on the whole ship is limited, certain weather conditions might exceed the capabilities of the propulsion system and limit the DP operations. The DP capability is a ship's ability to station keeping under specified environmental conditions (wind, wave, current).

During an early phase of ship design, propulsion type, dimensions and engines are selected to estimate the initial cost of a ship and prepare an offer for the customer. A designer must prove that the ship will fulfill the requirements and at the same time, propose a fine price. For those reasons, a specific software/tool for the assessment of DP capability needs to be at disposal of a Naval Architect. To assist in DP analysis a leading ship's classification society Det Norske Veritas (DNV) has developed a method for DP capability assessment provided in (DNV-ST-0111 2021). The results are documented by DP capability numbers (corresponding to the Beaufort scale) and capability plots (in polar form). The standard defines three different DP analysis levels.

Level 1 will be discussed in this paper. The calculation method at this level shall be based on a static balance of environmental and the vessel's actuator forces, where environmental forces are calculated with the empirical

equations based on the ship's main dimensions. The static balance shall determine the thrust distribution among thrusters (both magnitude and direction) called thrust allocation. This task, however, has no unique solution since the DP ships are over-actuated, meaning there are more control inputs than the number of equilibrium equations (2). The DP performance assessment evolves into an optimal thrust allocation problem.

The paper focuses on describing the application of two selected optimization algorithms: Quadratic Programming (QP) and Non-dominated Sorting Genetic Algorithm II (NSGAI), to the thrust allocation problem in DP performance. Based on both approaches applied to the DNV method, the power consumption on the ship is optimized. Subsequently, the thruster's dimensions, layout, and maximum power can be optimized by multiple analyzes in the context of ship design.

#### 1.1 Related work

The problem of optimal thrust allocation is raised in (de Wit 2009, Ruth 2008, Fossen 2011, Sørensen 2013). Based on the literature, optimization algorithms that can be applied to the problem can be generally divided into two groups. The first group of methods consists of gradient-based approaches. Among this group, the most used are the ones based on Quadratic Programming (QP) (de Wit 2009, Valčić 2020, Ruth 2008, Wang et al 2018, Zalewski 2016, Zalewski 2017, Piekło et al 2022) or Lagrangian multipliers (de Wit 2009). Both approaches assume that the objective function and constraints are smooth, and they guarantee to reach a global minimum. The second group of methods consists of the so-called non-gradient (derivative-free) methods. This group is represented by the so-called meta-heuristic algorithms (Luke 2013), such as genetic or evolutionary algorithms (Ding et al 2020, Rainer et al 2019, Goldstein, 1989, Baetz-Beielstein 2014, Kochenderfer et al 2019) or direct-search algorithms (Baeyens, 2016). Algorithms that introduce a multi-

\* Corresponding author e-mail: [pieklo.agnieszka@gmail.com](mailto:pieklo.agnieszka@gmail.com)

objective optimization in thrust allocation problem are NSGAI which are described in (Deb et al 2002, Gao et al 2019). In the latter group of algorithms, if certain requirements are met, algorithms tend to converge global optimum. However, they converge relatively slowly and do not guarantee the solution in a finite time.

### 1.2 Motivation and contribution

The main objective of this study was to apply an alternative optimization algorithm for optimal thrust allocation in DP performance. The previously developed tool with the application of QP optimization (Piekło et al 2022) revealed some difficulties in coding complicated constraints matrices. Formulation of spoiled zones and forbidden zones of azimuth thrusters (describing the interactions between the thrusters and the hull, with possible overlaps due to many adjacent thrusters) and rudder saturation constraints, introduced some simplifications and possible inaccuracies to the problem. A backup tool for verification was proposed based on derivative-free optimization, NSGAI. The structure of the algorithm allows for code simplification and application of the original functions describing the problem without the need to transform the problem to a quadratic form with linear constraints. Pros and cons of NSGAI application based on results comparison will be discussed in this paper.

### 1.3 Structure of the paper

The remaining sections of this research work are organized in the following manner. In section 2 the DP capability assessment problem has been formulated. Section 3 provides information on how to implement the methods (NSGAI and QP) and proposes a solution to the formulated problem. The methodology of application of QP is given in a short version as it has already been proposed comprehensively in (Piekło et al 2022). The results obtained by the application of both algorithms are discussed and compared in section 4. Section 5 concludes the paper.

## 2 PROBLEM FORMULATION

A DP analysis in an early design stage serves to estimate power consumption on a ship and assess the limiting capabilities of the propulsion system which is accomplished by applying an optimal thrust allocation. DP performance is estimated for a given environmental conditions and ship's heading. The environmental conditions are statically balanced by thrust forces and moment provided by the propulsion system, which can be simply expressed below (1).

$$\tau_{thr} = \tau_{env} \quad (1)$$

where  $\tau_{thr}$  is the vector of forces and moment produced by propulsion system and  $\tau_{env}$  corresponds to environmental forces and moment. Considering a planar movement of the ship, the balance equations yield (2):

$$\begin{aligned} \sum_{i=1}^N T_{x i} &= F_{env x} \\ \sum_{i=1}^N T_{y i} &= F_{env y} \\ \sum_{i=1}^N (-T_{x i} \cdot y_i + T_{y i} \cdot x_i) &= M_{env z} \end{aligned} \quad (2)$$

where  $F_{env x}$ ,  $F_{env y}$  and  $M_{env z}$  denote  $x$  and  $y$  direction net force components and moment resulting from the environmental influences (wind, wave, current), expressed in [N] and [Nm], respectively, also considered as disturbance inputs;  $T_{x i}$  and  $T_{y i}$  are forces generated by the  $i$ -th thruster in [N];  $x_i$  and  $y_i$  define position of the  $i$ -th thruster in the ship centered coordinate frame (DNV-ST-0111 2021);  $N$  denotes the total number of thrusters.

Since a typical DP ship with its propulsion is an over-actuated system, Eq. (2) has no unique solution in terms of thruster-generated forces  $T_{x i}$  and  $T_{y i}$ ,  $\forall i$ . Therefore, instead of solving (2), the thrust is to be allocated while optimizing the total power consumption, considering the balance equation (2).

## 3 METHODOLOGY

Two types of algorithms are proposed, QP and NSGAI. The primary objective (power minimization) is the same for both cases, however structure of the algorithms imposes a separate methodology for each of them.

To use the QP approach one must linearize the constraints and transform the power-thrust relation into a quadratic form which introduces some inaccuracies. On the contrary, NSGAI allows for using the original relation but introducing the equality constraint (2) is not explicitly possible. Imposing power and orientation of the thruster constraints is strait forward in the case of NSGAI however, forbidden zones of the azimuth thrusters, resulting from avoidance of flushing another working thruster are to be handled by applying a penalty function in the proposed method.

In the sections below, a brief methodology of solving optimal thrust allocation with QP algorithm will be given with reference to the author's recent work in (Piekło et al 2022), where the reader can find extended description. Subsequently, a comprehensive explanation of NSGAI application into the DNV method is presented.

### 3.1 Quadratic programming optimization

#### 3.1.1 Decision variables

In order to keep linear form of the equality constraints expressed in (2), the decision variables in the QP optimization are thruster's net forces vector  $u_{QP}$  (3).

$$u_{QP} \stackrel{\text{def}}{=} [T_{x 1}, T_{y 1}, T_{x 2}, T_{y 2}, \dots, T_{x N}, T_{y N}]^T \quad (3)$$

#### 3.1.2 Constraints

To solve the thrust allocation problem with the QP algorithm, the constraints must be linearized. The procedure of linearization of the constraints, both azimuth thruster and propeller with rudder is comprehensively given in (Piekło et al 2022) and it will not be repeated here.

Inequality constraints expressing thrust limitations, thruster operation range, forbidden zones, and spoiled zones of azimuth thruster, propeller with the rudder is linearized according to (Piekło et al 2022) and equality constraint given in (2) is considered.

### 6.1.3 Objective function

Based on (Fossen 2011) it can be assumed that consumed  $i$ -th thruster power given by non-linear relation  $P_i = a_{T_i} T_i^{3/2}$  (DNV-ST-0111 2021) (where  $T_i$  is a resultant thrust force and  $a_{T_i}$  is coefficient that can be estimated or determined by experiments) can be effectively approximated by a function of at most second degree. For all active thrusters the total power function can be expressed as follows (4).

$$P_{total}(u_{QP}) \stackrel{\text{def}}{=} u_{QP}^T W u_{QP} \quad (4)$$

where  $W \stackrel{\text{def}}{=} \text{diag}(w_1, w_1, w_2, w_2, \dots, w_N, w_N)$  is a diagonal matrix of weight coefficients  $w_i$ ,  $\forall i$ , corresponding to each mounted thruster. Weight coefficients are determined according to DNV standard (DNV-ST-0111 2021).

### 3.1.4 Optimization task

The objective function has one criterion, to minimize total power consumption on the ship (5).

$$\begin{aligned} \min_{u_{QP}} P_{total}(u_{QP}) \\ \text{s.t. } A u_{QP} = b \\ G u_{QP} \leq h \end{aligned} \quad (5)$$

where:  $A$  and  $G$  are the equality and inequality constraints matrices, respectively;  $b$  denotes a vector encompassing environmental forces and moments;  $h$  represents the thrust saturation and limiting operation angle. The internal structure of vectors and matrices results directly from expressions given in (Piekło et al 2022).

## 3.2 Non-dominated sorting genetic algorithm

### 3.2.1 Decision variables

Decision variables are partly control inputs on the ship: power and orientation angle of the thruster (6).

$$u_{NSGAI} \stackrel{\text{def}}{=} [P_1, \alpha_1, P_2, \alpha_2, \dots, P_N, \alpha_N]^T \quad (6)$$

where  $P_i$  is the  $i$ -th thruster brake power in [kW] and  $\alpha_i$  is thruster orientation angle in  $[\circ]$ .

Relation between power and thrust is given in (DNV-ST-0111, 2021) and can be expressed as below (7).

$$T_i = a_{P_i} P_i^{2/3} \quad (7)$$

where  $T_i$  is a resultant net thrust and  $a_{P_i}$  is a coefficient calculated based on propulsor data and according to (DNV-ST-0111 2021).

Considering  $T_i$  components on x and y direction (8):

$$(T_{x_i}, T_{y_i}) = f(P_i, \alpha_i) \rightarrow \tau_{thr} = f(u_{NSGAI}) \quad (8)$$

### 3.2.2 Constraints

Boundary constraints are imposed on the decision variables as presented below (9):

$$\begin{aligned} P_{i \min} \leq P_i \leq P_{i \max} \\ \alpha_{i \min} \leq \alpha_i \leq \alpha_{i \max} \end{aligned} \quad (9)$$

where  $\alpha_{i \min}$ ,  $\alpha_{i \max}$  are orientation angle upper and lower boundaries of the  $i$ -th thruster and  $P_{i \min}$ ,  $P_{i \max}$  are power upper and lower boundary values for  $i$ -th thruster. In case of tunnel thrusters,  $\alpha_i$  is a set between  $-1$  and  $1$  corresponding to tow angles:  $270^\circ$  and  $90^\circ$ . For propeller with rudder  $\alpha_i$  ranges from  $-30^\circ$  to  $30^\circ$  and for azimuth thrusters from  $0^\circ$  to  $360^\circ$ .  $P_{i \min}$  is always equal to zero.

To impose forbidden zones constraints a penalty is applied. Forbidden zones are due to possible interactions between two working thrusters and they create a non-convex region by division of the boundary set (9) into at least two parts.

### 3.2.3 Objective function

The objective function is two criteria. One objective is a sum of power consumption on each thruster (10).

$$P_{total} \stackrel{\text{def}}{=} \sum_{i=0}^N P_i \quad (10)$$

In case of genetic algorithms, the equality constraints expressed by the static balance (2) cannot be applied directly. Therefore, second objective is introduced to minimize the error (11) between environmental and thrusters forces and moment.

$$e(u_{NSGAI}) = \tau_{thr}(u_{NSGAI}) - \tau_{env} \quad (11)$$

To express vector  $e$  as a single number for two criteria optimization pursues, a quadratic penalty term  $J_e$  is introduced (12).

$$J_e = e^T Q e \quad (12)$$

where  $Q = \text{diag}(q_1, q_2, q_3)$  represents the penalty weight of the resultant force error on the three DOFs (Gao 2019).

### 3.2.4 Optimization task

Two criteria optimization is applied to the thrust allocation problem. Both, power consumption and balance error function (12) are minimized. The optimization task can be expressed as follows (13):

$$\begin{aligned} \min_u [P_{total}(u_{NSGAI}), J_e(u_{NSGAI})] \\ \text{s.t. } u_{NSGAI \min} \leq u_{NSGAI} \leq u_{NSGAI \max} \end{aligned} \quad (13)$$

where  $u_{NSGAI \min}$  and  $u_{NSGAI \max}$  are the decision variable boundaries.

The result of the algorithm is a Pareto front (Deb et al 2002) and the solution is found by applying the accepted error margin  $\tau_{e \min}$  (14) to the results. The minimum power consumption solution within the margin is selected.

$$\tau_{e \min} = [F_{x \min}, F_{y \min}, M_{z \min}] \quad (14)$$

where  $F_{x \min}$ ,  $F_{y \min}$ ,  $M_{z \min}$  are minimum defined forces on x and y direction and moment around z axis that the ship, by assumption is allowed to experience.

## 3.3 DP capability assessment

Finally, the ship's DP capability is assessed in the following manner. Problem (5) and (13) is solved with separately developed tools (based on the methodology

given in the previous subsections). The problem is resolved for discrete values of the angle of environmental impact, from 0° to 360°, to cover the whole considered domain of interest. For each angle, the optimization is performed for increasing discrete weather condition described by DP numbers from 1 to 11, (DNV-ST-0111 2021). Results of DP capability are typically presented in a graphic form, as a polar plot, where each circle in the plot represents a DP number. Power consumption is typically calculated for a given environmental condition and the whole headings range is presented in a form of a power envelope in the polar plot. In the following subsections, the parameters of the calculations using QP and NSGAI will be described.

### 3.3.1 Quadratic Programming parameters

The only two parameters that control the calculation with QP optimization is the linearization error that in this case is set to 1% and the rudder angle step, set to 5°. It was analyzed that decreasing the rudder angle step did not affect the results but increased the time of the calculation.

### 3.3.2 Non-dominated sorting genetic algorithm parameters

A list of parameters that control the calculation with NSGAI methodology is given in Table 1. The NSGAI is initiated several times and then the best result from all “tries” is selected. If the algorithm fails to find a solution the population and iterations are increased by 40 and “tries” is increased by 10. This process repeats 3 times and if the solution is found the parameters are valid for the next DP number, if not the parameters reset, and the next heading is analyzed starting from DP number 1. The parameters mentioned above were selected with a trial-and-error method.

The minimum acceleration that the ship can experience is assumed and the minimum forces and moment are calculated based on Newton’s second law, where the ship’s mass  $M$  and inertia  $I_z$  are known parameters. The forces error penalty  $Q$  is assumed in a way to avoid overloading of only one component of the force error vector  $e$  and be nearer to the minimum assumed margin vector  $\tau_{e\ min}$ .

**Table 1. NSGAI algorithm parameters**

Parameter	Value
population	100
iterations	200
tries	10
forbidden zones penalty	$N \cdot P_{i\ max}$
probability of crossing	0.65
probability of mutation	0.03
$Q$	$\left[ \frac{M_z\ min}{F_x\ min}, \frac{M_z\ min}{F_y\ min}, 1 \right]$
$\tau_{e\ min} = [F_x\ min, F_y\ min, M_z\ min]$	$[Ma_x, Ma_y, I_z a_r]$
allowed accelerations $[a_x, a_y, a_r]$	$[10^{-3}, 10^{-3}, 10^{-5}]$
	$[m/s^2, m/s^2, rad/s^2]$

<sup>1</sup> The free version of the application is limited to analysis of maximum four thrusters and does not share detailed results, just the DP capability plot.

Real numbers chromosomes were used in the algorithm. A binary selection tournament for the initial population and standard crossover and mutation were applied according to (Deb et al 2002).

## 4 RESULTS

The case study is being used to illustrate the use of the proposed approaches in assessing the DP capability of a rescue ship which total length is 96 m. The ship is equipped with five thrusters depicted in Fig.1: azimuth thrusters at the stern - 1,2, azimuth thruster at the bow – 3 and two tunnel thrusters at the bow - 4,5. The crucial ship’s parameters have been included in Table 2.

**Table 2. Ship main data**

Symbol	Value	Unit	Description
$L_{pp}$	86.6	$m$	Length between perpendiculars
$B$	18.8	$m$	Maximum breadth at waterline
$T$	5.0	$m$	Summer load line draft
$A_{F\ wind}$	392.0	$m^2$	Frontal projected wind area
$A_{L\ wind}$	1203.0	$m^2$	Longitudinal projected wind area
$A_{L\ current}$	441.0	$m^2$	Longitudinal projected submerged current area

Dedicated tools were developed using Python programming language to perform analysis with both QP and NSGAI optimization. First, the comparison between thrust allocation is presented in subsection 4.1. Second, in subsection 4.2, both DP capability results and power consumption in each condition are discussed. Additionally, QP optimization results in comparison with the results obtained from the DNV tool available online <sup>1</sup> are presented.

### 4.1 Optimal power distribution

An exemplary weather condition was analyzed corresponding to a DP number 7, where heading of the ship was 30° in respect to the weather. The total power consumption resulting from the optimal thrust allocation was 37% and 52% using QP and NSGAI algorithm respectively. Fig. 1 presents a power distribution over the available thrusters. The red areas near the rear thrusters indicate the azimuth thrusters forbidden zones. Power utilization per thruster is denoted with percentage values.

Due to random nature of the evolutionary algorithms, in general, the result presented in Fig. 1b is not repeatable per analysis. However, based on the obtained results it appears that the algorithm load one of the main stern thrusters much more than the other and does not utilize a bow azimuth thruster enough.

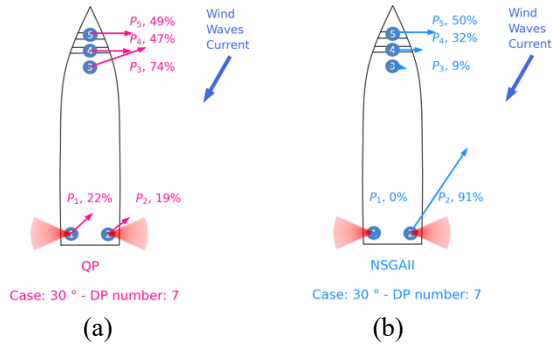


Figure 1. Optimal power distribution/thrust allocation

#### 4.2 DP Capability assessment

In Fig. 2,3 DP capability assessment results have been presented in a form of polar plots. Fig. 2 shows the maximum environmental condition that the ship can withstand. Fig. 3 presents the total power utilization in % at the given condition (DP number 6). Both plots present a comparison between QP and NSGAII algorithms.

The DP capability (Fig. 2) resulting from application of NSGAII algorithm is slightly reduced compared to the result of QP optimization. Moreover, the plot is asymmetrical, which in this case of a symmetric ship (hull, superstructure and propulsion layout) is an obvious inconsistency. Despite introduced the margin,  $\tau_{e min}$  (explained in section 3.2.2) in NSGAII optimization, the results are conservative compared to QP optimization results

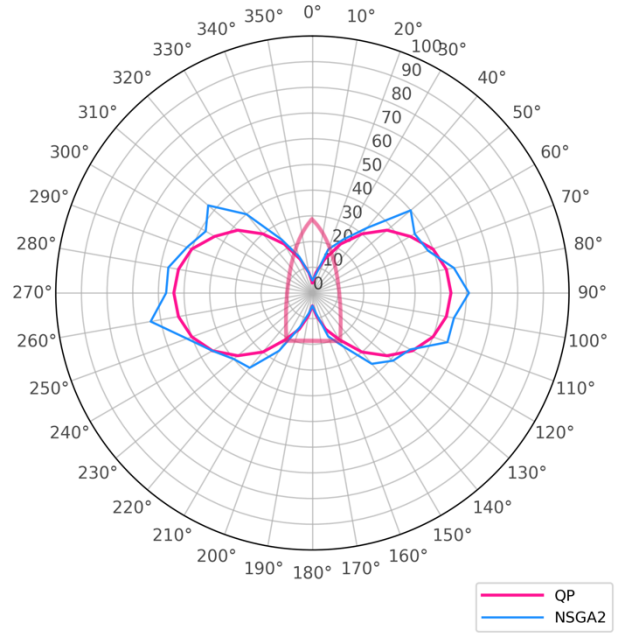


Figure 3. Power envelope at DP number 6

Based on the results and time consumption of the algorithms the QP optimization was chosen for further validation with the free web application from DNV. Only 4 thrusters can be analyzed with the online tool, therefore the foremost bow tunnel thruster was switched off. The validation presented in Fig. 4 showed 100% compliance with the QP optimization applied in this study for this case.

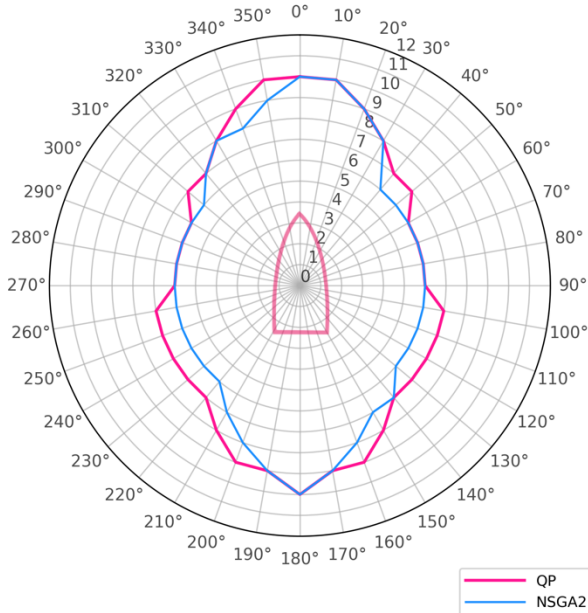


Figure 2. DP Capability plot

Fig. 3 presenting power envelopes for both approaches shows a relatively close result. However, also in this case the NSGAII optimization results in slight asymmetry.

Time of the calculation of DP capability in this ship case using NSGAII optimization is about 4 days while QP optimization takes around 2 – 3 seconds.

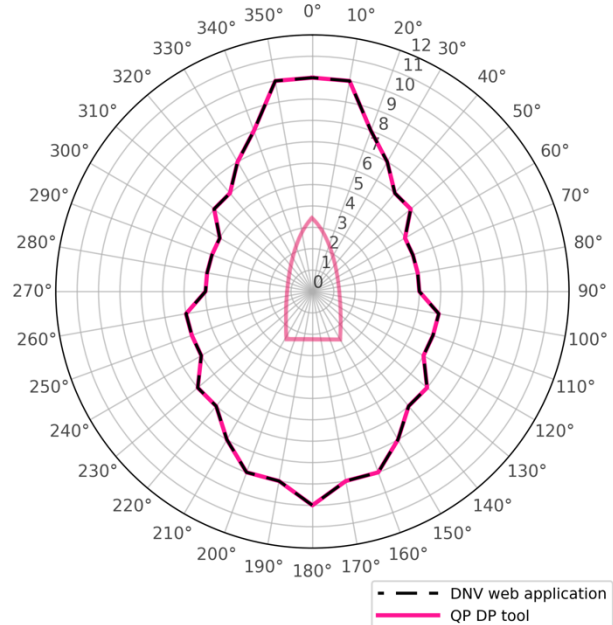


Figure 3. Validation of QP optimization with DNV web tool

Since the results of the NSGAII optimization differs from the QP optimization, while the latter was validated successfully (in a similar case), it can be concluded that the NSGAII tool shows some discrepancies based on the validation.

## 5 CONCLUSIONS

Based on the results of the application of the methodology described in this study, both developed tools can be used for assessing DP capability for a wide range of monohulls with a variety of propulsion types supporting the DNV method. However, the validation and comparison proved that the QP optimization have higher compliance with the DNV tool than the NSGAI optimization. Moreover, the NSGAI approach can give very random results, which are not globally optimal. At the same time, the NSGAI uses original functions describing constraints and the relation between the power and thrust. Therefore, no additional linearization is applied. For those reasons the code is much simpler and prevent from developer mistakes. On the contrary, NSGAI allows the force and moment error, and the ship is allowed to experience some accelerations which can lead to underestimation of the power consumption. However, this specific studied case showed otherwise.

Time of the calculations and the uncertainty of the results of the NSGAI algorithm can be reduced by tuning the calculation parameters for a specific ship and weather conditions (Gao et al 2020). The optimization of the parameters is very time consuming and potentially not applicable in case of a universal tool for DP capability assessment which development is the aim of this study.

Taking all aspects into account, the DP capability prognosis in an early design stage can be safely and efficiently performed by application of QP optimization. Its simplifications do not affect significantly the resulting power consumption and it ensures the global minimum. QP optimization can be very handy in the typical design office where many designs and configurations are to be assessed in a finite amount of time. NSGAI optimization can be treated as a secondary tool for some general checks in-between QP analyses of DP capability. A strong discrepancy between results from QP and NSGAI may be an indication of some errors in the code in QP tool, while the NSGAI code is straight forward and can be easier verified. Based on this study and referred literature a skilled engineer can implement both algorithms for the purpose of DP capability assessment in a typical design office.

The conducted studies showed that NSGAI may be difficult to apply to a universal DP capability tool for everyday use. However, a possibility of applying many objective functions can assist handling specific DP problems and DP simulations where also tear and wear of the thrusters can be optimized. Further optimization of the NSGAI parameters and research in this direction may result with a valuable alternative for a simpler approach like QP.

## REFERENCES

Baeynes, E, Herreros, A., Peran, J. (2016). A direct search algorithm for global optimization. Algorithms 9, 40, MDPI

- Beatz-Beielstein, T. (2014). Overview: Evolutionary Algorithms. PhD project. Cologne University of Applied Sciences.
- Deb, K., Pratap, A., Agarwal, S., Meyarivan, T. (2002). A Fast and Elitist Multiobjective Genetic Algorithm: NSGA-II. IEEE Transactions on Evolutionary Computations, Vol. 6, No.2.
- de Wit, C. (2009). Optimal thrust allocation methods for dynamic positioning of ships. M.Sc. Thesis. Delft University of Technology.
- Ding, G., Gao, P., Zhang, X., Wang, Y. (2020). Thrust Allocation of Dynamic Positioning based on Improved Differential Evolution Algorithm. Proceedings of the 39th Chinese Control Conference (CCC), pp. 1368-1373,Shenyang, China.
- DNV, DNV-ST-0111 (2021). Assessment of station keeping capability of dynamic positioning vessels.
- Fossen, T. (2011). Handbook of Marine Craft Hydrodynamics and Motion Control 1st edn. New York: John Wiley & Sons Ltd.
- Gao, D, Wang, T., Wand, Y., Xu, X. (2019). Optimal Thrust Allocation Strategy of Electric Propulsion Ship Based on Improved Non-Dominated Sorting Genetic Algorithm II. IEEE Access, IEEE 7, pp.135247-135255
- Goldstein, D. (1989). Genetic Algorithms in Search, Optimisation & Machine Learning. Addison-Wesley Publishing Company, Inc., USA
- Kochenderfer, M., Wheeler, T. (2019). Algorithms for Optimisation. MIT Press.
- Luke, S. (2013). Essentials of Metaheuristics. Lecture Notes, Lulu, Second Edition.
- Rainer, S., Prince, K. (2019). Differential Evolution - A simple and efficient adaptive scheme for global optimization over continuous spaces. Journal of Global Optimization. 23.
- Piekło, A., Witkowska, A. Zubowicz, T. (2022). Dynamic Positioning Capability Assessment for Ship Design Purposes. In: Kowalczyk, Z. (eds) Intelligent and Safe Computer Systems in Control and Diagnostics. DPS 2022. Lecture Notes in Networks and Systems, vol 545. Springer, Cham. pp. 386-397.
- Ruth, E. (2008). Propulsion control and thrust allocation on marine vessels. Doctoral Thesis. Norwegian University of Science and Technology.
- Sørensen, A. (2013). Marine Control Systems. Propulsion and Motion Control of Ships and Ocean Structures. Lecture Notes, Department of Marine Technology. Norwegian University of Science and Technology.
- Valčić, M. (2020). Optimization of thruster allocation for dynamically positioned marine vessels. Doctoral Thesis. University of Rijeka.

Wang, L., Yang, J., Xu, S. (2018). Dynamic Positioning Capability Analysis for Marine Vessels Based on A DPCap Polar Plot Program. China Ocean Eng. 32(1), pp. 90-98.

Zalewski, P. (2016). Convex optimization of thrust allocation in a dynamic positioning system. Sci. J. Mar. Univ. Szczecin 48(120), pp. 58-62.

Zalewski, P. (2017). Constraints in allocation of thrusters in a DP simulator. Sci. J. Mar. Univ. Szczecin 52(124), pp. 45-50.



## Experimental Powering Performance Analysis of M/V ERGE in Calm Water and Waves

Çağatay Sabri Köksal<sup>2</sup>, Batuhan Aktas<sup>1\*</sup>, Ahmet Yusuf Gürkan<sup>1</sup>, Emin Korkut<sup>2</sup>, Noriyuki Sasaki<sup>1</sup>, Mehmet Atlar<sup>1</sup>

<sup>1</sup>Department of Naval Architecture, Ocean & Marine Engineering, The University of Strathclyde, Glasgow, G4 0LZ, UK

<sup>2</sup>Istanbul Technical University, Faculty of Naval Architecture and Ocean Engineering, 34469 Maslak, Istanbul, Turkey

**Abstract:** The study is on the details and results of the resistance, propulsion and seakeeping (at a yaw angle) tests conducted with a scaled model of the GATERS target ship (M/V ERGE) made to a scale of 1/27.1. The comparative tests are conducted at the trial (ballast) loading condition of the ship appended with the conventional rudder system (CRS) and the Gate Rudder System (GRS) both in the calm water and waves at the Kelvin Hydrodynamics Laboratory's towing tank of the University of Strathclyde (UoS). The main objective of these tests is to contribute toward the establishment of the best procedure to estimate the powering prediction of a ship retrofitted with a GRS in calm water and waves using experimental methods. The resistance and propulsion tests were conducted in calm water to establish the accurate performance prediction methodologies for the prediction of Gate Rudder performance using traditional model test techniques. Furthermore, seakeeping tests at a yaw angle were conducted to evaluate the effect of waves on the comparative powering performance of the hull with the GRS and CRS to simulate the in-service operations of commercial ships at sea. These tests are conducted in regular waves and the hull at a yaw angle (to simulate an oblique wave condition) with a significant wave height of 1.25 m in full scale (corresponding to Beaufort 4) for a range of different wavelengths.

**Keywords:** Gate Rudder System (GRS); Resistance, Propulsion and Seakeeping Tests.

### 1 INTRODUCTION

As part of the EU H2020 Project GATERS activities (The EC - H2020 Project “GATERS”: GATE Rudder System as a Retrofit for the Next Generation Propulsion and Steering of Ships. (Project ID: 860337), 2021), this experimental investigation presents the details and results of the resistance, propulsion and seakeeping (at a yaw angle) tests conducted with a scaled model of the GATERS target ship (M/V ERGE, (a 90m and 7421 DWT general cargo vessel) made to a scale of 1/27.1 (LPP = 3.9m). The comparative tests are conducted at the trial (ballast) loading condition of the ship (3585 DWT) appended with the conventional rudder system (CRS) and the Gate Rudder System (GRS) both in the calm water and waves at the Kelvin Hydrodynamics Laboratory (KHL)'s towing tank of the University of Strathclyde.

The main objective of these tests is to contribute to the establishment of the best procedure to estimate the powering prediction of a ship retrofitted with a GRS in calm water and waves using experimental methods within the activities of T1.3 of WP1 of the GATERS project.

In achieving the objectives of the experimental investigations, the paper presents the experimental facility and equipment in Section 2. The information on the model preparations, experimental setup, and test matrix is given in Section 3. While Section 4 presents the results and their discussions regarding the resistance, propulsions and seakeeping (at a yaw angle) tests, Section 5 draws some concluding remarks from these investigations.

### 2 EXPERIMENTAL FACILITIES

#### 2.1 Kelvin Hydrodynamics Laboratory Towing Tank

Experiments were carried out in the towing tank of KHL of the University of Strathclyde, as shown in Figure 1, which has the following specifications and features;

- Tank dimensions ( $L \times W \times D$ ): 76×4.6×2.5 (m)
- Carriage: Driven along rails by a computer-controlled (digital) DC motor (Max speed 5 m/s).
- Wave-Maker: Variable water depth and computer-controlled four-flap absorbing wave-maker. Capable of generating regular and irregular waves of up to approximately 0.5 m.
- Beach: At the opposite end of the wave-maker, there is a beach for absorbing the waves and reducing wave reflections.



**Figure 1** Kelvin Hydrodynamics Laboratory Towing Tank Carriage.

\* Corresponding author e-mail: [Batuhan.aktas@strath.ac.uk](mailto:Batuhan.aktas@strath.ac.uk)

## 2.2 Rudder Load Measurement System

A dedicated rudder load measurement system was specifically designed and tailor-made for the target vessel model to accurately measure forces and moments acting on both CRS and GRS. The load cells can measure the horizontal (yawing) moment (or torque) and longitudinal (surge) and horizontal (side) forces acting on the rudder blade to enable an accurate interpretation of the cause of the potential savings provided by the GRS (Figure 2).



Figure 2 Rudder load measurement system.

## 2.3 Propeller load measurement System

The self-propulsion dynamometer for the system was also commissioned with the remaining parts of the system. The specially designed dynamometer has 250N thrust and 10Nm torque measurement range with up to 150% permitted overload. Self-propulsion dynamometer also has driving motor and shafting system that has a speed range up to 3000RPM at 1.5kW rated power.

## 3 EXPERIMENTAL SETUP & TEST MATRIX

### 3.1 Component Specification and Manufacture

The ship and propeller models were designed and manufactured following ITTC (2017) recommended guidelines. The scale factor of 21.7 was chosen to prevent blockage effects and consider the capacity of towing tank carriage, following ITTC (2011a). The ship model incorporated an interchangeable stern part (encircled on the model picture as shown in Figure 3) that enabled interchanging the CRS and GRS aft end configurations.

A single model propeller with parameters shown in Table 1 was used for both conventional and gate rudder tests. The model propeller was scaled from the newly designed propeller for M/V ERGE, which will be installed as part of the GRS retrofit on this vessel. The diameter of the model propeller is 165.9 mm (ITTC, 2011b). The model was manufactured from brass with a manufacturing tolerance of  $\pm 0.027$  mm under a scale factor of 21.7 following ITTC

guidelines (ITTC, 2017). In addition, the propeller open water characteristics were measured to be used for the self-propulsion analysis.



Figure 3 Appended model used for the tests.

Table 1 Gate rudder propeller parameters and characteristics.

Parameters	Index
Number of Blades	5
BAR ( $A_E/A_0$ )	0.4551
Diameter, $D$ (m)	0.1659
Pitch Ratio ( $P_{0.7}/D$ )	0.83
Material	Brass
Direction	Left-Handed

### 3.2 Test Conditions

The model tests were carried out corresponding to the ballast (trials) load condition of MV ERGE ( $T_{MEAN}=3.3$  m) due to weight limitations of the Kelvin Hydrodynamics Laboratory towing tank carriage. The corresponding ship and model characteristics for the ballast load condition are provided in Table 2.

Table 2 Model and ship characteristics for the ballast loading condition.

Parameters	Units	Model	Ship
$L_{OA}$	(m)	4.145	89.95
$L_{BP}$	(m)	3.915	84.95
$B$	(m)	0.710	15.4
$T$	(m)	0.152	3.30
$T_A$	(m)	0.175	3.80
$T_F$	(m)	0.129	2.80
$\Delta$	(ton)	0.363	3585
$C_B$	(-)	0.806	0.806
$C_P$	(-)	0.823	0.823
$C_M$	(-)	0.994	0.994
$C_{WP}$	(-)	0.854	0.854

### 3.3 Test Matrix

The test matrix in the ballast (trials) load condition for the resistance and the self-propulsion tests is given in Table 3.

Table 2 Resistance and self-propulsion test matrix.

Test Type	Condition	$V_s$ (knot)
Resistance	Bare Hull	7-13
Resistance	CRS	7-13
Resistance	GRS	7-13
Propulsion	CRS	11-13
Propulsion	GRS	11-13

The seakeeping tests were conducted with the ship model oriented in the towing carriage at a mean yaw angle of  $5^\circ$  oblique to the regular head waves for a range of different periods corresponding to Beaufort 4, as shown in Table 4.

**Table 4** Seakeeping test matrix.

$V_S$ (knot)	$H_S$	$T_S$	$\lambda/L_{WL}$
10	1.25	4.316	0.33 (BF4)
10	1.25	5.273	0.50
10	1.25	6.458	0.75
10	1.25	7.457	1.00

## 4 RESULTS AND DISCUSSIONS

### 4.1 Resistance Tests

The resistance tests were conducted in the ballast (trial) load condition without rudder (s) for the CRS and GRS configurations. The ship model was free to trim and sinkage whilst she was fixed to heel, sway and yaw motions. Form factor analysis and the extrapolation of the model test results to the full scale were carried out by Prohaska and the ITTC'78 methods, respectively (ITTC, 2011b). The effect of the appendages was calculated using the beta factor ( $\beta=0.70$ ). The CRS and GRS were considered appendages and extrapolated to the full scale accordingly.

The comparison of the full-scale effective power predictions for the CRS and GRS configurations is shown in Figure 4. As one can notice, there is a 4.3% effective power reduction at  $\sim 13$  knots for the hull with the GRS.

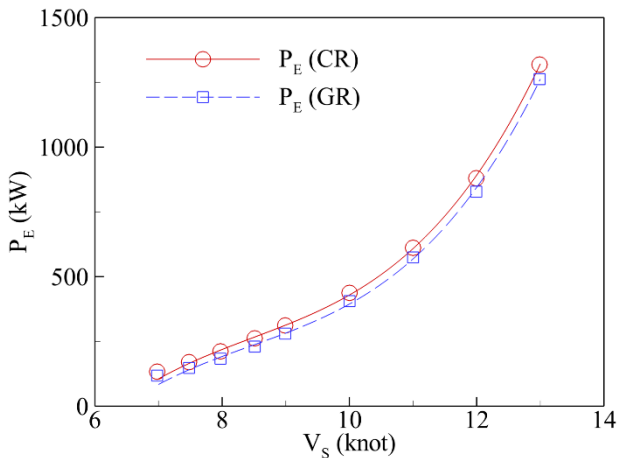


**Figure 4** Comparison of the effective power results for conventional rudder (CR) and gate rudder (GR) configurations.

### 4.2 Propulsion Tests and Powering Calculations

The self-propulsion test results obtained in the ballast load condition for the hull with the CRS (rudder amidship) and the GRS rudder angles at  $0^\circ$  configuration are given in Table 5 and Table 6, respectively. During the self-propulsion tests, an additional towing force should be applied to consider the frictional drag correction for the full-scale ship propulsion point. This external force  $F_D$  also called the Skin Friction Correction (SFC) takes into account the Reynolds effect of the model test and ship trial conditions. Therefore,  $F_D$  can be calculated according to (ITTC, 2011b) Procedure.

**Table 5** Power requirement of the ship with CRS.

$V_S$ (knot)	10.996	11.990	12.987
$P_E$ (kW)	608.887	875.599	1313.476
$\omega_{TS}$	0.377	0.387	0.43
$t$	0.193	0.204	0.259
$\eta_H$	1.294	1.298	1.299
$\eta_0$	0.514	0.521	0.527
$\eta_R$	0.904	0.875	0.807
$\eta_D$	0.601	0.592	0.552
$P_D$ (kW)	1013.252	1480.026	2378.349

**Table 6** Power requirement of the ship with GRS ( $0^\circ$ ).

$V_S$ (knot)	10.997	11.99	12.986
$P_E$ (kW)	573.817	830.413	1263.687
$\omega_{TS}$	0.279	0.275	0.273
$t$	0.134	0.119	0.167
$\eta_H$	1.201	1.215	1.145
$\eta_0$	0.475	0.483	0.505
$\eta_R$	1.222	1.23	1.152
$\eta_D$	0.697	0.721	0.666
$P_D$ (kW)	823.424	1151.682	1897.064

In order to analyse the self-propulsion test results and predict the delivered power in the full-scale for the ship with the CRS and GRS, the ITTC 1978 Performance prediction method is used with a slight modification to the full-scale wake correction for the GRS, which is described in the following.

The characteristics of the full-scale propeller are calculated from the model propeller characteristics in open water, which are corrected for the scale effect according to the 1978 ITTC (2011c). The model wake fraction is converted to the full-scale wake fraction, as in the procedure for the CRS. However, for the GRS, the wake fraction of the model and ship is assumed to be the same (i.e.  $1-\omega_M=1-\omega_S$ ) based on the recent experience with the limited number of ships with the GRS. The comparison of the delivered power predictions for the CRS (rudder amidship) and the GRS at  $0^\circ$  configurations are presented in Figure 5. As shown in this figure, the GRS results in an approximate 20% saving in the delivered power compared to the CRS.

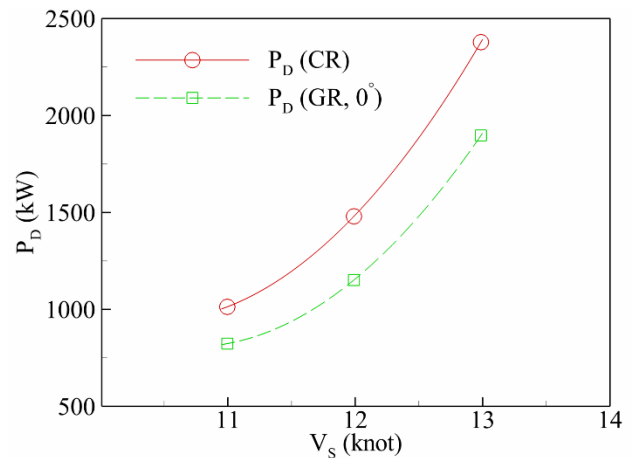


**Figure 5** Comparison of the delivered power results for conventional rudder and gate rudder configurations.

### 4.3 Seakeeping Test (Powering in Waves) at a Yaw Angle

Upon completion of the resistance and self-propulsion tests in calm water, the ship model towing point attachment was modified to allow for the yaw and roll motions, in addition to the heave and pitch. Following the modification, a series of seakeeping tests was conducted in regular waves at the propeller shaft speeds,  $n_{CRS}$  and  $n_{GRS}$ , corresponding to the self-propulsion points of the CRS and GRS configurations, respectively.

In order to avoid excessive yaw angles that may cause damage to the load cell, the rudder angle of both rudder systems ( $\delta_{Rudder}$ ) was measured at a critical regular wave condition (i.e.  $\lambda/L_{WL}=1.00$ ) for varying GRS, and CRS rudder angles to achieve a  $5^\circ$  of mean yaw angle with the model hull (i.e.  $5^\circ$  oblique to the incoming waves). A steady  $5^\circ$  yaw angle of the hull was achieved when the CRS' rudder angle was  $1.25^\circ$ , while the GRS' rudder angles (both Port and STB) were at  $5^\circ$ , as shown in Figure 6.

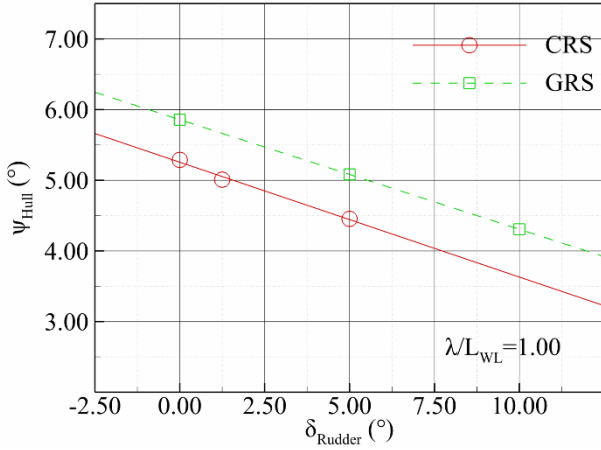


**Figure 6** Rudder angles of CRS, GRS versus hull yaw angles at ( $\lambda/L_{WL}=1.00$ ).

As shown in Figure 7, the mean yaw angle of the ship model was found to follow a similar pattern in each wave condition tested (i.e.  $\lambda/L_{WL}=0.33, 0.50, 0.75, 1.00$ ) to remain around a steady  $5^\circ$  yaw angle of the hull for both the CRS and GRS configurations.

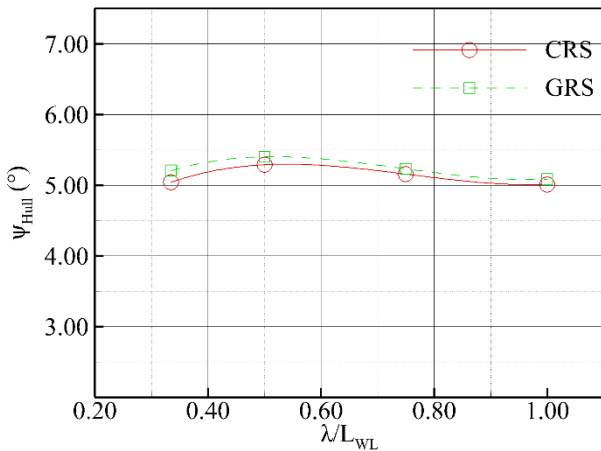


**Figure 7** Yaw angle variations of the hull ( $\Psi_{Hull}$ ) with the CRS and GRS configurations in different wave conditions tested.

In order to present the propulsion test results in waves relative to the results in calm water, the following non-dimensional coefficients are used for the ship model's performance (both with the CRS and GRS as appropriate):

$$C_1 = F / (0.5 \times \rho \times S_M \times V_M^2), \quad F = F_R + T \quad (1)$$

$$C_2 = D_R / (0.5 \times \rho \times S_M \times V_M^2) \quad (2)$$

$$\Delta C_{1,2} = [(C_{1,2,WAVES} - C_{1,2,CALM}) / C_{1,2,CALM}] \times 100 \quad (3)$$

$$\Delta K_{T,Q} = [(K_{T,Q,WAVES} - K_{T,Q,CALM}) / K_{T,Q,CALM}] \times 100 \quad (4)$$

In Eq. 1 and Eq. 2,  $F_R$  (resultant force) is measured force on towing load cell during the tests,  $T$  is propeller thrust,  $D_R$  is rudder drag,  $\rho$  is density,  $S_M$  is model wetted surface area and  $V_M$  is model speed. In Eq. 3 and Eq. 4,  $K_T$  is thrust coefficient, and  $K_Q$  is torque coefficient, whilst subscript *WAVES* and *CALM* denote the results in waves and calm water, respectively. As one can see in Figure 8, the difference in the total force measured on the hull model in waves ( $\Delta C_1$ ) is almost similar with both rudder systems in each wave condition tested (i.e.,  $\lambda/L_{WL}=0.33, 0.50, 0.75, 1.00$ ). However, the relative thrust and torque variations in waves and hence the loading on the propeller with the GRS are relatively lower, as shown in Figure 9 and Figure 10, for the relative thrust and torque, respectively.

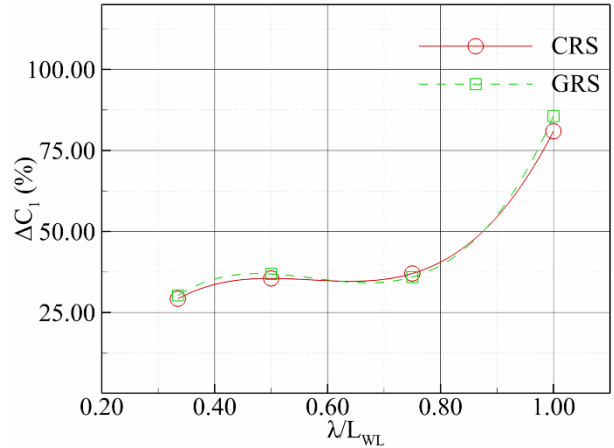


**Figure 8** The force coefficient difference (self-propulsion tests in waves) of CRS and GRS.

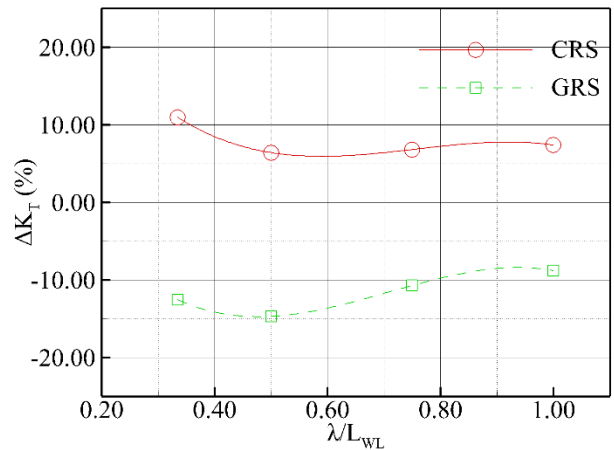


**Figure 9** The thrust coefficient difference (self-propulsion in waves) of CRS and GRS.

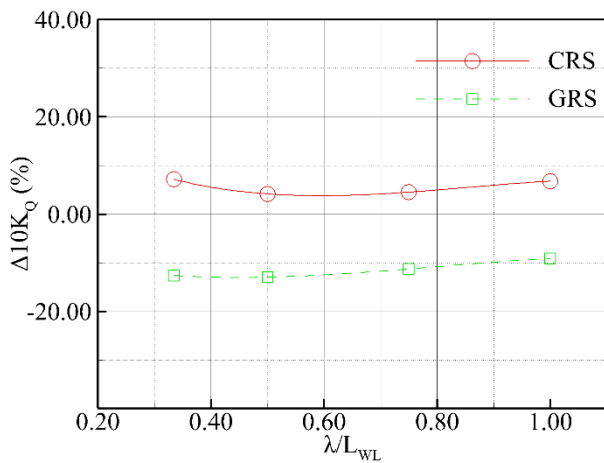


**Figure 10** The torque coefficient difference (self-propulsion and seakeeping tests) of CRS and GRS.

The most prominent finding from the propulsion tests in waves at a yaw angle has been the significant decrease in the power requirement with the GRS compared to the CRS. Furthermore, decreasing loading of the propeller with the GRS arrangement can be associated with the differences in the increasing drag on each rudder system, as shown in Figure 11, where the rudder drag increase of the CRS and GRS in waves were compared with reference to their calm water drag values. As one can see, in the wave conditions tested, the rudder drag increase in the CRS is almost five times compared to its calm water drag values, whilst the increase in the drag of the GRS in waves is virtually negligible.

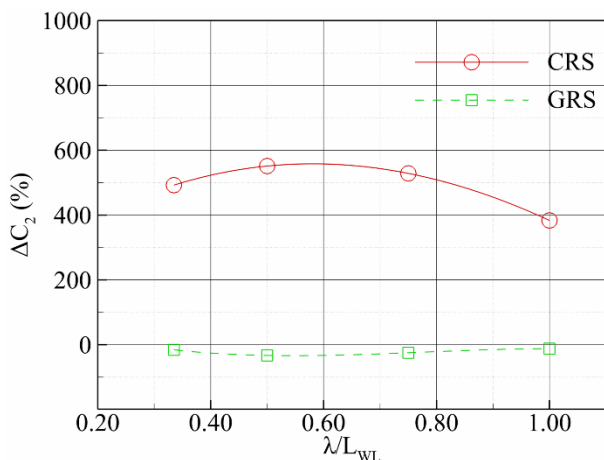


**Figure 11** The rudder force coefficient difference (self-propulsion and seakeeping tests) of CRS and GRS.

## 5 CONCLUDING REMARKS

As part of the experimental activities of the GATERS Project, this study presented the powering performance prediction and analysis of the project target vessel through model tests in calm water and waves. The resistance, propulsion and seakeeping (at a yaw angle) tests were conducted with a model made to a 1/21.7 scale (3.9m LPP) of the target vessel (M/V ERGE) at the University of Strathclyde's Kelvin Hydrodynamics Laboratory towing tank. The resistance and propulsion tests in calm water were conducted to establish accurate performance prediction methodologies for the powering performance of a ship

retrofitted with a GRS using traditional model test techniques. In addition, the seakeeping tests were conducted in waves to investigate the comparative powering performance of the ship with the CRS and GRS to simulate the in-service conditions.

The calm water resistance tests of M/V ERGE were first conducted with her bare hull, and then the hull was appended with the CRS and GRS configurations. The comparative resistance tests of the hull displayed up to a 4% reduction in the hull resistance with the GRS configuration over the CRS one.

The self-propulsion tests in calm water were also conducted for the model with the CRS and GRS configurations for the corresponding full-scale speeds of 10, 11 and 13-knots; while the CRS rudder was kept amidship, and the GRS rudder angles were set at 0°. The comparison of the delivered power requirements measured for these conditions showed a 22% benefit for the GRS configuration.

The seakeeping tests were conducted to assess the effect of waves on the comparative powering performance of M/V ERGE with the CRS and GRS. These tests were conducted in regular waves in the towing tank with the ship model fixed at a small yaw angle to simulate the oblique wave condition and with a significant wave height of 1.25m in full-scale (corresponding to Beaufort 4) for a range of different wavelengths. The rudder angles of both rudder systems were preset at the appropriate values to produce a mean hull yaw angle of 5° to avoid high yaw angles that could damage the load cell.

The comparison of the powering performance of the hull with the CRS and GRS indicated that the thrust and torque increase in waves for the model with the GRS was 20% less than those with the CRS. However, the additional resistance and ship motions in waves were comparable for the model with both rudder configurations. This was primarily due to the increase in the CRS' drag for almost five folds of the drag in calm water when maintaining a 5° yaw angle. For the equivalent condition, GRS has provided more thrust than calm water conditions. This combined effect has resulted in power savings of up to 20%.

## ACKNOWLEDGEMENTS

This paper is based on the activities conducted in the collaborative European project GATERS which is an Innovation Action Project funded by the EC H2020 Programme (ID: 860337) with the independent aim and objectives. The project has an official sub-license agreement with Wartsila Netherlands BV to utilise the Gate Rudder Patent (EP 3103715) at specific retrofit projects of vessel sizes below 15000 DWT.

## REFERENCES

The EC-H2020 Project "GATERS": GATE Rudder System as a Retrofit for the Next Generation Propulsion and Steering of Ships, Project ID 860337, (2021).

- ITTC. (2011a). Recommended Procedures and Guidelines, Resistance Test (7.5-02-02-01), Revision 3.
- ITTC. (2011b). Propulsion/Bollard Pull Test (7.5-02-03-01-01.1), Revision 4.
- ITTC. (2011c). 1978 ITTC Performance Prediction (7.5-02-03-01.4) Revision 2.
- ITTC. (2017). Ship Models. (7.5-01-01-01), Revision 4.

## Greener shipping: An investigation of an ORC-based waste heat recovery system for a methanol-fueled marine engine

Mehmet Akman<sup>1</sup>, Selma Ergin<sup>2\*</sup>

<sup>1</sup>Muğla Sıtkı Koçman University, Department of Motor Vehicles and Transportation Technologies, 48420 Bodrum-Muğla, Turkey

<sup>2</sup>Istanbul Technical University, Faculty of Naval Architecture and Ocean Engineering, 34469 Maslak-Istanbul, Turkey

**Abstract:** Energy-efficient and low-carbon transportation have recently been the major concerns for the maritime industry. Design improvements are being performed, innovative technologies and various fuels are being used and operational measures are being taken onboard ships to fulfil the IMO requirements and for greener shipping. One of the challenging technologies to increase energy efficiency and fuel economy is the organic Rankine cycle (ORC) waste heat recovery system (WHRS). In this study, an exhaust gas waste heat-driven regenerative ORC system for a methanol-fueled marine dual-fuel engine is analyzed and the thermal performance of the system is investigated. Thermodynamic and environmental impact analysis of the ORC is conducted to estimate the numerical effect of the ORC on the integrated power generation system (PGS). Low global warming and zero ozone depletion potential working fluids are used in the ORC WHRS. According to the results, the ORC WHRS can increase the thermal efficiency of the PGS by more than 3% leading to a remarkable decrease in carbon emissions.

**Keywords:** ORC, waste heat recovery, energy efficiency, methanol, dual-fuel

### 1 INTRODUCTION

The volumetric growth of maritime transportation over the years brings with it some environmental problems. The share of maritime shipping in total global emissions is 2.89% by 2018, and the number increased by 9.6% compared to its 2012 level (IMO, 2021). Therefore, strict measures have been put into effect by International Maritime Organization (IMO) to reduce and phase out gradually the GHG emissions sourced by international shipping. The Fourth IMO GHG Study underlines a strategy and determines the levels of emission reduction by baselining 2008 year; reduce CO<sub>2</sub> emissions by at least 40% as of 2030 and reduce the total GHG emissions by at least 50% as of 2050 (IMO, 2021). In addition, together with Energy Efficiency Design Index (EEDI), and Ship Energy Efficiency Management Plan (SEEMP), which were put into force in 2013 (IMO, 2011), new energy efficiency measures; Energy Efficiency Existing Ship Index (EEXI) and Carbon Intensity Indicator (CII) will come into force in 2023 (IMO, 2020). Regarding the energy efficiency and emission control agenda of IMO, the maritime industry has come a long way in energy-efficient designs, machinery systems and ship operations. On machinery systems, efforts in developing new technologies on GHG, NO<sub>x</sub> and SO<sub>x</sub> control and alternative marine fuels have accelerated. More specifically, methanol-powered dual-fuel engines have been started to be installed onboard ships since the beginning of the 2010s and the number of methanol-powered ships is increasing (Yilin, 2020). Compared to other available marine fuels, methanol has many advantages such as meeting sulphur requirements, low carbon emission, low price, availability worldwide, producibility from biomass and compact size

and low storage and delivery pressures onboard ships (Brynolf et al., 2014; MAN, 2014).

The majority of ships are still powered by diesel engines and after the combustion process about half of the fuel energy is dissipated by cooling and exhaust gas (Singh & Pedersen, 2016). Considering the energy flow in a marine diesel engine, about 25% of total fuel energy is converted to exhaust gas heat and the shares of scavenge air, jacket water and lubrication oil are about 14%, 6% and 4%, respectively (MAN, 2014). Organic Rankine Cycle (ORC), on the other hand, is a challenging technology for low and medium-grade waste heat recovery and seems a “powerful” option for ships to fulfil the requirements of IMO and green shipping. To reveal the impacts of ORC WHR systems onboard ships many studies have been conducted. On working fluid selection, Larsen et al. (2013) developed a methodology for using the optimum working fluids for ORC WHRS and they revealed that hydrocarbon-type fluids have better thermodynamic performance compared to wet and isentropic fluids. Zhu et al. (2018) analyzed the thermo-economic performance of various working fluids and optimized the evaporation and condensation temperatures. According to their results, R141b shows the best thermo-economic performance. Authors of this study, Akman and Ergin (2019; 2021) analyzed the thermodynamic and environmental performances of different ORC WHR configurations using jacket cooling water, scavenge air and exhaust gas under various operating conditions. According to their results, the exhaust gas ORC WHR system can increase the thermal efficiency of the power generation system (PGS) by more than 2%. Andreasen et al. (2017) investigated the thermodynamic performances of organic and steam

\* Corresponding author e-mail: [ergin@itu.edu.tr](mailto:ergin@itu.edu.tr)

Rankine cycles for WHR from a marine diesel engine and they underlined that the organic Rankine cycle generates more power at light loads compared to that of the steam Rankine cycle. Fang et al. (2019) analyzed the thermo-economic performances of natural hydrocarbon and hydrofluorocarbon-type working fluids and their mixtures for WHR from a diesel engine. They found that the natural hydrocarbon-type working fluids with high critical temperatures show better thermo-economic performance. Akman and Ergin (2021) analyzed and optimized the thermo-environmental performance of a transcritical ORC WHRS from a marine diesel engine. They found that using the analyzed model onboard ship increases the thermal efficiency of PGS by about 2.5% and saves up about 225 tons of fuel annually.

In this study, a regenerative ORC system recovering the exhaust gas waste heat of a methanol-powered dual-fuel marine engine is parametrically analyzed. R245fa, R245ca and R365mfc are used as the working fluids and their thermodynamic and environmental performances are analyzed under different evaporation temperatures and engine loads. The thermodynamic performance and environmental impact of ORC WHRS are evaluated considering the latest regulations.

## 2 ORC WASTE HEAT RECOVERY SYSTEM

The analyzed dual-fuel engine is MAN B&W 5S50ME-C9.6, designed to be operated under Tier II and Tier III modes and can burn methanol and marine diesel oil (MDO) (MAN, 2022). MDO is used as pilot oil to prevent knocking and misfiring during gas injection mode (Babiczy, 2015). The dual-fuel engine has an exhaust gas recirculation (EGR) unit to control the NO<sub>x</sub> emission and the unit is operated under Tier III mode. Computerized Engine Application System (CEAS) software (MAN, 2022) is used for obtaining the engine properties and exhaust gas waste heat data. According to CEAS data, the exhaust gas mass flow rate ranges from 7.9 kg/s to 15.2 kg/s at 50% MCR to 100% MCR, respectively. The temperature range of exhaust gas is 484 K to 492 K. The fuel consumption and exhaust gas data under various engine loads are shown in Figure 1 and Figure 2, respectively.

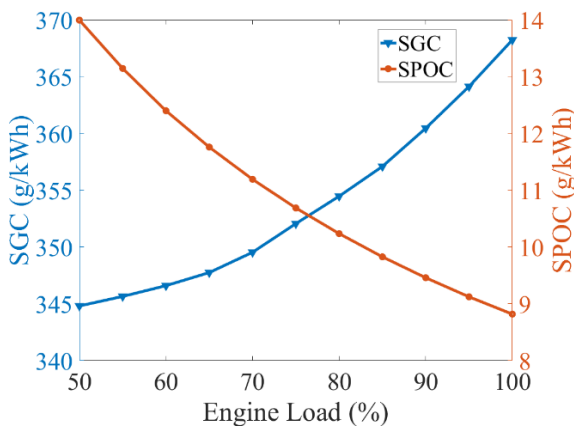


**Figure 1:** Specific Gas Consumption (SGC) and Pilot Oil Consumption (SPOC) of the main engine.

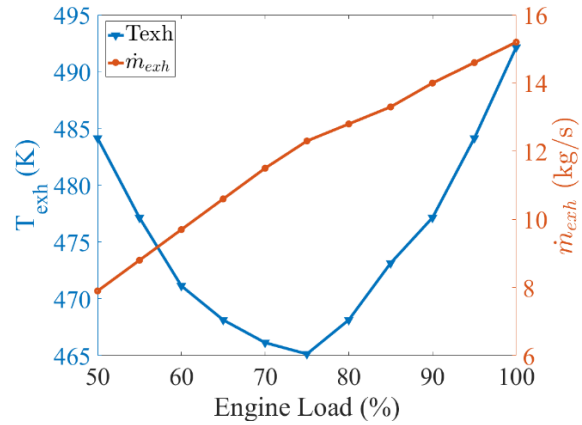


**Figure 2:** Exhaust gas mass temperature and mass flow rate with respect to engine load.

The properties of the main engine are presented in Table 1.

**Table 1:** Dual-fuel main propulsion engine properties.

Properties	Value (at full load and Tier III mode)
Engine brake power - P <sub>b</sub>	7860 kW
SGC	346.4 g/kWh
SPOC	8.40 g/kWh
Exhaust gas mass flow	15.2 kg/s
Methanol supply pressure	13 bar
Central cooler cooling	6590 kW

The ORC WHR system is operated to recover exhaust gas waste heat between 50% MCR and 100% MCR at Tier III mode. The WHR system consists of a boiler, turbine, regenerator, condenser and pump. The working fluid is preheated, evaporated and superheated in the exhaust gas boiler and delivered to the turbine to produce mechanical power which drives the alternator for electricity generation. After the turbine's expansion process, the working fluid's heat is transferred to the flow coming from the pump for regeneration. Then the fluid is sent to the condenser for saturation to be pumped back into the cycle.

During analysis, the evaporation pressure is increased from 1500 kPa to 3000 kPa for each fluid. The turbine and pump isentropic efficiencies are assumed to be 0.75 (Tempesti et al., 2014). The freshwater at 25 °C (T<sub>7</sub>) coming from the closed-loop central cooling system is used for the ORC cooling process and the condensation temperature (T<sub>1</sub>) is 40 °C. The regenerator effectiveness is 0.8 and the heat loss factor at heat exchangers is 0.95. The pressure drop at the heat exchanger is assumed to be 2%. The exhaust gas temperature after the boiler (T<sub>10</sub>) is assumed to be 100 °C. MATLAB 2016a software is used for cycle coding and the simulation process and, Refprop 9.0 (NIST, 2010) is used for integrating the thermodynamic properties into the cycle. The simulation process is run at a steady-state condition, and the results are plotted. The schematic model of the ORC WHR system and temperature–entropy diagrams are shown in Figure 3.

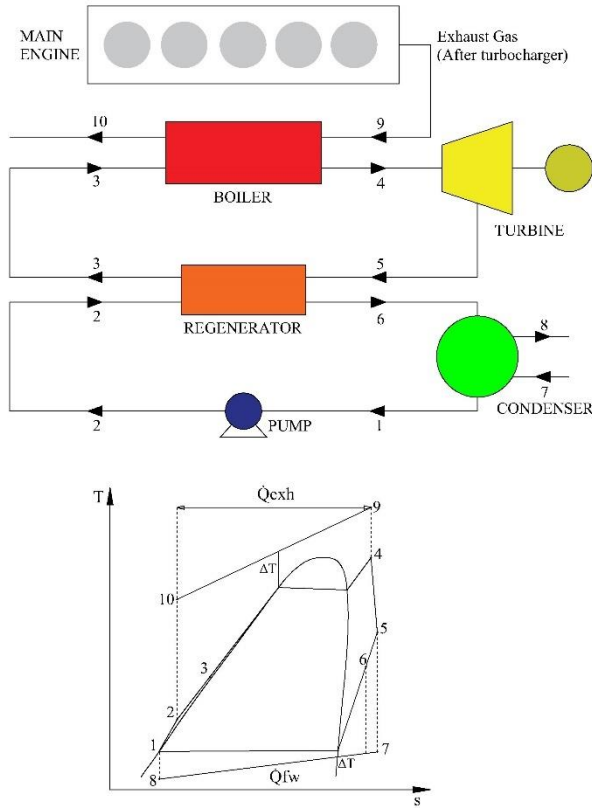


**Figure 3:** ORC WHRS and T-s diagram (below).

The selection of working fluid is an important step for an ORC WHRS. The thermodynamic properties of a working fluid directly affect the performance, system size, and cost. Moreover, as stated in MARPOL Annex VI regulation (IMO, 2013); the fluids to be used onboard ships must have zero ozone depletion potential (ODP) and according to the European Regulation; refrigerants with global warming potential (GWP) of 2500 or more have been prohibited since 1<sup>st</sup> January 2020 (JSRAE, 2015). In this study, hydrofluorocarbon (HFC) type working fluids as commonly used R245fa and rarely studied R245ca and R365mfc are selected for the ORC WHRS and the properties of the fluids are given in Table 2.

**Table 2:** The properties of selected working fluids.

Properties	R245fa	R245ca	R365mfc
N. boiling point (°C)	15.14	25.13	40.15
Critical temp. (°C)	154.01	174.42	186.85
Critical press. (kPa)	3651	3925	3266
GWP	1030	693	782
ODP	0	0	0

### 3 METHODOLOGY

The energy balance equations for the components in the ORC WHRS are given below. The minimum temperature difference for the heat exchangers is assumed to be 5 °C (Akman & Ergin, 2019).

The heat transfer from the exhaust gas boiler, regenerator and condenser can be calculated by;

$$\dot{Q}_{in} = \dot{m}_{exh} c_{p\_exh} (T_9 - T_{10}) = \dot{m}_f (h_4 - h_3) \quad (1)$$

$$\dot{Q}_{out} = \dot{m}_{fw} c_{p\_fw} (T_7 - T_8) = \dot{m}_f (h_6 - h_1) \quad (2)$$

$$\dot{Q}_{regen} = \dot{m}_f (h_5 - h_6) \epsilon = \dot{m}_f (h_3 - h_2) \quad (3)$$

where exh, fw, and f subscripts indicate exhaust gas, freshwater and working fluid, respectively. Regenerator effectiveness and enthalpy (kJ/kg) are symbolized with  $\epsilon$  and  $h$ , respectively.

The power output from the turbine ( $t$ ) is calculated by the inlet and outlet enthalpy difference of the turbine:

$$\dot{W}_t = \dot{m}_f (h_4 - h_3) \mu_t \quad (4)$$

The pump power and the net power are calculated as:

$$\dot{W}_p = \frac{\dot{m}_f (h_2 - h_1)}{\eta_p} \quad (5)$$

$$\dot{W}_{net} = \dot{W}_t - \dot{W}_p \quad (6)$$

The thermal efficiency of the ORC and ORC integrated power generation system are calculated by:

$$\eta_{th\_ORC} = \frac{\dot{W}_{net}}{Q_{in}} \quad (7)$$

$$\eta_{th\_PGS} = \frac{P_b + \dot{W}_{net}}{Q_{LCV} \dot{m}_{fuel}} \quad (8)$$

where  $P_b$  is the brake power of the main engine. The low calorific value (LCV) of methanol and MDO are 19900 kJ/kg and 42700 kJ/kg, respectively (IMO, 2016).

The recovered power ratio by ORC WHRS can be calculated by:

$$\epsilon = \frac{\dot{W}_{net}}{P_b} \quad (9)$$

Then the emission reduction ( $R$ ) by the ORC WHRS in g/kWh can be calculated by:

$$R = \epsilon \gamma_i \quad (10)$$

where  $\gamma_i$  is the emission factor used for a dual-fuel engine. Emission factors for CO<sub>2</sub> are 3.206 kg/kg for MDO and 1.375 kg/kg for methanol (Herdzik, 2021). The potential emission reduction can be converted to tonnes using corresponding brake power and operational hours. The annual operating hours of the dual-fuel engine are assumed to be 5796 hours.

### 4 RESULTS and DISCUSSION

The thermodynamic performance parameters of the working fluids are calculated under different engine loads and evaporation pressures. The net power output change concerning evaporation pressure is shown in Figure 4. According to the results, net power increases by increasing evaporation pressure until a specified value than it decreases. This is based on the specific temperature-enthalpy diagrams of the working fluids of which enthalpies generally decrease as the evaporation temperature gets closer to the critical temperature.

According to Figure 4, the calculated maximum net power outputs at 85% MCR are 185.3 kW, 211.9 kW and 230.4 kW, respectively. The corresponding evaporation

pressures of the maximum net power outputs for R245fa, R245ca and R365mfc are 2850 kPa, 3000 kPa and 2700 kPa, respectively. Results show that R365mfc has better power output compared to other working fluids.

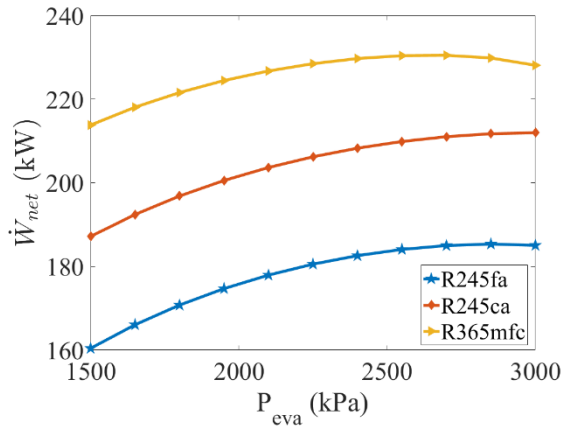


**Figure 4:** Net power output changes at different evaporation temperatures.

The change in thermal efficiency of organic Rankine cycle working fluids is shown in Figure 5. The regeneration decreases the heat loss by transferring the available heat after the expansion process and preheating the fluid before the entrance of the boiler. Therefore, the mass flow rate of the working fluid increases resulting in higher net power output and thermal efficiency. According to Figure 3, it is possible to increase the thermal efficiency of the ORC WHRS up to 17% by using R365mfc as the working fluid. Besides, R245fa, which is one of the most common working fluids used in WHRS applications, shows poor performance compared to R245ca and R365mfc.

Besides, Figure 6 shows the change in thermal efficiency of the PGS and ORC WHRS integrated power generation system at various engine loads. According to the results, the thermal efficiency of PGS at medium loads is higher compared to that at heavy loads and the calculated maximum PGS thermal efficiencies at 85% MCR are 51.61%, 51.81% 51.94% for R245fa, R245ca and R365mfc, respectively. It's worthy of note that the ORC WHR system can substantially increase the thermal efficiency of the PGS of which thermal efficiency without ORC WHR is 50.22% at 85% MCR.

The recovered power ratio is defined as the produced mechanical power by the ORC WHR system at the corresponding engine brake power. Figure 7 shows the change of recovered power ratio in terms of percentage with respect to engine load and evaporation pressure. Results show that using R265mfc as the working fluid, up to 3.4% of the mechanical power can be recovered when the engine is operated at 85% MCR. The calculated recovered power ratios of R245fa and R245ca at the same conditions are 2.7% and 3.1%, respectively. At full load, it is possible to recover about 3.9% of mechanical power using R365mfc as the working fluid.

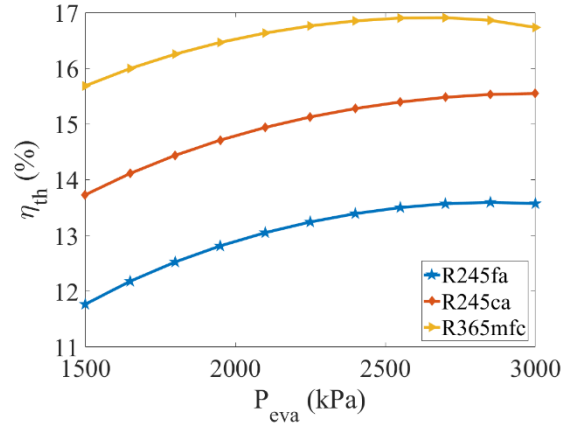


**Figure 5:** The change of ORC thermal efficiency at different evaporation pressures.

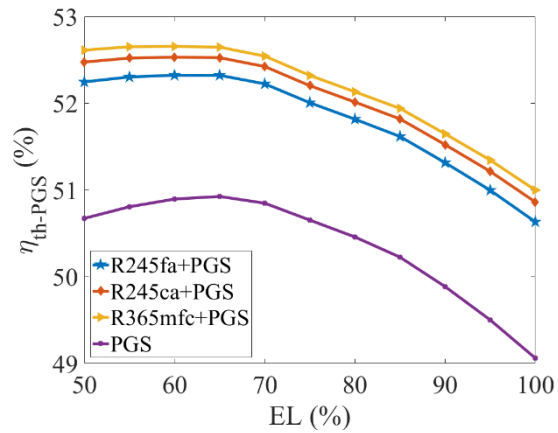


**Figure 6:** The change of PGS thermal efficiency at different engine loads.

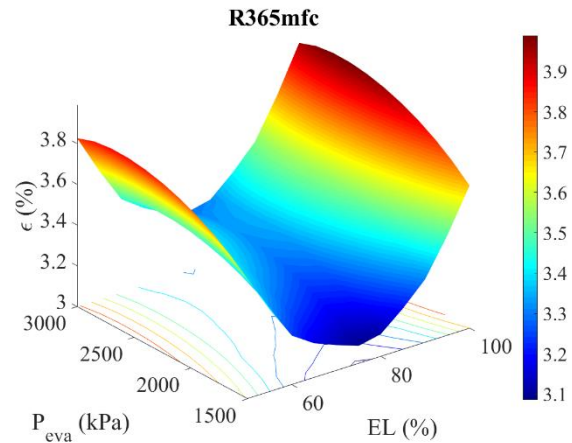


**Figure 7:** The recovered power ratio change with respect to engine load and evaporation temperature.

The recovered power by ORC WHRS has a counterpart of fuel and emission which are consumed and released by the main engine. Using this approach, the emission reduction provided by the ORC WHRS is shown in Figure 8. For gaining Proportional to the recovered power ratio, R365mfc shows the best thermo-environmental performance followed by R245ca and R245fa. The

\* Corresponding author e-mail: ergin@itu.edu.tr

calculated maximum CO<sub>2</sub> emission reductions at 85% MCR by R245fa, R245ca and R365mfc are 561.3 t/year, 641.9 t/year and 698.1 t/year, respectively. According to the results, up to 971.3 tons of fuel can be saved by R365mfc used ORC WHRS when the engine is operated under 5796 hours per year at full load.

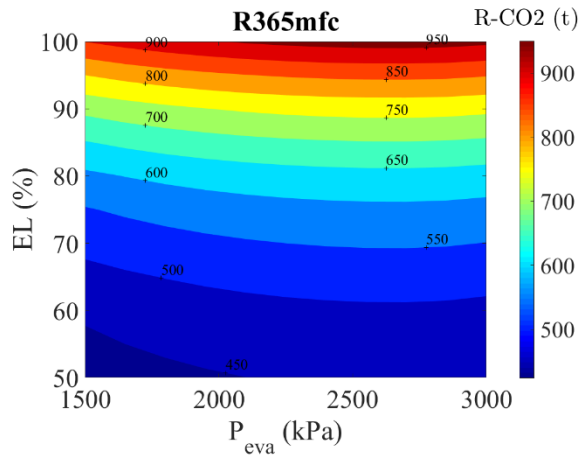


**Figure 8:** Potential amount of CO<sub>2</sub> reduction by ORC WHRS at different operating conditions.

## 5 CONCLUSIONS

The thermodynamic and environmental impact analyses of the exhaust gas-driven ORC WHRS are conducted for a methanol-fueled marine engine and the results are presented under various engine loads and evaporation pressures. According to the obtained results, the following conclusions are drawn:

- Thermodynamic study shows that it is possible to increase the thermal efficiency of the PGS about by 4%.
- The environmental impact evaluation of the onboard ORC WHRS shows that the CO<sub>2</sub> emissions can be reduced about by 4%.
- Even though the emission factor of methanol is less than half of the marine diesel oil, methanol-fueled engines have higher fuel consumption than marine diesel engines based on the methanol's low specific energy content. Therefore, to decrease the carbon footprint of methanol-fueled engines ORC integrated waste heat recovery systems can be a promising solution.
- R365mfc with zero ODP and low GWP shows an encouraging thermo-environmental performance to be used for onboard applications.

As a future study, the performance of the R365mfc mixtures will be investigated for ORC-based waste heat recovery. The waste heat potential of different marine fuels will be analyzed and the study will be expanded by including different waste sources and thermo-economic feasibility analysis.

## REFERENCES

- Akman, M., & Ergin, S. (2019). 'An investigation of marine waste heat recovery system based on organic Rankine cycle under various engine operating conditions'. *Proceedings of the Institution of Mechanical Engineers Part M: Journal of Engineering for the Maritime Environment*, 233(2), 586–601. <https://doi.org/10.1177/1475090218770947>
- Akman, M., & Ergin, S. (2021). 'Thermo-environmental analysis and performance optimisation of transcritical organic Rankine cycle system for waste heat recovery of a marine diesel engine'. *Ships and Offshore Structures*, 16(21), 1104 – 1113. <https://doi.org/10.1080/17445302.2020.1816744>
- Akman, M. & Ergin, S. (2021). 'Energy-efficient shipping: Thermo-environmental analysis of an organic Rankine cycle waste heat recovery system utilizing exhaust gas from a dual-fuel engine'. *Proceedings of TEAM 2020/21*, Dec. 6 - 8, 2021, Istanbul, Turkey
- Andreasen, J. G., Meroni, A., & Haglind, F. (2017). 'A comparison of organic and steam Rankine cycle power systems for waste heat recovery on large ships'. *Energies*, 10(4), 1–23. <https://doi.org/10.3390/en10040547>
- Babicz, J. (2015). *Wärtsilä Encyclopedia of Ship Technology*.
- Brynnolf, S., Fridell E., Andersson K. 2014. 'Environmental assessment of marine fuels: liquefied natural gas, liquefied biogas, methanol and bio-methanol'. *Journal of Cleaner Production*, vol. 74, pp. 86 – 95.
- Fang, Y., Yang, F., & Zhang, H. (2019). 'Comparative analysis and multi-objective optimization of organic Rankine cycle (ORC) using pure working fluids and their zeotropic mixtures for diesel engine waste heat recovery'. *Applied Thermal Engineering*, 157(July 2018), 113704.
- Herdzik J. (2021). 'Decarbonization of Marine Fuels—The Future of Shipping'. *Energies*, 14, 4311, 1-10.
- IMO. (2011). *Annex 19: Resolution MEPC.203(62)*. 203(July), 1–17.
- IMO. (2013). *MARPOL Annex VI*. 9(1), 76–99.
- IMO. (2016). MEPC.281(70).
- IMO. (2020). MEPC 76.
- IMO. (2021). *Fourth IMO GHG Study*.
- JSRAE. (2015). 'Risk Assessment of Mildly Flammable Refrigerants'. Progress Report. June.
- Larsen, U., Pierobon, L., Haglind, F., & Gabriellii, C. (2013). 'Design and optimisation of organic Rankine cycles for waste heat recovery in marine applications using the principles of natural selection'. *Energy*, 55, 803–812. [tps://doi.org/10.1016/j.energy.2013.03.021](https://doi.org/10.1016/j.energy.2013.03.021)

- MAN Diesel & Turbo. (2014). 'Using Methanol Fuel in the MAN B&W ME-LGI Series'.
- MAN Diesel & Turbo. (2014). 'Waste Heat Recovery System (WHRS) for Reduction of Fuel Consumption, Emissions and EEDI'.
- MAN. (2020). CEAS - Computerized Engine Application System.
- NIST. (2010). Standard reference database: reference fluid thermodynamic and transport properties-REFPROP (9.0).
- Singh, D. V., & Pedersen, E. (2016). 'A review of waste heat recovery technologies for maritime applications'. Energy Conversion and Management, 111(X), 315–328. <https://doi.org/10.1016/j.enconman.2015.12.073>
- Tempesti, D., Manfrida, G., & Madaia, L. (2014). 'Exergy and energy analysis of a dry steam power plant with a heler condenser'. International Journal of Thermodynamics, 17(1), 7–13. <https://doi.org/10.5541/ijot.403>
- Zhu, Y., Li, W., Sun, G., & Li, H. (2018). 'Thermo-economic analysis based on objective functions of an organic Rankine cycle for waste heat recovery from marine diesel engine'. Energy, 158, 343–356. <https://doi.org/10.1016/j.energy.2018.06.047>

## Low Cavitation Twisted Rudder Design for DTMB 5415 Surface Combatant

**Mustafa KÜLTÜR<sup>1\*</sup>, Serhan GÖKÇAY<sup>2</sup>, Ahmet Ziya SAYDAM<sup>2,3</sup>, Mustafa İNSEL<sup>2</sup>**

<sup>1</sup> Design Project Office, Turkish Naval Forces, Pendik, Istanbul, Turkey

<sup>2</sup> Hidroteknik Nautical Design Technologies Ltd., Turkey

<sup>3</sup> Piri Reis University, Turkey

**Abstract:** In this study, rudder improvement of the open source DTMB 5415 1/24.8 scale model hull was performed. CFD analyses of steady-state resistance, transient self-propulsion and cavitation tunnel test cases of the model were performed with RANS method at Froude Number 0.44. Effective propeller wake field downstream was applied to the existing rudder of the hull with steady-state CFD analysis. Massive sheet cavitation was detected on the inner surface of the NACA 0024 rudder geometry. Then, NACA 0024 rudder geometry was converted to NACA 64A024 while keeping the projected area. It was found that the cavitation decreased at certain rate compared to the first case. Then, the leading edge of the NACA 64A024 rudder geometry was twisted 6 degrees from the middle widest section of the rudder. The cavitation formed on the inner surface of the rudder was completely eliminated. The method used in the study enabled rapid calculation of rudder cavitation analyses.

**Keywords:** Resistance, Self-Propulsion, DTMB 5415, Cavitation, Twisted, Rudder.

### 1 INTRODUCTION

Ship hull form, propeller and rudder interaction is an important issue that has been studied for many years. In the past years, ship resistance and propulsion results were obtained from experiments. But experiments to determine local flow effects are time consuming and costly.

As a result of the experiment, possible areas for improvement in geometry (high cavitation, wave fallout, noise, etc.) can be detected. In this case, the geometry may need to be improved or optimized. This is a negative situation in terms of time and cost.

When the studies carried out in recent years are examined, it is observed that the results obtained from finite volume analyses for ship propulsion and resistance with the developing technology are very close to the experimental results.

In calculations with finite volumes, physical disadvantages in geometry can be detected prior to experiments.

With shape optimization or improvements applied with CAD on geometry, the final geometry shall lead to better results in experiments.

ANSYS CFX RANS CFD code was used in the study. The bare hull form of the DTMB 5415 at Froude number of 0.44 was analyzed for resistance with free surface modelling. Bare hull CFD resistance results were compared with towing tank test results of INSEAN 2340 (Olivieri A. Et al 2001). The CFD resistance results were consistent with the experimental results.

Appendage geometries (Kim D. Et al 2014) were added to hull form. Appendage resistance calculations were performed with CFD.

Open water performance calculations of the propeller model number 4058 (designed by MARIN Holland) for DTMB 5415 were analyzed with CFD. CFD results were consistent with the experimental results.

CFD calculations of resistance and open water propeller performance were performed in steady-state condition.

Self-propulsion analysis was also conducted with CFD. The ship's self-propulsion point has been identified. Self-propulsion and cavitation cases CFD calculations were conducted transient condition In order to better account for the interaction between hull, appendages and propeller.

In the self-propulsion calculations, the propeller advance coefficient (J) and wake coefficient (w) values were calculated. Then, the propeller revolution speed on the scale of the ship was calculated using the ITTC 78 method. The number of revolutions of the propeller in the cavitation tunnel was increased without changing the advance coefficient (J).

Hull form and propeller downstream line effective wake field were calculated in CFD tunnel calculations.

(Park I. et al 2021) used 11 million cells for an appended hull form in CFD cavitation analysis. They performed cavitation detection on the rudder behind the propeller in their study. The analyses were repeated for each angle of incidence of the rudder blades.

(Kultur M. 2022) calculated the downstream line effective wake field of the selected low cavitation propeller with transient CFD analysis in his PhD thesis study. Then, with this wake field, the cavitation behavior of different types of rudder geometries were calculated with steady-state CFD analyses. With this method, the total number of cells decreases up to 1-2 million. Therefore, the cavitation behavior of different types of rudder geometries at different angles can be calculated rapidly with CFD.

In this study, downstream line wake field was applied to the 4 digit 0024 NACA profile rudder geometry of the hull with same method.

Large sheet cavitation was seen on the inner surface of the existing rudder. 6 digit NACA 64A024 profiles were used instead of 4 digit NACA 0024 without changing the rudder projected area. It was seen that the cavitation decreased by about 50% compared to the initial state. Then the 6 digit NACA 64A024 rudder blade geometry was twisted 6

\* Corresponding author e-mail: mustafa.kultur@alumni.pru.edu.tr

degrees from the mid span. The same wake field was applied to the twisted rudder. It was found that the cavitation completely disappeared.

In addition, it was found that the open water performances of twisted rudder with a cross section of 6 digit NACA 64A024 and the rudder with a cross section of 4 digit NACA 0024 were similar in terms of  $C_L/C_D$ .

## 2 COMPUTATIONAL METHODS

The flow field has been modelled by the steady Reynolds-averaged Navier-Stokes equations for bare/appended hull and open water propeller performance and rudder cavitation; unsteady for the appended self-propulsion and cavitation tunnel CFD analysis. All numerical simulations reported in this study have been calculated with ANSYS CFX finite volume method RANS equation solver. The tetrahedral unstructured mesh was used in the control volume where the boundary conditions were determined. The fluid flow is assumed as 3-D, incompressible, transient and fully turbulent. Standard k-ε turbulence model has been adopted for the free surface computations. SST k-ω turbulence model was used in appendage resistance, open water propeller performance, self-propulsion and cavitation calculations. Y+ value was between 30-300 in the analyses. The free surface effects calculated in CFD simulations were performed using the Volume of fluid (VOF) method. The VOF method developed by (Hirt & Nichols 1981) is a fixed mesh technique designed for two or more fluids. Cavitation analyses were solved by using the simplified Rayleigh-Plesset bubble equation based Zwart cavitation model added to the two-phase flow VOF (Volume of Fluid) method. The fully coupled ANSYS CFX RANS flow solver has been used to solve the Navier-Stokes equations by an iterative method. ANSYS CFX has the ability to solve resistance, self-propulsion and cavitation calculations rapidly with its coupled solver feature.

### 2.1. Viscous Flow Governing Equations

In Ansys CFX, 3-D, constant incompressible viscous turbulent flow equations are the continuity equation involving the conservation of mass and the RANS equations used for momentum transport. These equations are given below:

$$\frac{\partial u_i}{\partial x_i} = 0 \quad (1)$$

$$u_j \frac{\partial u_i}{\partial x_j} = \frac{\partial}{\partial x_j} \left[ \vartheta \left( \frac{\partial u_i}{\partial x_j} + \frac{\partial u_j}{\partial x_i} \right) \right] + \frac{\partial}{\partial x_j} \left( -\overline{u'_i u'_j} \right) - \frac{1}{\rho} \frac{\partial p}{\partial x_i} \quad (2)$$

Where,

$$-\overline{u'_i u'_j} = \nu_t \left( \frac{\partial u_i}{\partial x_j} + \frac{\partial u_j}{\partial x_i} \right) - \frac{2}{3} k \delta_{ij} \quad (3)$$

### 2.2. Raylight Plesset Based Zwart Cavitation Model

Rayleigh-Plesset Zwart cavitation model was used for CFD cavitation analysis. In the cavitation model, the velocities of the vapor and liquid phases were considered the same. The mass transfer took place in the fluid and vapor phases. When the ambient pressure in the fluid drops below the vapor pressure, mass transfer from liquid to vapor occurs (Schnerr & Sauer 2001).

$$R_B = \frac{D^2 R_B}{Dt^2} + \frac{3}{2} \left( \frac{DR_B}{Dt} \right)^2 = \left( \frac{p_B - p}{\rho_l} \right) - \frac{4V_l DR_B}{R_B Dt} - \frac{2\gamma}{\rho_l R_B} \quad (4)$$

Where,  $R_B$  is the diameter of the bubble,  $\rho_l$  is the fluid density,  $\rho_B$  is the vapor density,  $\gamma$  is the surface tension of the fluid.  $p_B$  is the bubble surface pressure,  $p$  is the local pressure in the far region of the fluid. Since the bubble surface pressure and local pressure difference will be too large, the  $p_B - p$  difference is negligible. In this case, the Rayleigh Plesset equation becomes as follows (Li 2012):

$$\frac{DR_B}{Dt} = \sqrt{\frac{2}{3} \frac{p_B - p}{\rho_l}} \quad (5)$$

$$S_e = F_{vap} \frac{3\alpha_{nuc}(1-\alpha)p_v}{R_B} \sqrt{\frac{2}{3} \frac{p_v - p}{\rho_l}}, p_v \geq p \quad (6)$$

$$S_c = F_{cond} \frac{3\alpha p_v}{R_B} \sqrt{\frac{2}{3} \frac{p - p_v}{\rho_l}}, p_v \leq p \quad (7)$$

Where,  $S_e$  is the beginning of the mass transfer before the cavitation bubble burst,  $S_c$  is the end of the mass transfer after the cavitation bubble burst,  $R_B$  is the diameter of the bubble which was taken as  $10^{-6}$  m,  $\alpha_{nuc}$  is the core volume ratio which was taken as  $5 \times 10^{-4}$ ,  $F_{vap}$  is the mass conversion rate direction vaporization factor which was taken as 50,  $F_{cond}$  is the mass conversion rate direction condensation factor which was taken as 0.001.

### 2.3. Timestep Selection

Since ANSYS CFX is a fully coupled implicit solver, the time step was chosen as high as possible in steady free surface resistance and open water propeller performance analyses. On the other hand, selection of timestep for transient self-propulsion analysis the number of courant number was applied between 5-100.

## 3. COMPUTATIONAL RESULTS AND DISCUSSION

The open-source naval surface combatant DTMB 5415 has been chosen for resistance, self-propulsion, and rudder cavitation analysis. Bare hull model is represented in Figure 1 and appended hull (without bilge keel) model is represented in Figure 2. Bilge keel geometry was neglected because the resistance value was low and the mesh application was difficult to the geometry.



Figure 1. DTMB 5415 Bare Hull Model  
([www.SIMMAN2008.dk](http://www.SIMMAN2008.dk))



Figure 2. DTMB 5415 Appended(wo Bilgekeel) Hull Model  
([www.SIMMAN2008.dk](http://www.SIMMAN2008.dk))

The INSEAN model scale ( $\lambda=24.824$ ) of DTMB 5415 has been used for validating CFD method with experimental data. The principal geometric data for DTMB 5415 model are given in Table 1.

Table 1. Principal Geometric Data of 5415 (SIMMAN, 2008)

Description	Ship	Model
$\lambda$ (Scale Factor)	-	24.824
$L_{BP}$ (m)	142	5.72
$L_{WL}$ (m)	142.18	5.72
$B_{WL}$ (m)	18.9	0.76
$T_M$ (m)	6.15	0.248
$S(m^2)$	2949.5	4.786
$\nabla (m^3)$	8425.4	0.549
$C_B$	0.506	0.507
$C_M$	0.825	0.821
$F_n$	0.44	0.44

### 3.1 Sensitivity For Resistance Analysis

According to the ITTC 7.5-03-01-01 standard document a convergence study was carried out with different mesh sizes. The result of the analysis with a fine number of mesh is  $S_{k1}$ , the result of the analysis with a medium number of mesh is  $S_{k2}$ , and the result of the analysis with a coarse number of mesh is  $S_{k3}$ , the differences between the analysis are as follows. Analysis from coarse to fine, mesh sizes have been reduced by  $\sqrt{2}$ .

$$\epsilon_{k10} = S_{k1} - S_{k0} \quad (8)$$

$$\epsilon_{k21} = S_{k2} - S_{k1} \quad (9)$$

$$\epsilon_{k32} = S_{k3} - S_{k2} \quad (10)$$

The convergence rate is expressed as:

$$R_k = \epsilon_{k2} / \epsilon_{k32} \quad (11)$$

According to this definition, three different convergence states can be formed:

Monotonous Converge :  $0 < R_k < 1$

Oscillation :  $R_k < 0$

Diverge :  $R_k > 0$

Sensitivity analysis was performed at  $Fr=0.44$  for bare and appended hull analysis.  $R_k$  was 0.34 for bare hull and 0.35 for appendage resistance sensitivity analysis.

Table 2. Bare Hull Sensitivity Analysis Results

No	Fr	Mesh Relevance	Mesh Size(mm)	Rt (N)
3	0.44	Coarse	45	221
2	0.44	Medium	32	205.3
1	0.44	Fine	22	200
0	0.44	Very Fine	16	197.4

Table 3. Appendage Sensitivity Analysis Results

No	Fr	Mesh Relevance	Mesh Size(mm)	Rt (N)
3	0.44	Coarse	7	27
2	0.44	Medium	5	25
1	0.44	Fine	4	24.3
0	0.44	Very Fine	3	23.98

As a result of sensitivity analyses, both very fine mesh sizes were used for bare hull and appendage geometries.

### 3.2. Resistance Analysis

Bare and appended model CFD resistance validation study was performed at  $Fr=0.44$  ( $V_{model} = 3,297$  m/sec) according to ITTC 7.5-03-02-03 procedure. Owing to the symmetry condition, a half-model was used in analysis. Bare hull cfd analysis was performed with VOF method with 2 degrees of freedom moving mesh feature (sinkage + trim). Appendage CFD resistance analyses were performed using only underwater area of hull geometry. The moving mesh feature was turned off in appendage resistance analyses. Bare and appended hull resistance analysis control domain sizes are shown in Figure 3 and 4 respectively.

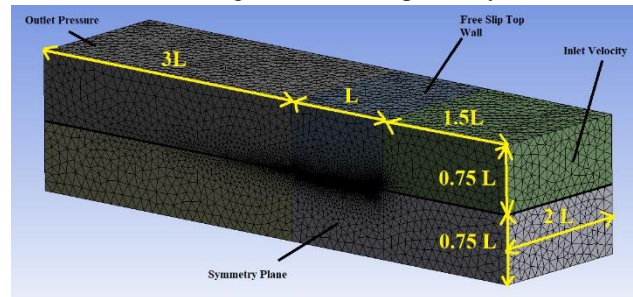


Figure 3. DTMB 5415 Bare Hull Resistance Analysis Control Domain

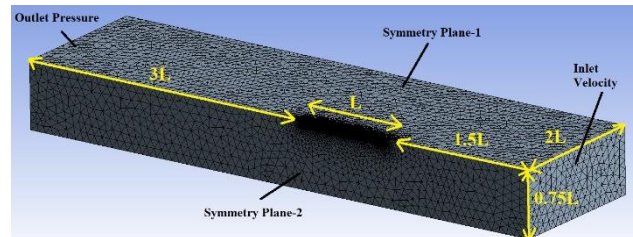


Figure 4. DTMB 5415 Appended Wetted Area Resistance Analysis Control Domain

Approximately 1.4 million cells were used in the half bare hull resistance analysis and 1.8 million meshes were used in appended wetted hull model resistance analyses. Mesh details of bare hull and appended hull are shown in Figure 5 and Figure 6 respectively.

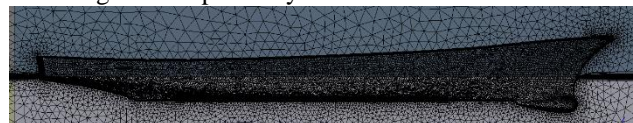


Figure 5. Bare Hull Mesh Detail for Resistance Analysis

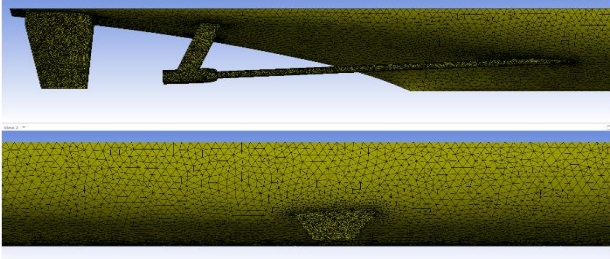


Figure 6. Appended Hull Mesh Detail for Appendage Resistance Analysis

k-ε turbulence model was used for resistance analysis. The Y+ value was applied between 30-100 for CFD validation analysis. The difference between the bare hull model CFD analysis results and the experimental results were less than 1%. The coefficients used in the calculations are presented below.

$$C_T = C_F + C_P \quad (12)$$

$$C_F = \frac{0.075}{\log_{10}(Re-2)^2} \text{ (ITTC 1957 Friction Res. Coeff.)} \quad (13)$$

$$C_P = C_W + C_V \text{ (Residual Resistance Coefficient)}$$

$$C_W = \text{Wave Making Resistance Coefficient}$$

$$C_V = \text{Viscous Pressure Coefficient}$$

$$R_T = \frac{1}{2} \rho x v^2 x S x c_{Tm} \text{ (Total Resistance)} \quad (14)$$

$$R_f = \frac{1}{2} \rho x v^2 x S x c_{Fm} \quad (15)$$

$$R_P = R_T - R_f \quad (16)$$

While the viscous pressure resistance is calculated, friction resistance ( $R_f$ ) is subtracted from the dynamic wetted area resistance of the model. Then viscous pressure force is subtracted from residual resistance. In this case pure wave resistance is calculated. Comparison of the Experiment and CFD Analysis is presented in Table 4.

Table 4. Bare and Appended Hull Experimental and CFD Results (Fr=0,44-V<sub>model</sub>=3.297 m/sec)

Description	R <sub>f</sub> (N)	R <sub>v</sub> (N)	R <sub>w</sub> (N)	R <sub>T-CFD</sub> (N)	R <sub>T-Exp</sub> (N)	Dif (%)
Bare Hull	54.27	42.586	100.546	197.4	197.23	0.1
Appendages				23.98	-	-

Free surface wave deformation of the model for Fr=0.44 is shown in Figure 7.

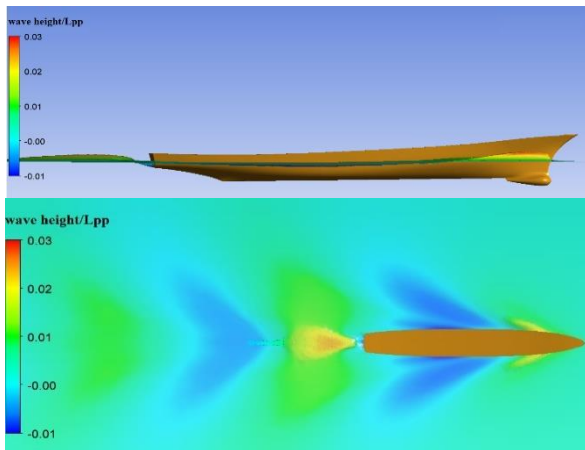


Figure 7. Bare Hull Wave Deformation at Fr=0.44

### 3.3. Open Water Propeller Performance

Prop No. 4058 (designed by Marin Holland), was used in the open water performance and self-propulsion calculations. Geometric data of the 4058 propeller is presented in Table 5. 3D model of the 4058 propeller model is shown in Figure 8.

Table 5. Main Particulars of DTMB 4058 Model Propeller

Description	Value
λ(Scale Factor)	1/24.824
D (m)	0.262
P/D (at 0.7 R)	0.87
Z	5
A <sub>E</sub> /A <sub>0</sub>	0.58

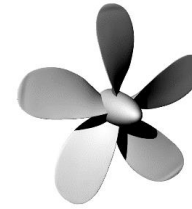


Figure 8. DTMB 4058 Model Propeller

The dimensionless coefficients used in propeller open water performance calculations are presented below.

*Propeller Advance Coefficient*

$$J = \frac{V_a}{nxD} \quad (17)$$

J : Advance Coefficient

V<sub>a</sub> : Propeller Advance Velocity (m/s)

n : Propeller Revolution Speed (1/s)

D : Propeller Diameter (m)

*Propeller Thrust Coefficient*

$$K_T = \frac{T}{\rho x n^2 x D^4} \quad (18)$$

K<sub>T</sub> : Thrust Coefficient

T : Propeller Blade Thrust Force

ρ : Water Density (kg/m<sup>3</sup>)

n : Propeller Revolution Speed (1/s)

D : Propeller Diameter (m)

*Propeller Torque Coefficient*

$$K_Q = \frac{Q}{\rho x n^2 x D^5} \quad (19)$$

K<sub>Q</sub> : Torque Coefficient

Q : Propeller Blade Torque Moment (Nm)

ρ : Water Density (kg/m<sup>3</sup>)

n : Propeller Revolution Speed (1/s)

D : Propeller Diameter (m)

Propeller Open Water Efficiency

$$\eta_o = \frac{K_T}{K_Q} \chi \frac{J}{2\pi} \quad (20)$$

- $\eta_o$  : Propeller Open Water Efficiency
- $K_T$  : Thrust Coefficient
- $K_Q$  : Torque Coefficient
- $J$  : Advance Coefficient

In open water analysis, the propeller rotation speed (rps) was determined according to the dimensionless Kempf's Reynolds number. Kempf's Reynolds Number is calculated as follows:

$$Re_{0.7} = \frac{c_{0.7} \sqrt{V_A^2 + (0.7\pi nD)^2}}{\nu} \quad (21)$$

- $C_{0.7}$  : Chord Length at 0.7R (m)
- $V_A$  : Advance Velocity (m)
- $n$  : Propeller Revolution Speed (rps)
- $\nu$  : Kinematic Viscosity (m<sup>2</sup>/s)

ITTC Procedure No. 7.5-02-03-02.1 recommended that Kempf's Reynolds number value should be above 200,000. In this study, the propeller rotation speed was taken as n=16 rps for the open water performance analysis. The Kempf Reynolds Number was calculated around 514000.

Two solution domains have been prepared for the analysis. First one was "rotor" domain volume which was located inside and was movable. The propeller was located inside the rotor domain. Second one was "stator" domain volume, which was the external domain with boundary conditions. Rotor and stator domains were in contact with each other by an "interface" surface. The rotor propeller was rotated within the boundary of the interface surface. SST k- $\omega$  turbulence model was used for resistance analysis. The Y+ value was applied between 30-300 for CFD validation analysis.

Open water analysis control domain sizes are shown in Figure 9.

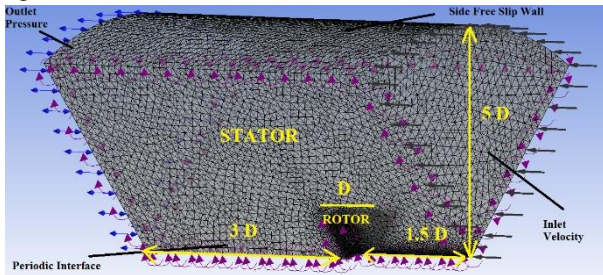


Figure 9. 4058 Propeller Open Water Analysis Control Domain

Propeller mesh size in open water calculations was determined by comparing the experimental performance at J=0.6. In the experimental study for J=0.6, K<sub>T</sub> was measured as 0.177, 10\*K<sub>Q</sub> was measured as 0.272 and  $\eta$  was calculated as 0.621. CFD analyses were performed periodically with a single blade model. 0.5 mm mesh size was used in the propeller blade which gave the closest

results with the experiments. Total number of cells was approximately 2.2 million. Mesh size CFD validation study is presented in Table 6.

Table 6. Open Water Sensitivity Analysis Results, J=0.6

Mesh (mm)	J	K <sub>T</sub> -CFD	10xK <sub>Q</sub> -CFD	$\eta$ -CFD	K <sub>T</sub> -%dif.	10xK <sub>Q</sub> -%dif	$\eta$ -%dif
1.44	0.6	0.175	0.290	0.576	1.304	-6.453	7.287
1	0.6	0.178	0.289	0.589	-0.821	-6.218	5.081
0.7	0.6	0.174	0.279	0.597	1.530	-2.396	3.834
<b>0.5</b>	<b>0.6</b>	<b>0.173</b>	<b>0.273</b>	<b>0.606</b>	<b>2.118</b>	<b>-0.374</b>	<b>2.483</b>

CFD-experimental comparison of propeller open water curves is shown in Figure 10. CFD showed close results with the experimental results.

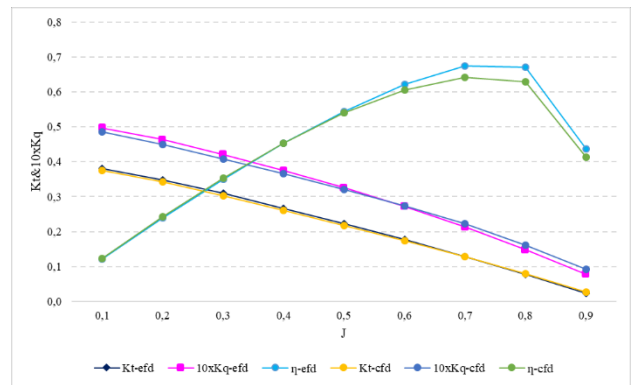


Figure 10. Thrust, Torque and Efficiency Coefficients Comparison of DTMB 4058 Propeller.

3.4. Self-Propulsion Analysis

Appended model CFD self-propulsion analysis was performed at Fr=0.44 ( $V_{model} = 3,297$  m/sec) according to ITTC 7.5-02-03-01.1, 7.5-02-03-01.4, 7.5-03-03-01 and the procedures. In self-propulsion calculations, propeller thrust and the appended model resistance under the influence of SFC are synchronized with each other. So following equation specified in ITTC 7.5-02-03-01.1 procedure is used in self-propulsion tests.

$$T_{sp} = R_{sp} - SFC \quad [22]$$

$T_{sp}$  : Self Propulsion Propeller Thrust (N)

$R_{sp}$  : Appended Hull Resistance in Self Propulsion (N)

SFC : Skin Friction Correction Resistance (N)

$$SFC = \frac{1}{2} \cdot \rho \cdot v_m^2 \cdot S \cdot (C_{FM} - (C_{FS} + \Delta C_F + C_A)) \quad [23]$$

$\rho$  : Water Density (kg/m<sup>3</sup>)

$S$  : Appended Hull Wetted Area (m<sup>2</sup>)

$C_{FS}$  : Friction Resistance Coefficient (Ship Scale)

$$C_{FM} = \frac{0.075}{\log_{10}(Re_m - 2)^2} \quad [24]$$

$C_{FM}$  : Friction Resistance Coefficient (Model Scale)

$Re_m$  : Model's Reynolds Number

$$C_{fs} = \frac{0.075}{\log_{10}(Re_s - 2)^2} \quad [25]$$

- $C_{FS}$ : Friction Resistance Coefficient (Ship Scale)  
 $Re_s$ : Ship Scale Reynolds Number  
 $\Delta C_f = 0.044 \left[ \left( \frac{k_s}{L_{WL}} \right)^{\frac{1}{3}} - 10 \cdot Re_s^{-\frac{1}{3}} \right] + 0.000125$  [26]  
 $\Delta C_f$  : Roughness Allowance  
 $L_{wl}$  : Ship Scale Water Line Length  
 $k_s$  : Roughness of Hull Surface ( $150 \times 10^{-6}$  m)  
 $Re_s$ : Ship Scale Reynolds Number  
 $C_A = (5.65 - 0.6 \log Re_s) * 10^{-3}$  [27]  
 $C_A$  : Correlation Allowance  
 $Re_s$ : Ship Scale Reynolds Number

Due to the symmetry condition, half-model was used in analysis. Appended hull self-propulsion CFD analysis have been performed using only underwater area of hull geometry. For the mesh sizes used in the self-propulsion calculations, the resistance and open water propeller performance calculations very fine mesh sizes were selected. Sst k- $\omega$  turbulence model was used for resistance analysis. The  $Y^+$  value was applied between 30-100 for CFD analysis. The total number of cells used in the calculations was about 12 million for propeller and appended hull models. Mesh details of self-propulsion model is shown in Figure 11.

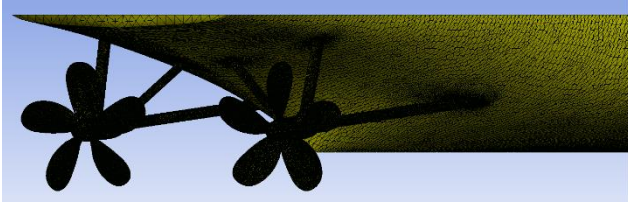


Figure 11. Appended Hull Mesh Detail for Resistance Analysis

The analysis was initiated as steady-state. Then it was continued as transient. Because there was an interaction between the model hull form appendages and propeller. When calculating the  $R_{sp}$  in the analyses, the model was submerged as much as the sinkage result in the free surface water resistance CFD calculations. Then the residual wave resistance of the model, rudder and fin resistances were later added to the self-propelled calculations. Self-propulsion point was calculated as 16.54 rps.

Propeller suction zone wake field is presented in Figure 12.

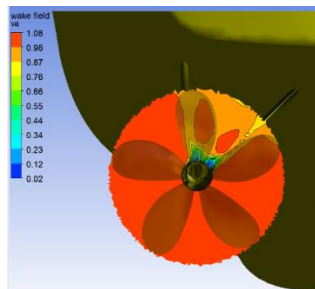


Figure 12. Velocity Distribution of the Propeller Suction Zone as a Result of the Self-Propulsion Calculations

The average speed value of the propeller suction zone was calculated as  $V_a=3.31$  m/s from the CFD results. As a result of the self-propulsion calculations, dimensionless Thrust Deduction ( $t$ ) and Wake Fraction ( $w$ ) coefficients were calculated as follows.

$$t = \frac{T-R}{T} \quad [28]$$

- $t$  : Thrust Deduction Factor.  
 $T$  : Propeller Thrust Force in Self-Propulsion (N)  
 $R$  : Appended Hull Resistance Force in Towing Tank Resistance Tests (N)

$$w = \frac{V_s - V_a}{V_s} \quad [29]$$

- $w$  : Wake Fraction Coefficient  
 $V_s$  : Model Velocity (m/s)  
 $V_a$  : Average Velocity of Propeller diameter suction zone in self-propulsion.

According to the ITTC reference document No. 7.5-02-03-01.4,  $w_m=w_s$  for twin screw ships and propeller revolution speed for ship scale is calculated by the following formula.

$$n_s = \frac{(1-w_s) \cdot V_s}{J_{TS} \cdot D_s} \quad [30]$$

- $w_s$  : Ship Scale Wake Fraction Coefficient  
 $V_s$  : Ship Scale Velocity (m/s)  
 $D_s$  : Ship Scale Propeller Diameter (m)  
 $J_{TS}$  : Ship Scale Propeller Advance Coefficient

Propeller advance coefficient ( $J$ ) is considered equal on model and ship scale.

$$J_{TS} = J_{TM} = \frac{V_A}{n_m \cdot D_m} \quad [31]$$

- $V_A$  : Model Ship Average Velocity of Propeller Diameter Suction Zone in self-propulsion.  
 $n_m$  : Self-Propulsion Propeller Revolution Speed (rps)  
 $D_m$  : Model Propeller Diameter (m)

The  $J$  coefficient was calculated as 0.8.

Then, cavitation  $\sigma$  number at the ship scale was calculated using the index formula in ITTC 7.5-02-03-03.1 document. The formula for the cavitation index coefficient is presented below.

$$\sigma = \frac{p_a - p_v}{\frac{\rho}{2} (\pi \cdot n \cdot D)^2} \quad [32]$$

- $\sigma$  : Cavitation Index Number  
 $p_a$  : Ambient Hydrostatic Pressure ( $\rho \cdot h \cdot g$ ) (Pa)  
 $p_v$  : Vapor Pressure (Pa)  
 $\rho$  : Water Density ( $\text{kg/m}^3$ )  
 $n$  : Propeller Revolution Speed (rps)

The distance between the propeller hub and the free surface was used as the height for ambient hydrostatic calculations. Tunnel pressure is calculated by considering the  $\sigma$  coefficient equal on ship scale and model scale.

$$\sigma_s = \sigma_M$$

The ship and model scale  $\sigma$  was calculated as 0.071. The propeller speed was determined as 25 rps in the model scale tunnel calculations.

The other parameters calculated in the Self-Propulsion Analysis are presented in Table 7.

Table 7. Resistance and Propulsion Estimates for Self-Propelled Model

Parameter	Value	Unit
$C_{FM}$	$2.75 \times 10^{-3}$	-
$C_{FS}$	$1.4 \times 10^{-3}$	-
$\Delta C_F$	$2.2 \times 10^{-4}$	-
$C_A$	$3.7 \times 10^{-4}$	-
SFC	28.67	N
$R_{SP}$	231.47	N
$T_{SP}$	202.8	N
$n_m$	16.4	rps
T	231.47	N
$R_{Appended\ Hull}$	221.38	N
t	0.044	-
$w_M=w_S$	-0.003	-
J	0.8	-
$n_s$	3.32	rps
$\sigma$	0.071	-

Propeller down streamline effective wake field profile is shown in Figure 13. This wake field profile was used in rudder cavitation calculations.

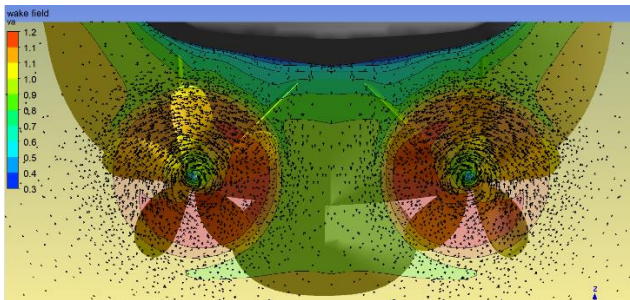


Figure 14. Downstream Line Effective Wake Field of Interacted Hull-Propeller and Appendages in Tunnel Conditions ( $n=25$  rps)

### 3.5 Open Water Rudder CFD Validation Case

CFD validation study was conducted to test the accuracy of the rudder performance prediction. Experimental results of NACA 0021 rudder geometry (Zhao D. et al., 2016) has been validated with CFD calculations. Geometric data of the NACA 0021 rudder geometry is presented in Table 8. 3D model of rudder model is shown in Figure 15.

Table 8. Main Particulars of NACA 0021 Rudder Geometry

Description	Value
Root Chord (m)	0.155
Tip Chord (m)	0.119
Span (m)	0.233
Root Chord NACA	0021
Tip Chord NACA	0021
Projected area (m <sup>2</sup> )	0.03184

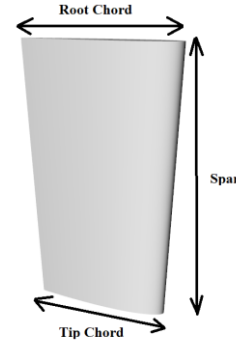


Figure 15. NACA 0021 Rudder Geometry

According to the ITTC 7.5-03-01-01 standard document a convergence study was carried out with different mesh sizes for the NACA 0021 rudder geometry. Sensitivity analyzes performed at a speed of 3.297 m/s and 20.15° rotation angle.  $C_L$  and  $C_D$  coefficients were calculated as follows.

$$C_L = \frac{F_L}{0.5 \cdot \rho \cdot v^2 \cdot S} \quad [33]$$

$$C_D = \frac{F_D}{0.5 \cdot \rho \cdot v^2 \cdot S} \quad [34]$$

- $C_L$  : Lift Coefficient
- $C_D$  : Drag Coefficient
- $F_L$  : Lift Force (N)
- $F_D$  : Drag Force (N)
- $\rho$  : Water Density (kg/m<sup>3</sup>)
- $v$  : Inlet Velocity (m/s)
- $S$  : Lateral Projected Area of the Rudder (m<sup>2</sup>)

Table 9. NACA 0021 Rudder Sensitivity Analysis Results

No	Rotation Angle(°)	Mesh Relevance	Mesh Size(mm)	CL	CD
3	20.15	Coarse	4	0.84	0.145
2	20.15	Medium	3	0.91	0.13
1	20.15	Fine	2.2	0.953	0.121
0	20.15	Very Fine	1.6	0.973	0.117

$R_k$  was 0.62 for  $C_L$  and 0.6 for  $C_D$  in sensitivity analysis. Since  $0 < R_k < 1$  for both  $C_L$  and  $C_D$ , sensitivity convergence was achieved. Validation studies were performed with very fine mesh size.

Sst k- $\omega$  turbulence model was used for resistance analysis. The Y+ value was applied between 30-300 for CFD validation analysis.

Approximately 1.4 million cells were used in open water rudder validation analyses. Mesh details and control domain sizes are shown in Figure 16.

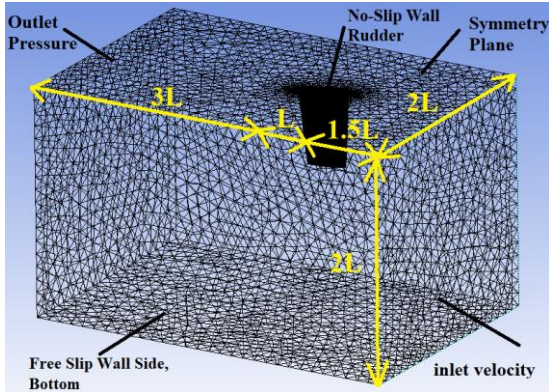


Figure 16. NACA 0021 Rudder Open Water Analysis Control Domain

CFD-experimental comparison of NACA 0021 rudder open water curves is shown in Figure 17 and Figure 18.

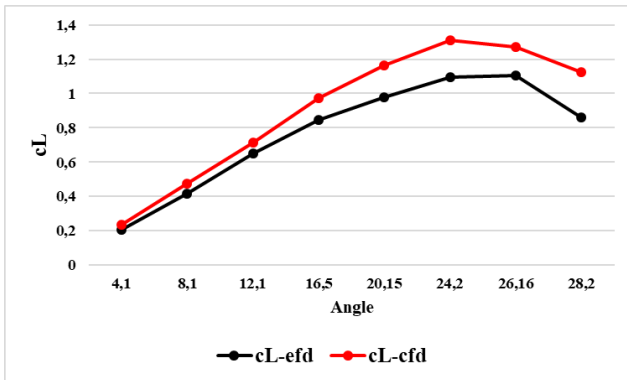


Figure 17. Rudder Open Water Analysis  $C_L$  efd vs. cfd Comparison

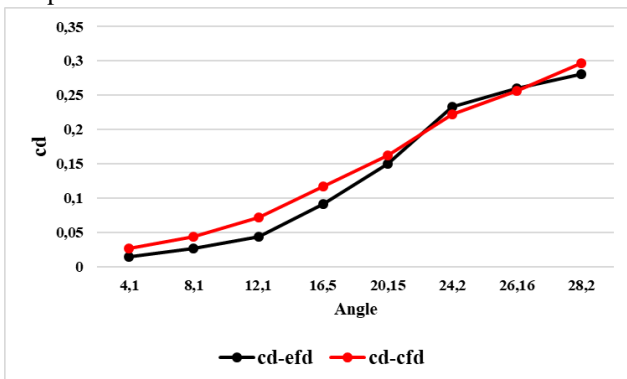


Figure 18. Rudder Open Water Analysis  $C_D$  efd vs. cfd Comparison

CFD results were consistent with the experimental results. The stall characteristics of the  $C_L$  curves of CFD and EFD were similar.

**3.6. Untwisted and Twisted Rudder Cavitation Analysis**  
DTMB 5415 model had NACA 0024 rudder geometry. Another rudder alternative has been designed for the DTMB 5415 hull. The new alternative was designed from the NACA 64A024 section. In the new alternative, only the section profile has changed, without changing the planform design.

Geometric data of the NACA 0024 and 64A024 rudder geometries are presented in Table 10.

Description	Rudder1	Rudder2
Root Chord (m)	0.173	0.173
Tip Chord (m)	0.115	0.115
Span (m)	0.191	0.191
Root Chord NACA	0024	64A024
Tip Chord NACA	0024	64A024
Projected area (m <sup>2</sup> )	0.02744	0.02744

Rudder NACA sections are shown in figure 19.

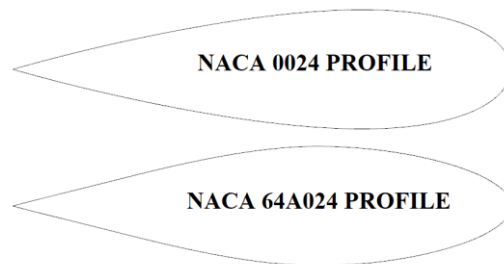


Figure 19. Rudder NACA Sections

When the sections are examined, it is seen that the center of pressure of NACA 0024 is closer to the leading edge when compared to NACA 64A024.

The mesh size used in the open water performance calculations of the rudders was the very fine mesh size used in the validation study.

The open water performance ( $C_L$  and  $C_D$ ) results of the rudders are shown in Figure 20 and Figure 21.

NACA 64A024 sectional rudder stall was detected at higher angles in open water performance calculations.

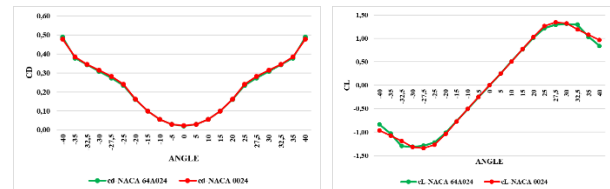


Figure 20.  $C_D$  and  $C_L$  Performances of NACA 0024 and NACA 64A024

The cavitation characteristics of both rudders were examined.

The image of the appended rudder on hull model is shown in Figure 22.

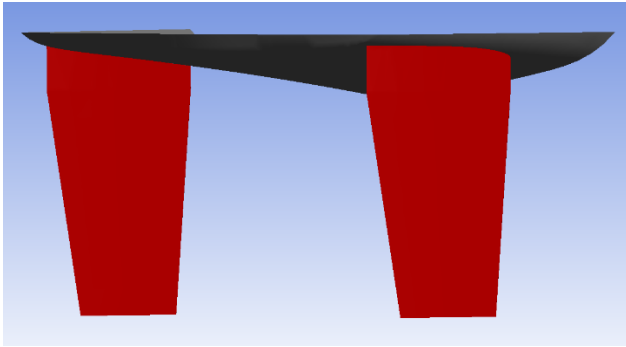


Figure 22. Rudder Connected to the Hull Model

The effective wake field calculated in the tunnel calculations was applied to the rudder geometries. The initial effective wake field image applied to the rudders is shown in Figure 23.

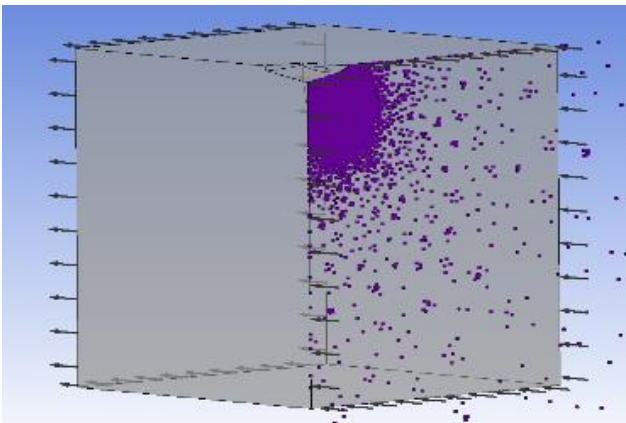


Figure 23. Initial Velocity Profile Used in Rudder Cavitation Calculations.

Cavitation calculations were performed in steady-state using the multi-phase (water+ water vapor) VOF method. In the analyzes, the ship and model  $\sigma$  numbers were accepted same and the tunnel pressure was calculated as 16692 Pa.

The cavitation patterns of both rudders are shown in Figure 24.

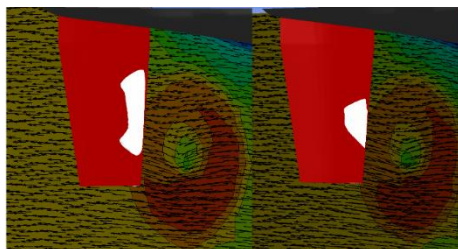


Figure 24. Cavitation Patterns of NACA 0024 and NACA 64A024 Profile Rudders

Cavitation on the rudder decreased by about 50% with change of the NACA profile. Angular velocity distribution at the leading edge of the untwisted rudder is shown in Figure 25.

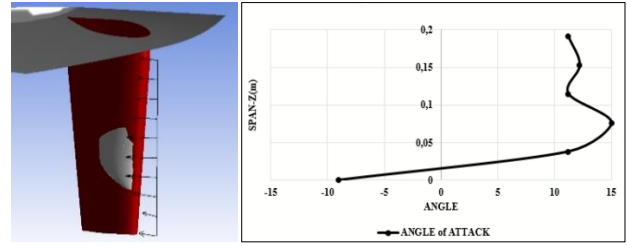


Figure 25. Angular Velocity Distribution at the Leading Edge of the Untwisted Rudder

In this case, low cavitation NACA 64A024 rudder span was twisted 6 degrees with reference to the center of the rudder shaft from the middle. The twisting method (Kültür M. 2022) is shown in Figure 26. In this method, the 20% span of the rudder from the root chord was not twisted. Because rudder shaft might be integrated to this height.

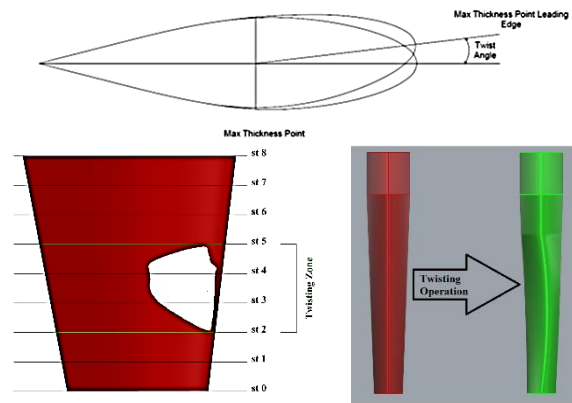


Figure 26. Twisting Method (Kültür M. 2022)

At the end of the twisting process,  $C_L$  and  $C_D$  performances of twisted and non-twisted rudders with NACA 64A024 cross section were compared.

Twisted rudder gave satisfactory results in terms of maneuvering performance.  $C_L$  and  $C_D$  performances of twisted and non-twisted rudders is presented in Figure 27.

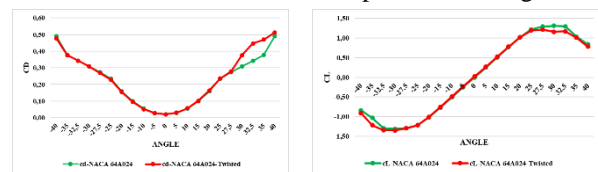


Figure 27.  $C_D$  and  $C_L$  Performances of NACA 64A024 Untwisted and Twisted Rudder

Also cavitation was completely eliminated on rudder surface. The image of the twisted rudders under the effective downstream line of the propeller is shown in Figure 28.

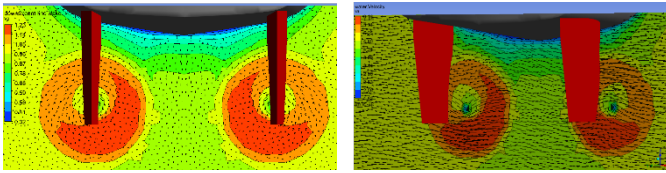


Figure 28. Twisted NACA 64A024 Rudders under the Effective Downstream Line of the Propeller

#### 4 CONCLUSION

Rudder cavitation is noisy, generates vibrations and is most probably erosive. It is highly recommended to avoid this phenomenon in full scale. One simple solution would be to turn the rudder blades towards each other in the neutral position which will certainly have a drag increasing influence on the propulsion behavior of the vessel. A much better solution would be a rudder with twisted leading edge being adjusted to the incoming swirl that is generated by the operating propeller. This way a propulsive gain would perhaps even be possible together with suppression of the rudder cavitation.

In this study, DTMB 5415 NACA 0024 rudder geometry was converted to NACA 64A024 without changing the projected area. It was found that the cavitation decreased up to %50. Then, the leading edge of the NACA 64A024 rudder geometry was twisted 6 degrees from the middle widest section of the rudder. The cavitation formed on the inner surface of the rudder was completely eliminated without decrease in maneuvering characteristics. Effective wake field of down streamline of the hull and propeller was calculated as transient. This effective wake field will allow to calculate quickly the cavitation behavior of different rudder geometries with less number of meshes.

#### 4 REFERENCES

- Hirt, C.W, and Nichols, B.D. (1981). "Volume of Fluid (VOF) Method for the Dynamics of Free Boundaries". *Journal of Computational Physics* 39 (1): 201–25.
- ITTC (2021). "Uncertainty Analysis in CFD, Validation and Validation Methodology and Procedures". 7.5–03-01–01.
- ITTC (2014). "Recommended Procedures and Guidelines, Practical Guidelines for Ship CFD Applications". 7.5–03-02–03.
- ITTC (2021). "Open Water Tests". 7.5–02-03–02.1.
- ITTC (2021). "Propulsion/Bollard Pull Test". 7.5–02-03–01.1.
- ITTC (2021). "1978 ITTC Performance Prediction Method". 7.5–02-03–01.4.
- ITTC (2014). "Practical Guidelines for Ship Self-propulsion CFD". 7.5–03-03–01.
- ITTC (2017). "Model Scale Cavitation Test". 7.5–02-03–03.1.
- Kim D, Rhee K.P., Kim N (2014). "The Effect of Hull Appendages on Maneuverability of Naval Ship by Sensitivity Analysis". *Article in Journal of the Society of Naval Architects of Korea*, Korea.
- Kultur M. (2022). "Interaction of Parametrically Designed Low Cavitated Propeller and Twisted Rudder" PHD Thesis, Istanbul/Turkiye.
- Li, Z. (2012). "Assessment of cavitation erosion with a multiphase Reynolds-Averaged Navier-Stokes Method", Ph.D. Thesis, Delft University of Technology.
- Olivieri, A., Pistani, F., Avanzini, A., Stern, F., and Penna R. (2001). "Towing Tank Experiments of Resistance, Sinkage and Trim, Boundary Layer, Wake, and Free Surface flow Around a Naval Combatant INSEAN 2340 Model" Technical Report 421.IHRHydroscience & Engineering: University of Iowa, USA.
- Park I., Paik B., Ahn J., Kim J. (2021). "The Prediction of the Performance of a Twisted Rudder". MPDI Applied Sciences, Korea.
- Schnerr, G. H. & Sauer, J. (2001). "Physical and numerical modeling of unsteady cavitation dynamics", 4th International Conference on Multiphase Flow, New Orleans, USA

## Data-Driven Fuel Consumption Rate Estimation by Using Deep Learning

Serhan Gökçay<sup>1\*</sup>, Ziya Saydam<sup>1</sup>, Gözde Nur Küçüksu<sup>2</sup>, Mustafa Insel<sup>3</sup>

<sup>1</sup>*Hidroteknik Nautical Design & Piri Reis University, Turkey*

<sup>2</sup>*Hidroteknik Nautical Design & Istanbul Technical University, Turkey*

<sup>3</sup>*Hidroteknik Nautical Design, Turkey*

**Abstract:** This paper focuses on the method of fuel consumption rate estimation by using deep learning algorithms. A method of real time fuel consumption rate prediction model is proposed which can be used during the optimization process of operational parameters of a ship and support the personnel during the decision of different voyage scenarios that can be used in various optimization purposes. As a case study, multi-purpose dry-cargo ship M/V ERGE was selected which is a target ship for a EU founded GATERS project (GATE Rudder System as a Retrofit for the Next Generation). Reliable data-driven deep learning model was established by utilizing data acquired during 2.5 months of voyage. Developed network model was tested and promising results show that the proposed method has high potential of predicting real time fuel consumption rate values accurately which can be used as a basis of a reliable decision support system.

**Keywords:** Performance monitoring, deep learning, artificial neural networks, energy efficiency.

### 1 INTRODUCTION

Increasing energy efficiency of ships has received much interest to reduce operational costs due to highly volatile fuel prices and greenhouse gas emissions due to environmental concerns. Adjusting parameters effecting ship power requirement on the voyage such as trim, draught, route, engine parameters, energy expenditure to optimized level can lead to significant levels of reduction in fuel consumption hence CO<sub>2</sub> emission reduction.

Real time optimization of various parameters can be a challenging task when considering other operational tasks of ships' personnel. To cope with these challenges, Decision support systems (DSS) were developed to support ship operators on their decisions of optimum operational parameters. These systems are either based on simplified models of ship performance, reinforced models combined with advanced engineering simulations (like CFD) or direct collection of operational data on route and system identification methodology such as neural network to generate the decision suggestions (Insel et al., 2018).

The recent contribution to literature on real-time decision support systems is extensive and focuses particularly on minimizing energy consumption and emissions. Much of the available literature on this topic deals with the question of reducing fuel consumption rate. Öztürk and Başar investigated several parameters, namely RPM/pitch, trim, mean draft, ballast condition, and weather routing, for reducing fuel consumption rate. The proposed Artificial Neural Network and Multiple Linear Regression Analysis based DSS's present energy savings are between 32-37%, 6.5-8%, 7-12%, and 6-8% for RPM, trim, weather routing, and ballast, respectively. Tarelko and Rudzki (2020) have set up ANN-based DSS using eight different input parameters to predict fuel consumption rate and speed. The input parameters were determined as pitch, rotational

speed, wind direction and speed, sea state, tidal current direction and speed, and last docking time. In a similar manner, Moreira and others (2021) built a DSS that uses the Levenberg-Marquardt (LM) backpropagation scheme to estimate ship speed and fuel consumption rate. The system uses engine torque, RPM, wave height, wave peak period, and encountered wave angle. A distinctive perspective has been adopted by Martić and others (2021) who argued ship added resistance effect on emissions. The proposed LM algorithm and Bayesian Regularization based ANN systems predict the added resistance by using 12 different input variables which are ship length, beam, draft, displacement, LCB, block coefficient, prismatic coefficient, ship speed, significant wave height, zero crossing period, sea spectra, and radii of gyration. The way of fuel consumption and ship power prediction was studied by Faraga and Ölçer (2020) by using traditional Noon Reports. The constructed ANN and Multi-Regression techniques use ship speed, depth, apparent wind speed, and direction, wave significant height and period, encounter angle, swell significant height and period, true swell angle, current speed, and true current speed to predict brake power.

A relatively small portion of the latest literature is concerned with collision avoidance, machinery maintenance, route optimization, and vessel positioning. There are a couple of studies handling the collision problem in the literature. Mohamed-Seghir and others (2021) proposed two methods: neural network and evolutionary algorithm. The given methods enable selection of the shortest trajectory to prevent collision as well as to reduce energy consumption. Another study (Banaszek and Lisaj 2022) stated the aim of connecting with the SAR Maritime Rescue Center in the case of collision. The closest trajectory and the estimated time of

\* Corresponding author e-mail: sgokcay@hidro-teknik.net

arrival to the safety area were calculated within the framework. Raptodim and others (2019) and Daya and others (2021) have mainly been interested in developing DSS concerning engine performance and health conditions. A relation exists between route optimization and the fisheries industry, which is the main consideration to develop a decision support system in Granado and others' paper (2021). On the other hand, Banaszek and Lisaj (2021) addressed the route optimization from a different viewpoint and used several navigational sensors from the bridge to generate the missing signals in the proposed ANN-based DSS.

Having reviewed the recent contributions to the literature, it is deduced that majority of these studies use limited number of input parameters acquired within long data sampling intervals starting from 5 minutes to a day. To the best of authors' knowledge, these studies lack the utilization of numerous number of parameters acquired in seconds to capture sudden variations for more sensitive deep learning predictions. Obviously, this is a crucial issue particularly for the vessels with operation profiles that have frequently changing operational parameters as in the case chosen for this study.

The aim of this study is to assess the ability of the deep learning model to be utilized as a reliable base for a decision support system. This is achieved by presenting a case study selected to obtain the data required for the establishment of the deep learning model and and by giving the details of the deep learning model that can predict real time fuel consumption rate parameter during the voyage.

The paper is organized as follows: Methods and input parameter selection is presented in Section 2. In section 3, details of the selected Case Study are given. Results of the proposed model is discussed in Section 4. General conclusions are derived and recommendations for further studies are given in Section 5.

## 2 METHODOLOGY

### 2.1 ARTIFICIAL NEURAL NETWORKS

Multilayer artificial neural networks (deep learning) applications had grown rapidly from the modelling of simple processing elements or neurons to massively parallel neural networks, which led to more sophisticated artificial intelligence and deep learning applications.

ANN finds out the complex relation between input and output information by using connected neurons which are inspired by human brain. The information is processed through network of neurons by utilizing weights and biases. Randomly selected weights are assigned at the initialization phase. During the learning process, the weights for each neuron are changed to minimize the calculated fitting errors. Following this process, relationship between input and output parameters can be determined.

The architecture of neural network plays an important role for the accuracy of the results. Selected architecture for this

study has three layers which are named as input, hidden and output layers. The input layer consists of selected 16 input parameters sensitive to energy consumption while the two hidden layers consists of 20 neurons. Output layer parameter consists of one output parameter which is fuel consumption rate. The architecture of the selected network is presented in Figure 1.

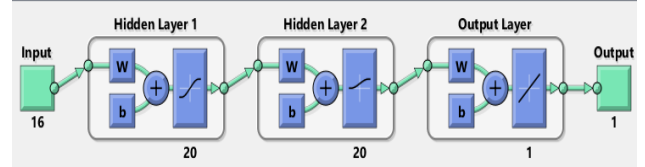


Figure 1: Deep learning networks architecture

Deep learning network is modelled in by developing a code that uses the Neural Network fitting tool included in the deep learning toolbox of a commercial software. The problem is reduced to solving a data fitting problem and input and output parameters were prepared as matrices. Levenberg-Marquardt backpropagation algorithm is assigned to train the neural network. The algorithm updates weight and bias values according to Levenberg-Marquardt optimization which is one of the fastest backpropagation algorithm in the toolbox.

### 2.2 INPUT PARAMETERS SELECTION

A cross-correlation analysis has been carried out on the acquired dataset to understand the impact of each parameter on output parameter, fuel consumption rate. Also, interrelation between each acquired parameters were captured. Heat map of cross-correlation analysis is given in Figure 2.

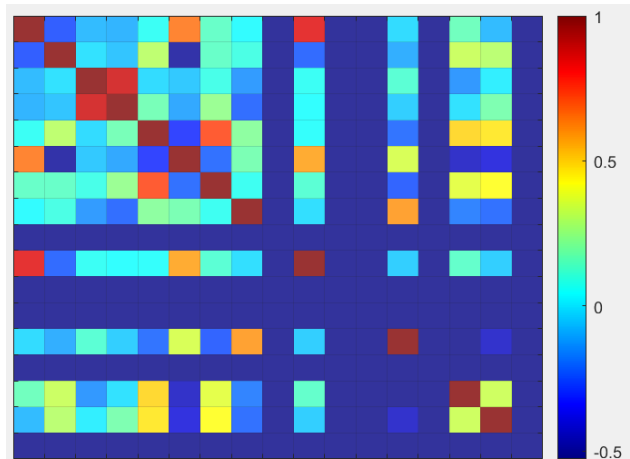


Figure 2: Heat map of cross-correlation analysis

As a conclusion of cross-correlation analysis; ship speed, cargo weight, displacement, trim, Sea State Number, Wave Heading, Wave Height, Apparent Wind Angle, Apparent Wind Speed, Leaway Angle, Shaft RPM, Shaft Torque, Engine Loading, Engine Power and Rudder Angle values were taken as input layer of the proposed deep learning architecture.

### 3 CASE STUDY

As a case study, voyage of multi-purpose dry-cargo ship M/V ERGE was selected. The vessel is a target ship for a

EU founded GATERS project (GATE Rudder System as a Retrofit for the Next Generation). The project aims to demonstrate the retrofit application of a novel Energy Saving and Manoeuvring Device. Particulars of M/V ERGE is given in Table 1.

Table 1: Ship Particulars

Name:	M/V ERGE
IMO No:	9508603
Vessel Type:	Multi Purpose Dry Cargo Ship
Owner:	ÇAPA DENİZCİLİK NAKLİYAT
Date Delivered:	2011
Length Overall:	89.7 m
Length Between Perp.:	84.9 m
Beam:	15.4 m
Design Draft:	6.46 m
Displacement:	7280 mt
Summer DWT:	5652 mt

Operational area of the ship is mainly within Mediterranean Sea and Marmara Sea with the addition of some southwest costs of the Black Sea. The photo of the ship is given in Figure 3.



Figure 3: GATERS project target vessel M/V ERGE

Within the scope of the project: design, manufacture, test and retrofit of the GATE Rudder System is planned. To validate the performance of the system, extensive series of sea trials including before and after retrofit application were scheduled. In addition, to acquire the voyage data, the ship is fitted with performance monitoring system provided by CETENA S.p.A. Centro per gli Studi di Tecnica Navale, one of the consortium members of the project.

The performance monitoring system consists of a PC with a dedicated software that records all available data on board. The system is connected to two main terminals located in bridge and engine room. The bridge terminal is connected to integrated navigation system and acquires the following data:

- Date, time, latitude, longitude, speed over ground and course over ground from GPS,
- Heading from gyrocompass,
- Apparent/True wind speed and direction from Anemometer,
- Water depth from echo sounder,
- Boat Speed (speed through water) from speed log.

Engine room terminal consist of a dedicated cabinet with installed hardware needed to receive analog data from shaft speed(RPM), torque sensors, mass flow meter (located at fuel transfer line) and rudder angle sensors installed by Bureau Veritas.

A “Repeater” software is provided to gather additional information such as draught, loading condition, cargo weight, environmental conditions for each voyage/trip. Ship deck officers are in charge to record on a spreadsheet and send them by email to CETENA on a weekly basis. Performance Monitoring system configuration is presented in Figure 4.

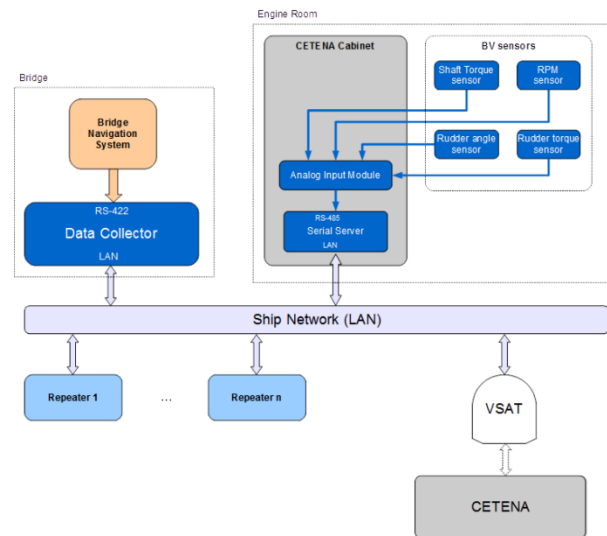


Figure 4: CETENA Performance Monitoring system configuration

The monitoring software can acquire signals with a sampling frequency of 1Hz; The system averages and stores the acquired values with a variable time interval (in this case study, intervals of 60 seconds was used).

For this study, voyage data on consecutive & continuous set of voyages between 01/03/2022 to 13/05/2022 was acquired and post processed. This dataset was used to establish a deep learning architecture which aims to perform accurate real-time fuel consumption rate estimations for the user defined energy efficiency scenarios. to train and validate the artificial neural network model. Route of the consecutive & continuous set of voyages are presented in Figure 5.

#### 4 RESULTS

A deep learning model is designed by developing a code that uses the Neural Network fitting tool included in the deep learning toolbox provided by a commercial software. The ideal network structure with high correlation number ( $R^2=0.999$ ) is determined by tuning the number of hidden layers, neurons in the hidden layer and training algorithm through trial-and-error method. Established network was trained by sea trial data acquired with performance monitoring system.



Figure 5: Route of voyages

Total of  $34 \times 101286$  discrete time domain signal was acquired during 7360nm of voyages. Time domain signals were post-processed and formatted in accordance with the required ANN input. In house developed sea trial data evaluation software was utilized during visualizing and data cleaning up process. Whole data is visualized in Figure 6.

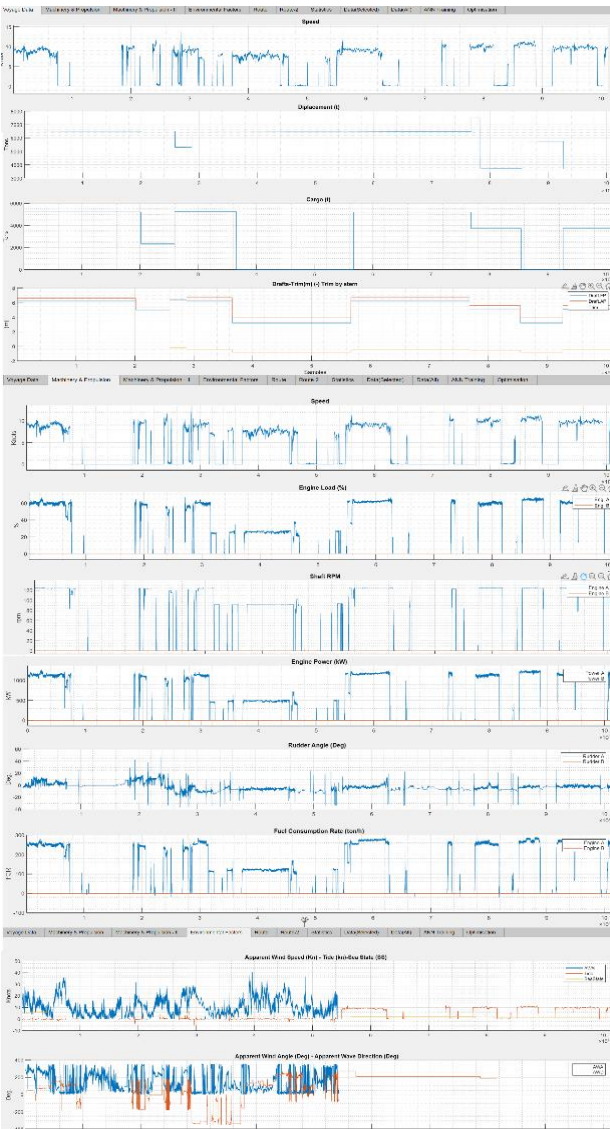


Figure 6: Time series signals acquired during the sea trial.

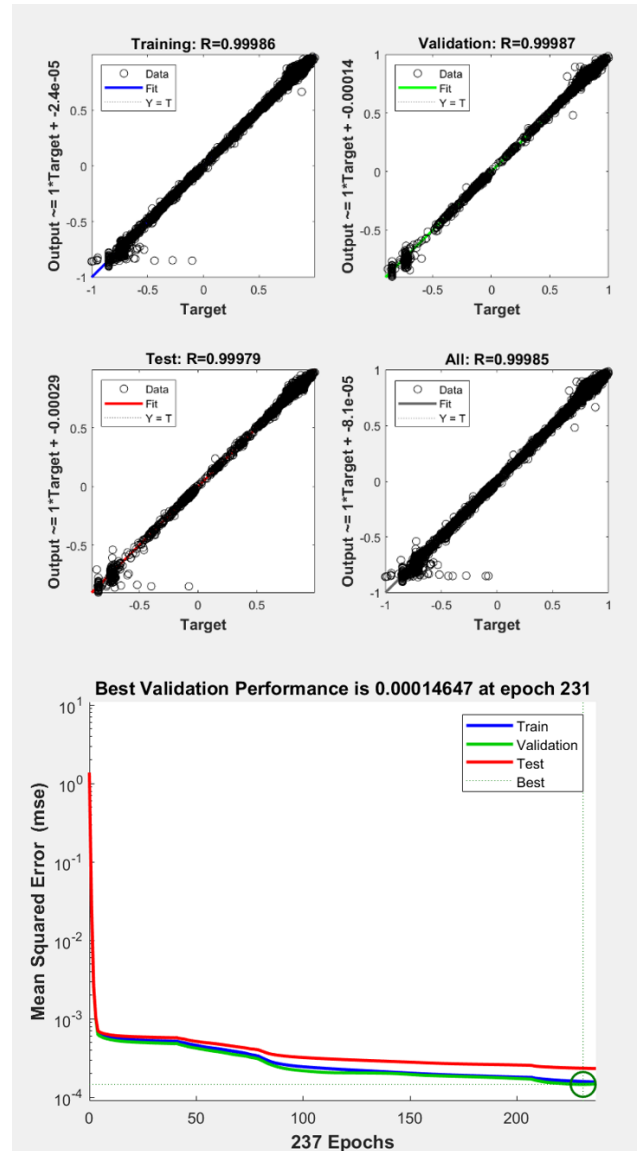


Figure 7: Performance plots of the selected network

Following the data clean-up process, acquired measurement data is randomized to incorporate in the input layer and 70900 samples (70%) are used to train the network while 15192 samples (15%) and another 15192 samples (15%) are used for validation and testing purposes. Levenberg-Marquardt learning algorithm is assigned with learning rate of 0.8. Hyperbolic tangent sigmoid and linear transfer functions are used, and the input parameters are normalized within the range of -1 and 1.

\* Corresponding author e-mail: sgokcay@hidro-teknik.net

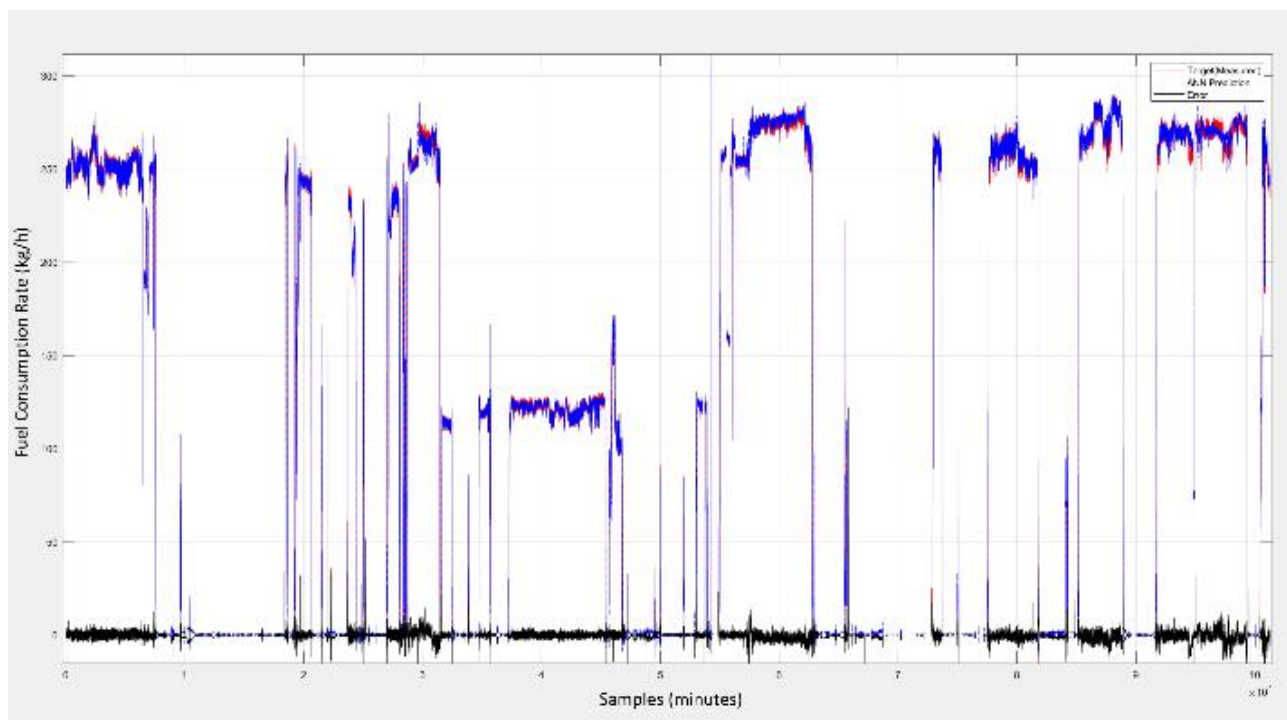


Figure 8: Prediction vs. measured data

Performance of the network structure is presented in Figure 7. The figure contains plots of the training, validation, test and overall fitting regressions and the mean squared error convergence of the values calculated for fuel consumption rate output parameter. Targets are the measured values during the sea trial while “output” ordinates correspond to calculated values of employed artificial neural network.  $R^2$  values for the validation are found to be satisfactory for training, validation, and test respectively.

the training of the network is performed by using randomized data to eliminate over fitting issues. Following to successful fit of the neural network, saved neural network is used for finding the output of sequential sea trial data. Figure 8 shows the comparison between measured and predicted values. Prediction error between estimated and acquired values are incorporated in the plot for clear understanding. Root Mean Square (RMS) value of the error values are calculated as 2.23kg/h that clearly indicates promising result, when the realized fuel consumption rate values are considered (This corresponds 1.8% error when compared with r.m.s value of fuel consumption matrix 119.7kg/h).

## 5 CONCLUSION

Decision support systems are becoming a widely addressed tools with high potential of supporting ship operators through their response to lowering fuel consumption.

A case study is selected to gather necessary data for deep learning model establishment. The details of the deep learning model that can predict real time fuel consumption rate parameter during the voyage is presented.

Results of the study show that, the ability of the model that can be a reliable base to decision support system for more

energy efficiently operating ships is satisfactory when the measured outputs are compared with the predicted ones.

Application of the proposed model to different ship types and integration of deep learning-based fuel consumption rate prediction to a decision support system with enhanced optimization algorithms may be included in future research.

## REFERENCES

- Insel, M., Gokcay, S., Saydam, A. Z., A decision support system for energy efficient ship propulsion, *Trends and Challenges in Maritime Energy Management, WMUSTUD, Volume 6, Pages 143-155*, 2018.
- Banaszek, A. & Lisaj, A. (2021). ‘The Concept of Advanced Maritime Integrated Data Processing System with Use of Neural Network Methods’. *Procedia Computer Science* **192**, pp. 2450-2459.
- Banaszek, A. & Lisaj, A. (2022). ‘The Concept of Intelligent Radiocommunication System for Support Decision of Yacht Captains in Distress Situations with Use of Neural Network Computer Systems’. *Procedia Computer Science* **207**, pp. 398–407.
- Farag B.A.Y. & Ölçer, A. I. (2020). ‘The development of a ship performance model in varying operating conditions based on ANN and regression techniques’. *Ocean Engineering* **198**.
- Granado, I., Hernando, L., Galparsoro, I. Gabiña, G., Groba C., Prellezo, R., Fernandes, J.A. (2021). ‘Towards a framework for fishing route optimization decision support systems: Review of the state-of-the-

art and challenges'. Journal of Cleaner Production **320**.

Martić I., Degiuli N., Majetić D., Farkas A. (2021). 'Artificial Neural Network Model for the Evaluation of Added Resistance of Container Ships in Head Waves'. Journal of Marine Science and Engineering **9(8)**:826.

Mohamed-Seghir M. & Kula K., Kouzou A. (2021). 'Artificial Intelligence-Based Methods for Decision Support to Avoid Collisions at Sea'. Electronics **10(19)**:2360.

Moreira L., Vettor R., Guedes Soares C. (2021). 'Neural Network Approach for Predicting Ship Speed and Fuel Consumption'. Journal of Marine Science and Engineering **9(2)**:119.

Öztürk, O. B. & Başar E. (2022). 'Multiple linear regression analysis and artificial neural networks based decision support system for energy efficiency in shipping'. Ocean Engineering **243**.

Raptodimos, Y. & Lazakis, I. (2020). 'Application of NARX neural network for predicting marine engine performance parameters'. Ships and Offshore Structures **15(4)**, pp.443-452.

Tarelko, W. & Rudzki, K. (2020). 'Applying artificial neural networks for modelling ship speed and fuel consumption'. Neural Computing & Application **32**, pp.1737–1739.

## On the Full-Scale Powering Extrapolation of Ships with Gate Rudder System (GRS)

Cihad Çelik<sup>1</sup>, Selahattin Özsayan<sup>1</sup>, Çağatay Sabri Köksal<sup>1\*</sup>, Devrim Bülent Danışman<sup>1</sup>, Emin Korkut<sup>1</sup>,  
Ömer Gören<sup>1</sup>

<sup>1</sup>Istanbul Technical University, Faculty of Naval Architecture and Ocean Engineering, 34469 Maslak-Istanbul, Turkey

**Abstract:** A novel energy-saving device known as the Gate Rudder system (GRS) has proved its effectiveness to improve the propulsive efficiency, hence reduce the fuel consumption of ships on full-scale sea trials. However, the power-saving measured on the sea trials has been more than the predictions, based on the CFD analyses and model tests. This study experimentally investigates the propulsive efficiency of the Gate Rudder system by introducing the four different extrapolation methods to estimate the required power, based on model test results. In view of this the comparative tests of the two sisterships of 2400 GT Containership model, SAKURA appended with the conventional rudder system (CRS) and SHIGENOBU appended with the Gate Rudder System (GRS) are carried out at the Ata Nutku Ship Model Testing Laboratory's towing tank of Istanbul Technical University (ITU). The results of extrapolations compared with the sea trial data to properly show the differences between the methods. Gate Rudder system assumed as an appendage shows better agreement with the sea trials. The powering predictions show that the GRS configuration is able to reduce the powering requirement by 2 % at the design speed as compared to that of the CRS configuration in full loaded condition.

**Keywords:** Energy saving devices, towing tank experiment, propulsion, Gate Rudder system.

### 1 INTRODUCTION

International Maritime Organization (IMO) will implement new restrictive regulations to decrease the carbon emissions by ships. Ship owners must provide the Energy Efficiency Design Index (EEDI) and Energy Efficiency Existing Ship Index (EEXI) values of the ships below a certain level. An energy-saving device which may reduce the required power by ships, resulting in less carbon emissions. Gate Rudder system is one of the energy-saving devices that can be integrated into existing ships or installed on newly design ships.

Gate Rudder system has several advantages in terms of propulsive efficiency, seakeeping, and maneuverability (Sasaki et al., 2016). The GRS works as a ducted propeller and accelerates the flow around the propeller to improve the propulsive efficiency. Gate Rudders are twin rudders that can be operated individually during sailing, which enhances the manoeuvring performance of ships. Comparative full-scale measurements of the two sisterships of 2400 GT Containership model, SAKURA (Fukazawa et al., 2018) appended with the conventional rudder system and SHIGENOBU (Sasaki et al., 2018) appended with the Gate Rudder System have been also performed, showing a 14% energy saving. Model scale investigations were carried out both experimentally and numerically on a large bulk carrier (Sasaki et al., 2016). GRS reduced the fuel consumption up to 7-8% in powering analysis. It is well known that conventional ducted propellers may have disadvantages in terms of cavitation and vibration. There are also available studies that focus on cavitation and vibration problems comparing the CRS and

GRS. Numerical (Yilmaz et al., 2018) and experimental (Turkmen et al., 2018) studies reported that sheet and tip vortex cavitation volumes have been reduced with the GRS. One further full-scale experience from the SHIGENOBU's captain is that GRS resulted in less vibration and quieter aft (Sasaki et al., 2019).

This study presents the analysis and the results of resistance and propulsion tests of two sisterships, SAKURA and SHIGENOBU of 2400 GT Containership were performed by aiming to investigate the differences, due to use of Conventional Rudder (CRS) and Gate Rudder (GRS) systems. The towing tank tests were performed in accordance with the EU Project entitled with acronym GATERS and hull form and other technical design details were supplied by the coordinator of the project.

Besides, four different full-scale extrapolations regarding the effect of GRS on total resistance and thrust deduction have been performed in powering analysis for the GRS. Details of the methods are presented in Section 3. Results are discussed in Section 4, which also shows the comparison of extrapolation methods with CRS.

### 2 EXPERIMENTAL SETUP

A wooden model with a scale of 1/21.75 coded as M445 was built in the workshop of ITU Ata Nutku Ship Model Testing Laboratory and tested in the towing tank of the laboratory. The tests were carried out for two loading conditions, namely full loaded ( $T_{mid}=5.208$  m) and ballast ( $T_{mid}=4.175$  m) conditions. The geometry and hydrostatic details are given in **Error! Reference source not found.** and Table 1.

\* Corresponding author e-mail: koksalcag@itu.edu.tr

### 2.1 Properties of Ship and Propeller

The model and hydrostatic details are given in **Error!** **Reference source not found.** and Table 1 respectively.

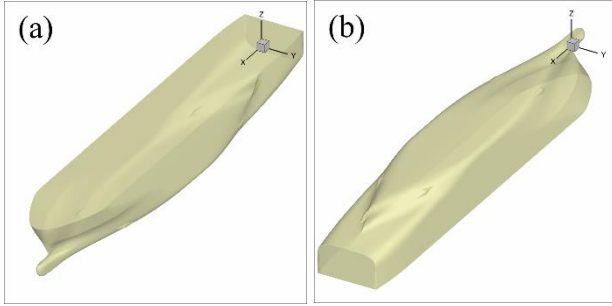


Figure 1. Perspective view of the hull.

Table 1. Model and ship characteristics.

M445	Loading Condition			
	Full Load		Ballast Load	
	Model	Ship	Model	Ship
Scale	21.75			
LOA (m)	5.127	111.51	5.127	111.51
LPP (m)	4.685	101.90	4.685	101.90
LWL (m)	4.860	105.71	4.808	104.57
BWL (m)	0.818	17.80	0.818	17.80
T (m)	0.239	5.208	0.192	4.175
∇ (m <sup>3</sup> )	0.614	6318.4	0.470	4835
Δ (ton)	0.614	6476.4	0.470	4955.9
S (m <sup>2</sup> )	4.859	2298.8	4.167	1971.1
C <sub>B</sub>	0.613	0.613	0.582	0.582

The ships have two different four-bladed controllable pitch propellers with different characteristics. In model tests, a scaled model propeller of the ship with the GRS ( $\lambda=21.75$ ) with fixed-pitch blades was used. This model propeller was used in all propulsion tests (w/GRS & w/CRS). Details of the model propeller are presented in Table 2.

Table 2. Properties of the model propeller.

Diameter (D)	0.152 m
P/D	0.835
BAR	0.512
Z	4
Direction of rotation	Right-handed

### 2.2 Test Procedure and Physical Configuration of Experiment System

All resistance and propulsion tests were performed in Ata Nutku Ship Model Testing Laboratory. The tank is 160 m long, 6 m wide, and 3.4 m deep and equipped with a manned carriage which is able to run at a speed of up to 6 m/s. Turbulence stimulation was obtained by the application of studs behind the stem (bow) as well as on the rudder. Resistance characteristics of the hull model were measured by using a single component electronic resistance dynamometer, OPN500.

The propulsion tests were carried out in order to determine the required power of the ship with CRS (Figure 2) and GRS (Figure 3) configurations at the full loading draught and ballast loading draught.

In GRS design, the propeller is slightly shifted towards the stern due to the Gate Rudders' position and the stern tube geometrical design changed accordingly.

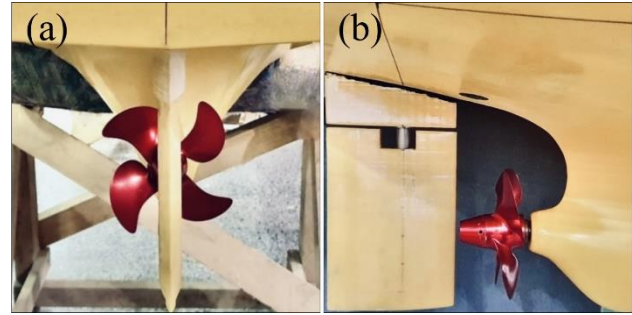


Figure 2. CRS configuration for propulsion test cases.

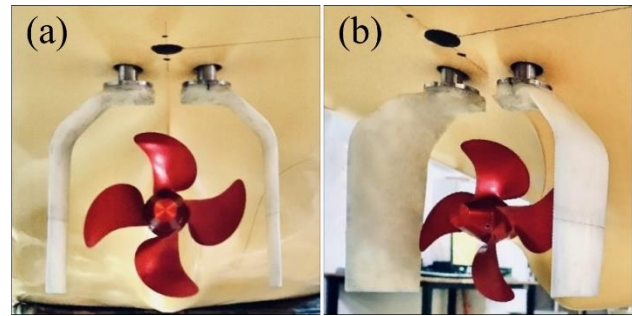


Figure 3. GRS configuration for propulsion test cases.

In the self-propulsion tests, an electric motor, one Cussons Technology R25 propeller dynamometer and a single component OPN500 electronic resistance dynamometer, bearings, etc. were installed in the 1/21.75 scaled M445 hull model. A right-handed model propeller whose open water characteristics have already been measured in Japan, was used for both configurations (CRS&GRS) during the tests.

During the self-propulsion tests an additional towing force should be applied or taken into account to obtain the full-scale ship propulsion point. This external force  $F_D$  also called as the Skin Friction Correction (SFC) takes into account the differences between Reynolds numbers of the model and the ship. The  $F_D$  can be calculated as in the following equation (1) according to ITTC Propulsion/Bollard Pull Test Procedure (7.5-02-03-01.1) as:

$$F_D = \frac{1}{2} \rho S V^2 [(1+k)(C_{FS} - C_{FM}) - \Delta C_F] \quad (1)$$

The characteristics of the full-scale propeller were calculated from the model propeller characteristics in open water, which were corrected for the scale effect according to 1978 ITTC Performance Prediction Method Procedure (7.5-02-03-01.4). The model wake fraction was converted to the full-scale wake fraction for CRS regarding the same procedure.

The load of the full-scale propeller is obtained from:

$$\frac{K_{TS}}{J_S^2} = \frac{1}{N_P} \frac{S_S}{2D_S^2} \frac{C_T}{(1-t)(1-w_{TS})^2} \quad (2)$$

With this  $K_T/J^2$  as input value the full-scale advance coefficient  $J_{TS}$  and the torque coefficient  $K_{QTS}$  are read off

from the full-scale propeller characteristics and the following quantities are calculated.

- propeller rate of revolutions

$$n_S = \frac{(1-w_{TS})V_S}{J_{TS}D_S} \quad (3)$$

- thrust of each propeller

$$T_S = \frac{K_T}{J^2} J_{TS}^2 \rho_S D_S^4 n_S^2 \quad (4)$$

- torque of each propeller

$$Q_S = \frac{K_{QTS}}{\eta_R} \rho_S D_S^5 n_S^2 \quad (5)$$

- delivered power

$$P_D = 2\pi Q_S n_S \quad (6)$$

### 3 DIFFERENT EXTRAPOLATION APPROACHES

Resistance tests were, initially, carried out for the bare hull and then repeated with the different rudder configurations. The effect of air drag was included in the analysis. The model was tested free to trim and sink in calm water, however, the model was fixed to roll, sway, and yaw. Form factor analysis was carried out by Prohaska's method.

Four different performance prediction methods have been compared for the GRS installed case. Details of the methods are explained in following subsections considering the effect of GRS on the total resistance and thrust deduction.

#### 3.1 ITTC 1978 Performance Prediction- Original Method

In this approach extrapolation to the full scale was carried out by the original ITTC 1978 method. The conventional rudder and gate rudder systems were considered as appendages and extrapolated to the full scale by means of the beta factor, which is  $\beta = 0.70$ . The effect of air drag was included in the analysis.

In the powering calculations, the total resistance ( $R_{TM}$ ) includes bare hull ( $R_{TBH}$ ) and the conventional rudder ( $R_\delta$ ) or the gate rudder ( $R_{GR}$ ) appendage resistances respectively as;

$$R_{TM} = R_{TBH} + R_\delta \text{ or } R_{GR} \quad (7)$$

The thrust deduction ( $t$ ) is calculated as;

$$t = \frac{T_M + F_D - R_{TM}}{T_M} \quad (8)$$

Here,  $T_M$  is the propeller thrust at the self-propulsion point.

The open water characteristics of the model propeller is directly utilized to determine the propulsion characteristics without considering the GRS effect on the propeller.

#### 3.2 Gate Rudder Assumed as a Propulsor - I

In this extrapolation approach, the propeller with GRS is considered as a propulsor unit. Evaluation of total resistance and thrust deduction is given in equations (9) and (10), respectively.

In powering calculations of GRS case, the  $R_{TM}$  is taken as a bare hull resistance.

$$R_{TM} = R_{TBH} \quad (9)$$

$t$  is calculated as;

$$t = \frac{T_M + T_{GRM} + F_D - R_{TM}}{T_M + T_{GRM}} \quad (10)$$

where,  $T_{GRM}$  is the thrust force generated by the GRS.

For this approach, open water characteristics with the GRS, which were calculated by Tacar et al., (2020) using CFD computations, were used for the propulsion analysis. A comparison of the open water curves with the gate rudder and without gate rudder cases in model-scale is shown in Figure 4.

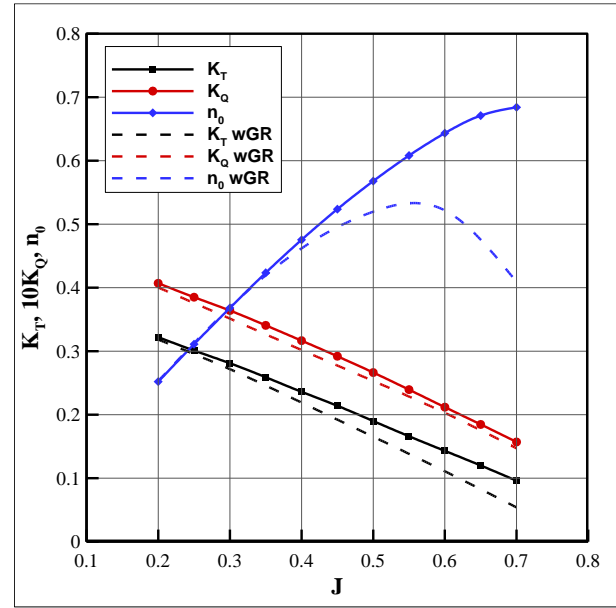


Figure 4. A comparison of the open water curves with the gate rudder and without gate rudder cases in model-scale.

#### 3.3 Modified ITTC1978, Gate Rudder Assumed as an Appendage -- II

This approach, in general, uses ITTC1978 method, but does not convert the model wake fraction to full-scale, instead uses the below approach:

$$\frac{(1-w_S)}{(1-w_M)} = 1 \quad (11)$$

Based on the previous sea trial results of ships with GRS.

#### 3.4 Modified ITTC1978, Gate Rudder Assumed as an Appendage -- III

This approach, in general, uses ITTC1978 method, but does not convert the model wake fraction to full-scale, instead uses the below approach:

$$\frac{(1-w_S)}{(1-w_M)} = 0.96 \quad (12)$$

### 4 RESULTS AND DISCUSSIONS

Depending on the low-speed model test data form factors as determined from the Prohaska's analysis are given in . The model scale resistance coefficients for the bare model is presented on both full loaded and ballast loaded conditions in Figure 5 and Figure 6, respectively.

Table 3. Form factors

Loading Condition (Bare hull)	Form Factor (1+k)
Ballast Load	1.187
Full Load	1.185

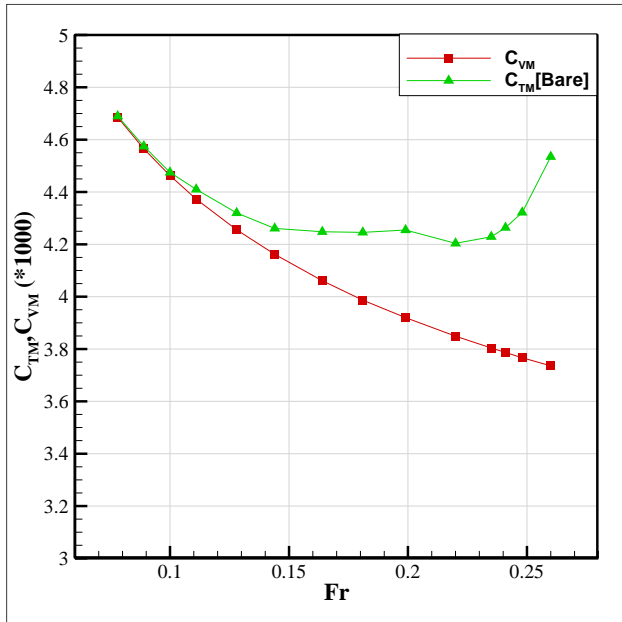


Figure 5. Model scale resistance coefficients for the ballast load.

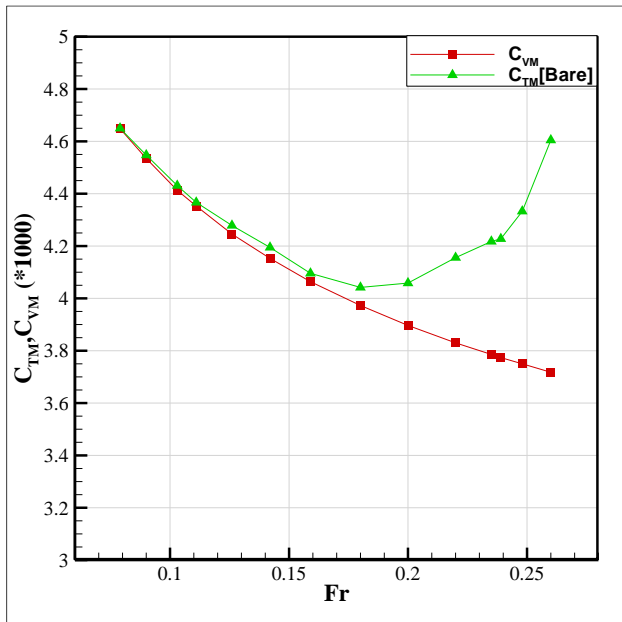


Figure 6. Model scale resistance coefficients for the full load.

The CRS powering calculations are carried out with respect to the 1978 ITTC Performance Prediction Method. Effective power and minimum break power were depicted in Figure 7 for the ballast loaded condition.

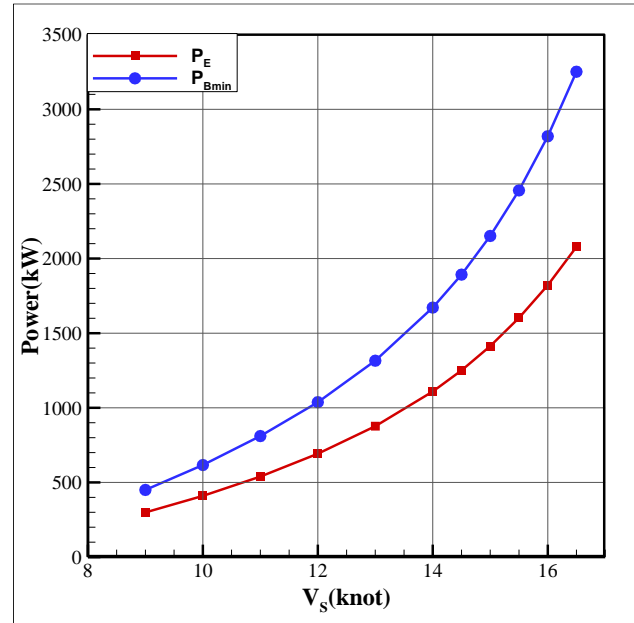


Figure 7. Power requirement plots of the ship with CRS for the ballast load draught.

The effective and break power results of GRS assumed as an appendage with different wake corrections are shown with the sea trails in Figure 8 and Figure 9 for the ballast loaded condition.

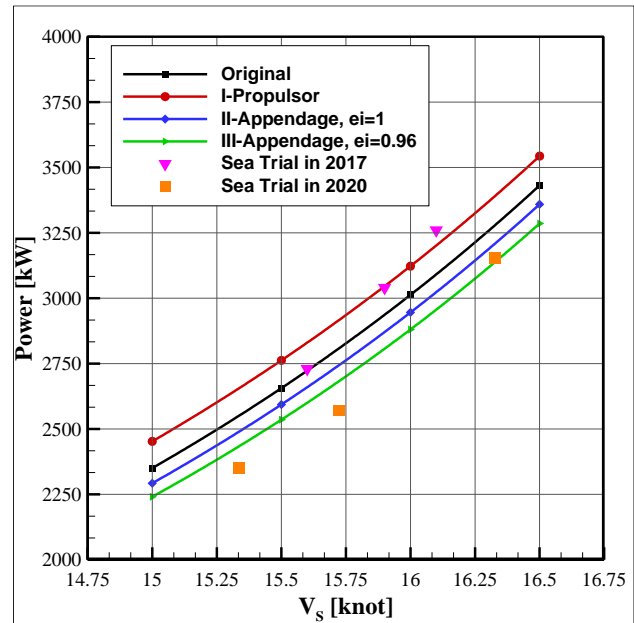


Figure 8. Comparison of the extrapolation methods with sea trial results at the ballast loading condition.

Break power predictions of GRS for the ballast loading have been analyzed regarding the corresponding extrapolation methods described in Section 3. Figure 8 shows comparisons of the prediction results and sea trial results. If the Gate Rudder assumed as a propulsor, the results show that this method overpredicted the sea trial results in 2020, but similar to the results in 2017. Once the original ITTC 1978 Method was applied, the results

\* Corresponding author e-mail: koksalcag@itu.edu.tr

underpredicted the sea trails obtained in 2017 but overpredicted those of 2020. In the case of modified ITTC 1978-II and III cases, the predictions are in good agreement with the sea trial results in 2020. Based on this information all the comparisons of the GRS are based on the modified ITTC 1978-II.

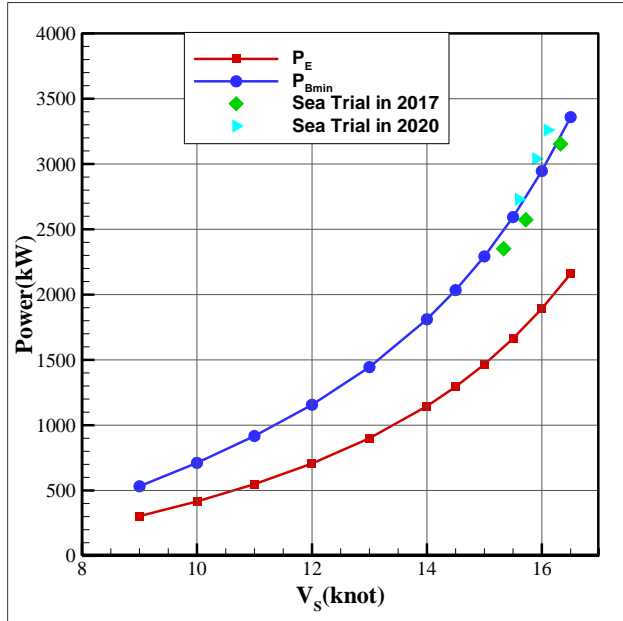


Figure 9. Power requirement plots of the ship with GRS and comparison of sea trial results for the ballast load draught.

Figure 10 and Figure 11 show the comparison between the CRS and GRS with for the full and ballast loading conditions.

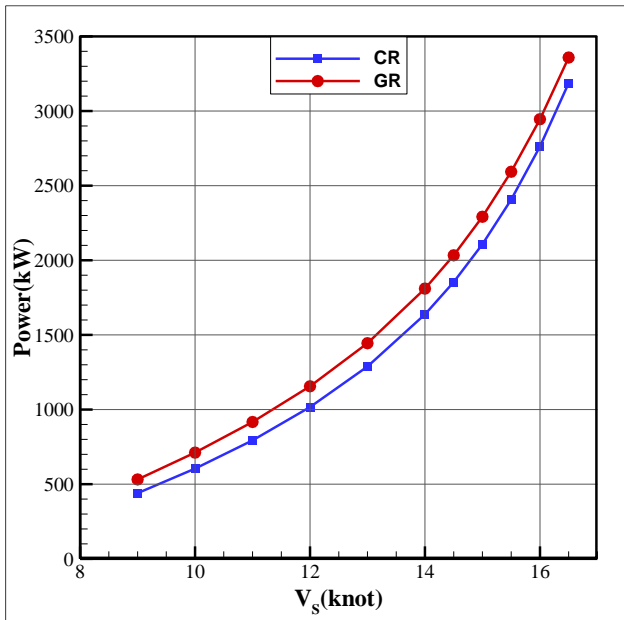


Figure 10. Comparisons of power requirements of the ship for the ballast load draught.

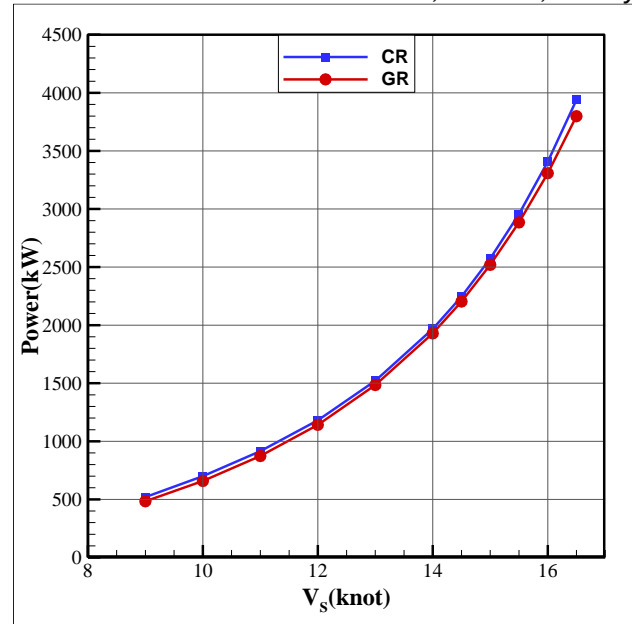


Figure 11. Comparisons of power requirements of the ship for the full load draught.

Results of the powering predictions show that GRS configuration is able to reduce the powering requirement by 2 % at the design speed as compared to CRS configuration in full loaded condition, but the powering requirement of GRS configuration appears to be increased by 6.5% as compared to CRS configuration in ballast condition.

## 5 CONCLUSIONS

Resistance and propulsion tests of two sisterships, SAKURA and SHIGENOBU of 2400 GT Containership were performed by aiming to investigate the differences, due to use of Conventional Rudder (CRS) and Gate Rudder (GRS) systems. The tests were carried out for two loading conditions, namely full loaded ( $T_{mid}=5.208$  m) and ballast ( $T_{mid}=4.175$  m) conditions. x- and y-component forces and turning moment on the CRS and GR are measured for full and ballast conditions in resistance tests as well. Extrapolations to full scale from model scale resistance data indicate that, although the resistances of the CRS and GRS cases are almost the same in full loaded condition, there is more than 2 % increase in the GRS resistance as compared to CRS resistance in ballast condition. Self-propulsion tests and powering predictions show that GRS configuration is able to reduce the powering requirement by 2 % at the design speed as compared to CRS configuration in full loaded condition, but the powering requirement of GRS configuration appears to be increased by 6.5% as compared to CRS configuration in ballast condition.

As a further study, the extrapolation methods will be evaluated considering the sea trials of the GATERS target ship, M/V ERGE.

## ACKNOWLEDGMENTS

This paper is based on the activities conducted in the collaborative European project GATERS which is an Innovation Action Project funded by the EC H2020 Programme (ID: 860337) with the independent aim and objectives. The project has an official sub-license agreement with Wartsila Netherlands BV to utilise the Gate Rudder Patent (EP 3103715) at specific retrofit projects of vessel sizes below 15000 DWT.

We thank the staff of Ata Nutku Ship Model Testing Laboratory for their efforts.

## REFERENCES

Fukazawa, M., Turkmen, S., Marino, A., & Sasaki, N. (2018, November). Full-scale gate rudder performance obtained from voyage data. In Proceedings of the A. Yücel Odabaşı Colloquium Series: 3rd International Meeting-Progress in Propeller Cavitation and Its Consequences: Experimental and Computational Methods for Predictions, Istanbul, Turkey (pp. 15-16).

ITTC (2017). 1978 ITTC Performance prediction method. Recommended procedure 7.5-02-03-01.4 Rev 04.

ITTC (2017). Propulsion/Bollard Pull Test. Recommended procedure 7.5-02-03-01.1 Rev 05.

Sasaki, N., Atlar, M., & Kuribayashi, S. (2016). Advantages of twin rudder system with asymmetric wing section aside a propeller. Journal of Marine Science and Technology, 21(2), 297-308.

Sasaki, N., & Atlar, M. (2018, November). Investigation into the propulsive efficiency characteristics of a ship with the Gate Rudder propulsion. In A. Yücel Odabaşı Colloquium Series 3rd International Meeting on Progress in Propeller Cavitation And its Consequences: Experimental and Computational Methods for Predictions.

Sasaki, N., Kuribayashi, S., & Miles, A. (2019). Full scale performance of Gate Rudder. In Royal Institution of Naval Architects (RINA)-Propellers and Impellers: Research, Design, Construction and Application. London, UK.

Turkmen, S., Fukazawa, M., Sasaki, N., & Atlar, M. (2018). Cavitation Tunnel tests and full-scale review of the first gate rudder system installed on the 400TEU container ship. In A. Yücel Odabaşı Colloquium Series 3rd International Meeting on Progress in Propeller Cavitation and its Consequences:

Experimental and Computational Methods for Predictions (pp. 29-39). Istanbul Turkey.

Tacar, Z., Sasaki, N., Atlar, M., & Korkut, E. (2020). ‘An investigation into effects of Gate Rudder® system on ship performance as a novel energy-saving and manoeuvring device’. Ocean Engineering, 218, 108250.

Yilmaz, N., Turkmen, S., Aktas, B., Fitzsimmons, P., Sasaki, N., & Atlar, M. (2018, November). Tip vortex cavitation simulation of a propeller in a Gate Rudder® system. In A. Yücel Odabaşı Colloquium Series 3rd International Meeting on Progress in Propeller Cavitation And its Consequences: Experimental and Computational Methods for Predictions.

## Predicting the Effect of Hull Roughness on Ship Resistance using a Fully Turbulent Flow Channel and CFD

**Roberto Ravenna<sup>1,\*</sup>, Ryan Ingham<sup>2</sup>, Soonseok Song<sup>3</sup>, Clifton Johnston<sup>3</sup>, Claire De Marco Muscat-Fenech<sup>4</sup>, Tahsin Tezdogan<sup>1</sup>, Mehmet Atlar<sup>1</sup>, Yigit Kemal Demirel<sup>5</sup>**

<sup>1</sup>Department of Naval Architecture, Ocean and Marine Engineering, University of Strathclyde, Glasgow, G1 0LZ, UK

<sup>2</sup>Department of Mechanical Engineering, Faculty of Engineering, Dalhousie University, Halifax, NS B3H 4R2, Canada

<sup>3</sup>Department of Naval Architecture & Ocean Engineering, College of Engineering, Inha University, Incheon, 22212, South Korea

<sup>4</sup>Department of Mechanical Engineering, Faculty of Engineering, University of Malta, MSD2080, Malta

<sup>5</sup>160 Bothwell Street, Glasgow, G2 7EA, UK

**Abstract:** The effects of poor hull surface conditions on fuel consumption and emissions are well-known yet not thoroughly understood. Therefore, the present study investigates the effect of widely adopted fouling control coatings and mimicked biofouling on a full-scale representative ship, the KRISO Containership (KCS). Different surfaces were tested in the Fully turbulent Flow Channel (FTFC) of the University of Strathclyde (including a novel hard foul-release coating, commonly used antifouling, barrier resin, soft foul-release coatings, and sandpaper-like surfaces). Then, the corresponding roughness functions developed for the test surfaces were embedded in Computational Fluid Dynamics (CFD) simulations using the modified wall function approach. Interestingly, the numerical predictions on the KCS hull showed that the novel hard foul-release coating tested had better hydrodynamic performance than the smooth case (maximum 3.6% decrease in the effective power requirements). Eventually, the present study confirmed the practicality of the FTFC used in combination with CFD-based studies to predict the effects of hull roughness on ship resistance and powering.

**Keywords:** Fully Turbulent Flow Channel; Roughness Functions; Ship Resistance; Marine Coatings; Computational Fluid Dynamics.

### 1 INTRODUCTION

A ship's hull surface condition is crucial to its hydrodynamic performance (Schultz, 2007). Hence, choosing the right fouling control coating (FCC) and drydock strategies for a vessel can offer significant economic and environmental advantages. Theoretical and numerical methods based on the turbulent boundary layer similarity law scaling technique, which was proposed by Granville (Granville, 1978, 1958), can accurately predict the hull roughness effect on ship resistance, provided that the roughness function of the surface is known (Demirel, 2015).

The aim of this study is to obtain new roughness functions for commonly used marine coatings and biofouled hull conditions from Fully turbulent Flow Channel (FTFC) experiments and predict their effect on full-scale ship resistance and powering. Also, an important objective was to utilise the FTFC of the UoS, which is a more practical facility than a towing tank. Therefore, various types of FCCs were tested in the FTFC, including antifouling, soft foul-release, barrier resin coatings and the newly developed and patented hard foul-release coating (FR02) by Graphite Innovation & Technologies (GIT, 2021). Similarly, roughness functions were developed from FTFC tests for widely adopted sandpaper-like surfaces mimicking biofouled conditions (medium light slime and medium slime) as similarly done in towing tests (Schultz,

2004; Song et al., 2021c). Furthermore, the roughness functions developed for a sandpaper-like surface (*Sand 220*) from the FTFC experiments was compared with previous towing tank tests. Finally, the present study also aims to confirm the robustness of CFD-based methods to predict the effect of hull roughness on ship resistance and powering using FTFC-based roughness function models.

The remaining of the paper is structured as follows: Section 2 presents the methodology adopted, including the experimental setup, roughness functions development, CFD simulations, and experimental uncertainty analysis. Section 3 of the paper discusses the results of the current experimental and numerical investigation. Furthermore, the novel roughness functions of the test surfaces are presented and used to predict the variation of resistance coefficients and effective power requirements for the full-scale KRISO Container Ship (KCS) hull. Section 4 presents the conclusions of the study with some concluding remarks and recommendations for future studies.

### 2 METHODOLOGY

#### 2.1. Approach

Figure 1 shows a schematic illustration of the experimental and numerical methodology adopted to investigate the roughness effects of marine coatings and hull roughness on the well-known KRISO Container Ship (KCS) ("KCS Geometry and Conditions," 2008). Drag characterisation

of arbitrary rough surfaces on flat plates can be evaluated by the indirect method for pipes (Granville, 1987) that uses the pressure drop  $\Delta p$  which can be measured along the streamwise length of the coatings (i.e., the pressure drop method). The FTFC was used to determine the skin friction coefficients  $c_f$ , by measuring the pressure drop  $\Delta p$  on the test surfaces. Eventually, the roughness functions for the test surfaces were obtained (i.e., roughness functions,  $\Delta U^+$ , roughness Reynolds numbers  $k^+$ , roughness length scale,  $k$ , etc.), and compared with literature, e.g., previous towing tests (Ravenna, 2019).

The modified wall function CFD simulations were adopted in the present study to predict the effect of the test surfaces on the full-scale KCS hull. The experimental roughness functions were embedded in CFD using the modified wall function approach to predict the effect of such surfaces on ship resistance and powering. The resistance coefficient results of the numerical predictions were then compared and validated across similar studies assessing the KCS resistance in smooth and rough conditions (Ravenna et al., 2022a; Song et al., 2020a; Yeginbayeva et al., 2020). Finally, the variations in effective power,  $\Delta P_E$  due to each test surface were estimated to give an immediate understanding of the effects of marine coatings and hull roughness on ship resistance and powering. Comparison and validation of the  $\Delta P_E$  values were conducted across the two numerical methods adopted and among similar studies (Schultz et al., 2011).

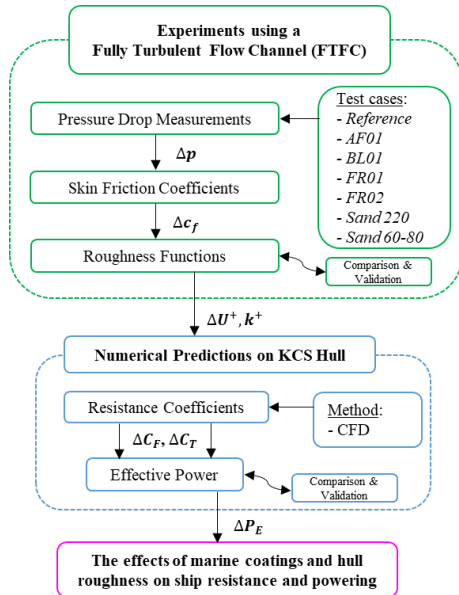


Figure 1: Schematic illustration of the methodology adopted.

## 2.2. Experimental Setup

### 2.2.1. Fully Turbulent Flow Channel

The University of Strathclyde's Fully Turbulent Flow Channel (FTFC), as shown in Figure 2-a, was designed to conduct a series of measurements for various types of fouling control coatings and rough surfaces in the freshly applied condition. Delivered to the UoS in 2019, the FTFC is a closed-circuit flow channel that can accommodate two opposing panels in its test section (Figure 2-b) located

downstream of a single centrifugal pump. The results from the FTFC can be accurately analogised to the turbulent boundary layer formed on a ship's hull at cruising speed. In fact, the FTFC enables the measurement of much higher flow speeds that would not be otherwise achievable in a typical towing tank with flat friction test plates (Ravenna et al., 2019). Table 1 summarises the main particulars of the FTFC upper limb section. For more information on the FTFC design, operation and calibration, the reader is advised to see (Marino et al., 2019).



(a) On-site picture of the FTFC.



(b) Top view of the test section accommodating a couple of transparent smooth reference panels.

Figure 2: The Fully Turbulent Flow Channel (FTFC) of the University of Strathclyde.

Table 1: Main particulars of FTFC upper limb.

Name	Symbol	Unit	Value
Length (Tolerance)	l	mm	3000 ( $\pm 0.05$ )
Height (Tolerance)	h	mm	22.5 ( $\pm 0.05$ )
Beam (Tolerance)	b	mm	180 ( $\pm 0.05$ )
Mean bulk velocity range	$U_M$	m/s	1.5 – 13.5
Flow rate	Q	l/s	10 – 60
Reynolds number	$Re_M$	-	$\approx 3.0 \cdot 10^5$
Material	-	-	Stainless steel (316L)
Centrifugal Pump power	P	kW	22

### 2.2.2. Test Panels Design and Preparation

In the present experimental campaign, four different types of FCCs were tested in the FTFC, including the newly developed hard foul-release coating (FR02) manufactured by GIT and marine coatings type that are commonly used in the shipping industry manufactured at Dalhousie University (DU), i.e., a self-polishing antifouling coating (AF01), a gelcoat barrier coating (BL01), and a soft foul-release coating (FR01). Furthermore, two sandpaper-like surfaces mimicking slime biofouling, i.e., Sand 220

(medium light slime) and the coarser, *Sand 60-80* (medium slime) manufactured at the UoS were tested. The coated panels (*Figure 3-a*) were tested along with an uncoated “control surface” or the “reference” to represent a hydraulically smooth surface, *Figure 3-b*. *Table 2* describes the dimensions of the test panels, while a breakdown of the type of each marine coating applied and the method of application is provided in *Table 3*.



(a) Test panels coated with different fouling control coatings and sand grit.



(b) Uncoated smooth reference panel.

**Figure 3:** Surfaces tested in the FTFC.

**Table 2:** Dimensions of the FTFC test panels.

Dimension	[mm]
Inner length	599
Inner breadth	218
Inner thickness	14
Outer length	662
Outer breadth	282
Outer thickness	16
Tolerance	0.1

**Table 3:** Overview of each test panel set.

Panel Set Name	Description (Prepared/Manufactured by)	Arithmetic mean roughness $R_a$ [ $\mu\text{m}$ ]
Reference	Smooth reference panel (UoS)	0.04
AF01	Self-Polishing antifouling coating (DU)	0.96
BL01	Gelcoat barrier coating (DU)	1.44
FR01	Soft foul-release coating (DU)	0.10
FR02	Hard foul-release coating (DU/GIT)	0.22
Sand 220	Aluminium oxide sand grit 220 (UoS)	294
Sand 60-80	Aluminium oxide sand grit 60-80 (UoS)	509

### 2.2.3. Pressure Drop Measurements

The UoS’ FTFC facility is fitted with six pressure taps on the side opposite the laser window to measure the pressure drop (*Figure 4*). Pressure taps 2-5 were chosen for pressure drop measurements because this tap configuration showed the lowest uncertainty (1.48% - 1.23%) at the lowest and highest pump frequency, respectively (Marino et al., 2019). It is of note that the pressure taps are 120 mm apart from each other, and the pressure drop  $\Delta p$  is used in relation to the linear distance  $\Delta x$  to assess the skin friction of the surfaces, according to the following formulae from equations 1 to 4:

$$\text{Skin friction coefficient: } c_f = \frac{\tau_w}{\frac{1}{2}\rho U_M^2} \quad (1)$$

$$\text{Wall shear stress: } \tau_w = -\frac{D_h \Delta p}{4 \Delta x} \quad (2)$$

$$\text{Hydraulic diameter: } D_h = \frac{2hb}{h+b} \quad (3)$$

$$\text{Reynolds number: } Re_M = \frac{U_M h}{\nu} \quad (4)$$

where  $\rho$ , the water density, is specified based on the formulae provided by (ITTC, 2011a), including the correction for the temperature of the channel flow (i.e., around 18 °C), which is continuously recorded by the channel sensor.

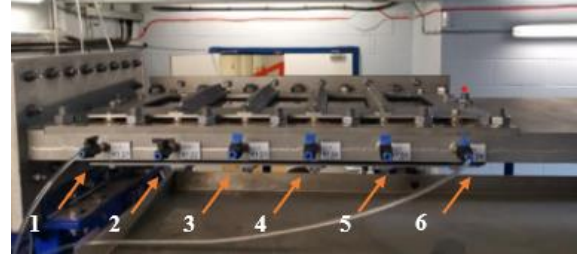


**Figure 4:** Pressure taps distribution numbered from 1 to 6 on test section of the FTFC.

### 2.3. Roughness Functions Determination

Roughness Function (or velocity loss function),  $\Delta U^+$ , is further retardation of flow in the boundary layer over a rough surface due to the physical roughness of that surface, which manifests itself as additional drag relative to a smooth surface. Different surfaces are characterised by different roughness functions to be modelled experimentally (Granville, 1958). The roughness function,  $\Delta U^+$  is a function of the roughness Reynolds number,  $k^+$ , which is defined by Eq (5):

$$k^+ = \frac{kU_\tau}{\nu} \quad (5)$$

where,  $k$  is the roughness length scale of the surface, and  $U_\tau$  is the friction velocity based on wall shear stress defined by Eq (6):

$$U_\tau = \sqrt{\tau_w/\rho} \quad (6)$$

where,  $\tau_w$  is the wall shear stress.

For this study, the indirect method for fully developed pipe flow proposed by (Granville, 1987) is used to calculate the roughness function  $\Delta U^+$  and roughness Reynolds number  $k^+$  for each coating as follows:

$$\text{Roughness function: } \Delta U^+ = \sqrt{\frac{2}{c_{f,s}}} - \sqrt{\frac{2}{c_{f,r}}} \quad (7)$$

$$\text{Roughness Reynolds number: } k^+ = \frac{1}{\sqrt{2}} Re_{M,r} \sqrt{c_{f,r}} \frac{k}{D_h} \quad (8)$$

where,  $c_{f,s}$  and  $c_{f,r}$  are the skin friction factors measured in the smooth and rough pipes, respectively, at the same value of  $Re_M \sqrt{c_f}$ . Furthermore, the hydraulic diameter,  $D_h$  of the channel was calculated by Eq (3).

It is of note that the selection of the roughness length scale,  $k$ , is critical to define a roughness function model, although  $k$  only affects the roughness Reynolds number,  $k^+$ . Therefore,  $k$  can be selected so that the roughness function models obtained are in agreement with the Nikuradse (Cebeci and Bradshaw, 1977; Nikuradse, 1933) or Colebrook type (Colebrook et al., 1939), provided that the

observed behaviours are still deemed appropriate relative to each other. Accordingly, the  $k$  values were selected (Table 6) to get a good agreement between the present roughness functions and the Nikuradse type reference roughness function model.

## 2.4. CFD simulations

The present simulations were developed in the Star-CCM+ software package (Version 15.06.007-R8), adopting the Unsteady Reynolds Averaged Navier–Stokes (URANS)-based CFD with the modified wall-function model recently validated by Song et al. (Song et al., 2020c). The governing equations of the present CFD simulations are as in (Ferziger et al., 2020). Furthermore, the  $k$ - $\omega$  SST (Shear Stress Transport) turbulence model was used with a second-order convection scheme and the Volume of Fluid (VOF) model with Eulerian multiphase was used to simulate surface gravity waves on the interface between air and water. Finally, the free surface effects were modelled using High-Resolution Interface Capturing (HRIC). It is of note that the rationale behind the present CFD modelling choices can be found in (Ravenna et al., 2022b).

### 2.4.1. Geometry and Physical Settings

CFD simulations were carried out on the container ship KCS in full-scale, at a towing speed of 24 knots (12.35 m/s), Froude number  $Fn = 0.26$ . The Reynolds number based on the ship speed and length was in the range of  $Re_L = 2.72 \times 10^9$ , which corresponds to the design speed of the full-scale KCS hull. Table 4 presents the particulars of the full-scale and model KCS adapted from Kim et al. (Kim et al., 2001) and (Larsson et al., 2013).

Table 4: KRISO Container Ship (KCS) full-scale principal characteristics.

Parameters		
Scale factor	$\lambda$	1
Length between the perpendiculars	$L_{PP}$ (m)	230
Length of waterline	$L_{WL}$ (m)	232.5
Beam at waterline	$B_{WL}$ (m)	32.2
Depth	$D$ (m)	19.0
Design draft	$T$ (m)	10.8
Wetted surface area w/o rudder	$WSA_{Total}$ (m <sup>2</sup> )	9424
Displacement	$\nabla$ (m <sup>3</sup> )	52030
Block coefficient	$C_B$	0.6505
Design speed	$V$ (kn; m/s)	24; 12.35
Froude number	$Fn$	0.26
Reynolds number	$Re$	$2.72 \cdot 10^9$
Centre of gravity	$KG$ (m)	7.28
Metacentric height	$GM$ (m)	0.6

The computational domain of the present simulations is a virtual towing tank (Figure 5), and the size of the domain was chosen following the International Towing Tank Committee (ITTC) recommendations (ITTC, 2011b) and similar studies (Song et al., 2021a, 2021b, 2020b). For clean hull case, the smooth type of wall-function was used, whereas the rough type of wall-functions, containing the roughness functions of the test surfaces, were used for the rough surfaces of the hull. Finally, the model ship was free to sink and trim, as no constraints were given. Figure 6 shows the volume mesh used for the present CFD analysis. The built-in automated mesher of Star-CCM+ software was used to generate the trimmed hexahedral-dominant finite element mesh. Further near-wall mesh refinements were

applied using prism layer meshes on the critical regions such as the free surface, the bulbous bow, and the stern. It is of note that for the present simulations, the wall  $y^+$  values were kept between 30 and 300 and higher than  $k^+$  values, as recommended by (Siemens, 2020), Figure 7. Furthermore, the average wall  $y^+$  value is 190 and the number of cells is in the range of 1.4 million, and these values are in close agreement with (Dogrul et al., 2020). Finally, all the simulations used the same mesh regardless of the hull roughness scenarios.

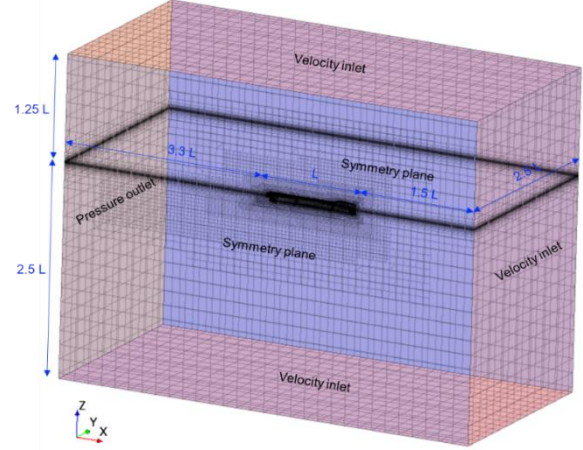


Figure 5: Computational domain and boundary conditions of the full-scale KCS simulations.

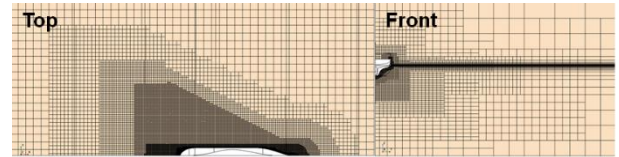


Figure 6: Volume mesh used for the KCS full-scale simulations.

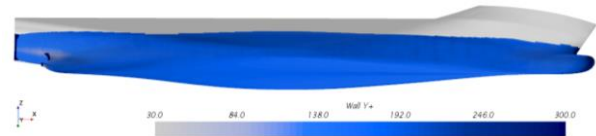


Figure 7: Non-dimensional wall distance  $y^+$  of the full-scale KCS with homogenous hull roughness (Sand 60-80) towed at 24 knots ( $Fn = 0.26$ ).

### 2.4.2. Modified Wall Function Approach

Eq (9) shows the roughness function model employed in the CFD software to represent the roughness conditions examined and obtain the variance in frictional resistance coefficients.

$$\Delta U^+ = \begin{cases} A & \rightarrow k^+ < k_{smooth}^+ \\ \frac{1}{\kappa} \ln C_s k^+ \sin \left[ \frac{\pi \log(k^+/3)}{2 \log(25/3)} \right] & \rightarrow k_{smooth}^+ \leq k^+ < k_{rough}^+ \\ \frac{1}{\kappa} \ln C_s k^+ & \rightarrow k_{rough}^+ \leq k^+ \end{cases} \quad (9)$$

(Cebeci and Bradshaw, 1977) recommended the following constants:  $k_{smooth}^+ = 2.25$ ,  $k_{rough}^+ = 90$ ,  $A = 0$  and  $C_s = 0.253$  for traditional Nikuradse roughness function and  $C_s = 0.5$  for other roughness types. (Demirel et al., 2017) proposed  $k_{smooth}^+ = 3$ ,  $k_{rough}^+ = 15$  and  $C_s = 0.26$  when

fitting the roughness function proposed by (Schultz and Flack, 2007). In the results section of the present study (Section 3), different constants to develop the roughness function models for the surfaces tested will be introduced.

#### 2.4.3. Verification and Validation

The verification procedure of the present CFD study was carried out to assess the spatial uncertainty of the simulations. Richardson's Grid Convergence Index (GCI) method (Richardson, 1911) was adopted as below. According to (Celik et al., 2008), the final expression for the fine-grid convergence index is defined as in equation (10):

$$GCI_{fine}^{21} = \frac{1.25e_a^{21}}{r_{21}^{p_a} - 1} \quad (10)$$

where,  $e_a^{21}$  is the approximate relative error of the key variables,  $\phi_k$ , obtained by equation (11), i.e., total resistance coefficient,  $C_T$ , as in equation (16):

$$e_a^{21} = \left| \frac{\phi_1 - \phi_2}{\phi_1} \right| \quad (11)$$

$r_{21}$  is the refinement factor given by  $r_{21} = \sqrt[3]{N_1/N_2}$ , where  $N_1$  and  $N_2$  are the fine and medium cell numbers, respectively. Also, the apparent order of the method,  $p_a$ , is determined by solving equations (12) and (13) iteratively:

$$p_a = \frac{1}{\ln(r_{21})} \ln \left| \frac{\varepsilon_{32}}{\varepsilon_{21}} \right| + q(p_a) \quad (12)$$

$$q(p_a) = \ln \left( \frac{r_{21}^{p_a} - s}{r_{32}^{p_a} - s} \right) \quad (13)$$

where  $s = \text{sign} \left( \frac{\varepsilon_{32}}{\varepsilon_{21}} \right)$ ,  $\varepsilon_{32} = \phi_3 - \phi_2$ ,  $\varepsilon_{21} = \phi_2 - \phi_1$  and  $r_{32}$  is the refinement factor given by  $r_{32} = \sqrt[3]{N_2/N_3}$ , where  $N_3$  is the coarse cell number.

The extrapolated value of the key variables is calculated by equation (14):

$$\phi_{ext}^{21} = \frac{r_{21}\phi_1 - \phi_2}{r_{21} - 1} \quad (14)$$

The extrapolated relative error,  $e_{ext}^{21}$ , is obtained by equation (15):

$$e_{ext}^{21} = \left| \frac{\phi_{ext}^{21} - \phi_1}{\phi_{ext}^{21}} \right| \quad (15)$$

Table 5: Parameters used for the discretisation error for the spatial convergence study, key variable:  $C_T$ .

Full-scale KCS simulation	
$N_1$	729,830
$N_2$	1,413,800
$N_3$	2,287,881
$r_{21}$	1.17
$r_{32}$	1.25
$\phi_1$	$1.988 \cdot 10^{-3}$
$\phi_2$	$1.996 \cdot 10^{-3}$
$\phi_3$	$1.965 \cdot 10^{-3}$
$\varepsilon_{32}$	$-3.07 \cdot 10^{-5}$
$\varepsilon_{21}$	$7.10 \cdot 10^{-6}$
$s$	-1
$e_a^{21}$	0.36%
$q$	-0.33
$p_a$	7.04
$\phi_{ext}^{21}$	$1.985 \cdot 10^{-3}$
$e_{ext}^{21}$	0.17%
$GCI_{fine}^{21}$	0.53%

Table 5 depicts the required parameters for the calculation of the spatial uncertainty of the simulation. A grid convergence index,  $GCI_{fine}^{21}$ , of 0.53% was estimated for

the fine-grid simulations conducted in the smooth surface condition with the inlet speed of 24 kn ( $R_n = 2.72 \cdot 10^9$ ), when using ten iterations every time step of 0.1 s. It is of note that the time step was selected following the recommendations of (ITTC, 2011b), for which  $\Delta t = 0.005 \sim 0.01 L_{WL}/V$ , where  $L_{WL}$  is the ship length at waterline and  $V$  is the ship speed. In comparison to the simulations in (Song et al., 2020c), the number of cells in the present study is considerably less, guaranteeing a reduced computational cost without compromising the accuracy of the results. In fact, the estimated GCI value of 0.53% indicates the great accuracy of the present CFD resistance prediction. Furthermore, the resistance coefficient results of the smooth case agree with the results found in the literature. In fact, the discretisation errors for the spatial convergence study, GCI, found by (Dogrul et al., 2020; Song et al., 2020b) for the KCS model scale hull were 0.40% and 0.10%, respectively. Therefore, the present CFD simulations to predict the effect of hull roughness on ship resistance and powering are further validated.

#### 2.5. Experimental Uncertainty Analysis

The uncertainties of the measurements in the FTFC tests were assessed following the ITTC-recommended procedures (ITTC, 2014). The standard errors for the coefficient of friction were calculated based on four to six replicate runs of the *FROI* panel at the minimum and maximum flow velocities, respectively. The precision uncertainty in the skin friction coefficient,  $c_f$  was calculated at a 95% confidence interval by multiplying the standard error by the two-tailed t values ( $t = 3.182, 2.571$ ) for three to five degrees of freedom, according to (Coleman and Steele, 2012).

Notably, the accuracy of the differential pressure sensor is  $\pm 0.075\%$ , and the accuracy of the magnetic flow meter was  $\pm 0.2\%$ , according to the manufacturer's specifications. The total uncertainty in the roughness function ( $\Delta U^+$ ) was  $\pm 14.4\%$  or 0.04 (whichever was larger) at the lowest  $Re_M \pm 6.5\%$  or 0.04 (whichever was larger) at the highest  $Re_M$ . For comparison, the high Reynolds number turbulent flow facility at the US Naval Academy achieved a relatively similar level of uncertainty, with their skin friction data being  $\pm 1.2\%$  at  $Re_M$  between  $4.0 \cdot 10^4 - 3.0 \cdot 10^5$  (Schultz et al., 2015). The total bias limit and precision limit for the skin friction coefficients ( $c_f$ ) were combined to give a total uncertainty of  $\pm 0.74\%$  at the lowest  $Re_M$  and  $\pm 0.47\%$  at the highest  $Re_M$ .

### 3 RESULTS AND DISCUSSION

#### 3.1. Fully Turbulent Flow Channel Experiments

##### 3.1.1. Roughness Function Models

As discussed in the methodology section (Section 2), provided that the roughness functions of the test surfaces are known, the CFD simulations can be used to predict the effect of hull roughness on ship resistance. Once the roughness functions have been calculated, they were directly compared with both Colebrook-type (Grigson,

1992) and Nikuradse-type (Cebeci and Bradshaw, 1977) roughness functions. Furthermore, the roughness functions of the sandpaper-like surfaces were compared for validation purposes with results obtained from other studies. In fact, previous flat plate towing tank experiments conducted for the same surface roughness (*Sand 220*) were used for comparison to the present results, *Figure 8*, (Ravenna, 2019). Finally, the new roughness functions have been developed using STAR-CCM+'s built-in features, as in Eq (9).

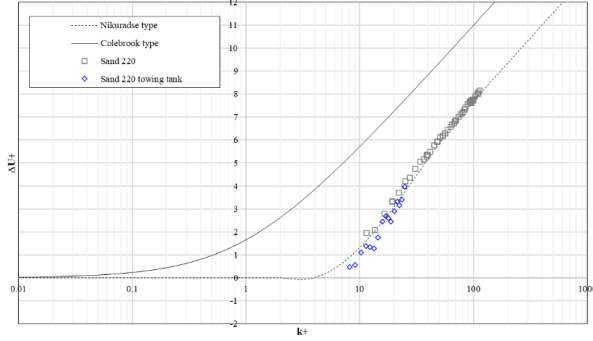


*Figure 8*: Experimental roughness function of the *Sand 220* surface developed from FTFC pressure drop measurements and from towing tank tests in (Ravenna, 2019).

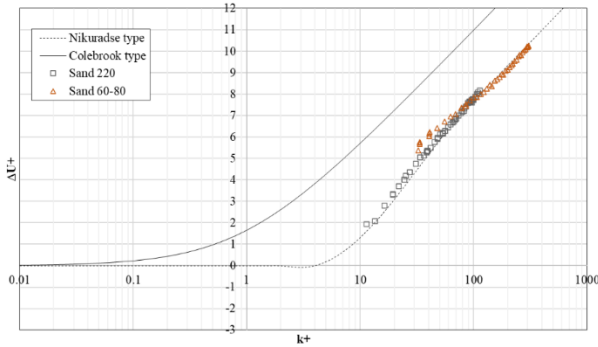


*Figure 9*: Experimental roughness functions of the sanded rough test surfaces (*Sand 220* and *Sand 60-80*) developed from FTFC pressure drop measurements.

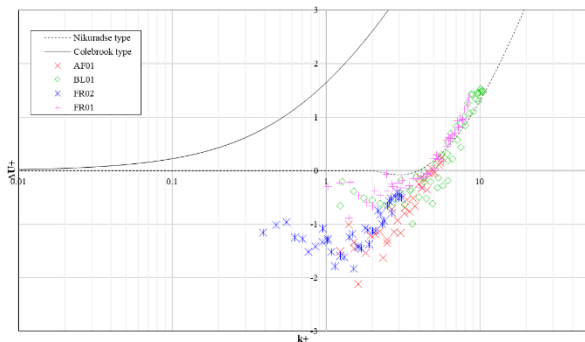


*Figure 10*: Experimental roughness functions of the sanded rough test surfaces (FCCs) developed from FTFC pressure drop measurements.

*Figure 9*, and *Figure 10* show the experimental roughness functions,  $\Delta U^+$ , vs roughness Reynolds numbers,  $k^+$  obtained from the FTFC pressure drop measurements

following Granville's approach (Granville, 1987). It is of note that the experimental roughness functions of the FCCs tested were modelled by curve fitting to the roughness function model of Nikuradse. For completeness, in *Table 6* are presented the curve fitting coefficients used for all the surfaces tested, where  $E$  is the so-called turbulent wall function coefficient. In fact, in StarCCM+, the wall roughness is modelled by moving the logarithmic region of the boundary layer closer to the wall. To decrease roughness,  $E$  must be increased to incorporate this effect. Therefore, for the smoother and best performing surfaces (*AF01* and *FR02*) to which corresponded negative roughness function values,  $E$  was increased from the standard  $E = 9$  to  $E = 12$  and  $E = 15$ , respectively.

*Table 6*: Curve fitting coefficients of the roughness functions for the test surfaces.

Test Surface	Roughness length scale, $k$ [m]	A	$C_s$	$E$	$k_s^+$	$k_r^+$
AF01	$9.598 \cdot 10^{-6}$	-1.5	0.2	12	1	15
BL01	$1.822 \cdot 10^{-5}$	-0.5	0.26	9	3	25
FR01	$1.544 \cdot 10^{-5}$	-0.5	0.2	15	3	25
FR02	$5.840 \cdot 10^{-6}$	-1.5	0.26	9	2	15
Sand 220	$1.532 \cdot 10^{-4}$	0	0.35	9	3	25
Sand 60-80	$3.530 \cdot 10^{-4}$	0	0.49	9	3	25

### 3.2. Numerical Prediction on full-scale KCS hull

#### 3.2.1. Ship Resistance Coefficients

Numerical predictions were conducted on the benchmark KRISO containership hull at a towing speed of 24 knots ( $Fn = 0.26$ ). The variance of resistance and powering requirements due to different test surfaces were calculated by incorporating the newly developed roughness functions into the Granville similarity law. The total resistance coefficient,  $C_T$ , is defined in equation (16) as a function of the total drag,  $R_T$ , the dynamic pressure,  $1/2 \rho V^2$ , and the hull wetted surface area,  $S$ :

$$C_T = \frac{R_T}{1/2 \rho S V^2} \quad (16)$$

where,  $V$  is the towing speed (i.e., the inlet velocity). It is well-known that the total ship resistance coefficient,  $C_T$ , can be decomposed into the frictional,  $C_F$ , and the residuary,  $C_R$  resistance coefficients, as given by Eq (17):

$$C_T = C_F + C_R \quad (17)$$

The variation of the frictional resistance coefficient  $\Delta C_F$  is the difference between the rough,  $C_{F,rough}$ , and smooth,  $C_{F,smooth}$ , conditions at the same Froude number can be given by Eq (18):

$$\Delta C_F = C_{F,rough} - C_{F,smooth} \quad (18)$$

Hence, the variation of the frictional resistance due to the presence of roughness can also be expressed in percentage, as in equation (19):

$$\% \Delta C_F = \frac{C_{F,rough} - C_{F,smooth}}{C_{F,smooth}} \cdot 100 \quad (19)$$

The total resistance for the rough ship,  $C_{T,rough}$ , is determined by:

$$C_{T,rough} = C_{T,smooth} + \Delta C_T \quad (20)$$

where the total roughness allowance,  $\Delta C_T$  is the variation in the total resistance coefficient between the rough,

$C_{T_{rough}}$ , and smooth,  $C_{T_{smooth}}$ , conditions, and can be given by Eq (21):

$$\Delta C_T = C_{T_{rough}} - C_{T_{smooth}} \quad (21)$$

Figure 11 presents the resistance coefficients of the test cases obtained from the CFD simulations analysis compared to a hydrodynamically smooth ship hull. It is notable that the total resistance coefficient results are in good agreement and show similar trends to the frictional resistance coefficients. Interestingly, the test cases *AF01* and *FR02* show a negative  $\Delta C_T$  of 2.1% and 3.6%, respectively. As expected, the phenomena of reduced  $\Delta C_T$  values are due to the negative roughness functions,  $\Delta U^+$  observed from the experimental measurements. On the other hand, the *BL01* and *FR01* cases lead to light  $\Delta C_T$  increases (0.9% for *BL01* and 0.2% for *FR01*) compared to the total added resistance due to mimicked slime (27.7% for *Sand 220* and 36.1% *Sand 60-80* cases). Above all, it can be noted that the *FR02* is the best performing FCCs tested while the sanded surface, *Sand 60-80*, leads to a higher increase in the total resistance coefficients.

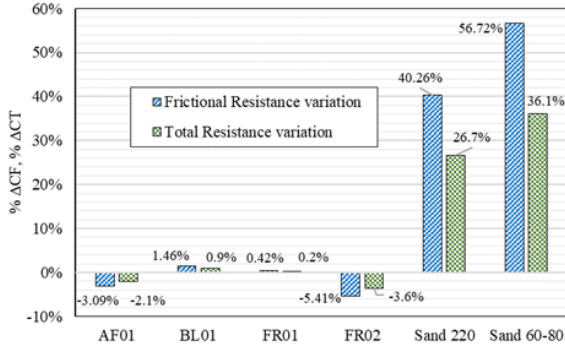


Figure 11: Frictional and total resistance coefficients variation in different hull roughness conditions.

Table 7, Table 8 and Figure 12 show the frictional and total resistance coefficients obtained for the test surfaces. It is also notable that the total resistance coefficient results are in good agreement and show similar trends to the frictional resistance coefficients. Furthermore, the results are reasonably in agreement with other studies found in the literature such as (Schultz, 2004; Yeginbayeva and Atlar, 2018).

Furthermore, the results are reasonably in agreement with other studies found in the literature such as (Schultz, 2004; Yeginbayeva and Atlar, 2018). In fact, (Schultz, 2004; Yeginbayeva and Atlar, 2018) found that a foul-release coating as applied measured an added frictional resistance  $\% \Delta C_F$  equal to 2.6%, and for a 150 m flat plate at 12 knots coated with sand 60-80 calculated  $\% \Delta C_F = 59\%$ .

Table 7: Frictional resistance results ( $C_F$ ) results on the full-scale KCS hull at 24 knots ( $Fn = 0.26$ ).

Test Surface	CFD simulations		
	$C_F$	$\Delta C_F$	$\% \Delta C_F$
Reference	$1.309 \cdot 10^{-3}$	-	-
AF01	$1.268 \cdot 10^{-3}$	$-4.05 \cdot 10^{-5}$	-3.09%
BL01	$1.328 \cdot 10^{-3}$	$1.91 \cdot 10^{-5}$	1.46%
FR01	$1.314 \cdot 10^{-3}$	$5.44 \cdot 10^{-6}$	0.42%
FR02	$1.238 \cdot 10^{-3}$	$-7.08 \cdot 10^{-5}$	-5.41%
Sand 220	$1.835 \cdot 10^{-3}$	$5.27 \cdot 10^{-4}$	40.26%

Sand 60-80  $2.051 \cdot 10^{-3}$   $7.42 \cdot 10^{-4}$  56.72%

Table 8: Total resistance coefficients of the full-scale KCS at 24 knots ( $Fn = 0.26$ ).

Test Surface	CFD simulations		
	$C_T$	$\Delta C_T$	$\% \Delta C_T$
Reference	$1.996 \cdot 10^{-3}$	-	-
AF01	$1.955 \cdot 10^{-3}$	$-4.096 \cdot 10^{-5}$	-2.05%
BL01	$2.015 \cdot 10^{-3}$	$1.860 \cdot 10^{-5}$	0.93%
FR01	$2.001 \cdot 10^{-3}$	$4.668 \cdot 10^{-6}$	0.23%
FR02	$1.925 \cdot 10^{-3}$	$-7.096 \cdot 10^{-5}$	-3.56%
Sand 220	$2.528 \cdot 10^{-3}$	$5.320 \cdot 10^{-4}$	26.66%
Sand 60-80	$2.717 \cdot 10^{-3}$	$7.210 \cdot 10^{-4}$	36.12%

### 3.2.2. Ship Effective Power, $\Delta P_E$

The change in effective power,  $\% \Delta P_E$  due to the different surfaces tested can be expressed by:

$$\% \Delta P_E = \frac{C_{T_{rough}} - C_{T_{smooth}}}{C_{T_{smooth}}} \cdot 100 = \frac{\Delta C_T}{C_{T_{smooth}}} \cdot 100 \quad (22)$$

similar to that used by (Tezdogan et al., 2015), where  $C_{T_{smooth}}$  is the total resistance coefficient of the hull in smooth conditions obtained from the present CFD simulations. It is of note that  $\% \Delta P_E$  is equal to  $\% \Delta C_T$ .

Table 9 shows the change in effective power,  $\% \Delta P_E$  due to the different test cases obtained from the CFD simulations and Granville's approach. It is of note that the largest difference between coating types for powering requirements is an average of 4.75%, between *FR02* and *BL01*. As expected, if the coatings *AF01* and *FR02* were applied on the ship hull, they would lead to a reduction in effective power requirements. In fact, *AF01* guarantees a maximum decrease of power requirements of 2.31%, while *FR02* of 3.79%.

As expected, the phenomena are again due to the negative roughness functions,  $\Delta U^+$  observed from the experimental measurements to which correspond negatively  $\Delta C_T$  values. On the other hand, the *BL01* and *FR01* cases lead to positive  $\% \Delta P_E$ , which translates into increases in effective power requirements of 0.93% for *BL01* and 0.23% for *FR01*. On the other hand, the total added effective power due to mimicked slime is 26.66% for *Sand 220* and 36.12% *Sand 60-80* cases. Above all, the *FR02* is the best performing FCCs tested while the sanded surface, *Sand 60-80*, would lead to a higher increase in the effective power. Finally, it can also be noted that the ratio  $\% \Delta P_E / \% \Delta C_F$  is in the range of 65% ÷ 70%, as would be expected (Schultz et al., 2011).

Table 9: Effective power variation ( $\% \Delta P_E$ ) of the full-scale KCS at 24 knots ( $Fn = 0.26$ ).

Test Surfaces	$\% \Delta P_{E_{CFD}}$
AF01	-2.05%
BL01	0.93%
FR01	0.23%
FR02	-3.56%
Sand 220	26.66%
Sand 60-80	36.12%

## 4 CONCLUSIONS AND FUTURE WORK

An experimental and CFD study was carried out to investigate the full ship hydrodynamic performance of different fouling control coatings and mimicked biofouling. The experimental part of the study led to the

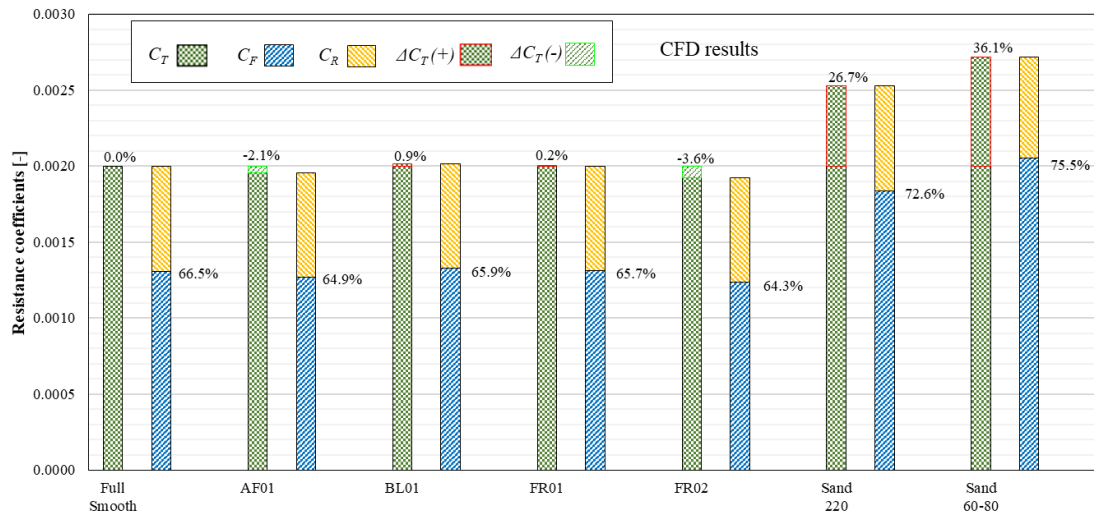


Figure 12: Percentage bar diagram of the resistance coefficients in different hull roughness.

introduction of novel experimental roughness functions for the FCCs tested including GIT's novel hard foul-release coating (*FR02*), while the numerical part scaled up the laboratory results to the size of a full ship length. The experimental roughness functions of the test surfaces were developed based on the pressure drop measurements conducted with the Fully Turbulent Flow Channel (FTFC) facility of the University of Strathclyde. The newly developed roughness functions of the fouling control coatings and sanded surfaces were implemented into the modified wall function approach in CFD using the Star-CCM+ software to provide scale-up results to ship length. The benchmark KRISO containership (KCS) hull in full-scale was chosen to calculate the variance of resistance and powering requirements due to different test surfaces at the design speed of 24 knots ( $Fn = 0.26, Re = 2.72 \cdot 10^9$ ).

Among the four fouling control coatings (FCCs) that were tested in the FTFC, the *FR02* coating (hard foul-release) displayed the best hydrodynamic performance across the entire Reynolds number range. In fact, *FR02* displayed lower frictional resistance coefficients than if the ship was considered as smooth as the acrylic reference panel (5.57% decrease). Furthermore, *FR02* led to a maximum decrease in effective power requirements of 3.6%. The results of the numerical prediction also show that the *AF01* (self-polishing antifouling coating) have better hydrodynamic performance than the smooth reference case (maximum decrease in effective power requirements of 2.1%). In contrast, *Sand 220* (medium light slime) and *Sand 60-80* (medium slime) have, as expected, the highest resistance due to their rougher characteristics. In fact, a ship hull with medium light slime (*Sand 220*) and medium slime (*Sand 60-80*) surface roughness characteristics as the test surfaces would experience a maximum increase in effective power requirements of 26.7% and 36.1%, respectively.

Further investigation could be conducted on the prediction of resistance of the coatings at different speeds, on different hulls, and using heterogeneous patch distribution of the roughness. It will also be beneficial to investigate the hydrodynamic performance of the same fouling control

coating under the effect of biofouling growth. Exposing surfaces to dynamically grown biofouling will give shipowners and operators a better indication of what powering penalty they should expect from these coatings after a certain time in active service. Finally, applying different mimicked biofouling to the panels before or after the coating application could also serve as a better method to predict the resistance behaviour of the as-applied condition to an existing rough ship hull.

Above all, the present study has provided several important findings, including the procedure to conduct pressure drop measurements with a FTFC, the application of Granville's method for pipes to develop roughness functions, as well as the introduction of roughness functions for novel or widely adopted marine surfaces and mimicked biofouling. The findings presented can help predict the required power, fuel consumption and greenhouse gas emissions of ships with hulls coated with certain fouling control coatings and/or in the fouled condition. As a final remark, the authors would like to emphasise that there is an enormous opportunity for growth around research on FTFCs. Indeed, the present study only represents an infinitesimal fraction of the number of coating products and surface roughness conditions that can be tested.

#### ACKNOWLEDGEMENTS

The research presented in this paper was carried out as a collaboration across the University of Strathclyde (<https://www.strath.ac.uk/>) and Dalhousie University (<https://www.dal.ca/>), with the support of Graphite Innovation and Technologies (<https://www.grapheneenterprise.ca/>). Furthermore, the authors gratefully acknowledge that the research presented in this paper was carried out as part of the EU funded H2020 project, VENTuRE (grant no. 856887, <https://h2020venture.eu/>), and the present work was also supported by Inha University Research Grant (<http://eng.inha.ac.kr/>). It should be noted that the results presented in this study were obtained using the ARCHIE-

WeSt High-Performance Computer ([www.archie-west.ac.uk](http://www.archie-west.ac.uk)).

## REFERENCES

- Cebeci, T., Bradshaw, P., 1977. Momentum transfer in boundary layers. Washington, D.C., Hemisph. Publ. Corp.; New York, McGraw-Hill B. Co. 407.
- Celik, I., Ghia, U., Roache, P., Freitas, C., Coleman, H., Raad, P., 2008. Procedure for Estimation and Reporting of Uncertainty Due to Discretization in CFD Applications. *J. Fluids Eng.* 130. <https://doi.org/10.1115/1.2960953>
- Colebrook, C.F., Inst. A.M.C.E., Thomas, M., 1939. A New Theory of Turbulent Flow in Liquids of Small Viscosity. *J. Inst. C.E* 11, 611.
- Coleman, H.W., Steele, W.G., 2012. Engineering application of experimental uncertainty analysis 33, 1888–1896. <https://doi.org/10.2514/3.12742>
- Demirel, Y.K., 2015. Modelling the Roughness Effects of Marine Coatings and Biofouling on Ship Frictional Resistance. University of Strathclyde. <https://doi.org/https://doi.org/10.48730/4b6n-9153>
- Demirel, Y.K., Uzun, D., Zhang, Y., Fang, H.-C., Day, A.H., Turan, O., 2017. Effect of barnacle fouling on ship resistance and powering. *Biofouling* 33, 819–834. <https://doi.org/10.1080/08927014.2017.1373279>
- Dogrul, A., Song, S., Demirel, Y.K., 2020. Scale effect on ship resistance components and form factor. *Ocean Eng.* 209, 107428. <https://doi.org/10.1016/j.oceaneng.2020.107428>
- Ferziger, J.H., Perić, M., Street, R.L., 2020. Computational Methods for Fluid Dynamics, Computational Methods for Fluid Dynamics. Springer International Publishing. <https://doi.org/10.1007/978-3-319-99693-6>
- Granville, P.S., 1987. Three indirect methods for the drag characterization of arbitrarily rough surfaces on a flat plates. *J. Sh. Res.* 31, 70–77.
- Granville, P.S., 1978. Similarity-law characterization methods for arbitrary hydrodynamic roughnesses. Bethesda: Rockville, MD, USA.
- Granville, P.S., 1958. The Frictional Resistance and Turbulent Boundary Layer of Rough Surfaces. *J. Sh. Res.* 2, 52–74. <https://doi.org/10.5957/jsr.1958.2.4.52>
- Grigson, C., 1992. Drag Losses of New Ships Caused by Hull Finish. *J Sh. Res* 36, 182.
- ITTC, 2014. Executive Committee Final report and recommendations to the 27 th ITTC.
- ITTC, 2011a. ITTC-Recommended Procedures-Fresh Water and Seawater Properties, in: 26th International Towing Tank Conference. Rio de Janeiro, pp. 1–45.
- ITTC, 2011b. ITTC-Recommended Procedures and Guidelines Practical Guidelines for Ship CFD Applications.
- KCS Geometry and Conditions [WWW Document], 2008. . SIMMAN 2008, FORCE Technol. URL [http://www.simman2008.dk/KCS/kcs\\_geometry.htm](http://www.simman2008.dk/KCS/kcs_geometry.htm)
- Kim, W.J., Van, S.H., Kim, D.H., 2001. Measurement of flows around modern commercial ship models. *Exp. Fluids* 31, 567–578. <https://doi.org/10.1007/s003480100332>
- Larsson, L., Stern, F., Visonneau, M., 2013. CFD in ship hydrodynamics - Results of the Gothenburg 2010 workshop, in: Computational Methods in Applied Sciences. Springer Netherland, pp. 237–259. [https://doi.org/10.1007/978-94-007-6143-8\\_14](https://doi.org/10.1007/978-94-007-6143-8_14)
- Marino, A., Shi, W., Atlar, M., Demirel, Y.K., 2019. Design specification, commission and calibration of the University of Strathclyde’s Fully Turbulent Flow Channel (FTFC) facility, in: 6th International Conference on Advanced Model Measurements Technologies for The Maritime Industry (AMT’19). Rome.
- Nikuradse, J., 1933. Laws of flow in rough pipes, NACA Technical Memorandum, 1292.
- Ravenna, R., 2019. Experimental Investigation on the Effect of Biomimetic Tubercles and Roughness on the Hydrodynamics of a Flat Plate. University of Strathclyde, Università degli studi di Trieste.
- Ravenna, R., Marino, A., Song, S., Atlar, M., Turan, O., Day, S., Demirel, Y.K., 2022a. Experimental study on the effect of biomimetic tubercles on the drag of a flat plate. *Ocean Eng.* 255, 111445. <https://doi.org/10.1016/J.OCEANENG.2022.111445>
- Ravenna, R., Marino, A., Song, S., Demirel, Y.K., Atlar, M., Turan, O., 2019. Experimental Investigation on the Effect of Biomimetic Tubercles on the Hydrodynamics of a Flat Plate. *Int. J. Mech. Ind. Eng.*
- Ravenna, R., Song, S., Shi, W., Sant, T., De Marco Muscat-Fenech, C., Tezdogan, T., Demirel, Y.K., 2022b. CFD analysis of the effect of heterogeneous hull roughness on ship resistance. *Ocean Eng.* 258, 111733. <https://doi.org/10.1016/J.OCEANENG.2022.111733>
- Richardson, L.F., 1911. IX. The approximate arithmetical solution by finite differences of physical problems involving differential equations, with an application to the stresses in a masonry dam. *Philos. Trans. R. Soc. London. Ser. A, Contain. Pap. a Math. or Phys. Character* 210, 307–357. <https://doi.org/10.1098/RSTA.1911.0009>
- Schultz, M.P., 2007. Effects of coating roughness and biofouling on ship resistance and powering.

- Biofouling 23, 331–341. <https://doi.org/10.1080/08927010701461974>
- Schultz, M.P., 2004. Frictional resistance of antifouling coating systems. *J. Fluids Eng. Trans. ASME* 126, 1039–1047. <https://doi.org/10.1115/1.1845552>
- Schultz, M.P., Bendick, J.A., Holm, E.R., Hertel, W.M., 2011. Economic impact of biofouling on a naval surface ship. *Biofouling* 27, 87–98. <https://doi.org/10.1080/08927014.2010.542809>
- Schultz, M.P., Flack, K.A., 2007. The rough-wall turbulent boundary layer from the hydraulically smooth to the fully rough regime. *J. Fluid Mech.* 580, 381–405. <https://doi.org/10.1017/S0022112007005502>
- Schultz, M.P., Walker, J.M., Steppe, C.N., Flack, K.A., 2015. Impact of diatomaceous biofilms on the frictional drag of fouling-release coatings. *Biofouling* 31, 759–773. <https://doi.org/10.1080/08927014.2015.1108407>
- Siemens, 2020. STAR-CCM+, User Guide. Version 15.06.
- Song, S., Dai, S., Demirel, Y.K., Atlar, M., Day, S., Turan, O., 2021a. Experimental and theoretical study of the effect of hull roughness on ship resistance. *J. Sh. Res.* 65, 62–71. <https://doi.org/10.5957/JOSR.07190040>
- Song, S., Demirel, Y.K., Atlar, M., 2020a. Penalty of hull and propeller fouling on ship self-propulsion performance. *Appl. Ocean Res.* 94, 102006. <https://doi.org/10.1016/j.apor.2019.102006>
- Song, S., Demirel, Y.K., Atlar, M., 2020b. Penalty of hull and propeller fouling on ship self-propulsion performance. *Appl. Ocean Res.* 94, 102006. <https://doi.org/10.1016/j.apor.2019.102006>
- Song, S., Demirel, Y.K., Atlar, M., Dai, S., Day, S., Turan, O., 2020c. Validation of the CFD approach for modelling roughness effect on ship resistance. *Ocean Eng.* 200, 107029. <https://doi.org/10.1016/j.oceaneng.2020.107029>
- Song, S., Demirel, Y.K., De Marco Muscat-Fenech, C., Sant, T., Villa, D., 2021b. Investigating the Effect of Heterogeneous Hull Roughness on Ship Resistance Using CFD. *J. Mar. Sci. Eng.* 9. <https://doi.org/10.3390/jmse9020202>
- Song, S., Ravenna, R., Dai, S., De Marco Muscat-Fenech, C., Tani, G., Demirel, Y.K., Atlar, M., Day, S., Incecik, A., 2021c. Experimental investigation on the effect of heterogeneous hull roughness on ship resistance. *Ocean Eng.* 223. <https://doi.org/10.1016/j.oceaneng.2021.108590>
- Tezdogan, T., Demirel, Y.K., Kellett, P., Khorasanchi, M., Incecik, A., Turan, O., 2015. Full-scale unsteady RANS CFD simulations of ship behaviour and performance in head seas due to slow steaming. *Ocean Eng.* 97, 186–206. <https://doi.org/10.1016/j.oceaneng.2015.01.011>
- Yeginbayeva, I.A., Atlar, M., 2018. An experimental investigation into the surface and hydrodynamic characteristics of marine coatings with mimicked hull roughness ranges. *Biofouling* 34, 1001–1019. <https://doi.org/10.1080/08927014.2018.1529760>
- Yeginbayeva, I.A., Atlar, M., Turkmen, S., Chen, H., 2020. Effects of ‘in-service’ conditions–mimicked hull roughness ranges and biofilms–on the surface and the hydrodynamic characteristics of foul-release type coatings. *Biofouling* 36, 1074–1089. <https://doi.org/10.1080/08927014.2020.1855330>

## The Effect of the Addition of Tubercles on the Performance of Moth-T-foil

**Margot G. C. Cocard<sup>1\*</sup>, Sandy Day<sup>1</sup>, Tahsin Tezdogan<sup>1</sup>, Moritz Troll<sup>1</sup>, Tonio Sant<sup>2</sup>**

<sup>1</sup>University of Strathclyde, Department of Naval Architecture, Ocean and Marine Engineering, Glasgow, UK

<sup>2</sup>University of Malta, Department of Mechanical Engineering, Malta

### Abstract:

Tubercles have proven, in the nature (e.g., the humpback whale) as well as in engineering (e.g., rudders, wind and tidal turbine blades, propellers, etc.), to be an efficient device to control the flow and to delay stall. This study focusses on the implementation of tubercles on the main lifting foil of a moth sailing dinghy. To do so, a ‘‘Bladerider’’ flapped T-foil with and without tubercles was tested in the Kelvin Hydrodynamics Laboratory in Glasgow, at a range of speeds, angles of attack, flap angles but also immersions. The results of these full-scale tow-tests, including the lift and drag data of the bare foil, are presented in this paper. The measurement data was used to investigate the effect of the addition of tubercles on the performance of a T-foil.

**Keywords:** Hydrodynamics; Hydrofoil; Moth; Tubercles; Biomimicry.



**Figure 1 - Moth Worlds 2017 (Photo: Martina Orsini, Cat Sailing News)**

### Nomenclature

$D$ [N]	Drag Force
$DA$ [m <sup>2</sup> ]	Drag Force Area
$L$ [N]	Lift Force
$LA$ [m <sup>2</sup> ]	Lift Force Area
$V$ [m/s]	Speed
$\rho$ [kg/m <sup>3</sup> ]	Density

Other symbols are defined as required in the text.

### 1 INTRODUCTION

Nature is a great source of inspiration to create substantial, innovative designs and applications to solve human challenges in a variety of fields. In the energy, aero- and hydrodynamic sectors, some of the most common nature-inspired designs come from the humpback whale (*Megaptera Novaeangliae*, *Figure 2*); a 40-50 feet long baleen whale weighing 80,000 pounds which has been studied extensively over the last two decades due to its advantageous maneuverability and agility capabilities. In fact, its surprising dexterity is attributed, in part, to its high aspect ratio flippers, which have distinctive bumps, so called tubercles, on the leading edge (LE).

\* Corresponding author e-mail: [margot.cocard@strath.ac.uk](mailto:margot.cocard@strath.ac.uk)



**Figure 2 - Humpback Whale Flippers with Tubercles (Photo: AAP, The Guardian)**

These large and irregular protuberances are believed to act as passive flow control devices (*Fish & Battle, 1995*) and have proven to delay flow stall and maintain lift over a greater range of angles of attack (AoA) (*Miklosovic, Murray, Howle, & Fish, 2004*). Indeed, (*Miklosovic & al. 2004*) have shown through wind tunnel experiments, that the addition of leading-edge tubercles to a scale model of an idealized humpback whale flipper delays the stall angle from 12 to 18 degrees, while increasing lift by approximately 8% and decreasing drag by nearly a third.

According to (*Fish & al. 2006, 2011*), this is explained by the deflection of the fluid approaching the LE into the troughs and the generation of spanwise vortices. In fact, the tubercle leading edge (TLE) is believed to act as a vortex generator (i.e., similar to those used on aircraft); the wave-shaped vortices, seen in *Figure 3*, energise the fluid flow by adding momentum within the boundary layer. This results in the flow remaining attached and therefore stall to be delayed.

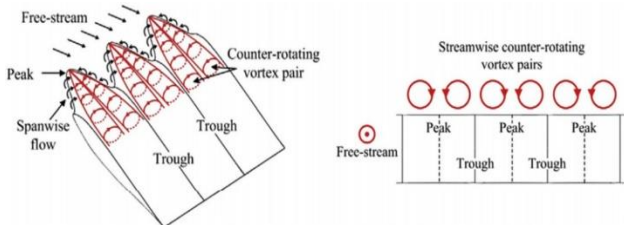


**Figure 3 - Vortex Structures Resulting from the Leading-Edge Tubercles (Shin & al., 2018)**

On the other hand, (*Van Nierop & al. (2008)*) suggested that the tubercles essentially alter the pressure distribution on the foil so that the flow does not separate in the close proximity of the leading edge. However, their research led to different results than *Miklosovic & al.'s (2004)* (e.g., smaller maximum lift coefficient and a less sudden stall). According to *Zhu (2008)*, these are due to the neglect of the tip effects but also the application of the potential flow theory of an inviscid and irrotational flow to a rotational flow problem (*Aftab al., 2016*).

So even though the working mechanism of tubercles, as well as their optimum configuration, have still not been clearly understood, their implementation into the engineering domain has proven to be effective (i.e., by

improving lifting surface performance) and economically feasible (*Pechlivanoglou, 2012*). Indeed, Juan Kouyoumdjian has for example designed a dual tubercle rudder system for the ClubSwan 50 sailing yacht whereas WhalePower has integrated tubercles on the LE of wind-turbine and fan blades as seen in *Figure 4*. In fact, by using this technology, WhalePower has managed to significantly increase their efficiency by capturing more energy out of lower-speed winds (i.e., TLE “turbines generate the same amount of power at 10 miles per hour that conventional turbines generate at 17 miles per hour”) (*Hamilton, 2008*).



**Figure 4 - WhalePower Wind Turbine (Photo: Whalepower, Earth Magazine)**

It is clearly believed that the benefits of tubercles could be implemented into the design of other lifting devices and more exactly into the design of foiling vessels (i.e., sailing yacht, high speed, or support vessels). Indeed, even though hydrofoils have an old history, their evolution is still to be discussed as their use in a field such as the maritime transportation, which is driven by speed and energy efficiency, is of critical importance. This is why, this study focusses on experimentally investigating the effects of tubercles on the performance of a hydrofoil and more exactly on a Moth sailing foil. The results of these findings could then be applied and extended to any other application involving the generation of lift from an airfoil or hydrofoil and obviously to any future design of foiling vessels.

The International Moth dinghy (*Figure 5*) is actually one of the most advanced boat classes in the world, capable of reaching speeds of over 30 knots. It was invented by Len Morris in 1928 and since then has evolved to a carbon-fibre mono-hull fitted with two fully-submerged T-foils on the centreline (i.e one on the centreboard for primary support and the other on the rudder for support and control).

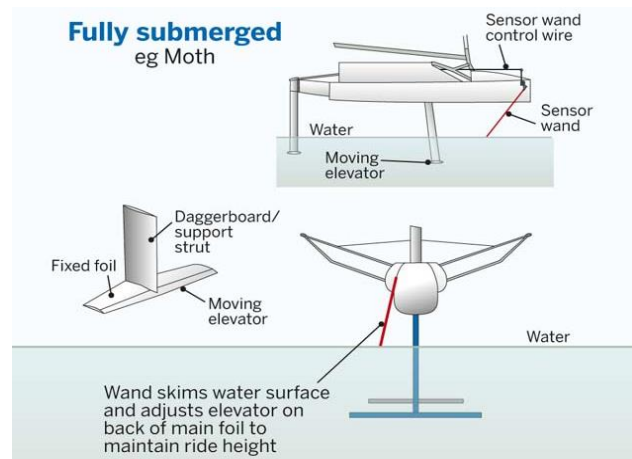


**Figure 5 - Moth Foil Configuration (Photo: Yachting World)**

These twin foils are capable of generating a lift that is large enough to raise the hull out of the water. Both foils have an elevator flap which is used to vary the camber of the foil. The daggerboard flap actually controls the ride height mechanically thanks to a bow-mounted wand sensor whereas the rudder one is controlled by the skipper via a rotating tiller extension.

For this purpose, the main foil of a Moth was used and fitted with 3D printed LET. This enabled to obtain experimental measurements of flapped T-foils but also to quantify the difference in the performance of the foil with and without tubercles.

## 2 TANK TESTING

This paper documents a series of full-scale tow-tests intended to investigate the effect of incorporating LET onto a “Bladerider” flapped T-foil. It was processed in two stages at the Kelvin Hydrodynamic Laboratory (KHL) at the University of Strathclyde (UoS) in Glasgow, Scotland.

The first stage was conducted in early 2018 as part of a Bachelor project aiming at studying the effect of tubercles on the performance of a foil. It enabled to commission a test rig as well as develop a valid procedure for testing flapped T-foils in a towing tank. Indeed, it was used to troubleshoot the test set-up in order to, at a later stage, with the combination of Computational Fluids Dynamics (CFD), investigate some of the complex flow phenomena associated with flapped T-foils. These include the interaction between the flow on the horizontal and vertical components of the foil, the free surface effects, the effects of the change of immersion, the effects of heel, yaw and tip immersion, ventilation, etc.

This was part of Stage 2 even though it will obviously be required to conduct more experiments in the future. Thus, the second stage took place in late 2018 and was also used to deepen the study of the effect of the addition of tubercles, which is presented in this paper. Both stages were, however, conducted using different 3D printing materials. More information is enclosed in the “Tubercles” sub-section.

The technique used during these experiments, including the building of the rig, was inspired by (Beaver & Zselezky, March 2009). They carried out an extensive study of the aero- and hydrodynamic flow around a Moth dinghy they designed and built, the “Hungry Beaver”, considering different hydrofoil configurations.

### 2.1 Moth ‘Bladerider’

As mentioned earlier, as part of this project, the main (i.e., dagger board) foil of a “Bladerider” International Moth sailing dinghy (2006), as seen in Figure 6, was used. This foil belongs to one of the authors and was utilized mostly due to its availability but also because it invites comparison with the “Vendor 1” foil from (Beaver & Zselezky, March 2009). It is composed of two components made from carbon skins and a foam core: a vertical symmetrical strut and a horizontal assymmetric tip tapering lifting foil.

These are joint together using a silicone-based sealant and reinforced by a squashed bulb. The flap, on the other hand, is attached to the foil thanks to a hinge composed of black rubber and represents around 35% of the chord of the lifting foil.

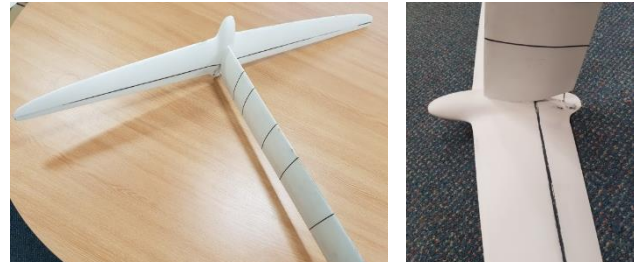


Figure 6 - “Bladerider”-type Foil

The geometry and the main dimensions of the foil are shown in Figure 7. Because the sections of the foil were unknown and not published, the geometry and the main dimensions of the foil, including the wing profile, were derived from the digital representations of the hydrofoil. These 3D-scans were performed using the Advanced Forming Research Centre (ARFD). They enabled the authors to derive sections and to remodel the foil using the 3D-modeler Rhinoceros 5 for conducting Computational Fluid Dynamics (CFD) simulations to study the complex flow phenomena associated with flapped T-foil. The foil jigs, which are used to hold the flap at a neutral position when the hinge has to be renovated, were also utilized to obtain the main dimensions and the section shapes.

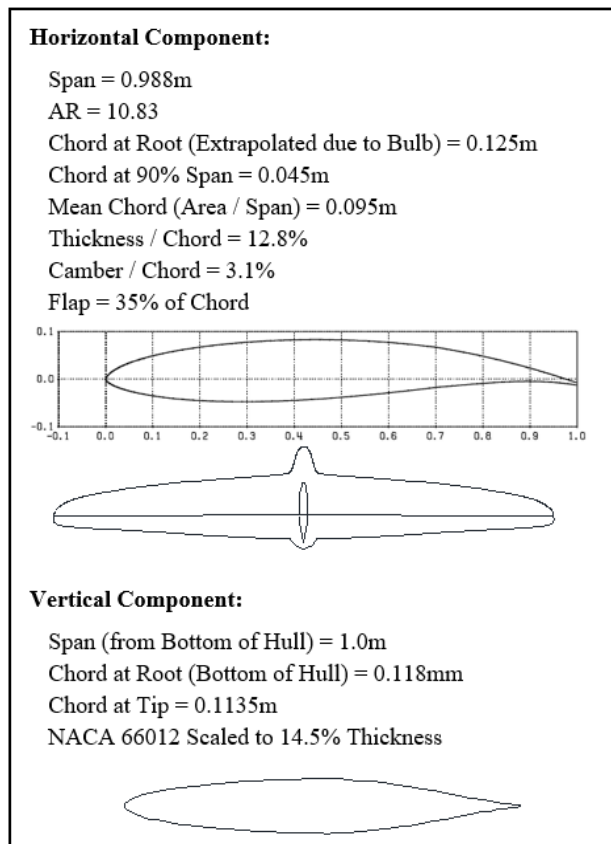


Figure 7 - “Bladerider” Dagger-board T-foil Geometry and Dimensions

## 2.2 Tubercles

The tubercles were designed in a way that they could be attached and detached from an existing appendage easily. This was done by designing tubercles with flexible, thin but strong arms. In fact, the tubercles which are shown in Figure , were designed in a ‘Taco’ shape, which basically consists of two components: the arms and the protuberance. *Table 1* shows the specification of the tubercles.

**Table 1 - Tubercle Specifications**

Length (Extreme)	40mm
Height (Extreme)	9.2mm
Arm Thickness	0.5mm
Protuberance Wavelength	50mm
Protuberance Amplitude	11mm

During the first set of experiments (i.e., Stage 1), in early 2018, the tubercles were printed with a combination of ‘‘TangoBlack’’ and ‘‘Tango Plus’’ material (i.e., which acts as printed rubber) using a ‘‘Object Eden 350’’ printer at the Design, Manufacture and Engineering Management (DMEM) department at the UoS. However, because the tubercles, including the protuberance, were too flexible and showed signs of distortion under the loads applied and probably deformation (i.e., leading to a large drag penalty), another material, ‘‘PolyLactic Acid’’ (PLA), was used for the second set of experiments (i.e., Stage 2). This enabled to enhance their rigidity and was done using an ‘‘Ultimaker 2+ Extended’’ printer owned by one of the authors.

A first attempt to apply the tubercles was done using ‘‘Copydex’’, a white water-based glue, but was replaced by silicon adhesive as it failed. Silicone adhesive was in fact judged as more appropriate as it enabled to smoothen the lips of the tubercle arms.

To have a better understanding of the effects of tubercles, it was decided to test different configurations of tubercle coverage during Stage 1. Indeed, three different configurations were tested: no tubercle coverage, one third tubercle coverage (i.e., 3 tubercles were fitted on each side of the foil, close to the tips) and full tubercle coverage (i.e., 8 tubercles were fitted on each side of the foil).

On the other hand, during Stage 2, only the full tubercle coverage, as seen in *Figure 8*, was investigated, as it proved to be the configuration with more effects on the performance of the foil.



**Figure 8 - Foil with Full Coverage of Tubercles**

## 2.3 Test Rig and Instrumentation

As mentioned earlier, the tests took place in the Kelvin Hydrodynamics Laboratory (KHL) at the UoS in Glasgow; a 76m long, 4.6m wide and 2.5m deep tank equipped with a towing carriage of a maximum speed of 4.6m/s. The foil was tested upright in different conditions. Indeed, angles of attack (pitch/ trim), flap angles but also immersion were varied at a range of speed to experimentally measure their effect on lift and drag. On the other hand, tubercles were fitted to the appendage to investigate their effect on the performance of the foil.

The rig used during these experiments, a bespoke test rig shown in *Figure 9*, was inspired by (*Beaver & Zselezky, March 2009*). It was restricted to zero yaw and zero roll conditions. In fact, the rig was built in a way that the foil could be mounted in a pivoting frame (i.e., which was rotating thanks to a pitch angle adjustment plate attached to the fixed part of the rig) and supported by two softwood moulds/ saddles at two points along its vertical component. These were used to adjust the angle of attack (AoA) of the horizontal foil (i.e., in one degree of increments over a range of 15 deg.) but was also an easy way to vary the immersion (i.e., by sliding the foil up and down in the saddles). On the other hand, the flap angle of the horizontal foil was controlled using the original rod/ bell crank in the strut and an extended pointer/ needle which enabled a more accurate measurement at the top of the foil. This is shown in *Figure 9*.

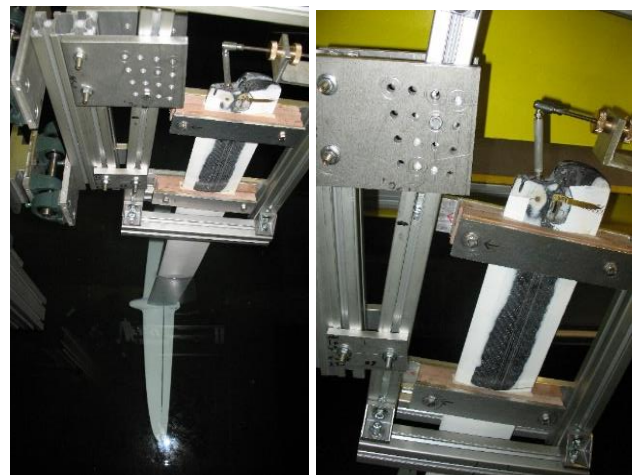


**Figure 9 - Towing Tank Test Rig**

The rig was then fitted to the vertical member of the standard towing post using a rig support which could be regarded as a classical simply-supported beam mounted in the vertical direction. Indeed, it was constituted of two tri-axial loadcells (i.e., with a maximum measurable load of 250kg) attached to two mounts with a bearing releasing moments in the pitch axis and for the upper mount, a low friction slide (i.e., to release the vertical force). These loadcells were calibrated individually along the X, Y and Z directions, so the cross-coupling error could be determined.

A total of close to 450 tests (i.e., including repeats) were carried out during stage 2 whereas close to 145 tests were

performed during the first one. It followed a straightforward procedure as once the different conditions (i.e., the immersion, the AoA, and the flap) were set, it was only necessary to accelerate the carriage up to required speed in order to measure the load in the cells (i.e. lift and drag in the X and Y directions respectively). *Figure 10* shows the foil without (left) and with (right) tubercles during the tests.

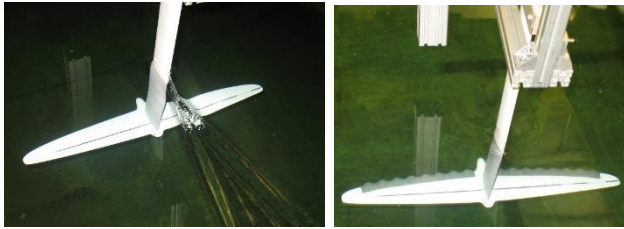


**Figure 10 - Towing Tank Experiment (Stage 2)**

In fact, the tests were performed with a range of speed from 0.5 to 4.5m/s, close to the maximum speed the carriage can achieve (i.e., corresponding to Reynolds numbers of  $2.0 * 10^4$  to  $1.8 * 10^5$  ). This obviously did not replicate the operational speed of a Moth in foiling conditions but was deemed satisfactory for this study as it corresponds to a speed slightly higher than the take-off speed (i.e., around 3.5m/s). It also enabled to gain some insight into the hydrodynamics of foil and tubercle technology.

During the second set of experiments (i.e., Stage 2), most of the tests were actually conducted at a submergence of 457mm. This was chosen in accordance to (Beaver & Zselezky, March 2009) but also because it corresponds to a relatively appropriate depth for Moth take-off, knowing that the maximum speed which could be achieved with the carriage was 4.5 m/s. On the other hand, it was found to be convenient because it reduced the impact of wave-making and free surface effects on the horizontal foil. Other tests were carried out at an immersion of 100mm and 334mm (i.e., the speed believed to be the optimum depth for this foil) to explore the effects of immersion but also to compare the results to the first set of experiments conducted in early 2018.

Regarding the flap angle, it was decided to study the effect of positive and negative angles on the performance of the foil. This is why it was changed from -6 to +6deg. The AoA, on the other hand, was adjusted from 0 to +6deg. The test matrix of the first set of experiments is shown in *Table 2* whereas the text matrix of the second slot of experiments' is enclosed in *Table 3*.

**Table 2 - Test Matrix (Stage 1)**

Test Characteristics	Immersion	Speed	AoA	Flap
Tests 001 to 054 (w/o Tubercles)	334mm	0.5 to 4.0m/s in increments of 0.50m/s	0, 2 and 5deg.	0, 3, 2 and 6.4deg.

Tests 055 to 099 (1/3 Tubercle Coverage)	334mm	2.0, 3.0 and 4.0m/s	0, 2 and 5deg.	0, 3, 2 and 6.4deg.
Tests 100 to 143 (Full Tubercle Coverage)	334mm	2.0, 3.0 and 4.0m/s	0, 2 and 5deg.	0, 3, 2 and 6.4deg.

**Table 3 - Test Matrix (Stage 2)**

Test Characteristics	Immersion	Speed	AoA	Flap
Tests 001 to 024 (w/o Tubercles, Deep Immersion, Neutral Flap)	457mm	0.5 to 4.5m/s in increments of 0.25m/s	0 to 6deg. in steps of 1deg.	0deg.
Tests 025 to 322 (w/o Tubercles, Deep Immersion, Different Flap Angles)	457mm	0.5 to 4.5m/s in increments of 0.50m/s	0 to 6deg. in steps of 2deg.	-6, 0, +6deg.
Tests 323 to 347 (w/o Tubercles, Optimum Submergence, Different Flap Angles)	334mm	2.5 to 4.5m/s in increments of 0.50m/s	0, 2, 5deg.	0, +6deg.
Tests 348 to 405 (w/o Tubercles, Shallow Immersion, Different Flap Angles)	100mm	3.0 to 4.5m/s in increments of 0.50m/s	0 to 6deg. in steps of 2deg.	-6, 0, +6deg.
Tests 406 to 441 (With Tubercles, Deep Immersion, Different Flap Angles)	457mm	0.5 to 4.5m/s in increments of 0.50m/s for AoA 0 Flap 6, AoA 6 Flap 0 and AoA 6 Flap -6 and from 3 to 4.5m/s for others	0 to 6deg. in steps of 2deg. for Flap 0 and only 6deg. for Flap -6deg.	-6, 0deg.

It is important to note that the zero position of both the AoA of the horizontal and the angle of the flap were difficult to determine as they are specific to the foil arrangement/assembly. For this foil, it was assumed that the strut was raked forward at around 7 deg. (i.e., 7deg. of pitch on the strut corresponds to 0deg. of pitch on the foil horizontal). This is usually done using shims before bonding the two components together to reduce the risk of ventilation. On the other hand, the natural resting point of the horizontal, when it is not under load, was taken as the neutral flap angle. During some tests (i.e., at high speed and large AoA/flap angle) of Stage 2, it was noticed that the needle indicating the flap angle moved. This was associated with the bending of the slender push rods which controls the flap inside the strut and was videoed to be estimated.

### 3 EXPERIMENT RESULTS

This section compares the lift and drag results of the bare foil and the foil with tubercles of Stage 2. The results of Stage 1 are, on the other hand, just briefly explained but not extended. However, a comparison of both stages is included.

For this purpose, the results of the experiments are shown in terms of lift and drag areas (i.e., see equations (1) & (2)). This was judged as being more convenient as it did not require the decomposition of the forces between the horizontal and the vertical components of the foil (i.e., which have different chords, thicknesses and areas) but also because it enables to correct the issue with the flap that occurred during the tests (i.e., the flap angle moved under load especially at high speed, high AoA and high flap angle, which are however not realistic conditions for Moths). The lift to drag (areas) ratio, on the other hand, assesses the performance of the foil.

$$LA = \frac{D}{\frac{1}{2}\rho V^2} \quad (1)$$

$$DA = \frac{D}{\frac{1}{2}\rho V^2} \quad (2)$$

Other conclusions regarding the general trend of the lift and drag, the performance of the foil and the effect of immersion are not included in this paper but were discussed in (Day, Cocard, & Troll, March 2019).

#### 3.1 Tubercles Effects

The lift and drag (area) results of the bare foil (BF) and the foil with the full coverage of tubercles (FT) over speed are shown in

Figure 11 and Figure 12. The empty markers show the results of the foil with tubercles whereas the full ones correspond to the foil without tubercles.

It clearly shows that for all conditions, except from the low speed (i.e., up to 1.5m/s) at zero AoA and zero flap, the retrofitting of LET results in a penalty in drag. This could be related to different reasons. One of the most obvious ones is the increase in skin friction resulting from the additional surface area of the tubercles. On the other hand, it could also be a consequence of the surface finish of the tubercles or the smoothness of the assembly. Indeed, both

were just a prototype, and it was possible to see that the tubercles were rougher than the gelcoat of the foil but also that a rough edge, coming from the arms of the tubercle and the silicone adhesive, could be felt. They could have affected the flow over the leading edge of the foil.

They could have affected the flow over the leading edge of the foil.

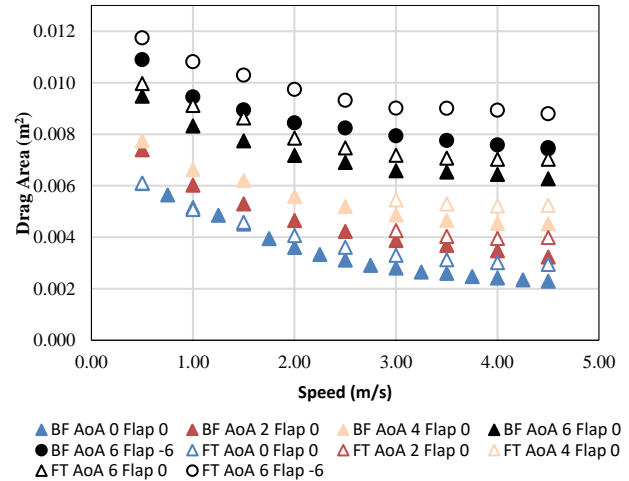


Figure 11 - Drag Area Comparison of Bare foil (BF) and Foil with Full Coverage of Tubercles (FT) (Stage 2)

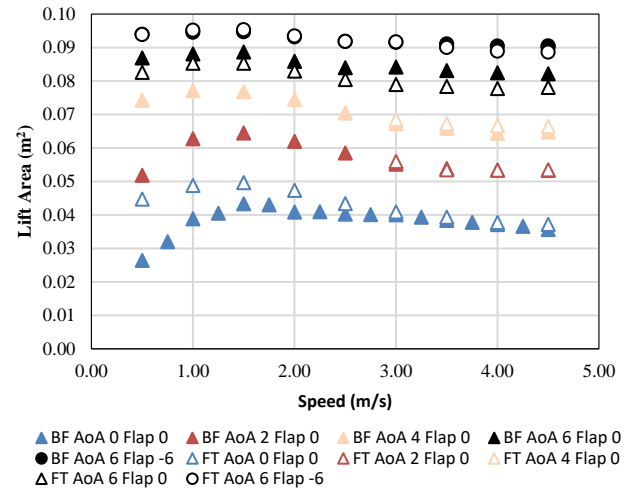
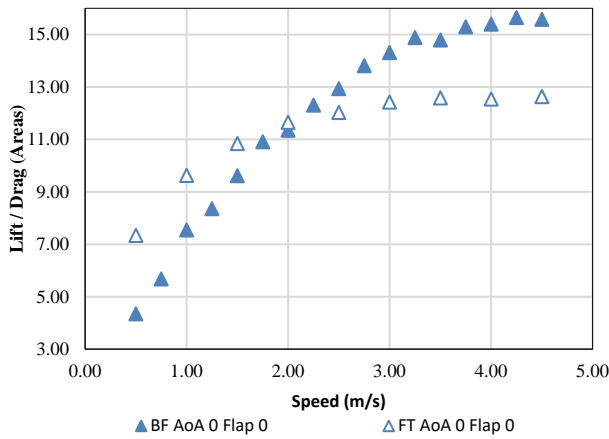


Figure 12 - Lift Area Comparison of Bare foil (BF) and Foil with Full Coverage of Tubercles (FT) (Stage 2)

On the other hand, it can be seen that fitting tubercles have a beneficial effect on the lift over the entire speed range for angles of attack up to four deg. for the zero flap conditions. Indeed, for these cases, lift increases and especially at low speeds (0 to 2.5m/s). This is clearly shown for the zero AoA case, in which the lift significantly improves up to 40% at 0.5m/s. On the contrary, for higher speeds, it only increases slightly.

The improvement in lift associated with the drop in drag results in a better performance of the foil with tubercles at low speed (i.e., up to 2m/s), as Figure 13 demonstrates. On the contrary, at higher speed, the bare foil performs better. Actually, the performance of the foil with tubercles degrades with speed. This is due to the fact that, as speed increases, the drag penalty becomes too important and outweighs the lift generated.

At large AoA, tubercles seem to result in a drop of lift over the full range of speed whereas, at high AoA and high flap angles, tubercles do not seem to have an important effect on lift. In fact, at the lowest speeds, the foil with tubercles seem to produce more lift whereas at higher speed the bare foil produces more.



**Figure 13 - Lift/ Drag (Areas) Comparison of Bare foil and Foil with Full Coverage of Tubercles (Stage 2)**

### 3.2 Stages 1 & 2 Comparison

As mentioned earlier, some of the conditions of the first set of experiment (i.e., corresponding to the 334mm immersion without tubercles) were repeated during the second stage to compare the results of both stages. This was done for the bare foil as the effect of tubercles was studied at a deeper immersion during stage 2 (i.e., 457mm compared to 334mm).

In general, there was a good agreement between the results of both stages. Indeed, the same conclusions could be drawn concerning the effect of tubercles even though the material used was not the same (i.e., the tubercles used during stage 2 were more rigid). However, it was observed that both the lift and drag forces observed during stage 2 were smaller than during the first stage. Indeed, a difference of up to 73 % in drag and 62 % in lift at neutral flap could be observed. This is shown in *Figure 14*.

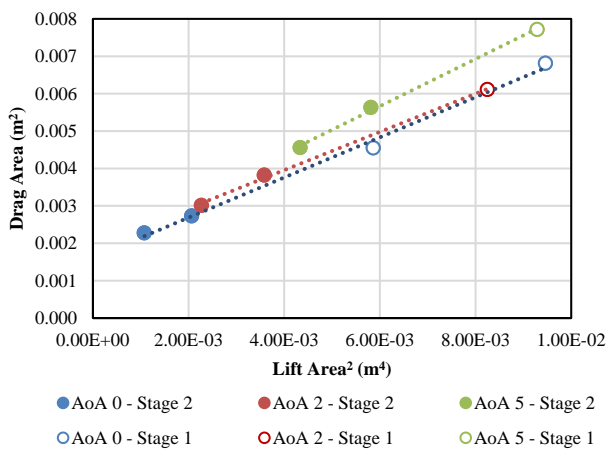


**Figure 14 - Stages 1 & 2 Results Comparison**

This graph shows the drag area versus the lift area of Stages 1 (i.e., solid markers) and 2 (i.e., empty marker) for the

4.0m/s condition. The first point of each case corresponds to the zero-flap condition whereas the second one (i.e., when applicable) corresponds to the six-deg. flap angle. It clearly shows that the results of both stages are quite aligned. On the other hand, the lift to drag ratios are relatively close for both sets of experiments (around 2 to 3 % at neutral AoA). This is why the difference in lift and drag is believed to result from a change in flap or AoA. Hypothetically, this could be related to the fact that the zero position of the AoA of the horizontal and/ or the angle of the flap used during both stages were not the same. Indeed, even though the hinge has not been refurbished between the two stages, the foil was used to sail. Therefore, the natural resting point of the horizontal, which was taken as the neutral flap angle, could have changed and induced some uncertainties.

## 4 CONCLUSIONS

Because tubercles have proven to successfully improve the efficiency of foils (i.e., blade, rudder, etc.), it was decided to study their implementation onto a Moth hydrofoil. From this study, it was found out that tubercles only improve the performance of the foil at low Reynolds Number and are, therefore, in no way beneficial for high performance foil such as the Moth foil. Indeed, such foils only perform at high speed, and it appears that at high speed, tubercles result in a large increase of drag which outputs the gain in lift. On the other hand, it was not possible to study their effect on the onset of stall and post stall regimes because these conditions could not be achieved due to the limitations of the foil, test rig, and loadcells; the maximum AoA at which the tubercles could be tested was 6deg., angle at which flow separation does not usually occur.

On the other hand, these experiments gave some valuable insights into the advantages and limitations of LET technology as it showed the conditions at which tubercles have the greatest impact. Indeed, it was clearly proven that tubercles only have a beneficial impact (i.e., by increasing the lift) at low AoA and flap angles. In fact, the greatest improvement was shown at zero pitch angle and was less substantial as the AOA of the horizontal increases.

Further studies on the effect of tubercles could be accomplished using CFD analysis. This would enable to understand if the increase in drag of the foil with tubercles is related to the material of the protuberances or the surface finish. It would also help to understand properly the flow interaction.

On the other hand, this study shows the success of using 3D printing to implement LET on an existing appendage. Indeed, the manufacturing process of the tubercles has proven to be satisfactory and therefore this technology has proven to be a cost-friendly testing approach to modify an existing model even though it would require some improvement (i.e., material, surface finish, assembly, etc.).

Finally, it enabled to design, build, and test an appropriate rig as well as develop an effective experimental procedure to study flapped T-foils. It also enabled to obtain a benchmark data set for analysis of flapped T-foils.

## ACKNOWLEDGEMENTS

The authors would like to acknowledge the AFRC for scanning the hydrofoil and to the DMEM department at the UoS for printing the LET used during the first stage of the study. Additionally, they would like to express their appreciation to the technical staff of the KHL: Steven Black and Bill Wright for building the test rig and Dr. Sashuai Dai and Grant Dunning for supporting the experiments. Lastly, they would like to thank Thomas King and Dr. Weichao Shi for carrying out the first stage of the study.

Also, the authors gratefully acknowledge that the research presented in this paper was carried out as part of the EU funded H2020 project, VENTuRE (grant no. 856887).

## REFERENCES

- Aftab, S. M., Razak, N. A., Mohd Rafie, A. S., & Ahmad, K. A. (2016). Mimicking the humpback whale: An aerodynamic perspective. *Progress in Aerospace Sciences* 84, 48-69.
- Beaver, B., & Zselezky, J. (March 2009). Full Scale Measurements on a Hydrofoil International Moth. *The 19th Chesapeake Sailing Yacht Symposium (Annapolis, Maryland)*.
- Day, S., Cocard, M. G., & Troll, M. (March 2019). Experimental Measurement and Simplified Prediction of T-foil Performance for Monohull Dinghies. *The 23rd Chesapeake Sailing Yacht Symposium*. Annapolis, Maryland.
- Fish, F. E., Weber, P. W., Murray, M. M., & Howle, L. E. (2011). The Tubercles on Humpback Whales' Flippers: Application of Bio-Inspired Technology. *Integrative and Comparative Biology* 51, 203-213.
- Fish, F. E., & Battle, J. M. (1995). Hydrodynamic Design of the Humpback Whale Flipper. *Journal of Morphology*, 225 (1), 51 – 60.
- Fish, F. E., & Lauder, G. V. (2006). Passive and Active Flow Control by Swimming Fishes and Mammals. *The Annual Review of Fluid Mechanics* 38, 193-224.
- Hamilton, T. (2008). Whale-Inspired Wind Turbines. *MIT Technology Review*.
- Miklosovic, D. S., Murray, M. M., Howle, L. E., & Fish, F. E. (2004). Leading-Edge Tubercles Delay Stall on Humpback Whale (Megaptera Novaeangliae) Flippers. *Physics of Fluids* 16 (5), 39-42.
- Pechlivanoglou, G. (2012). Passive and Active Flow Control Solutions for Wind Turbine. *Ph.D. Dissertation (Universitätsbibliothek der Technischen Universität Berlin)*.
- Shin, Y. J., Kim, M. C., Lee, J.-H., & Song, M. S. (2018). A Numerical and Experimental Study on the Performance of a Twisted Rudder with Wavy Configuration. *International Journal of Naval Architecture and Ocean Engineering* 11 (1), 131-142.
- Van Nierop, E. A., Alben, S., & Brenner, M. P. (2008). How Bumps on Whale Flippers Delay Stall: An Aerodynamic Model. *Physical Review Letters* 100 (5), 54502.
- Zhu, G.-H. (2008). Comment on How Bumps on Whale Flippers Delays Stall: an Aerodynamic Model. *Physical Review Letters* 101 (10), 109401.

## **Investigation of Gate Rudder Blade Design for Ship Powering Using the Design of Experiment (DoE) Method**

Ahmet Yusuf Gurkan<sup>1,2</sup>, Batuhan Aktas<sup>2</sup>, Uğur Oral Unal<sup>1</sup>, Mehmet Atlar<sup>2</sup>

<sup>1</sup>*Faculty of Naval Architecture and Ocean Engineering, Istanbul Technical University, 34469, Maslak – Istanbul – Turkey*

<sup>2</sup>*Naval Architecture, Ocean & Marine Engineering, University of Strathclyde Glasgow G4 0LZ, UK*

### **Abstract**

The Gate Rudder System (GRS) is a novel steering and energy-saving device that has proved itself on the first newbuilt container vessel, "Shigenobu" in 1998, followed by three other newly built vessels operating in the coastal regions of Japan. Although there is a clear indication that these vessels with GRS presented attractive powering savings based on different scale model tests, sea trials and voyage monitoring, no comprehensive investigation has been reported in the open literature so far describing the best-performing GRS design. This paper presents a geometric sensitivity study, the best design selection procedure for a GRS, and its application to a 90m general cargo vessel (MV ERGE) from the powering performance point of view. MV ERGE is the target ship used in the H2020 project GATERS (ID: 860337) which aims to design and demonstrate the benefits of retrofitting a GRS system on a full-scale ship.

In this paper, a Design of Experiment (DoE) study was performed with a wider range of design space to investigate the sensitivity of the chosen design variables by focusing on the powering performance. The computational Fluid Dynamics (CFD) method was used to calculate each design point flow variable. Based on the application, the most effective geometrical parameter was determined to be the rudder angle from the correlations made between the input and output parameters. Further scrutinisation of the input parameters vs output parameters indicated that the best powering performance was not achieved with the highest rudder force (thrust). Instead, the best GRS design could be obtained by achieving the most favourable interaction amongst the propeller, hull and GR blades to maximise the overall energy saving. For further verification, a comprehensive comparison was made using further high-fidelity CFD modelling of the propeller action.

**Keywords:** Energy-saving device; Gate Rudder System; Optimisation; Design of Experiment; Computational Fluid Dynamics.

### **1 Introduction**

In order to contribute to the global fight against climate change, IMO announced varying levels of regulations to meet CO<sub>2</sub> emission reduction by ships at least 40% by 2030, pursuing efforts towards 70% by 2050 compared to 2008 (IMO, 2018). Hence, many technology solutions have been proposed to address this challenge. The applications of the proposed solutions range from newbuilt ships to existing ships as a retrofit, from individual solutions to holistic ones, and from existing technologies to newly introduced ones. For example, the recent H2020 project GATERS (INEA et al., 2020) (ID: 860337), aims to exploit the application of a novel propulsion and manoeuvring energy-saving device (ESD) called "Gate Rudder System" (GRS) that provides a sound base for the most attractive power-saving hence reduced emission option (Sasaki, et al., 2015). More specifically, GATERS aims to design, manufacture and install a retrofit GRS on a

general cargo vessel MV ERGE and prove the effectiveness of the new technology through sea trials and voyage monitoring. Additionally, GRS's powering, seakeeping and manoeuvring benefits for a wider range of ship types, including Short Sea Shipping (SSS) and Oceangoing Shipping (OS) operations are being explored in the GATERS project.

As shown in Fig. 1, a GRS involves the arrangement of a twin rudder system differently than a conventional rudder system (CRS) by replacing the single rudder behind the propeller with the independently controlled twin rudders aside from the propeller. This novel arrangement has many advantages compared to the CRS. A comprehensive investigation of the early version of the GRS, called the twin rudder system, was made for the first time by Sasaki et al. (2015). Based on the first measurements, it was understood that the state-of-the-art GRS has a number of superiorities over a high lift rudder on propulsion

(Turkmen et al., 2016), manoeuvrability (Carchen, et al., 2016) and seakeeping capabilities (Sasaki, et al., 2019).

The first GRS application was made to a newly built container ship, "Shigenobu". Her sister ship, "Sakura", with a conventional high lift rudder (CRS) was enabled to make comprehensive performance comparisons through numerous sea trials and voyage monitoring since 2018. The collected performance data in the first sea trials indicated that Shigenobu had 14% lower energy consumption at the design speed than Sakura. A further energy saving was also observed in rough sea conditions, where Shigenobu's energy efficiency could be as high as 30% (Sasaki et al., 2020).

Although there are clear indications of the energy-saving capabilities of the GRS based on model tests and full-scale monitoring, there are no detailed investigations of the GRS that would provide a further understanding of the effect of some important GRS design parameters on the hydrodynamic interaction amongst the hull, propeller and gate rudder blades, and powering performance of a vessel with a GRS.



**Fig. 1.** Shigenobu, the first Gate Rudder System fitted ship

Therefore, this paper aims to provide systematic design data for GRS based on the calm water powering performance by conducting a comprehensive Design of Experiment (DoE) study by creating the fully parametric design of a GRS and mainly concentrating on the vertical part of the rudder blades. Parametric model preparation and the DoE study were performed within an optimisation-based CAD software environment called CAESSES (FSYS, 2022). The parametric gate rudder model was prepared over four geometrical design variables, which control only the vertical part of the Gate Rudder blade.

The detail of the definitions of each parameter and general geometrical constraints are presented in Section 2 of the

paper. In order to evaluate the powering performance of the ship, RANS-based Computational Fluid Dynamics (CFD) calculations were conducted for each design point created in the design space with the commercial CFD solver Star CCM+ (StarCCM+, 2022). The details of the CFD methodology used for the verification & validation, sensitivity analysis and design validation study are given in Section 3 of the paper.

The particulars of both the target vessel MV ERGE and the benchmark vessel, Shigenobu, used for the validation and verification are given in Table 1. Validation in a full-scale ship was performed with the extrapolated data. In order to realise optimisation within a reasonable run time, some simplifications were made on both the propeller modelling approach and the computational domain. Although the Virtual Disk (VD) model approach was used to evaluate the propulsion performance for the DoE study, the calculated average forces for verification in Section 3.4 and design validation in Section 5.3 were made by using the rigid body motion of the propeller using the sliding mesh (SM) model approach.

In order to derive the correlations between the design variables versus some hydrodynamic parameters, a design space should be solved over the nodes represented by the design points. For this purpose, the "Sobol" approach was employed for the design space generation. The Sobol algorithm (Sobol, 1967), which is an example of a quasi-random low-discrepancy sequence, creates random design points evenly distributed within the design space. The theoretical background of the Sobol sequence and detail of the sensitivity study is given in Section 4 of the paper.

**Table 1.** Ships particulars

		<b>ERGE Ship</b>	<b>JCV Ship</b>	<b>JCV Model</b>
Scale, m	$\lambda$	1	1	10.938
Length Over All, m	LOA	89.95	111.4	10.110
Length Between perp., m	LBP	84.95	101.9	9.316
Breadth, m	BWL	15.40	17.80	1.627
Draught (AP), m	T <sub>A</sub>	6.46	5.51	0.504
Draught (FS), m	T <sub>F</sub>	6.46	4.91	0.449
Displacement, ton	$\Delta$	7462.7	6489	4.958
Block Coefficient	C <sub>B</sub>	0.806	0.591	0.591
Service Speed, m/s	V <sub>S</sub>	6.173	1.650	2.333
<b>Propeller Diameter, m</b>				
Conventional Rudder		3.42	3.5	-
Gate Rudder		3.60	3.3	0.302

The results of the applications of the algorithm are presented in Section 5, while the details of the calculated correlations between the input and output parameters are presented in Section 5.1. Rudder angle, " $\delta$ ", was observed to be the most critical parameter investigated over the rudder forces, propeller thrust and delivered power

variations. Detailed performance evaluation on some selected design cases and overall relations between variables of the GRS on ship powering are discussed in Section 5.2. Finally, the best-performing GRS design was validated with the SM approach in 5.3. The concluding remarks deduced from the study are presented in Section 6 of the paper.

## 2 Parametric Model

In order to parametrise the GRS blades effectively and the contribution of these parameters to powering performance, it was decided to divide the GRS blade into sub-sections and examine the effectiveness of these sections in detail. These sections are described as shown in Fig. 2. Considering the interaction level of the GRS blades and the propeller, only the vertical part (the first part) of the GRS was chosen as the subject within the context of the current sensitivity study.

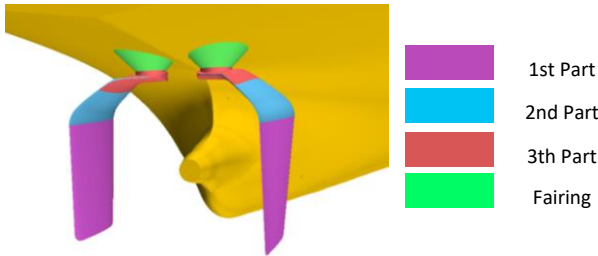


Fig. 2. Parametric model definitions

The current GRS blade called Base Design (BD) was used to create a fully parametric CAD model. Some existing characteristics of the rudder such as; blade profile shape, 2nd, 3rd par of the rudder and finally fairing shape were kept same with the BD.

In the CAESES environment, four independent parameters are chosen for this study. These parameters include as the first parameter, i.e., 'Rudder angle ( $\delta$ )', presenting the rotation of the whole rudder around the centre of the rudder shaft. Rudder motion and rotation direction are defined as shown in Fig. 3. The second parameter is 'Rudder X shift ( $dx$ )', the rudder's axial position relative to the propeller. The base design's relative position to the propeller was assumed to be zero. The third parameter is 'Rudder tip skewness ( $\beta$ )', i.e. the angle relative to the top profile of the first part of the rudder. And the last parameter is the 'Blade tip-chord ratio', which is the ratio of the blade tip chord (at the bottom) to the top chord length. Each design was prepared to have an identical rudder area equivalent to the base GRS design. Therefore, the last parameter inherently changes the aspect ratio of the rudder blade. The lower and upper bounds are listed in Table 2 for each parameter.

In order to prevent each GRS design considered would have physical contact with the propeller or hull, a limiting

criterion is introduced. This is required if the rudder gets closer to the propeller boss cap less than 5% of the propeller diameter at the rudder's  $+110^\circ$  helm position; such design will be disregarded. None of the design points is allowed to take place in the design space, which violates this rule.

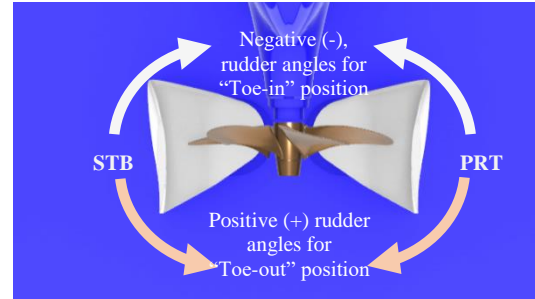


Fig. 3. Parametric model definitions

Table 2. Geometric parameters and limits

Name		Lower Band	Upper Band
Rudder angle <sup>1</sup> , degree	$\delta$	-6.0	6.0
Rudder X shift <sup>2</sup> , m	$dx$	-0.40	0.17
Rudder tip skewness <sup>1</sup> , degree	$\beta$	0	8
Blade tip chord ratio, -	$C_T$	0.68	0.74

<sup>1</sup> '+' sign represents toe-out direction

<sup>2</sup> '+' sign represents head direction of the ship

## 3 CFD Methodology

The theoretical background and the detail of the numerical model, such as the computational domain grid generation and discretisation of the governing equations, are given in this section.

### 3.1 Theoretical Background and Numerical Models

The CFD calculations were carried out via the Start-CCM+, which is a commercial viscous flow solver. The governing equations were discretised by finite-volume approach and were solved using a segregated approach.

Calculations were done using the Reynolds Average Navier-Stokes (RANS) equations in the transient domain. Multiphase calculations were done in a transient domain, while the DoE study (the calculation with simplified fluid domains) was performed in a steady-state domain.

Multiphase flow, where the free-surface effects were considered, was solved using the Volume of Fluid (VoF) approach. Regarding the turbulence modelling, Realisable  $k-\epsilon$  was employed with all wall treatment approaches. All the multiphase calculations were performed in calm water conditions by allowing ships in two Degrees of Freedom (DoF), i.e., heave and pitch motion.

The propulsion calculations were performed in two different approaches.

The first one is the sliding mesh (SM) approach which is based on rigid body motion. The defined motion moves the mesh vertices according to user-specified rotation, translation or trajectory. Around the corresponding rotation, the centre was defined as rigid body motion Eq 1, where  $V_g$ : mesh velocity,  $\omega_g$ : prescribed angular velocity,  $r$ : position vector of a mesh vertex (StarCCM+, 2022).

$$V_g = \omega_g \times r \quad (1)$$

In applying the SM method, the propeller speed should be set to the operation point where the propeller thrust is equivalent to the ship resistance, additionally considering friction drag in the model scale.

The second model adopted is the Virtual Disk (VD) model which is based upon the principle of representing rotary machinery such as propellers, turbine rotors, etc., as an actuator disk and hence, provides considerable computational time and resource-saving. The action of the actuator disk on the flow field enters the momentum equations in the form of a source term that is distributed over the virtual disk. Various distributions of different fidelity are possible to model the action of the actuator depending on the application area. "Body Force Propeller Method", which simulates the effects of a marine propeller, were used for the VD-based calculations as the actuator disk (StarCCM+, 2022).

As a result, the distribution of the axial and tangential forces of the modelled propeller and its effect on the flow is calculated. The integration of these forces over the disk gives the thrust and torque of the propeller.

Both approaches shown in Fig. 4 were performed in the validation and verification study in Section 3.4 and design validation for the best-performing GRS design is chosen from the DoE as described in Section 5.3.

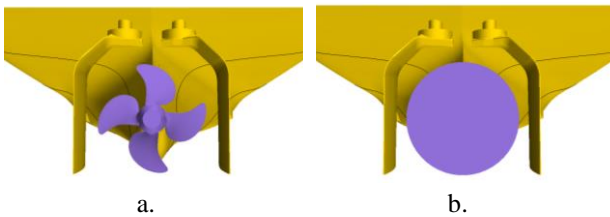


**Fig. 4.** Propeller modelling approaches; a. Rigid body motion (Sliding Mesh), b. Actuator disk (Virtual Disk)

### 3.2 Computational Domain and Boundary Conditions

Following the ITTC recommended procedure (ITTC, 2014) for ship hydrodynamic calculations, the computational domain for CFD was prepared for both the target ship MV ERGE and benchmark vessel Shigenobu for validation study, whose dimensions are given in Table 1. Fig. 5 shows the dimensions of the general computational domain for the full-scale and model-scale

ships. The fluid domains for the CFD modelling were prepared according to the ship and/or model length and they are also shown in Fig. 5. There are  $2L$  distances between the boundaries at either side and the fore and  $3L$  distances at the aft end of the ship, where  $L$  represents the length of the water line. The upper and lower boundaries are located at  $1L$  and  $2.5L$ , respectively.

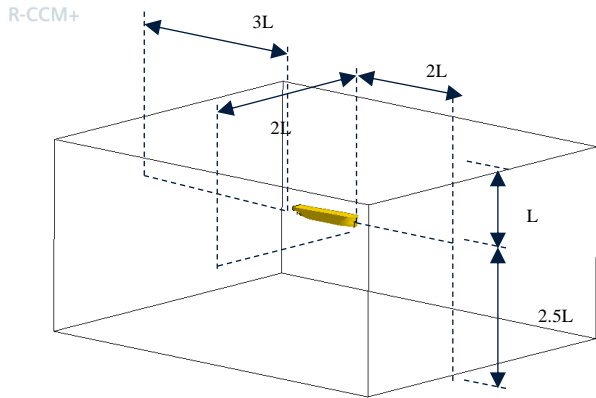


**Fig. 5.** Main dimensions of the computational domain.

In order to reduce the computational cost of the DoE study, the simulation simplifications were implemented over three levels, including the propulsion modelling approach. The process was performed starting from the most complex case to the simplest one, as given in Table 3. The chosen mesh structure and cell counts are given in Section 3.4.

The first level of simplification (Case 1) is on the propeller modelling approach. This case has a significant number of mesh cells, around 23 M. The existence of the propeller with the SM approach causes an additional 6.6 M over Case 2, which solves propeller interaction with the VD approach. As a result, the mesh count in Case 2 reduces by 30% relative to Case 1.

Both Case 1 and Case 2 require transient simulation because of ship motion (pitch & heave) and propeller rotation (for only Case 1). Therefore, these cases have significantly high run times (more than ten times) compared to Cases 3 & 4, as it is shown in

Table 6.

The second simplification was made by focusing only on the underwater part of the ship. The free-surface effects were not considered for Cases 3 and 4, as shown in Fig. 6, b and c. Instead, the wave resistance is calculated from the total resistance difference between Case 2 and 3, and then the calculated wave resistance is added to the VD thrust expression and the rest of the resistance calculations. Case 3 has an additional 16% reduction in the total cell number relative to Case 2.

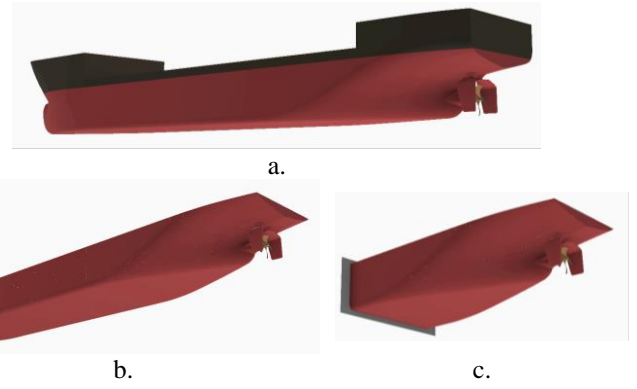
The last simplification was implemented in Case 4 by cutting and removing the forebody of the ship, as shown in

Fig. 6,c. In order to practice this cutting process at a convenient location, the effective stern region interacting with the propeller was determined by comparing the distribution of the pressure coefficient " $C_p$ " and the friction coefficient  $C_f$  along the three different reference lines on the hull. These lines named the bottom ( $z:-0.8D$  from the propeller centre line), centre ( $z:0$  propeller shaft centre), and top ( $z:+0.9D$  from the propeller centre line) are shown in Fig. 8. From the graphs in Fig. 8, the propeller interacts with only the aft 15% of the ship, which is equivalent to 12.7 m. Therefore, just the aft 30 m of the ship is kept in Case 4, which is the most simplified ship domain, considering the parallel body. The detailed results are presented in Section 3.4.

As the inlet surface of Case 4's fluid domain starts from the ship cross-section, the detailed velocity ( $x$ ,  $y$  and  $z$ ) components were defined on the surface instead of uniformly distributed inlet velocity. These velocity and turbulence components data were derived from the corresponding cross-section in Case 3. The velocity distribution is shown in Fig. 7.

**Table 3.** Geometrical model detail for the simplification study

Name	Ship Detail	Propeller Detail
Case 1	Full-model	Sliding Mesh
Case 2	Full-model	Virtual Disk
Case 3	Double-model	Virtual Disk
Case 4	Clipped double-model	Virtual Disk



**Fig. 6.** Simplified fluid domains; a.Full domain, b.Double model, c.Trimmed double model

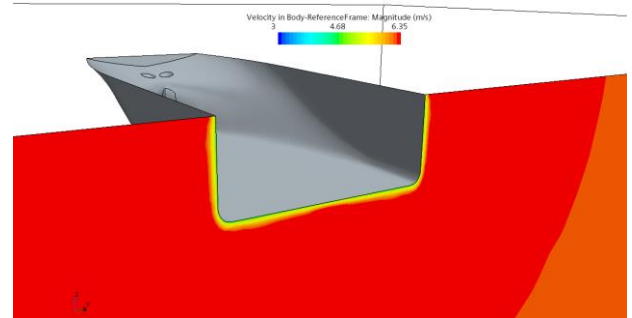


**Fig. 7.** The defined non-uniform velocity distribution at the inlet surface of Case 4

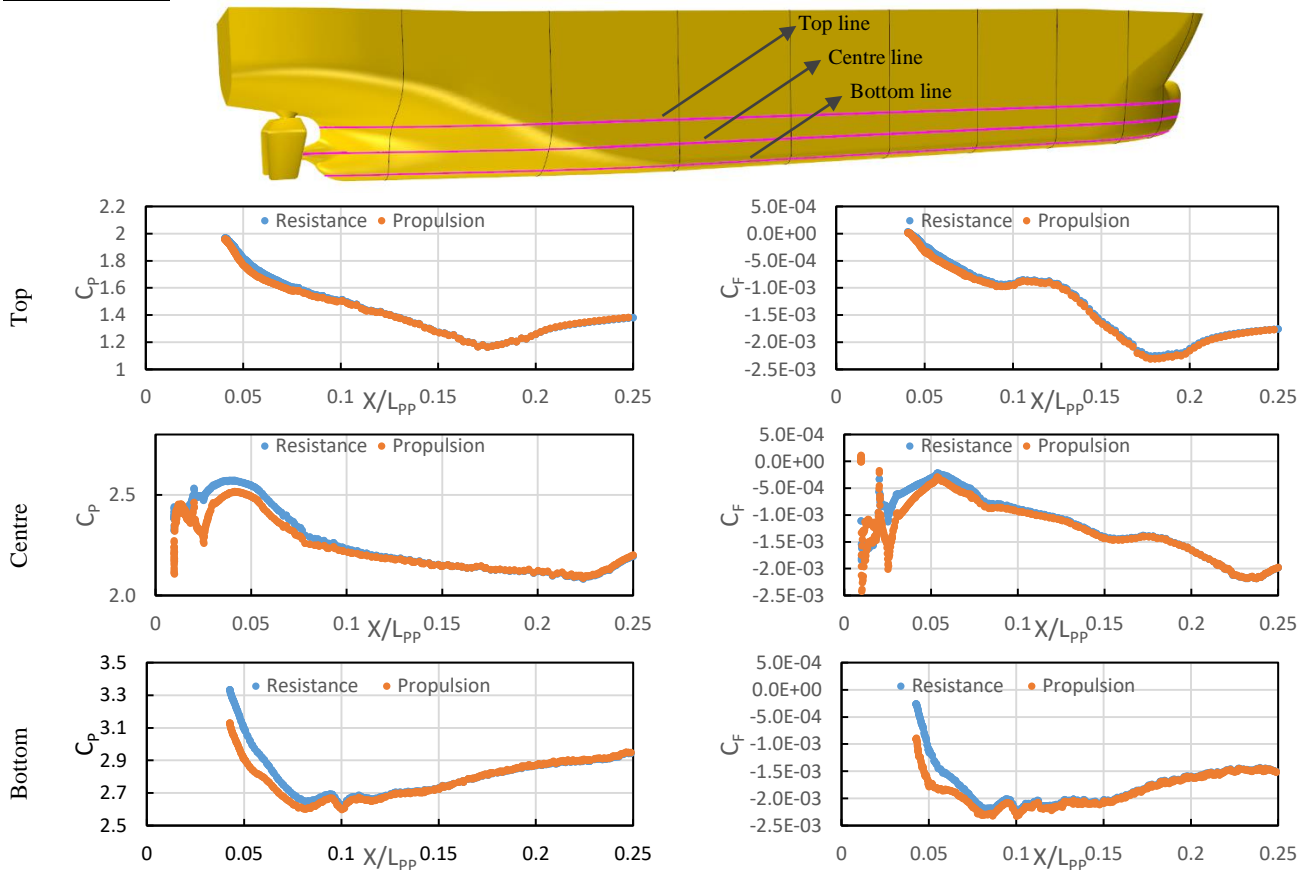


**Fig. 8.** Propeller-hull interaction investigation at the stern of MV ERGE over  $C_p$  and  $C_f$

### 3.3 Mesh Generation and Physics Set-up

STAR CCM+ meshing tool was employed for mesh generation. The trimmer-type technique used for the surface and volumetric mesh is a hexahedral-type grid structure. In order to capture high gradient velocity normal to the walls, prism layers were defined along the wall. Further local mesh refinements have defined locations like; the bow and stern of the ship, the rudder surrounding, and the free surface to capture high gradient flow and wave evaluations.

Extra grid refinement was applied at the rudder region. In the case of self-propulsion simulation, extra grid refinement was done around the disk. For the full-scale ship calculations, there were ten layers of boundary-layer meshes near the hull, and the average wall function  $y^+$  value was kept between 30 and 60, as calculated and

suggested by similar numerical studies. For the model scale calculations, there were 20 layers of boundary-layer meshes normal to the wall. The average  $y^+$  value was  $<1$  to solve the viscous sub-layer. Calculated  $y^+$  values are shown in **Fig. 9** for both scales. The realisable k-ε turbulence model was used as the RANS closure model. The volume of fluid method (VOF) for multiphase flows was used to account for free surface effects. The model was unconstrained to move in 2 degrees of freedom (with sinkage and trim) using Dynamic Fluid Body Interaction (DFBI), allowing the simulation to attain a consistent dynamic attitude for V&V study and Case 1 & 2.

Since the free-surface effects did not include in the calculations for Case 3 & 4, no degree of freedom was allowed. Instead, the heave and pitch values calculated from Case 2 were introduced to Case 3 & 4 domains.

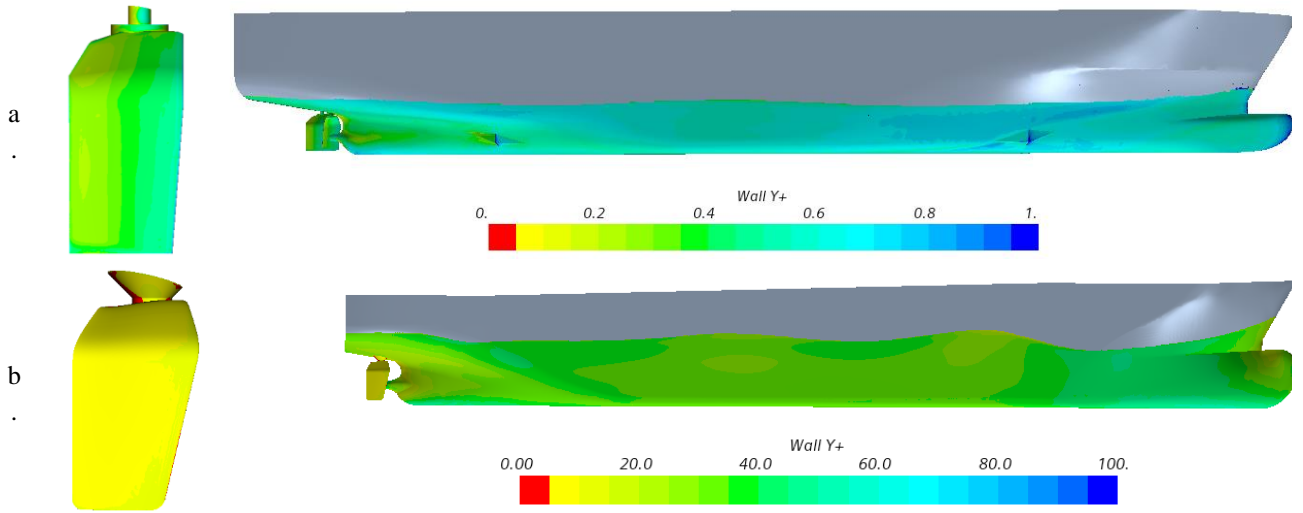


**Fig. 9.** Calculated  $y^+$  distribution on the hull; a. Shigenobu (validation ship), b. MV ERGE (subject ship)

### 3.4 Verification and Validation Study

Richards Extrapolation based Grid Convergence Index (GCI) was used to demonstrate the accuracy level of the CFD calculations (Richardson & Gant, 1927). that is based on the Richards Extrapolation (Richardson L. F., 1911; Richardson & Gant, 1927) to calculate the numerical described by (Celik et al., 2008).

GCI which are calculated using Eqs. 2 to 4, where  $r_{21}$  and  $r_{32}$  are refinement factors,  $\phi_k$  represents the corresponding CFD output variable (resistance, thrust, torque and RPM) and  $\epsilon_{21}$  and  $\epsilon_{32}$  are the difference between the results obtained from relevant grids 1 (fine), 2 and 3 (coarse), respectively. For this study, the refinement ratio was set as  $\sim 2$  for the model-scale ship and 2.2 for the full-scale ship.

$$p = \frac{1}{\ln(r_{21})} |\ln|\epsilon_{32}/\epsilon_{21}| + q(p)| \quad (2)$$

$$q(p) = \ln\left(\frac{r_{21}^p - s}{r_{32}^p - s}\right) \quad (3)$$

$$s = 1 \cdot \text{sign}\left(\frac{\epsilon_{32}}{\epsilon_{21}}\right) \quad (4)$$

The extrapolated values by using associated results and refinement ratio are obtained by Eq. 5.

$$\phi_{ext}^{21} = \frac{(r_{21}^p \phi_1 - \phi_2)}{(r_{21}^p - 1)} \quad (5)$$

The approximate and extrapolated errors are calculated using Eqs. 6 and 7, and the Grid Convergence Index between the two finest grids ( $GCI_{21}$ ) is given by Eq. 8.

$$e_a^{21} = \left| \frac{\phi_1 - \phi_2}{\phi_1} \right| \quad (6)$$

$$e_{ext}^{21} = \left| \frac{\phi_{ext}^{12} - \phi_1}{\phi_{ext}^{12}} \right| \quad (7)$$

$$GCI^{21}_{fine} = \frac{1.25 e_a^{21}}{r_{21}^p - 1} \quad (8)$$

The GCI for both model and full-scale version of Shigenobu demonstrates the level of variation of the result relative to the grid structure. Three different mesh structures (shown in Fig. 12) were generated to perform GCI. The calculations were done for the  $Fr = 0.234$ , which corresponds to 15knots ship speed (service speed) in full scale. Performed verification study with varying mesh density demonstrated that the grid independency level is quite high for both scales. Calculated  $GCI^{21}_{fine}$  for fundamental ship hydrodynamic variables are lower than 1%, as shown in Table 4 and In addition to the test results conducted by HSVA, the extrapolated powering results based on the model tests conducted at the ITU towing tank with a smaller model of Shigenobu ( $\lambda=21.5$ ) model and using the ITTC'78 method were added in Fig. 11. The average difference between calculated  $P_E$  values and ITU measurements is  $\sim 1.8\%$ , while  $\sim 11\%$  with the HSVA measurements. Similarly, the average  $P_D$  difference between the CFD and predictions are 0.6% and 14% compared to the ITU and HSVA model test based extrapolations, respectively.

Table 5. Although  $GCI^{21}_{fine}$  average ratio of rudder axial forces, which present the resistance forces in the model scale, are  $\sim 6\%$ , the reason is the force values are significantly close to zero.

Based on the comparison between the CFD results and the model test results conducted in the HSVA towing tank with a model scale of  $\lambda=10.938$ , the accuracy level of the best mesh (JM G1) is quite high by showing 0.8% difference from the EFD on resistance and torque. The Experimental Fluid Dynamics (EFD) results of HSVA given in Table 4 have not been published yet.

Further comparisons of the effective and delivered power results for a wide range of ship speeds are given in Fig. 10 and Fig. 11 for the model and full-scale versions of the Shigenobu, respectively.

**Table 4.** GCI study for the model scale JCV with gate rudder propulsion prediction;  $Fr:0.234$  at loaded condition

	EFD	JM G1	JM G2	JM G3	$GCI^{21}_{fine}$	$\delta\phi_2$
Cell Count	-	8.6M	4.3M	2.3M	-	-
$R_{TM}$ , N	197.3	194.0	193.4	189.1	0.0039	0.8%
$T_M$ , N	161.5	161.6	161.0	155.9	0.0003	0.1%
$Q_M$ , kN.m	7.15	7.20	7.19	7.02	0.0000	0.8%

$n_M$ , rps	10.96	10.90	10.90	10.91	0.0003	0.6%
$P_{Dm}$ , W	492.18	493.37	492.11	481.17	0.0002	0.2%
$R_{GRS PRT}$ , N	-	1.05	1.14	1.33	0.0720	-
$R_{GRS STB}$ , N	-	1.29	1.37	1.54	0.0468	-

In addition to the test results conducted by HSVA, the extrapolated powering results based on the model tests conducted at the ITU towing tank with a smaller model of Shigenobu ( $\lambda=21.5$ ) model and using the ITTC'78 method were added in Fig. 11. The average difference between calculated  $P_E$  values and ITU measurements is  $\sim 1.8\%$ , while  $\sim 11\%$  with the HSVA measurements. Similarly, the average  $P_D$  difference between the CFD and predictions are 0.6% and 14% compared to the ITU and HSVA model test based extrapolations, respectively.

**Table 5.** GCI study for the full scale JCV with gate rudder propulsion prediction;  $Fr:0.234$  at loaded condition

	JF G1	JF G2	JF G3	$GCI^{21}_{fine}$
Cell Count	18.0 M	8.3 M	4.0 M	hyp
$R_{TS}$ , kN	219.2	219.3	216.1	hyp
$T_S$ , kN	240.6	241.6	239.3	hyp
$Q_S$ , kN.m	116.0	116.7	116.0	hyp
$N_S$ , rpm	200.6	201.8	202.3	0.0069
$P_{DS}$ , kW	2437	2465	2457	hyp
$R_{GRS PRT}$ , kN	0.42	0.44	0.36	hyp
$R_{GRS STB}$ , kN	0.00	0.35	0.13	hyp

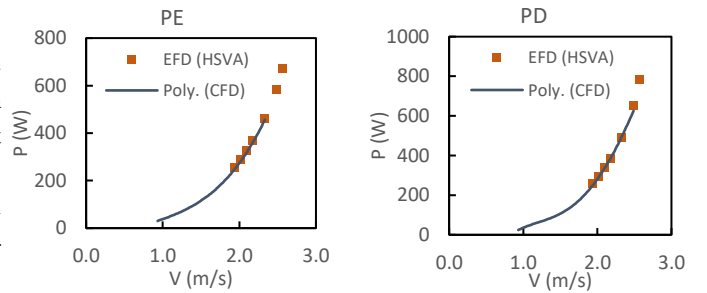


**Fig. 10.** Model-scale Shigenobu EFD vs CFD comparison for varying speeds

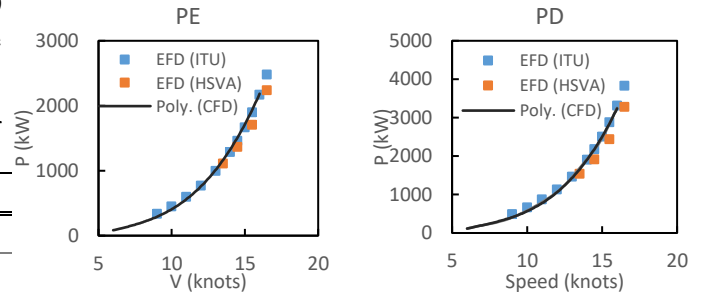


**Fig. 11.** Full-scale Shigenobu EFD vs CFD comparison for varying speeds

**Table 6.** Hydrodynamic variable comparison for fluid domain simplification

Case	Mesh Count (M)	Run Time (h)	$F_{GRS PRT}$ (kN)	$F_{GRS STB}$ (kN)	$F_{GRS T}$ (kN)	$\delta F_{GRS T}$ (%)	T (kN)	Q (kN.m)	N (RPM)	$P_D$ (kW)	$\delta P_D$ (%)
------	----------------	--------------	--------------------	--------------------	------------------	------------------------	--------	----------	---------	------------	------------------

Case 1	22.0	>160	6.31	5.10	11.40	-	188.97	93.78	136.8	1344	-
Case 2	15.4	~72	5.61	5.67	11.28	-1.1	185.80	96.17	137.0	1380	2.7
Case 3	11.9	~6	6.28	6.31	12.59	10.4	184.82	95.03	135.0	1343	0.0
Case 4	7.0	~4	6.10	6.17	12.27	7.6	184.01	94.69	134.9	1338	-0.4

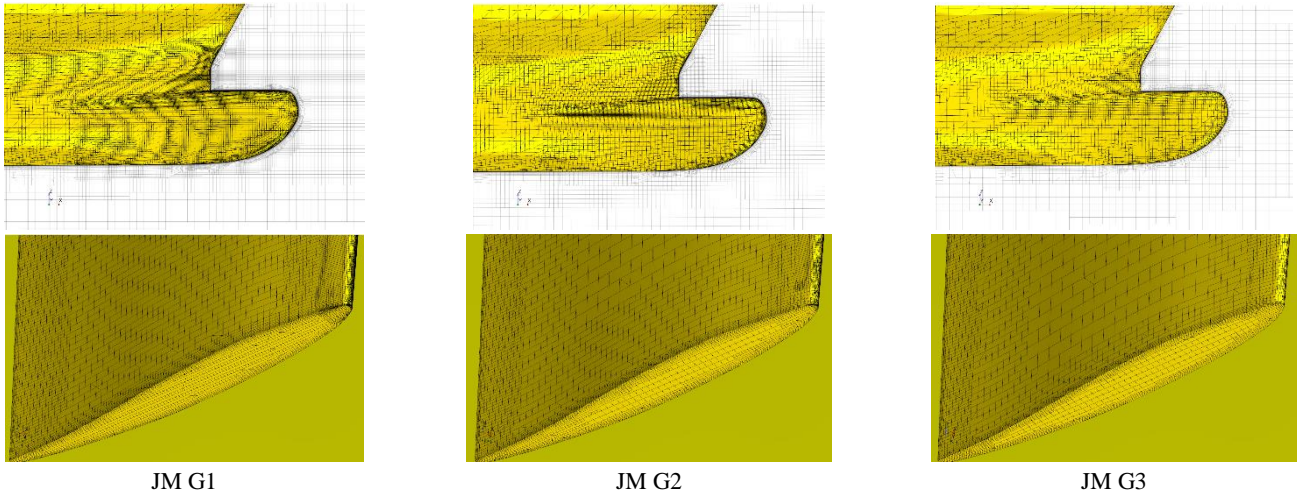


Fig. 12. Three different mesh structures for model scale ( $\lambda:10.938$ ) Shigenobu

#### 4 Sensitivity Methodology

The Design of Experiment was conducted by using the Sobol Algorithm within the explored space that was limited by defined minimum and maximum bounds for each design variable.

The Sobol sequence sampling method used for the study is a quasi-random sequence which is the replacement of the full factorial distributed in a uniform way (Sobol, 1967).

In the Sobol sequence, two uniform partitions of the same interval are utilised, and then it reorders the coordinates in each dimension. If we let  $I^S = [0,1]^S$  be the  $s$ -dimensional hypercube, and  $f$  be a real integral function over  $I^S$ , in this case, the Sobol sequence should construct a sequence  $x_n$  in  $I^S$  in a way that (Sobol, 1967);

$$\lim_{n \rightarrow \infty} \frac{1}{n} \sum_{i=1}^n f(x_i) = \int_{I^S} f \quad (2)$$

Where  $x_i$  is a set of points uniformly distributed in a hypercube unit as  $H^n$ , like  $x_i = (x_i^1, \dots, x_i^n)$ . The inequality called Koskma-Hlawka gives a higher bound for this integration error (Niederreiter, 1992),

$$\varepsilon \leq V(f)D_n \quad (3)$$

$V(f)$ ,s the variation of  $f(x)$  by the Hardy and Krause expression, and  $D_n$  function in which the first derivatives are continuous,  $V(f)$  is defined as the following expression (Niederreiter, 1992),

$$V(f) = \int_{H^*} |df(x)/dx| dx \quad (4)$$

In higher dimensions, it will be possible to identify the durable-Krause variation in terms of partial derivatives. On the other hand,  $f(x)$  is assumed to be a function of limited

change. Meanwhile, the smaller the discrepancy identified for the  $D_n$ , the better the integration convergence will be accessible. Therefore, convergence will be possible.

The design space was investigated with 100 samples. There are two design points that failed because of some geometric complication, but the rest of the design points were completed. In order to evaluate the performance of the GRS, the following output parameters were monitored to understand the degree of interactions between the hull, propeller and gate rudder:

**Rudder parameters;**  $T_{GRS\ Total}$  (Total thrust on both rudders),  $F_Y$  (Side forces on each rudder separately)

**Propeller parameters;**  $T_{Propeller}$  (Thrust on the propeller),  $Q$  (Torque on the propeller),  $N$  (Propeller rotation speed),  $J$  (Propeller advance coefficient) and  $P_D$  (Delivered power)

**Hydrodynamic parameters;**  $\eta_H, \eta_R, \eta_B, \eta_0, \eta_D$  are the Hull, relative-rotative, behind-hull, open-water and propulsion efficiencies, respectively.  $\omega$  (wake fraction),  $t$  (Thrust deduction).

Although a best-performing design is chosen in Section 5, this paper does not contain any objective-based optimisation. Therefore, the best performing design chosen from the DoE study is not guaranteed that it is the best reachable design within the design space. The aim is to perform a sensitivity study to demonstrate a clear dependency level of the overall powering performance of the GRS over the geometrical design variables.

#### 5 Results

The results of the DoE are presented in three sections in the following. The sensitivity results including the correlations graphs (Fig. 13 through Fig. 16) are given in Section 5.1, the detailed resistance and propulsion investigations by

comparing the four selected cases are in Section 5.2, and the design validation results with SM method are included in Section 5.3.

### 5.1 Sensitivity Analysis

The DoE study was performed by creating 100 design points employing the earlier mentioned four geometrical parameters introduced in Section 2. There are 98 successfully completed nodes, while two design points failed because of a geometrical error.

This comprehensive sensitivity study determined the rudder angle as the most sensitive parameter.

Sasaki (2015) reported that the GRS has a strong interaction with the propeller as the rudders have higher flow velocity at their inner surfaces than the outers. This relation was clearly observed with the rudder's increasing angle of attack, i.e. "toe-in" position of the rudder leading edge (indicated by the negative "-" sign) relative to the upstream flow. Therefore, unlike the conventional rudder systems, almost all design points have positive axial rudder force (i.e. thrust) within the solved design space, as shown in Fig. 13.

Contrary to expectations, high rudder thrust force does not decrease the propeller load. As shown in Fig. 14, the propeller thrust correlation with the rudder angle indicates that the propeller loads are maximum at rudder angles where the highest rudder thrust forces are recorded. Similarly, the delivered power correlation in Fig. 15 shows that the lowest power values are predicted at the rudder angles where low rudder thrusts are calculated.

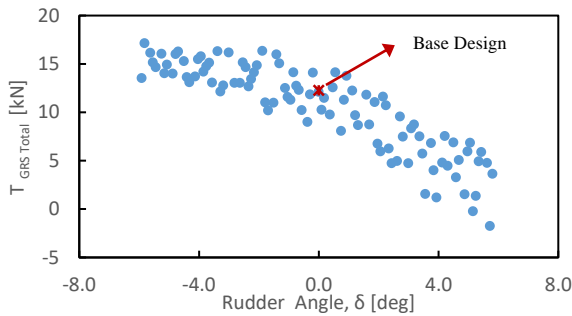


Fig. 13. Correlation graph of rudder angle,  $\delta$  vs GRS Thrust Force

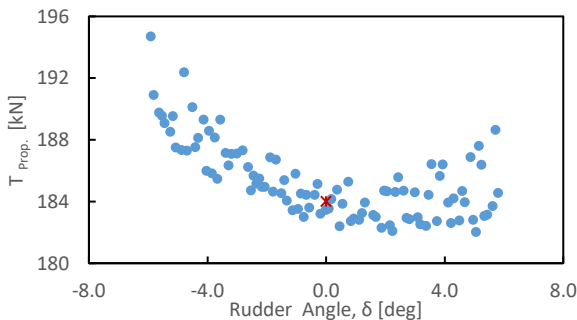


Fig. 14. Correlation graph of rudder angle,  $\delta$  vs Propeller Thrust

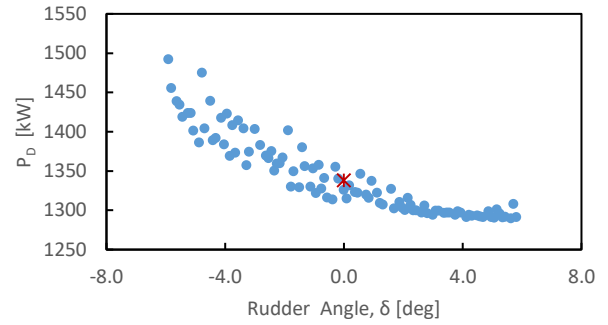


Fig. 15. Correlation graph of rudder angle,  $\delta$  vs  $P_D$

Regarding the rest of the design variables, there is a slightly positive correlation of the rudder X shift "dx" with the GRS thrust force, which means increasing dx values (in "+" direction) tends to give higher rudder thrusts, and a negative correlation with the propeller thrust. No significant effect is observed on the  $P_D$ . The correlation derivatives of the rudder tip skewness and the blade tip chord ratio are almost zero to the output parameters. Therefore these correlation graphs are not included in the paper.

In order to get a better understanding of GRS, further investigation was carried out over correlation graphs of the output parameters between one another. The  $P_D$  reaches the threshold between 0 to 6° rudder angle based on the current GRS propeller. No reduction in  $P_D$  was observed with decreasing rudder forces, as shown in Fig. 16. The minimum  $P_D$  was calculated at 1298.7 kW at Design Point 20 (DP20) with a 3.6% power reduction relative to the base design, which is indicated by a red cross (x) sign in the correlation graphs.

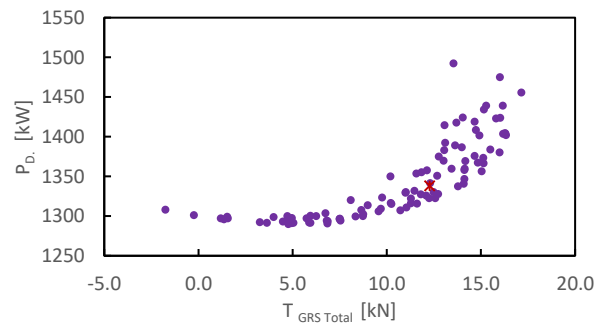


Fig. 16. Correlation between GRS thrust force vs  $P_D$

### 5.2 Case-by-Case Investigation

A comprehensive comparison of hull, rudder and propeller forces were conducted over the four cases, which are: Bare Hull (without rudder system); Base (original) Design (BD); DP20, the chosen design point where the lowest shaft power was obtained within the design space; and DP50, the chosen design point where the highest gate rudder positive force was calculated

The case-by-case investigation is made for both towing and propulsion conditions described in the following.

#### 5.2.1 Towing Condition

In order to present a physical insight to the effect of the design variables on the hydrodynamic interaction Fig. 18 is included

to present pressure coefficient variations at the aft end including the GRS blades in towing condition for the three design cases (ie. BD, DP20 and DP50) etc.

Based on the stern shape of the ship and local flow alignment with the gate rudder blade, the axial force on the rudder could change. Even with the higher rudder angle in the toe-in direction, axial rudder force can tend to be positive, as it is almost 0 resistance for DP50, which has a rudder angle of  $-5.8^\circ$ . This phenomena is shown in Fig. 18, the stagnation point on the rudder is shifting outward from the leading edge of the rudder for DP50. On the contrary, the stagnation point moves inward of the blade leading edge for DP20 as it is more aligned with the flow. As a result, the rudder has significantly higher resistance relative to the BD and DP50 cases.

As it is for DP50, a higher toe-in angle could be considered an advantage in getting high positive rudder forces. However, the results in

Table 9 indicate that the Pressure Recovery Force ( $F_{PR}$ ) shown in Eq 5 has more influence over the effective power.

$$F_{PR} = F_{H(App)} - F_{H(Bare)} \quad (5)$$

Shifting the high-pressure region towards the leading edge or inner surface, the stern of the ship starts interacting with the rudders relatively in the positive pressure area. As a result, a higher pressure recovery force is obtained from the hull.

As shown in

Table 9, the total rudder force ( $F_{GRS,T}$ ) calculated on DP50 reduced significantly to  $-0.63$  kN from  $-2.63$  kN relative to BD, while it increased to  $-7.13$  kN for DP20. On the contrary, the pressure recoveries are negative (additional resistance) for BD and DP50 at  $-1.46$  and  $-9.28$  kN, respectively. Meanwhile, the calculated  $F_{PR}$  for DP20 is positive (resistance recovery) at  $3.34$  kN, which means the  $F_H$  of DP20 is lower than the resistance of the bare hull.

To sum up, DP20 has a  $+0.33$  kN additional resultant force (net force of  $F_{PR}$  and  $F_{GRS,T}$ ) over BD, while DP50 has a  $-5.82$  kN (extra resistance). The resistance advantage of DP20 can be seen in calculated effective power as well in

Table 9. DP20 has slightly lower  $P_E$  at  $-0.2\%$  over BD. Meanwhile, DP50 has a  $3.7\%$  higher effective power than BD.

### 5.2.1 Propulsion Condition

Similar investigations were conducted, including the action of the propeller in the propulsion condition. In this condition, unlike the calculated negative axial forces (resistance) on the rudders, there is a significant increment in the forces (i.e. developing positive thrust force) due to the effect of the propeller. As DP has a higher angle of attack, the rudder force ratio (F/T) of DP50 has the highest value of  $9.0\%$  among the results presented in

Table 9. Because of its more inline with the incoming flow, DP20 has the lowest F/T of  $2.6\%$ , while BD has a value of  $+6.8\%$ .

Similar to the towing condition, the pressure recovery was found to be significantly higher for DP20. While the pressure recovery rates are negative for the DP50 and BD cases, displaying an extra  $18.56$  kN and  $6.81$  kN resistance values (equal to F/T values of  $-9.7\%$  and  $-3.7\%$ , respectively), the DP20 case displays a pressure recovery of  $1.0$  kN, (i.e., F/T of  $0.6\%$ ). The resultant force for DP20 is  $0.32$  kN and  $7.18$  kN higher than the BD and DP50 cases, respectively.

As shown in

Table 9, there is a  $3.6\%$  saving in  $P_D$  calculated for the DP20 relative to the BD case. The  $P_D$  for DP20 is even  $0.8\%$  lower than the  $P_D$  for the Bare Hull case. DP50, the design with the highest  $F_{GRS,T}$ , presents  $1455$  kW of  $P_D$ , which is  $8.8\%$  higher than the BD case.

The force distributions along the gate rudder blade (height or span) in terms of the pressure coefficients are given in Fig. 19 for the BD, DP20 and DP50 cases at both towing and propulsion conditions. The vertical part of the rudder is divided into eight equal sections starting from the blade tip at the bottom) to the rudder stock at the top. The shoulder and upper sections are kept in separate parts, which are parts 9 and 10, respectively, for the force discretisation. It is clearly seen that the DP20's force distribution is significantly lower than other designs, as shown in Fig. 19. However, especially the calculated values at the blade tip region (part 1) are similar to the BD case, while it has the weakest blade tip vortex. The reason is that the DP20 is more aligned with the flow, and hence the tip vortex and force (thrust) reduction are relatively less than the other two designs, as can be shown in Fig. 20. Especially, DP50 has the strongest tip vortex structure and, as a result, the dramatic force reduction at the blade tip.

From Table 7, behind hull efficiency ( $\eta_B$ ) is the highest at DP50 since the propeller's operation point is at a favourable advance coefficient of  $J = 0.58$ , while others are at less favourable smaller  $J$ s as shown in Table 9. Although the propeller efficiency for the DP50 case is higher than the rest of the design cases, it is still the least favourable design in terms of the delivered power. It means the significant difference comes from the hull efficiency ( $\eta_H$ ), which is a function of the thrust deduction fraction ( $t$ ) and wake fraction ( $\omega$ ) as given in Eq. 6.

$$\eta_H = \frac{1 - t}{1 - \omega} \quad (6)$$

Here the thrust deduction ( $t$ ) is not changing based on the GRS rudder design or rudder angle for the investigated cases. Therefore, it is necessary to give a clear answer to the question of how the power requirements are  $-3.6\%$  for the DP20 and  $+8.8\%$  for the DP50 case relative to the BD case, while the propeller thrusts are only  $-0.2\%$  and  $+4.8\%$  of the BD's thrust.

As shown in Table 7, DP20 is the GRS design case with the highest  $\eta_H=1.24$ , while the contributing values of  $\omega$  and  $t$  are similar for the three selected GRS design cases. The highest calculated  $\omega$  is 0.305 for DP20 within the three design cases. This means there is a relatively lower velocity at the propeller cross-section. As a result, there is higher static pressure (as shown in Fig. 18) and higher  $\eta_H$ . Also, the correlation graphs for the wake and  $P_D$  give a global indication which shows that lower  $P_D$  is calculated with a higher wake fraction, as shown in Fig. 17.

**Table 7.** Non-dimensional coefficients for the chosen cases

Case	$t$	$\omega$	$\eta_o$	$\eta_R$	$\eta_B$	$\eta_H$	$\eta_D$
Bare Hull	0.181	0.344	0.59	1.003	0.59	1.25	0.74
Base Design	0.135	0.261	0.63	1.000	0.63	1.17	0.73
DP20	0.135	0.305	0.61	1.002	0.61	1.24	0.76
DP50	0.135	0.210	0.64	0.997	0.64	1.09	0.70

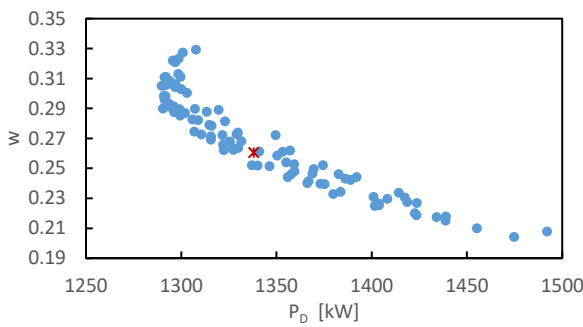


**Fig. 17.** Correlation between GRS thrust force vs  $P_D$

### 5.3 Design Validation

As stated earlier, the simplified approach was used for both modellings of the fluid domain and propeller (using VD) in the DoE study and the case-by-case comparisons. However, here in the design validation study, the full domain was modelled by employing the SM approach in order to make sure that predicted power in DoE saving was met with high the fidelity CFD calculation.

The force variables are compared between the BD and DP20 cases in Table 8. With the more comprehensive design validation case, an additional 1.6% per cent reduction in  $P_D$  was calculated. As a result, the optimum rudder design, at the optimum rudder angle, provides a 5.2% power saving relative to the base design. For further information the powering performance parameters for CRS are also included in Table 8.

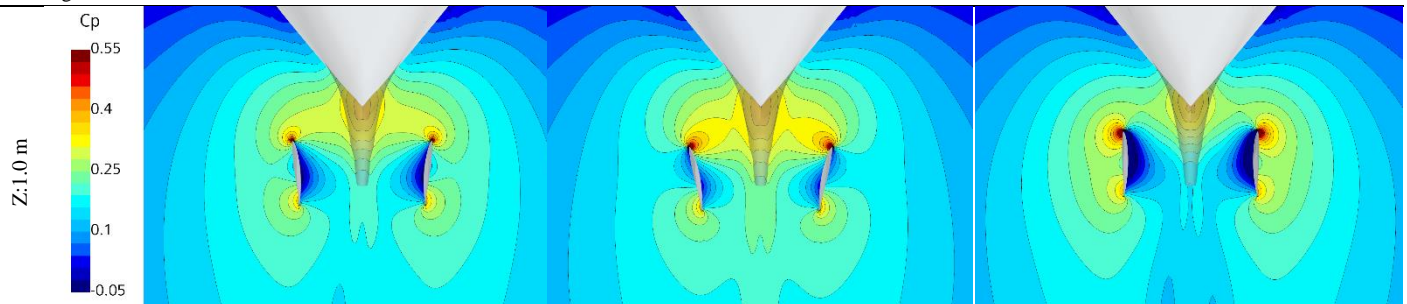
**Table 8.** High fidelity CFD results for CRS, GRS BD and DP20

	CRS	GRS BD	GRS DP20	$\delta\phi_{DP20 \text{ vs BD}}$
T, N	212.2	189.0	187.4	-0.8%
Q, kN.m	98.1	93.8	91.3	-2.6%
N, rpm	151.5	136.8	133.20	-2.6%
$P_D$ , kW	1556	1344	1274	-5.2%
$R_{GRS \text{ PRT}}$ , kN	-	6.3	1.9	-70.5%
$R_{GRS \text{ STB}}$ , kN	-	5.1	1.6	-69.3%

**Table 9.** Forces and power values for different cases

Case	$F_{Ship}$ (kN)	$F_H$ (kN)	$F_{PR}$ (kN)	$F_{GRS\_T}$ (kN)	T (kN)	Q (kN.m)	N (RPM)	J [1]	w [1]	t [1]	$P_E$ kW	$P_D$ kW
Bare Hull (T)	-155.17	-155.17	-	-	-	-	-	-	-	-	958	-
(P)	-189.50	-189.50	-	-	189.51	95.10	130.5	0.517	0.344	0.181	-	1300
Base Design (T)	-159.26	-156.63	-1.46	-2.63	-	-	-	-	-	-	983	-
(T)	-184.04	-196.31	-6.81	12.27	184.01	94.69	134.9	0.564	0.261	0.135	-	1338
DP20 (T)	-158.93	-151.80	3.38	-7.13	-	-	-	-	-	-	981	-
(P)	-183.72	-188.50	1.00	4.78	183.71	93.41	131.8	0.542	0.305	0.135	-	1290
DP50 (T)	-165.08	-164.45	-9.28	-0.63	-	-	-	-	-	-	1019	-
(P)	-190.09	-208.06	-18.56	17.16	190.90	99.27	140.0	0.581	0.210	0.135	-	1455

Towing Condition



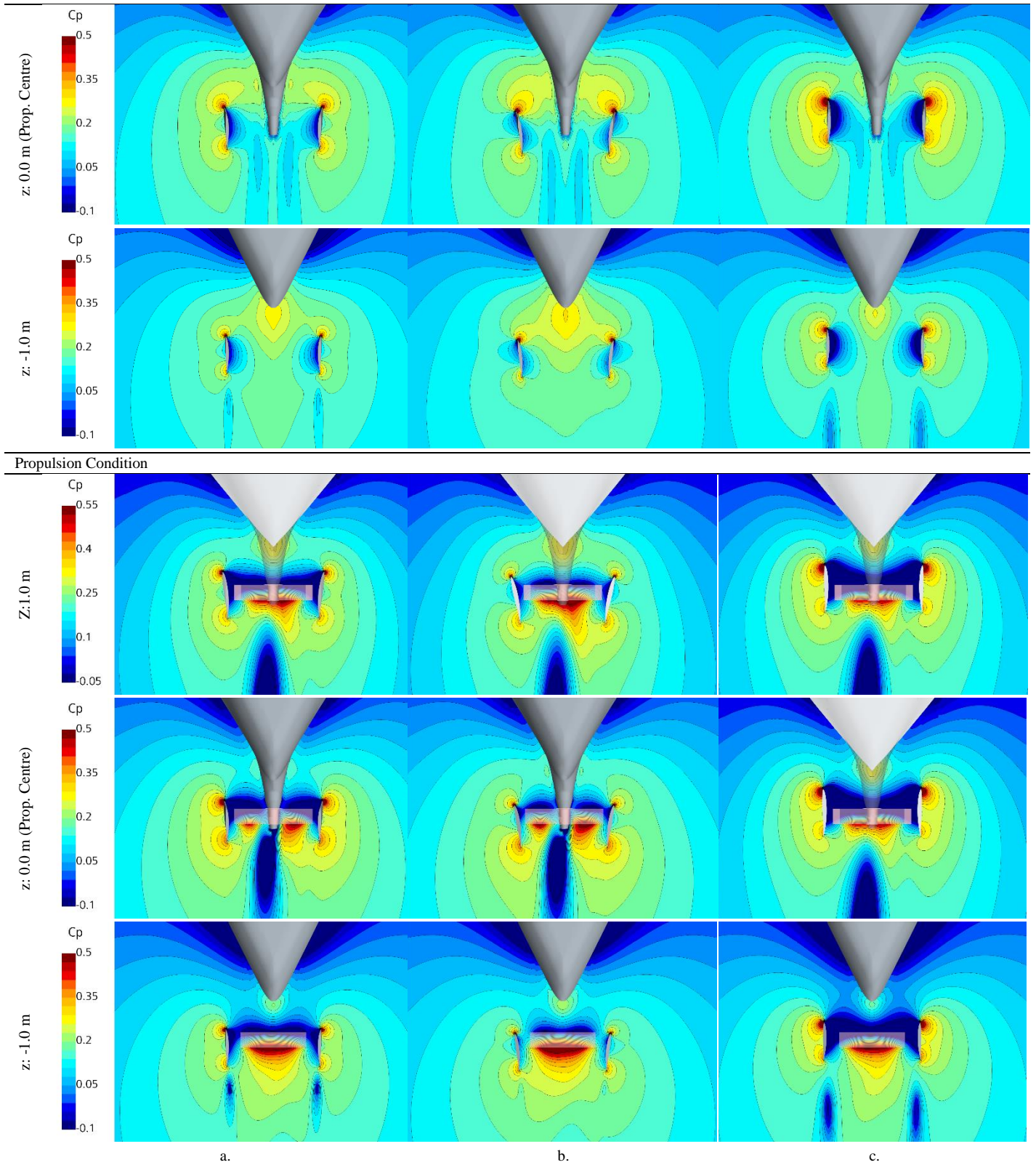


**Fig. 18.** Pressure coefficient at the stern of the ship at different horizontal sections; a.BD, b.DP20, c.DP50

---

Towing Condition

---

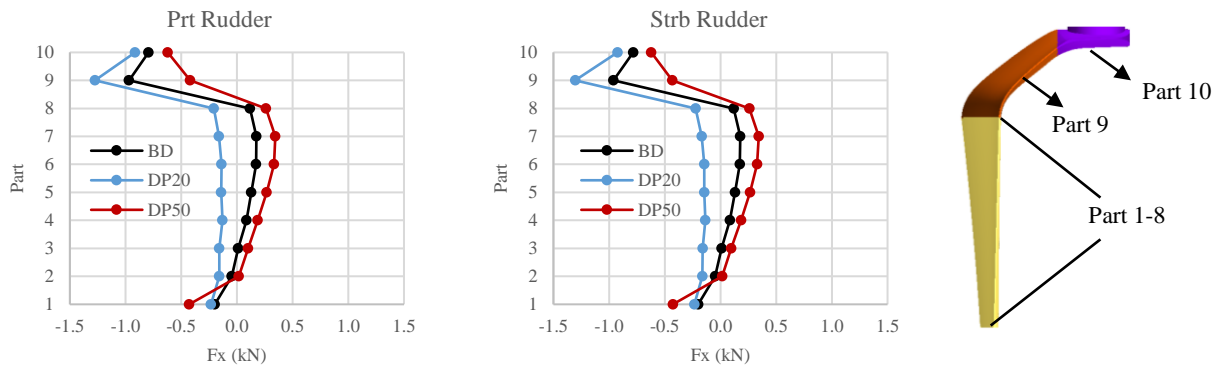
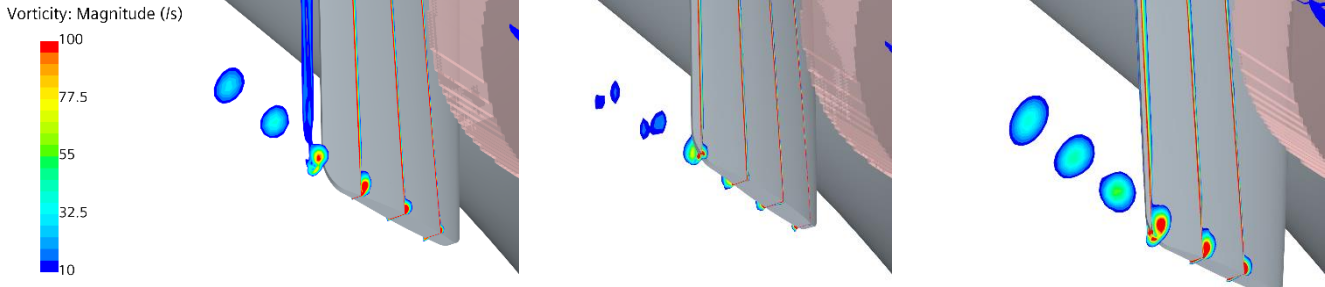


Fig. 19. Pressure coefficient along the gate rudder height at different horizontal sections; a.BD, b.DP20, c.DP50

Towing Condition



Propulsion Condition

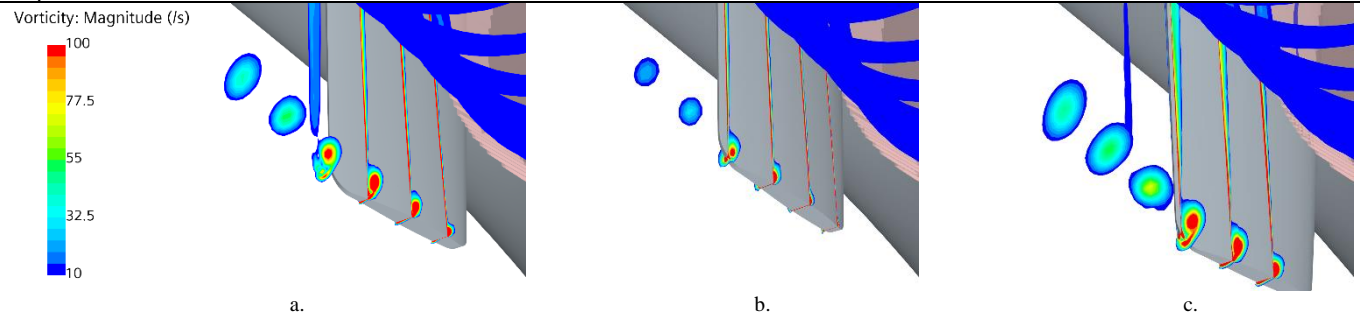


Fig. 20. Vorticities at rudder tip region; a.BD, b.DP20, c.DP50

6 Conclusions

The main objective of this paper is to provide a design/optimisation perspective for the GRS design methodology development in the GATERS project.

In order to determine the critical (fundamental) design parameters for the GRS influencing the ship's powering performance, the DoE approach based on the Sobol Algorithm can be effective.

Based on the DoE set-up conducted and applied on a 90m cargo vessel in this study, the most critical GRS design parameter was found to be the rudder angle. With an optimised rudder angle, the propulsion performance of the GRS can be improved by decreasing the power requirement around 5%. In this study, it was proved that improvement in power saving relative the CRS is for 13.7% for BD while this saving become 18.1% for DP20 by means of DoE. Indeed, a further improvement would also be possible with a new wake-adapted propeller design.

Although the positioning of the GRS relative to the propeller could be another influential design parameter to explore, this may be constrained probably by the steering room arrangement, especially for retrofit GRS design cases.

However, the main design objective for the best GRS design should not be the GRS thrust force. Instead, powering performance could be optimised by maximising the wake fraction and pressure recovery through the mutual interaction amongst the aft end, propeller and gate rudder blades.

## 7 References

- Agreement, G. (2020). *GATERS-H2020-MG-2018-2019-2020/H2020-TwoStages* - No: 860337. The European Commissions .
- Carchen, A., Turkmen, S., Piaggio, B., & Shi, W. (2020). Investigation of the manoeuvrability characteristics of a Gate Rudder system using numerical, experimental, and full-scale techniques. *Applied Ocean Research*.
- Carchen, C., Shi, W., Sasaki, N., & Atlar, M. (2016). A prediction program of manoeuvrability for a ship with a Gate Rudder system. *2nd International Meeting on Recent Advances in Prediction Techniques for Safe Manoeuvring of Ships and Submarines*. Istanbul.
- Celik, I. B., Ghia, U., Roache, P. J., Freitas, C. J., Coleman, H., & Raad, P. E. (2008). Procedure for estimation and reporting of uncertainty due to discretization in CFD applications. *Journal of Fluids Engineering-Transactions of the ASME 078001-078001-4* , 130(7).
- Celik, I. B., Ghia, U., Roache, P. J., Freitas, C. J., Colmena, H., & Raad, P. E. (2008). Procedure for estimation and reporting of uncertainty due to discretization in CFD applications. *Journal of Fluids Engineering-Transactions of the ASME 0078001-078001-4*, 130(7).
- FSYS. (2022, November). *CAESES*. Retrieved from Friendship System: <https://www.caeses.com/about-us/>
- IMO. (2018). *Adoption of the initial IMO strategy on reduction of GHG emissions from ships and existing IMO activity related to reducing GHG emissions in the shipping sector*. International Maritime Organization.
- ITTC. (2014). *Partical Guidelines for Ship Self-Propulsion CFD*.
- Navid, A., Khalilarya, S., & Abbasi, M. (2018). Diesel engine optimization with multi-objective performance characteristics by non-evolutionary Nelder-Mead algorithm: Sobol sequence and Latin hypercube sampling methods comparison in DoE process. *Fuel*, 349-367.
- Niederreiter, H. (1992). Random number generation and quasi-Monte Carlo methods. *Soc.for Ind. and Appl. Math.*
- Richardson, L. F. (1911). The approximate arithmetical solution by finite differences of physical problems involving differential equations, with an application to the stresses in a masonry dam. *Transactions of the Royal Society of London*, 210(459-490).
- Richardson, L. F., & Gant, J. A. (1927). The deferred approach to the limit. *Transactions of the Royal Society of London*, 226(636-646).
- Richardson, L. F., & Gant, J. A. (1927). The deferred approach to the limit. *Transactions of the Rotal Society of London*, 266(636-646).
- Sasaki, N., Atlar, M., & Kuribayashi, S. (2015). Advantages of twin rudder system with asymmetric wing section aside a propeller. *Journal of Marine Science and Technology*.
- Sasaki, N., Kuribayashi, S., & Miles, A. (2019). Full scale performance of gate rudder. *Propellers & Impellers – Research, Design, Construction & Applications*. London.
- Sasaki, N., Kuribayashi, S., Atlar, M., & Fukazawa, M. (2020). Towards a realistic estimation of the powering performance of a ship with a gate rudder system. *Journal of Marine Science and Engineering*.
- Sobol, I. (1967). Distribution of points in a cube approximate evaluation of integrals. *U.S.S.R. Comput. Maths. Math. Phys. 7 (in English)*, 86-112.
- StarCCM+. (2022, November). *Star CCM+*. Retrieved from Siemens: <https://www.plm.automation.siemens.com/global/en/products/simcenter/STAR-CCM.html>
- Turkmen, S., Carchen, A., Sasaki, N., & Atlar, M. (2016). A New Energy Saving Twin Rudder System - Gate Rudder. *International Conference on Shipping in Changing Climates (SCC 2015)*. Glasgow.